The development of biomimetic scaffolds for osteochondral tissue engineering

A thesis submitted to the University of Dublin in partial fulfilment of the requirements for the degree of Doctor in Philosophy

2020

Pedro J. Díaz Payno

Supervisor: Professor Daniel J. Kelly

Declaration

I declare that this thesis has not been submitted as an exercise for a degree at this or any other university and it is entirely my own work.

I agree to deposit this thesis in the University's open access institutional repository or allow the Library to do so on my behalf, subject to Irish Copyright Legislation and Trinity College Library conditions of use and acknowledgement.

The thesis includes the unpublished and/or published work of others, duly acknowledged in the text wherever included.

Pedro Jose Díaz Payno

27/09/2019

Summary

Articular cartilage (AC) is a soft tissue lining the ends of the bones in our joints. Even minor lesions in AC cause pain, impaired mobility and can develop to osteoarthritis (OA), a disease affecting millions of adults worldwide. Within damaged or diseased synovial joints, such as the knee, this damage can penetrate to the underlying bone, creating an osteochondral (OC) defect. OC defect repair remains a significant clinical challenge and necessitates unique tissue engineering strategies.

In the recent years, there has been an increased interest in the use of decellularized extracellular matrix (ECM) derived scaffolds as they contain structural and soluble biomolecules supportive of tissue and organ regeneration. While ECM-based materials tend to be highly biocompatible and promote a pro-regenerative immune response, a number of studies have demonstrated that the specific tissue from which the ECM is extracted plays a crucial role in instructing the differentiation of infiltrating cells, helping to direct the type of new tissue formed. In the field of orthopaedic tissue engineering, ECM extracted from articular cartilage (AC) and growth plate (GP) has previously been used to generate scaffolds with chondro- and osteo-inductive properties, respectively. While the direct use of such decellularized ECMs is highly promising, clinical translation is hindered by a number of key challenges. Firstly, the mechanical properties of ECM derived scaffolds are commonly insufficient for use in high load bearing region such as synovial joints. Secondly, the internal architecture of such scaffolds is typically not conducive to facilitate rapid cellular infiltration. In addition, the architecture of such scaffolds needs to be carefully designed as it plays a role in directing cell differentiation and the organization of the resulting tissue. Thirdly, the different physicochemical treatments used during the decellularization of ECM can deplete it of its resident growth factors, thus diminishing its capacity to support tissue-specific differentiation.

The overall aim of this thesis is to develop a biomimetic ECM derived scaffold that can spatially direct the differentiation of adult stem cells. The specific aims are (i) to characterise the ECM proteome of AC and GP tissues, (ii) to develop scaffolds mimicking the composition of these tissues, (iii) to engineer scaffolds recapitulating aspects of the native tissue architecture to promote the recruitment of infiltrating cells and to direct their organization and differentiation, and (iv) to evaluate its potential for cartilage, bone and osteochondral tissue engineering *in vitro* and *in vivo*.

In this thesis, it is demonstrated that the cartilaginous ECM of AC and GP contain distinct soluble factors that may play important roles in promoting stable chondrogenesis and endochondral bone respectively. The ECM of AC contained factors such as Gremlin-1 (GREM1), transforming growth factor-β induced (TGBI) and frizzle-related protein (FRZB), critical for maintaining cartilage homeostasis; while GP ECM contained osteolectin (CLEC11A), s100a10, collagenase 13 (MMP13) and osteonectin (SPARC), which are known to be integral to joint and long bone development. The chosen AC ECM factors and GP ECM factors were supplemented in the media to assess their effect on chondrogenesis and osteogenesis of MSCs. Based on this analysis, GREM1 was further studied to assess its effect on cartilage tissue deposition by MSCs in an optimised scaffold model, which was made of the collagenous fraction of pepsin-solubilised AC ECM. A novel freeze-drying process combining directional freeze-casting and annealing process was developed to fabricate an AC ECM derived scaffolds with tailored pore size and anisotropic microarchitecture. Increased pore size enhanced cell infiltration, while an anisotropic architecture enabled oriented matrix deposition mimicking aspects of the collagen architecture of articular cartilage. Finally, it was possible to develop a bilayered scaffold made up of AC ECM and bone ECM for osteochondral tissue engineering applications, that was able to support spatially defined MSC differentiation *in vitro* and the development of spatially distinct tissues *in vivo*. The results of the preclinical studies in a caprine model, although preliminary, would appear to demonstrate that the scaffolds can promote more consistent repair of osteochondral defects, particularly in animals with a low endogenous capacity for spontaneous bone regeneration.

Acknowledgements

And though I'm nobody's poet I thought it wasn't half bad.

- Rupert Holmes

Glossary of abbreviations

Abbreviation	Meaning
3D	Three-dimensional
3DP	Three-dimensional printing
ABC	Ammonium bicarbonate
AC	Articular cartilage
ACI	Autologous chondrocyte implantation
AER	Apical ectodermal ridge
AMIC	Autologous matrix-induced chondrogenesis
ANGPTL2	Angiopoietin-related protein 2
bFGF	basic Fibroblast growth factor
BMP	Bone morphogenic protein
BMS	Bone marrow stimulation
BN	Bone
CAD	Computer aided design software
CaP	Calcium phosphate
CDM	Chemically modified medium
CLEC11A	Osteolectin
CM	Chondrogenic medium
COL1	Collagen type I
COL10	Collagen type X
COL2	Collagen type II
CRISPR	Clustered regularly interspaced short palindromic repeats
DNA	Deoxyribonucleic acid
DTT	Dithiothreitol
ECM	Extracellular Matrix
EGF	Epidermal growth factor
ESCs	Embryonic stem cells
FDA	Food and Drug administration
FDM	fused deposition modelling
Fe	Iron
FFF	Fused filament fabrication
FRZB	Frizzle-related protein
GAG	Glycosaminoglycans
GAPDH	Glyceraldehyde 3-phosphate dehydrogenase
GelMA	Gelatine methacrylate
GnHCL	Guanidine Hydrochloride
GP	Growth plate
GREM1	Gremlin-1
HxP	Hydroxyproline
IAA	Iodoacetamide
ICP	Injectable calcium phosphate

iPSCs	Induced pluripotent stem cells
LG	Ligament
MACI	Matrix-induced autologous chondrocyte implantation
Mg	Magnesium
MMP13	Metalloproteinase 13
MMP9	Metalloproteinase 9
Mn	Manganese
mRNA	Messenger RNA
MS/MS	Tandem Mass Spectrometry
MSC	Mesenchymal stem/stromal cell
OA	Osteoarthritis
OC	Osteochondral
OCP	Octacalcium phosphate
OM	Osteogenic medium
OPF	Oligo(poly(ethyleneglycol)fumarate)
P11	S100 calcium-binding protein A10
PCL	Polycaprolactone
PCR	polymerase chain reaction
PEGMA	Poly(ethylene glycol) methacrylate
PGA	polyglycolic acid
PLA	polylactic acid
RNA	Ribonucleic acid
RUNX2	Runt-related transcription factor 2
S100A10	S100 calcium-binding protein A10
SAS	Subarticular spongiosa
SBP	Subchondral bone plate
sGAG	Sulphated glycosaminoglycans
SLA	Stereolithography
SLS	Selective laser sintering
SOX9	Sex-determining region Y-related high mobility group-box 9
TCA	Trichloroacetic
TCP	Tricalcium phosphate
TGBI or βIGH3	Transforming growth factor-β induced protein
TGFβ3	Transforming growth factor beta 3
TIPS	Thermally induced phase separation
TRPV	Transient receptor potential cation channel subfamily V
TTCP	Tetracalcium phosphate

Publications arising from this thesis

Articles

Cunniffe, G. M.*, Díaz-Payno, P. J.*, Sheehy, E. J., Critchley, S. E., Almeida, H. V., Pitacco, P., Carroll, S. F., Mahon, O. R., Dunne, A., Levingstone, T. J., Moran, C. J., Brady, R. T., O'Brien, F. J., Brama, P. A. J. & Kelly, D. J. Tissue-specific extracellular matrix scaffolds for the regeneration of spatially complex musculoskeletal tissues. *Biomaterials* **188,** 63–73 (2019).

Browe, D. C., Mahon, O. R., Díaz-Payno, P. J., Cassidy, N., Dudurych, I., Dunne, A., Buckley, C. T. & Kelly, D. J. Glyoxal cross-linking of solubilized extracellular matrix to produce highly porous, elastic, and chondro-permissive scaffolds for orthopedic tissue engineering. *J. Biomed. Mater. Res. Part A* **107,** 2222–2234 (2019).

Fiona Freeman *et al.* Biofabrication of multiscale bone extracellular matrix scaffolds for bone tissue engineering. Accepted for publication in *European cells & materials* (2019).

Conferences

Diaz-Payno PJ, Browe DC, Freeman FE, Nulty J, Burdis R, Kelly DJ. Engineering phenotypically stable articular cartilage using tissue-specific extracellular matrix inspired scaffolds. Gordon Research Conference (Biomaterials and Tissue engineering), Barcelona, Spain. Jul 27-Aug 28, 2019. Accepted for poster presentation.

Diaz-Payno PJ, Browe DC, Kelly DJ. Effect of Pore Microarchitecture in Extracellular Matrix Derived Scaffolds on Chondrogenesis of Bone Marrow Cells. Tissue Engineering and Regenerative Medicine Society (EU Chapter), Rhodes, Greece. May 27-31, 2019. Accepted for poster presentation.

Diaz-Payno PJ, Browe DC, Freeman FE, Nulty J, Burdis R, Kelly DJ. Engineering phenotypically stable articular cartilage using tissue-specific extracellular matrix inspired scaffolds. Tissue Engineering and Regenerative Medicine Society (EU Chapter), Rhodes, Greece. May 27-31, 2019. Accepted for Oral presentation.

Diaz-Payno PJ, Kelly DJ. Regeneración tisular de lesiones de cartílago en rodilla. Thesis in 3, Spanish Research Society in Ireland, Dublin, Ireland. Mar 27, 2019. Oral presentation.

Diaz-Payno PJ, Browe DC, Freeman FE, Nulty J, Burdis R, Kelly DJ. Extracellular matrix inspired scaffolds for engineering phenotypically stable articular cartilage. 25th Bioengineering in Ireland, Limerick, Ireland. Jan 18-19, 2019. Oral presentation.

Diaz-Payno PJ, Browe DC, Kelly DJ. Effect of pore microarchitecture in extracellular matrix derived scaffold on chondrogenesis of mesenchymal stem cells. Tissue Engineering and Regenerative Medicine Society (World Congress), Kyoto, Japan. Sep 4-7, 2018. Poster presentation.

Díaz-Payno PJ, Cunniffe GM, Sheehy EJ, Critchley SE, Almeida HV, Pitacco P, Carrol S,

Mahon O, Dunne A, Levingstone T, Moran C, Brady R, Brama PAJ, O'Brien FJ, Kelly DJ. Layering of tissue-specific ECM scaffolds for the regeneration of spatially-complex musculoskeletal tissues. Tissue Engineering and Regenerative Medicine Society (World Congress), Kyoto, Japan. Sep 4-7, 2018. Poster presentation

Diaz-Payno PJ, Browe DC, Kelly DJ. Effect of pore microarchitecture in extracellular matrix derived scaffold on chondrogenesis of mesenchymal stem cells. World Congress of Biomechanics, Dublin, Ireland. Jul 8-12, 2018. Poster presentation

Diaz-Payno PJ, Scheurer S, Browe DC, Kelly DJ. Salt and vinegar C.H.I.P.S. (collagen harvested Irish porcine scaffolds) for cartilage tissue engineering. International Postgraduate Research Conference, Trinity College Dublin, Ireland. Mar 15, 2018. Poster presentation.

Diaz-Payno PJ, Scheurer S, Browe DC, Kelly DJ. Salt and vinegar C.H.I.P.S. (collagen harvested Irish porcine scaffolds) for cartilage tissue engineering. 4th Multidisciplinary Research Showcase, Trinity College Dublin, Ireland. Mar 13, 2018. Poster presentation.

Diaz-Payno PJ, Browe DC, Kelly DJ. Effect of pore microarchitecture in extracellular matrix derived scaffold for cartilage tissue engineering. 24th Bioengineering in Ireland, Dublin, Ireland. Jan 26-27, 2018. Oral presentation.

Díaz-Payno PJ, Cunniffe GM, Sheehy EJ, Critchley SE, Almeida HV, Pitacco P, Carrol S, Mahon O, Dunne A, Levingstone T, Moran C, Brady R, Brama PAJ, O'Brien FJ, Kelly DJ. A bi-layered scaffold derived from decellularized articular cartilage and growth plate extracellular matrix for osteochondral defect repair. 4th Matrix Biology Ireland. Nov 30-Dec 1, 2017. Oral presentation.

Díaz-Payno PJ, Browe D, Cunniffe GM, Kelly DJ. Pore alignment regulates MSC differentiation in solubilized extracellular matrix derived scaffolds. Tissue Engineering and Regenerative Medicine Society (TERMIS), EU Chapter, Davos, Switzerland. Jun 26-30, 2017. Poster presentation.

Díaz-Payno PJ, Cunniffe GM, Critchley SE, Carrol S, Sheehy EJ, Pitacco P, Almeida HV, Levingstone T, Moran C, Brady R, Brama PAJ, O'Brien FJ, Kelly DJ. Development of a bilayered decellularized extracellular matrix (ECM) derived scaffold for osteochondral tissue regeneration in a caprine model. International Postgraduate Research Conference, Trinity College Dublin, Ireland. May 5-6, 2017. Poster presentation.

Díaz-Payno PJ, Cunniffe GM, Critchley SE, Carrol S, Sheehy EJ, Pitacco P, Almeida HV, Levingstone T, Moran C, Brady R, Brama PAJ, O'Brien FJ, Kelly DJ. Development of a bilayered decellularized extracellular matrix (ECM) derived scaffold for osteochondral tissue regeneration in a caprine model. 3rd Multidisciplinary Research Showcase, Trinity College Dublin, Ireland. Mar 14, 2017. Poster presentation.

Díaz-Payno PJ, Cunniffe GM, Sheehy EJ, Critchley SE, Almeida HV, Levingstone T, Moran C, Brady R, Brama PAJ, O'Brien FJ, Kelly DJ. Development of a bilayered decellularized extracellular matrix (ECM) derived scaffold for osteochondral tissue regeneration in a caprine model. 3rd Spanish Research Society in Ireland meeting, University College Dublin. Jan 26, 2017. Poster presentation.

Díaz-Payno PJ, Browe D, Kelly DJ. Effect of the pore alignment in solubilized extracellular matrix derived scaffolds for osteochondral tissue engineering. 23rd Bioengineering in Ireland, Queen's University Belfast, Northern Ireland. Jan 20-21, 2017. Oral presentation.

INDEX

1. CHAPTER: Introduction

1.1. Cartilage damage and Osteoarthritis

Articular cartilage is a soft hydrated tissue lining the bones in our synovial joints which helps to distribute the high loads passing through these joints. It has unique viscoelastic, compressive, tensile and frictional properties[1] which enable for a smooth, pain free articulation between bones. The main components of cartilage are water (65-85% w/w), collagen (12-24% w/w) and sulphated glycosaminoglycans (sGAG, 3-6% w/w), among other less abundant proteins or factors[2].

Cartilage injuries are relatively common and can be very painful, leading to impaired mobility and often progressing to osteoarthritis (OA) if left untreated. Amongst all types of arthritis (from greek *arthron* 'joint' and *itis* 'inflammatory disease'), OA is the most prevalent form and it affects millions of adults worldwide (Figure 1-1). In Europe, more than 50% of the population over 60 years old suffers from this disease. In Ireland, OA costs the state €1.6 billion *per annum* in lost working hours and early retirement due to this substantial prevalence in middle-aged persons[3,4]. Generally, the incidence is greater in women than men and specifically, it affects more the knee than any other joint[5] (Figure 1-2).

DALY rates from Osteoarthritis per 100,000 inhabitants.
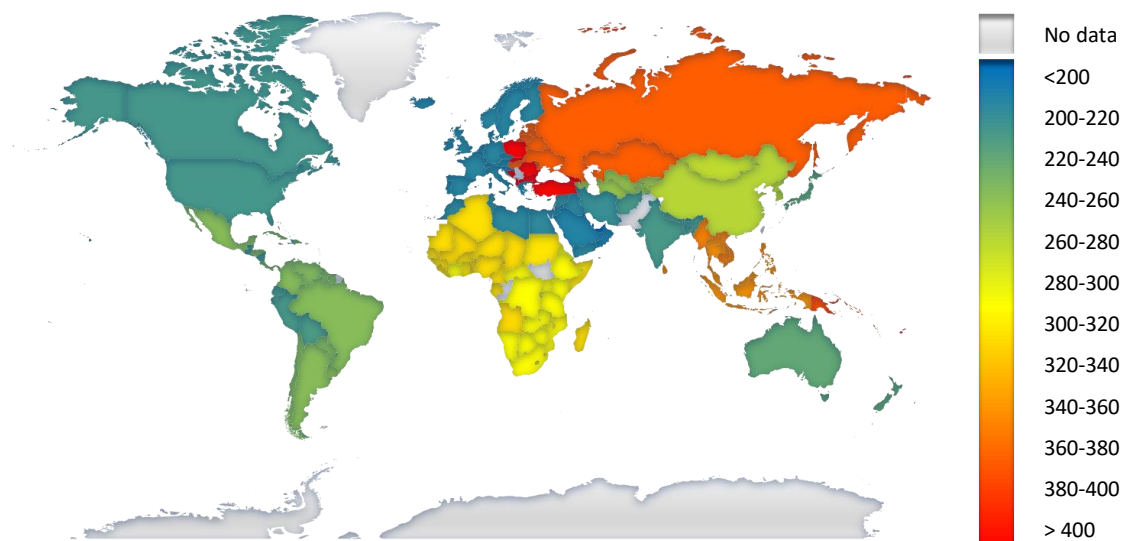
Figure 1-1. Pandemic prevalence of Osteoarthritis: colour heat worldwide map showing the age-standardised disability-adjusted life year (DALY) rates for osteoarthritis by country (per 100,000 inhabitants) in 2004. Figure made with data from World Health Organisation[6].
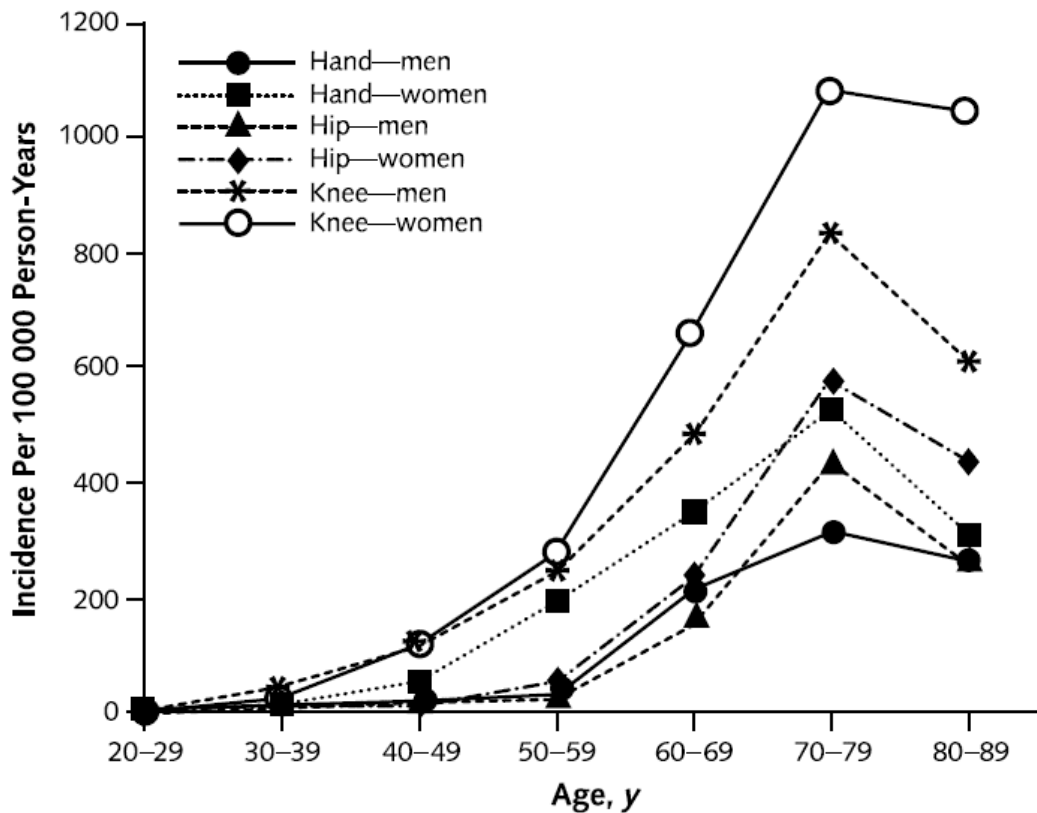
Figure 1-2. Incidence of OA in hand, hip and knee in members of the Fallon Community Health Plan, 1991-92, by age and sex[5].

The lack of an extended vascular network in hyaline cartilage prevents critical size defects following the typical scar tissue remodelling cascade of bleeding, inflammation, proliferation and remodelling. Consequently, injured cartilage degenerates and loses its protective functionality, ultimately compromising the integrity of the underlying subchondral bone and the joint itself. This process was described by William Hunter in 1753 "[…], the malignancy, having got root in the bone, will daily gain ground, the caries will spread, and at last the unhappy person will submit to extirpation, a doubtful remedy, or wear out a painful, though probably a short life [...]" [7].

The reference above demonstrates OA is not a new problem and its development is well known. However, despite all previous attempts to repair chondral and osteochondral defects, its regeneration still remains a significant clinical challenge. This motivates the development of new tissue engineering (TE) strategies to regenerate articular cartilage and its complex interface with the subchondral bone.

1.2. ECM derived scaffolds for bone and joint regeneration

In the recent years there has been an increased interest in the use of the extracellular matrix (ECM) of mammalian tissues as biomaterials for tissue regeneration as they provide cells with the complex microenvironment of a natural tissue. This ECM may contain both the soluble (*e.g.* growth factors) and structural (*e.g.* collagen) molecules to drive the desired differentiation of progenitor cells, that are either seeded onto such constructs prior to implantation or are recruited into the scaffold post-implantation[8–10]; and facilitate the repair of specific tissues[11–16].

It is important to establish a classification criterion for the different types of ECM used in tissue engineering (Figure 1-3). First, to delineate between the sources of ECM, either derived from native tissue or derived from matrix produced by cultured cells *in vitro*. Secondly, to characterise the ECM based on the processing method, *i.e.*, untreated, devitalised or decellularized. Last but not least, to define the ECM depending on the final form it takes prior to implantation: particulate, solubilised, as a scaffold or unmodified.
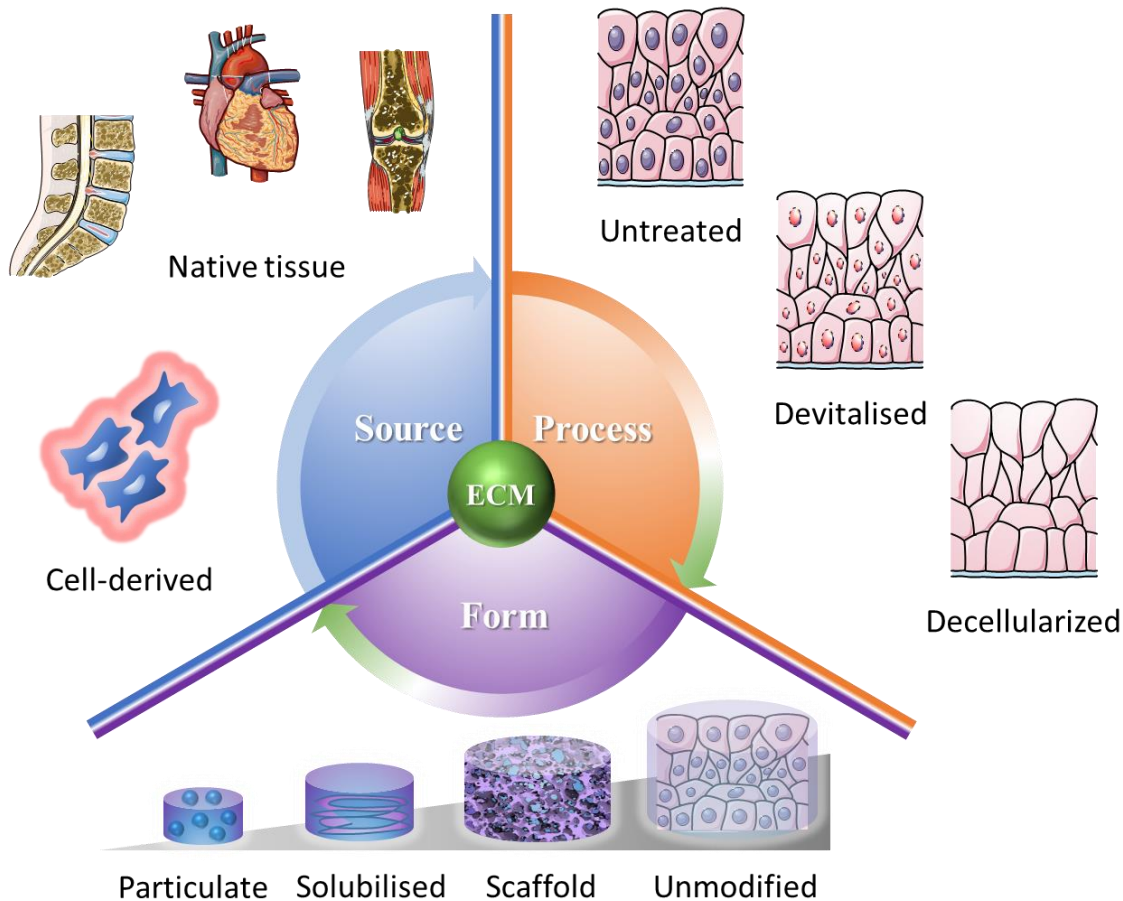
Figure 1-3*. Classification of ECM depending on (i) source: native tissue or cell-derived matrix; (ii) process method: untreated, devitalised or decellularized; and (iii) form: particulate, solubilised, in scaffold form or unmodified.*

Devitalisation and decellularization of ECM derived biomaterials are the main prerequisites to clinical translation. Thus, regenerative medicine approaches based on decellularized scaffolds derived from biological tissues are rapidly expanding[10,17–19]. The process consists of physically and/or chemically removing cells from a tissue, leaving behind the complex mixture of structural and soluble biomolecules that constitute the ECM[20]. Some preclinical studies underscore the benefits of devitalized/decellularized ECM material over live ECM as newly accessible bioactive sites may encourage rapid synthesis of new tissue in cartilage[21] and bone[22,23]. However, there are other studies reporting opposite outcomes, as decellularization may deplete key tissue-specific growth factors[24,25]. The inability to point out specific indications where decellularized products have added or not value in trauma reconstruction may be due to the lack of a standard

treatment to decellularize ECMs, which varies extensively the composition and amount of tissue-inductive factors.

In addition, decellularization efficiency depends on the physical or chemical properties of the tissue. Due to the dense nature of cartilage ECM in which cells are embedded, more vigorous protocols are required to achieve the standard of < 50 ng DNA per dry tissue[20,26,27] proposed in the literature by Badylak[27].The disadvantages associated with a harsher decellularization treatment are the destruction of ECM components or structure[28]. On the other hand, the decellularized ECMs can also be rebuilt into a scaffold through lyophilisation and crosslinking of the construct[29–31]. Alternatively, the ECM derived material can be combined with other materials to achieve the desired mechanical properties. Pre-clinical studies have demonstrated that cartilage ECM derived scaffolds support chondrogenesis *in vitro*, and can improve the healing of osteochondral defects when implanted into critically sized defects in large animals[32]. In spite of this, regeneration with hyaline cartilage was not consistently observed in these studies, pointing to the need for further improvements in ECM scaffold design to enhance joint regeneration.

1.3. Aims of the thesis

A large number of materials have (and are currently) being explored for osteochondral TE, suggesting that the ideal scaffold composition, to restore normal joint function, has yet to be identified. The overall goal of this thesis is to develop a new biomimetic scaffold for osteochondral defect regeneration, where the structure and composition of the scaffold was inspired by ECM of the growth plate and articular cartilage. The following specific aims are proposed to realise this:

Specific aim 1: To characterise the ECM proteome of Growth Plate and Articular Cartilage in order to identify osteo- and chondro-inductive factors

The complexity and diversity of the biomolecules present in the ECM is not yet fully characterised, hence their mechanism of therapeutic action remains poorly understood[33]. In order to shed some light on this complex topic, the first objective of this thesis is to undertake a proteomic characterization of the extracellular matrix of two

different musculoskeletal tissues, which our lab have previously demonstrated to promote tissue-specific differentiation, both *in vitro* and *in vivo*[29,34]. These tissues are porcine articular cartilage and growth plate. The goal is to identify soluble factors within these tissues that may impart specific chondro-inductivity or osteo-inductivity.

Specific aim 2: To assess the effect of soluble factors identified in the ECM of articular cartilage and growth plate on stabilising chondrogenesis and enhancing osteogenesis of MSCs

Mesenchymal stem cells seem a particularly attractive cell source for osteochondral tissue engineering. They can be easily extracted using standardized procedures and they are largely available. However, MSC derived chondrocytes tend to become hypertrophic and progress along an endochondral pathway, ultimately forming bone *in vivo*. We hypothesise that there are proteins in AC ECM that can regulate this process and help to engineer phenotypically stable cartilage. The second aim of this thesis is to examine if soluble factors predominantly expressed in (i) AC ECM can be used to engineer phenotypically stable cartilage with MSCs and (ii) GP ECM can be used to enhance osteogenesis of MSCs.

Specific aim 3: To optimise the pore morphology (size and microarchitecture) and mechanical properties of ECM derived scaffolds for musculoskeletal tissue engineering

The field of osteochondral tissue engineering has extensively investigated how the composition and bulk mechanical properties of scaffolds determine their efficacy[35,36]. While it is also well established that scaffold architecture is a key determinant of scaffold success[37], the ideal microarchitecture of ECM derived scaffolds targeting osteochondral defect repair has yet to be identified. Thus, the second objective of this thesis involves (i) developing a directional freeze-drying protocol in order to fabricate ECM derived scaffolds with aligned pores mimicking aspects of the architecture of the GP and deep zone of AC, (ii) optimising a freeze-drying protocol to control pore size and (iii) exploring the design and 3D printing of synthetic polymeric reinforcements for ECM scaffolds with the ultimate aim of optimising their mechanical properties for musculoskeletal applications.

Specific aim 4: To assess the effect of pore morphology on chondrogenesis and endochondral ossification of MSCs seeded onto ECM derived scaffolds

Mesenchymal stem cells seem a particularly attractive cell source for osteochondral tissue engineering. They can be easily extracted using standardized procedures and they are largely available. The fourth objective of this thesis is to determine the effect of ECM scaffold pore size, pore microarchitecture and composition on chondrogenesis of MSCs and the tendency of such engineered tissues to progress along an endochondral pathway.

Specific aim 5: To develop a biomimetic bilayered ECM derived scaffold for osteochondral tissue engineering

The final objective of this thesis first involves integrating the key developments outlined above to develop a freeze-dried, bilayered scaffold. A scaffold with an optimised anisotropic pore size structure, composed of two different tissue-specific ECMs with chondro-inductive (AC ECM) and osteo-inductive (bone ECM) properties will be produced using an iterative freeze-casting technique during the freeze-drying process. The capacity of this bilayered ECM scaffold to support spatially defined tissue development will be next assessed *in vitro*, followed by a large animal model study to assess its potential as an 'off-the-shelf' scaffold for osteochondral tissue regeneration.

2. CHAPTER: Literature review

2.1. The osteochondral unit

Osteochondral tissue of synovial joints has a very particular architecture and composition (Figure 2-1). It is broadly divided into articular cartilage and the underlying bone, which are very different tissues with a specific interface that connects the two of them. Articular cartilage is divided into three layers: superficial, middle and deep zone, which share the basic cartilage framework made from fibrillary type II collagen copolymerized with type XI and IX collagens[38,39] and aggrecan as main glycosaminoglycan[1,2]. In the superficial zone collagen fibres are laid parallel to the surface. The middle zone is characterized by the perpendicular and aligned distribution of fibres to the surface. In this middle zone, collagen is assembled with other glycosaminoglycans such as biglycan and decorin[40]. The deep zone is characterised by a denser collagen network that is aligned perpendicular to the articular surface and includes a well-defined tidemark that represents the start of the hypertrophic calcified cartilage and serves as a transition between the soft cartilaginous tissue of the above zones and the underlying hard bone. The composition of the deep zone engages this transition by the presence of degraded collagen type II fibres (by hypertrophic chondrocytes or osteoblasts) which leads to the formation of C-propeptide of type II collagen, aka. chondrocalcin, a calcium-binding protein involved in bone formation[41–44]. In addition, more non-fibrillar collagen type X is synthesized in the deeper regions of this zone which plays a role in facilitating and regulating endochondral bone formation. It has been hypothesized that the non-fibrillar nature of collagen type X, while still offering some structural support, makes it easier to reabsorb when remodelling the cartilaginous matrix tissue into bone[45].

The anatomy of the subchondral region is highly variable in density thickness and composition. Typically, the underlying bone is divided in two layers: subchondral bone plate and cancellous bone or subarticular *spongiosa*, confining the bone marrow[46].

The subchondral bone plate consists of two mineralized layers (calcified cartilage and cement line), which together form a single phase, separating articular cartilage from the bone marrow. As noted above, the tidemark separates the calcified from the uncalcified cartilage, and therefore can be considered a calcification front[47]. It is not a

straight line across the joint, but a complex three-dimensional tissue structure. Articular cartilage tissue is well integrated with the irregular surface of the underlying calcified cartilage, somewhat like a jigsaw puzzle, where collagen fibrils cross from one layer to another, resulting in a strong junction. This type of union appears to have important biological and biomechanical functions as it responses to microinjuries and allows transformation of shear forces during compression and traction[48]. The biomechanical functionality relies on the native structure and thus recapitulating this interface is critical to developing successful tissue engineering approaches. From the tidemark, the calcified cartilage progresses into the cement line where it is remodelled and replaced by the underlying bone or subchondral bone. Occasional vascular channels are connected to the osteochondral junction or cement line by small canals, however, no collagen fibres are continuous between the calcified cartilage and the cortical endplate. Thus, the cement line represents a region of weakness[49,50]. The cement line has the appearance of a solid mass of bone fenestrated by numerous intercommunicating spaces. When, however, it is viewed in a section tangential to the articular surface, it is clear that the bone consists of plates which join together to enclose intervening spaces. The plates are relatively thick (0.2–0.4 mm), and the spaces are relatively narrow (0.4–0.6 mm). Just below the articular surface these spaces are roughly as long as they are broad, resembling a honeycomb.

Below the subchondral bone plate, the spaces enlarge and gradually tend to elongate forming lamellated mineralised sheets of parallel collagen type I fibrils. Such sheets are oriented perpendicular to the articular surface and form a trabecular structure, known as the cancellous bone[51]. Based on its architecture, three different types of cancellous bone have been described: Type I consists of a very delicate meshwork of fine rods. It is widely distributed and is typically seen in the deeper parts of the ends of long bones. Type II is made up of both rods and plates and is typically seen at the end of the long bones (subtype IIa), in the calcaneum (subtype IIb) and the lower end of the femur (IIc). Type III is made up entirely of plates. Delicate plates can form a meshwork in which a directional orientation may or may not be apparent (Sub-type IHIa). Elsewhere better defined, larger plates may enclose tubular spaces (Sub-type HIIb). In some areas (where cancellous bone is very dense) small relatively thick plates enclose irregular spaces; the appearance may closely resemble that of a honeycomb when the spaces are small, but elsewhere the spaces tend to show a defined orientation. Due to this differences in the

described trabecular structure, distinct mechanical properties of weight- and non-weight bearing areas have been described[46].
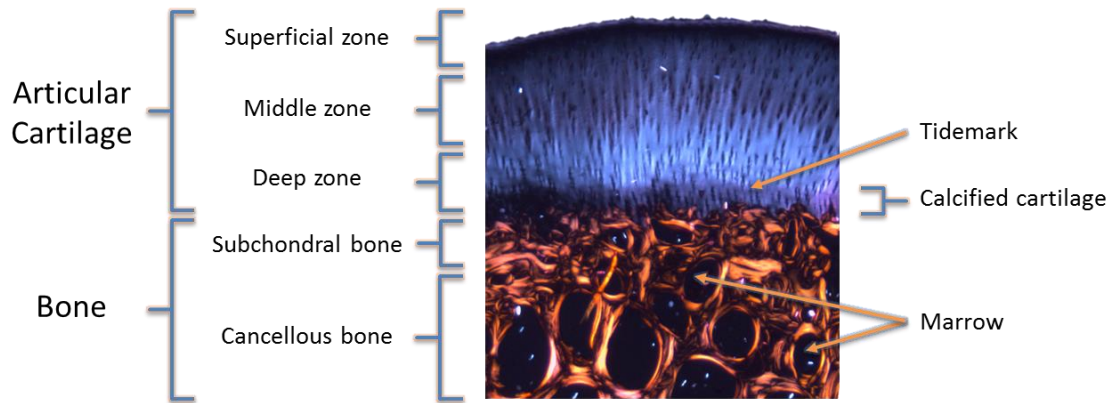
Figure 2-1. Haematoxylin and eosin stained histological sample of an osteochondral tissue under polarized light microscopy showing the main tissue sections.

2.2. Tissue engineering

The field of tissue engineering is an interdisciplinary effort that couples concepts from engineering and the life sciences. When the term 'tissue engineering' was first coined, the aim was to develop tissue or organ substitutes in order to maintain, restore or augment functions of their injured or diseased counterparts in living organisms. Today, the field of tissue engineering has expanded to include anatomical replicas and *in vitro* tissues to enhance surgery practice; organ-on-a-chip systems to better understand disease and to aid in drug development; as well as to tissue engineer meat and skin for the food and leather industry. The focus of this literature review will be on the more traditional definition of the discipline: tissue regeneration, and specifically regeneration of cartilage and bone.

Tissue engineering aims to combine a series of key elements: the smallest unit of life (cells), supportive biomaterials (often called 'scaffolds') and appropriate biochemical and/or physical cues; together these components provide cells with an appropriate environment to promote and/or maintain a desired phenotype, which enables functional regeneration of damaged or diseased tissues[52,17,8]; as illustrated in Figure 2-2.
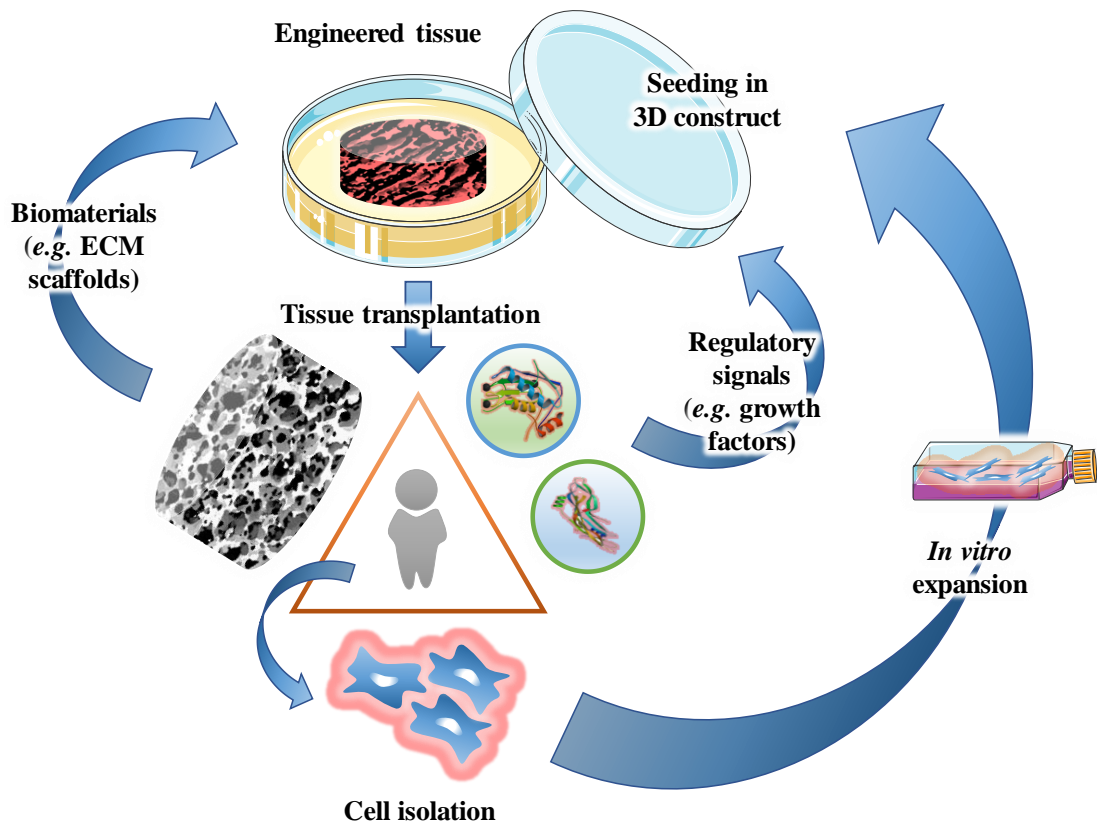
Figure 2-2. The concept of tissue engineering.

From a surgical and commercial standpoint, the ideal graft for osteochondral defect repair would be an off-the-shelf cell free product that would allow for host cell infiltration and promote differentiation. While conceptually attractive, realising this vision is complicated. This type of construct tends to require the use of additional biological factors to recruit and/or differentiate the host cells[53]. However, in some cases, the high amount of such growth factors needed also leads to undesirable side effects, such as rapid up-growth of osseous tissue and vascular buds in the cartilage compartment[54,55].

2.3. Current clinical approaches for cartilage & subchondral bone repair

Attempts have been made to repair almost every existing human tissue or organ. It has been suggested that articular cartilage is the perfect candidate for tissue engineering applications due to its avascular and aneural nature and relatively simple composition.

However, its complex microarchitecture and its mechanical functionality have proven difficult to recapitulate, making the regeneration of articular cartilage a significant challenge[56].

An injury to the joint surface that only affects the hyaline cartilage tissue is known as chondral defect. However, as previously mentioned, such wounds, if left untreated, can develop the complication of progressing towards surrounding tissues and compromising the subchondral bone. Such injuries are called osteochondral defects (OC).

Progress of orthopaedic surgery and tissue engineering is evolving the way focal cartilage and OC lesions are treated. The 5 techniques most used[57], herein called traditional approaches, are:

(i)   Joint debridement. It is associated with pain alleviation by eliminating debris from the joint surface.

(ii)   Autologous osteochondral (OC) grafts / Mosaicplasty. OC grafts are cylindrical plugs of hyaline cartilage and underlying subchondral bone – harvested from an unaffected area – that are implanted in the defect. Mosaicplasty is a variant of this approach where a "mosaic" pattern of OC grafts is used to treat a larger sized defect.

(iii)   Bone marrow stimulation (BMS) includes techniques such as abrasion chondroplasty, drilling or microfracture. The later has become the most popular BMS technique. Microfracture facilitates migration of progenitor cells from the bone marrow cavity into the defect through small osteochondral openings. Although microfracture is still consider the gold standard by the FDA, it often results in the generation of a mixed repair tissue with mainly fibrous or fibrocartilaginous properties, limited collagen type II and sGAG levels, and poor mechanical properties compared to native hyaline cartilage. This inferior quality tissue comparing to hyaline cartilage, both biochemically and biomechanically, makes microfracture a short-term solution with some reports showing a failure repair starting as early as 24 months post-treament[58–60].

(iv)   Autologous chondrocyte implantation (ACI). It consists of chondrocytes isolation from a low-weight-bearing area of the knee joint during a first arthroscopic operation and then expansion of the cells *in vitro* before

transplantation into the lesion during a second operation (Figure 2-3). This technique has two major advantages: using autologous cells avoids potential immune-related complications and the relatively small biopsy minimizes donor site morbidity. However, there is insufficient evidence at present to say that ACI is cost-effective compared with microfracture or mosaicplasty[61].

(v)   Matrix-induced autologous chondrocyte implantation (MACI). It is currently the most common scaffold plus cell-based cartilage repair technique in clinical practice. Similar to ACI, MACI requires two surgical procedures. In the first surgery, chondrocytes are harvested from autologous tissue biopsy and then seeded onto an absorbable porcine-derived collagen scaffold. An arthrotomy procedure debrides the lesion to allow for the construct implantation, which is secured using fibrin glue. MACI has shown to have similar or superior functional outcomes to either ACI or microfracture[62,63].While MACI is technically attractive, evaluation of its cost-effectiveness warrants further long-term studies before the technique is widely adopted[64].
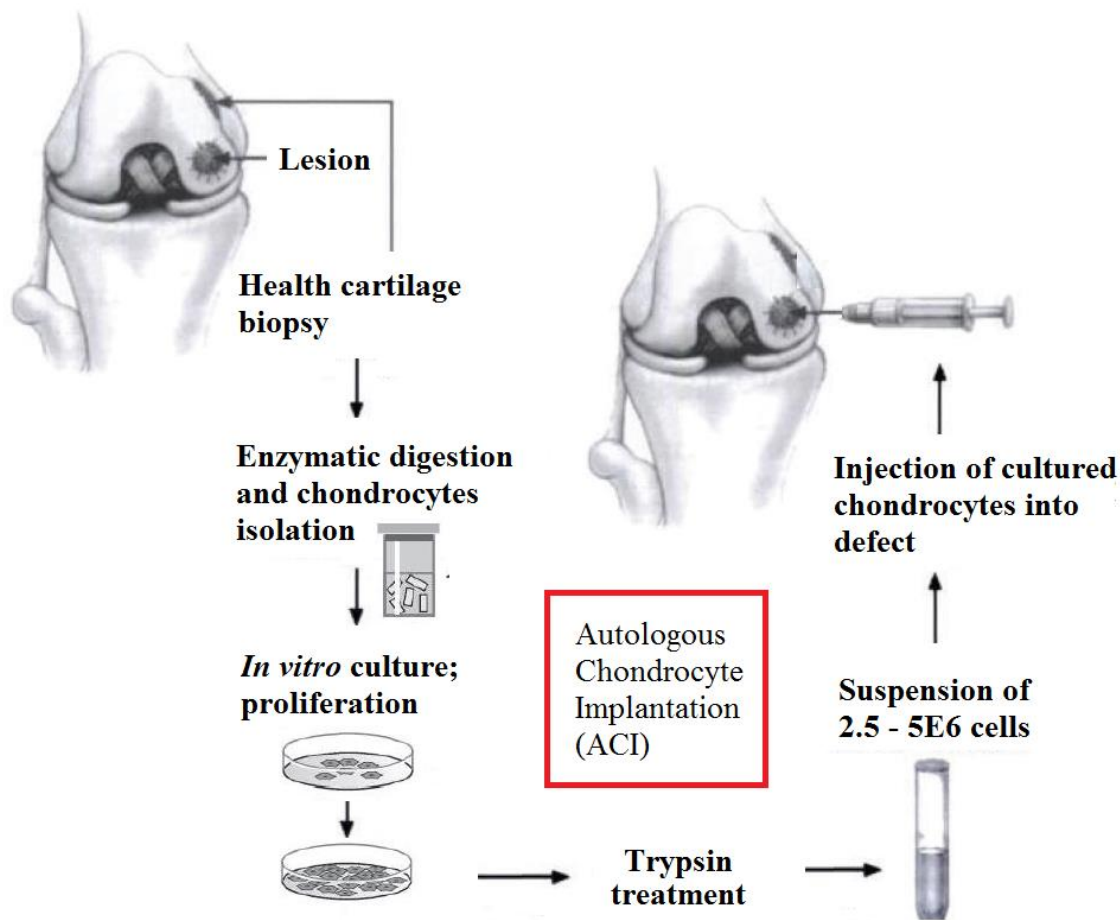
Figure 2-3. Diagram of autologous chondrocyte implantation (ACI) in a femoral condyle[65]

In general, these techniques do not lead to consistent hyaline cartilage regeneration and over time the damage can progress to OA. Most of the current "solutions" for OA treat the symptoms of the disease and include conservative measures such as physiotherapy, weight loss, non-steroidal anti-inflammatory drugs (NSAIDs), injections of glucocorticoids or delivery of hyaluronic acid[66]. The specific treatment option adopted will depend on the defect size, the patient's age, the extent of damage and the requirements of the patient[67]. In addition, the above-mentioned options have shown limited long-term success, eventually necessitating the need for osteotomies or prosthetic joint replacement. Regeneration of complex chondral and osteochondral lesions, therefore, remains a significant clinical challenge[56,68].

2.4. Chondral & osteochondral tissue engineering

The relatively poor outcomes associated with the current clinical approaches to cartilage regeneration has motivated the development of innovative tissue engineering strategies to regenerate chondral and osteochondral tissues and to stop its debilitating progression. The most well-known approaches are:

(i) *In vitro* maturation of cell laden constructs to engineer functional cartilage grafts. Although the technical advantages make MACI an attractive approach, clinical studies show a similar outcome to ACI[64]. A possible explanation is that cells do not have enough time to attach to the constructs or that engineered tissues are implanted without achieving the necessary mechanical functionality and therefore vulnerable to the high loads that go through our joints. A solution to this problem could be the extended *ex vivo* culture of the construct pre-implantation to enhance its mechanical properties and/or cell attachment[69]. Additional advantages of this technique include the robust and stable differentiation of stem cells into chondrocytes[70] or the enhanced chondrogenesis of isolated chondrocytes that may have dedifferentiated during monolayer expansion[71].

(ii) Novel cell-free biomaterials: from a surgical and commercial perspective, the ideal graft for osteochondral regeneration would be an off-the-shelf product, free of the challenges associated with the use of autologous cells. The different approaches so far investigated to fabricate cell-free osteochondral composites have been developed based on a variety of fundamental principles, but with the common goal to provide the correct ''regenerative'' signals to local host cells that are recruited into the biomaterial post-implantation.

a. Autologous matrix-induced chondrogenesis (AMIC). This technique is meant to enhance the cartilage regeneration potential by BMS. A bioactive scaffold such as type I collagen scaffold is implanted into the cartilage defect during BMS treatment. Scaffolds currently in

29

veterinary or human clinical use include *Chondrocoll*[72] or *Maioregen*[73].

    b. Active *in situ* approaches consist on the delivery of key molecules that may facilitate cartilage repair, such as growth factors or glycosaminoglycans. This approach has recently become very popular as it is technically attractive. Delivery of biomolecules is done through injections in the joint and thus avoiding unnecessary arthrotomy procedures[74]. On the other hand well-designed comparative studies with long follow-up time points are needed to confirm the therapeutic potential and economic benefits[75].

(iii) Self-aggregating or self-assembling process: a scaffold-free approach[76]. In a first surgery, cells are isolated and then cultured *in vitro*. At this stage, the cells gather together and condensate to form a self-assembled tissue. In a second surgery, the self-assembled tissue is implanted on the defect site. Although the concept is simple and articular cartilage-like tissue is generated *in vitro*[77–79], there are technical difficulties associated with tissue stabilization or fixation on site[80].

2.5. Challenges in osteochondral tissue engineering

As the goal of this thesis is to develop a scaffold for treating OC defects, this review will next focus on describing the challenges associated with developing constructs for functional regeneration of OC defects. These challenges include:

- Providing the implant with appropriate mechanical, chemical or biological properties.
- Recapitulation of the architectural complexity of the native tissue.
- Ensuring vascularization of the osseous region while preventing vascularization of the chondral region.
- Engineering the complex interface between the articular cartilage and subchondral bone.

- In the case of cell-based approaches, identification of a suitable cell source(s) capable of promoting regeneration of the different tissue types within the osteochondral unit.
- Immunological compatibility and immunomodulation of host response, which are critical to avoid the initiation of a cascade of cellular events leading to inflammation, fibrosis and damage to the implant and the surrounding tissues. In the medium-long term, the ideal scaffold will facilitate a pro-healing immune response.

In order to overcome these limitations, particular focus has been placed on the following three areas of research (Figure 2-4): the engineering of materials, architectures and cells. Each of these areas is introduced below, with subsequent sections providing a more detailed review of each topic.
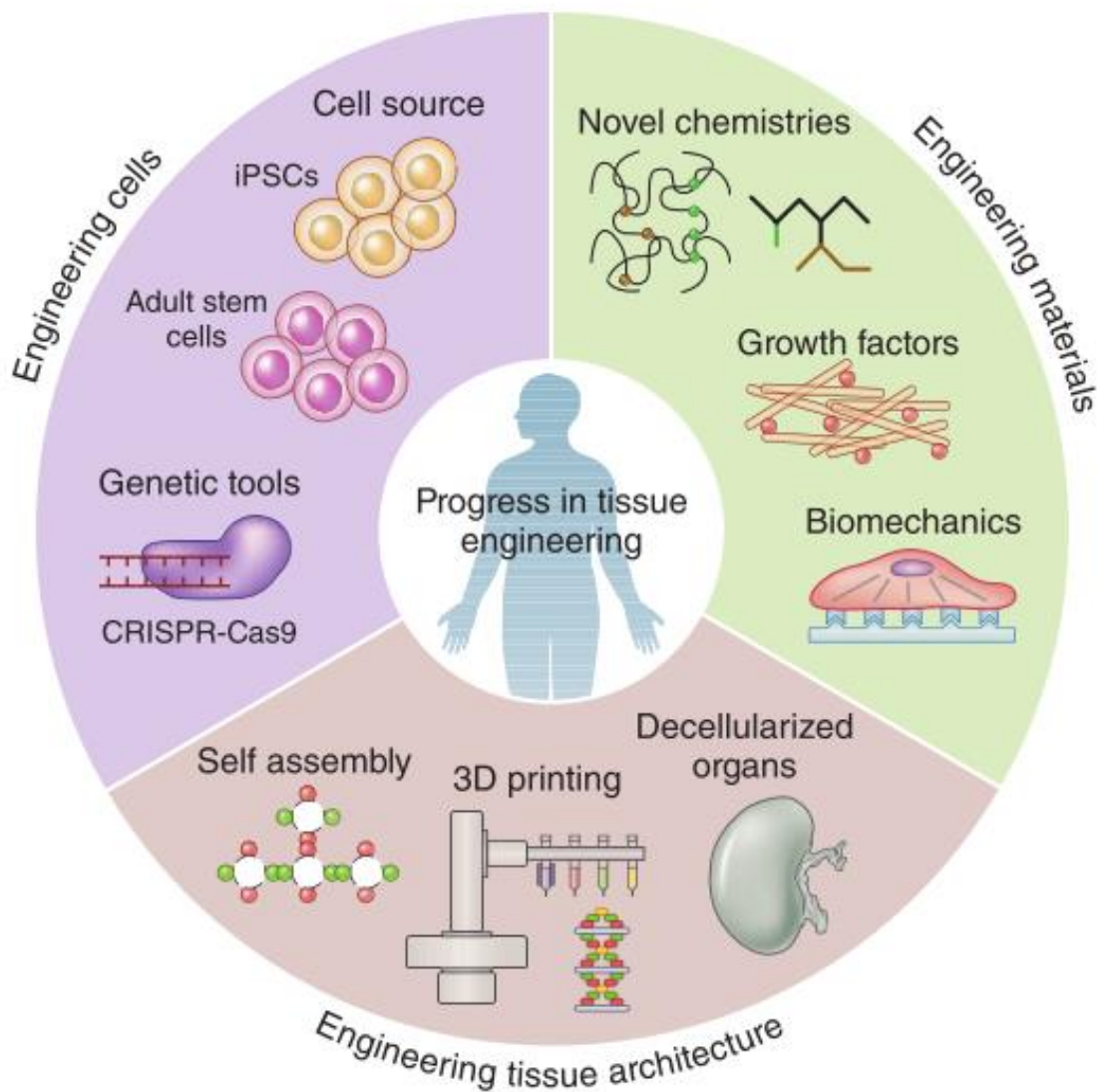
Figure 2-4. Summary of tissue engineering progress in the past decade. Availability of additional cell sources, such as iPCS and adult stem cells, and genetic editing tools has increased. Improved structural, compositional and functional properties of tissue engineered constructs mimicking their native counterparts has been possible due to the advances in new factor delivery mechanisms, understanding biophysical cues and tissue architecture technologies.[81]

(i)   *Materials in tissue engineering:* successful osteochondral tissue engineering requires the development of compliant biomaterials to actively modulate adhesion, proliferation, migration, differentiation and maturation of cells that are either seeded into the construct pre-implantation or recruited into the scaffold post-implantation. There are typically two different types of materials used to fabricate constructs in osteochondral tissue engineering: synthetic materials and natural biomaterials. Significant effort has gone into optimising the composition and mechanical properties of such materials, including their functionalisation with bioactive factors, to enhance their therapeutic potential. For example, conjugation technology (either covalently or affinity-mediated) has been shown to be useful for functionalizing materials with bioactive molecules such as growth factors or small peptides involved in cellular attachment and differentiation[30]. The development of increasingly versatile delivery systems further allows the presentation of multiple factors mimicking *in vivo* dynamics[82]. On the other hand, the field of mechanobiology has highlighted that the mechanical properties of scaffolds will also modulate cell behaviour. Physical forces such as substrate stiffness has been shown to play a key role in cell response and differentiation of stem cell lineages[83]. In addition, it has been found that stem cells remember features of past microenvironments and can undergo reversible or irreversible activation as a consequence of a mechanical stimulus[84]. Another area of interest from the material perspective is the immunomodulation of biomaterial-host interactions. For instance, the use of implanted spheres with a diameter larger than 1.5 mm significantly reduced foreign body reactions compared to smaller spheres[81,85].

(ii) *Architectures in tissue engineering:* Scaffold architecture is also known to play a key role in regulating cell migration and differentiation, tissue organization as well as integration with the host[86]. There is a number of methodologies that allow for the ability to create controlled porosity, structural strength and specific-3D architectures useful for tissue engineering. There are a number of techniques reported in the literature, including: (i) solvent casting and particulate/porogen-leaching, (ii) gas foaming, (iii) phase separation, (iv) electrospinning, (v) fiber bonding, (vi) self-assembly, (vii) additive manufacturing (including fused deposition modelling, selective laser sintering, stereolithography or 3D bioprinting) and (viii) freeze-drying.

(iii) *Cells in tissue engineering:* a number of different cell types have been explored for osteochondral tissue engineering, including autologous, allogeneic, xenogeneic, non-transformed clonal, immortalised and sarcoma cell lines; among the most important ones[81]. Moreover, our understanding of cell biology and how we can "reprogram" them for better satisfy our needs have changed. Since the discovery of methods to generate induced pluripotent stem cells (iPSCs), the availability of cell autologous sources has been increased for many tissue engineering applications[87]. It is also possible to modify cells using innovative genetic manipulation methods, such as clustered regularly interspaced short palindromic repeats (CRISPR) technology, which have revolutionized the potential of genomic editing and personalized biomedical engineering[88,89]. Despite the extensive use of such different cell types (sarcoma cell lines, immortalised cells, xenogeneic, allogeneic, autologous cells) in experimental or pre-clinical studies, there are relatively few cell types used clinically[90]. For short-medium term clinical applications, perhaps a more attractive cell type are adult stem cells, which include mesenchymal stem cells (MSCs), adipose-derived stromal cells and amniotic-fluid-derived stem cells[91,92]. Adult stem cells have powerful tissue repair applications due to their renewability and ability to differentiate into several lineages. On top of that, stem cells have been shown to possess

33

immunomodulatory properties in affected or injured tissues[93] and can secrete factors that can promote regeneration[94,95].

2.6. Materials in tissue engineering: Scaffold composition

Numerous different materials have been explored for use in osteochondral tissue engineering. In part, this reflects the fact that our understanding of the requirements to restore normal joint function is still poor[96,97]. Such biomaterials can be divided into inorganic and organic components. In chemistry, "organic" refers to a molecule that contains carbon and a hydrogen backbone. For tissue engineering, organic components are divided into synthetic and natural biomaterials. Inorganic molecules are composed of other elements. They can contain hydrogen or carbon, but if they have both, they are organic. In turn, inorganic components can be divided into metals and ceramics.

2.6.1. Inorganic components

Metals and ceramics have contributed to major advances in medicine over the past century, particularly in the field of orthopaedics. Their most common use is as biocompatible materials for tissue replacements or prosthetic implants. However, these types of materials are also widely used in tissue engineering approaches.

(i)   Metals: typical metals used in regenerative medicine are known as biodegradable metals and include magnesium (Mg), iron (Fe) and derived alloys. The strength and malleability of metals are attractive features for hard tissue applications such as bone, tooth enamel and cementum[98,99]. Mg has been used in combination with calcium and zinc as absorbable alloy to explore medical applications for bone regeneration[100,101] and bone response to its corrosion[102,103]. Fe has been explored in its pure form for cardiovascular stent development[104,105] and as a foam and combined with manganese (Mn) for biomedical applications[106]. The main advantage of these metals is that they are essential elements largely present in the body with multiple biological functions. For instance, Mg has osteoconductive

capacity (Figure 2-5) and its presence is beneficial for growth and strength of the bone; while Fe plays a key role in cell metabolism as it forms part of molecules such as haemoglobin, in charge of oxygen distribution and storage, or enzymes involved in degradation of damaged lipids, proteins or nucleic acids. On the other hand, the main disadvantage is the potentially toxic by-products derived from either degradation or corrosion.
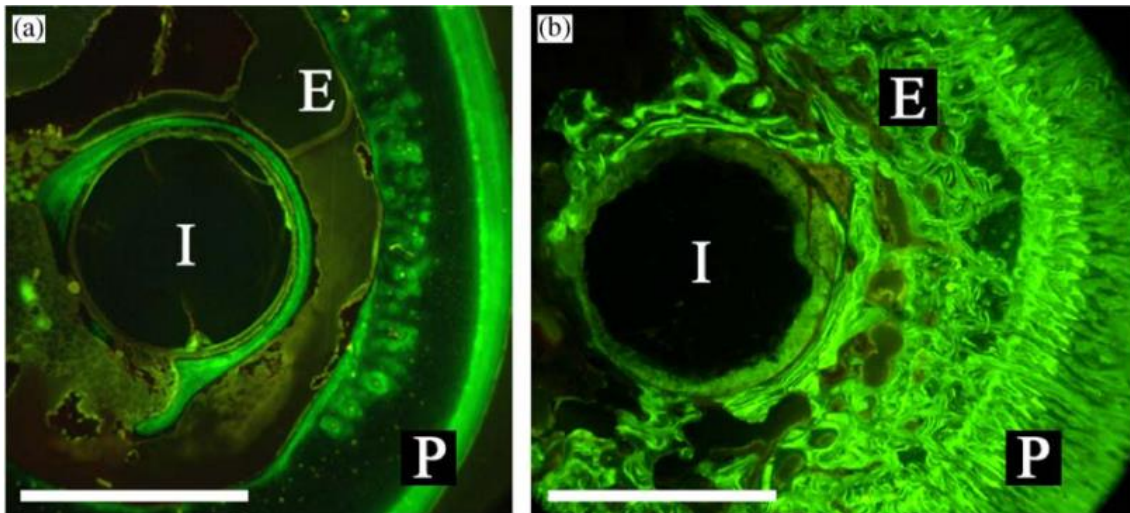
Figure 2-5. *Microscope fluorescent images of the cross-section of (a) a degradable polymer rod and (b) a magnesium rod in guinea pig femur after 18 weeks postoperatively. Staining of newly bone formation by calcein green. Bar = 1.5 mm; I = implant residual; P = periosteal bone formation; E = endosteal bone formation*[103].

(ii)   Ceramics: inorganic materials known for their corrosion resistance, high compressive strength and high stiffness. Disadvantages of ceramics include brittleness, low fracture strength, difficult to fabricate, relative weakness in shear and tension and high density. Some of these materials show biocompatible behaviour and thus are known as bioceramics[107,108]. Most common bioceramics include materials such as bioactive glass and calcium phosphate ceramics (CaP).
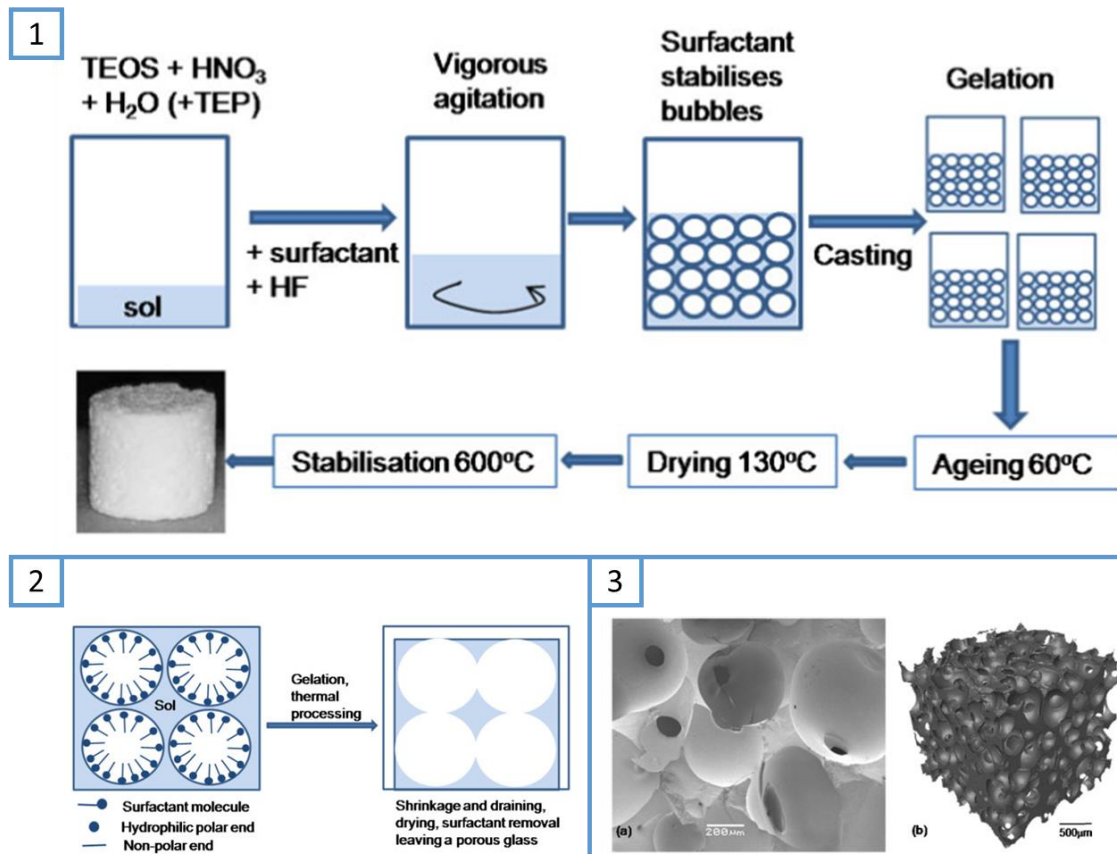
Figure 2-6. (1) A flow chart of the sol-gel foaming process. (2) Role of surfactant molecules in creating interconnected pore networks. (3) (a) SEM and (b) µCT images of the macropore structure of a sol-gel derived bioactive glass foam scaffold.[109]

Bioactive glasses are a group of surface reactive glass-ceramic composites made of different percentages of SiO_2, Na_2O, CaO and P_2O_5, and which are synthesized by melt or sol-gel process (Figure 2-6) to create interconnected pore networks[109]. The most famous and the original bioactive glass is known as Bioglass® and it has been used in many bone tissue regeneration approaches such as cranial defects or mandibular traumas (Figure 2-7) due to its high osteoinductivity[109–111]. The main disadvantage of bioactive glass is its lack of bioresorbability (not to be confused with biodegradability[112] as in principle, CaP derived materials can be degraded by cell activity, however, their chemical conversion to more stable hydroxyapatite makes them very difficult to be resorbed and removed from the body[113]). Other non-resorbable bioceramics include yttria-stabilized

zirconia and alumina-wollastonite ceramic glass that have better mechanical properties. However, these ceramics need to be combined with other more biologically active components[114] due to their biological inertness, thus, they are less attractive from a tissue engineering perspective.
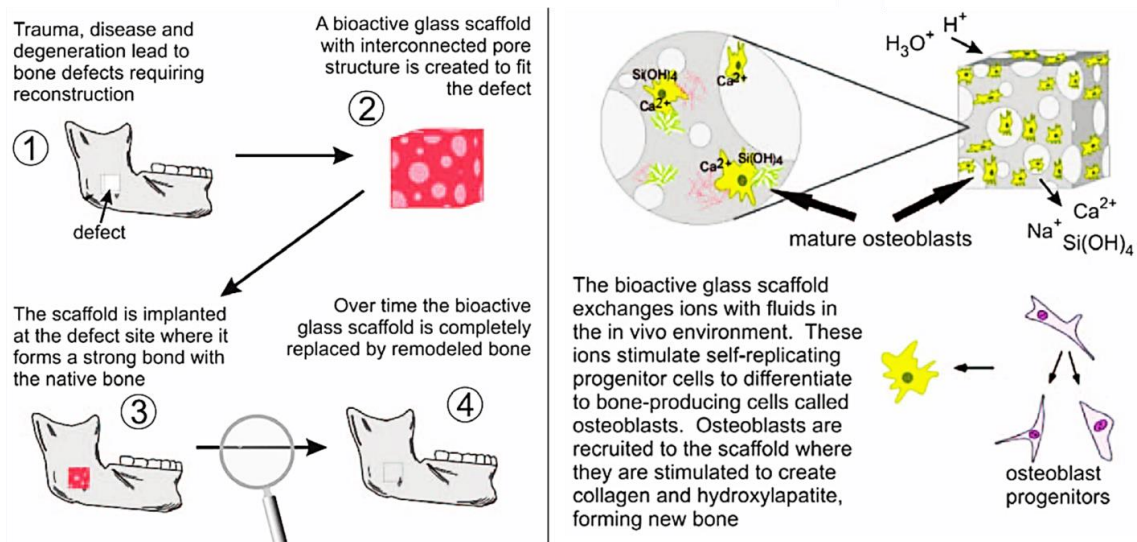
Figure 2-7. Diagram illustrating how a porous bioactive glass scaffold could be used to regenerate a bone defect. The scaffold is placed at the site of the injury or defect, where it releases ions that stimulate cells of the native tissue to differentiate, migrate and remodel the scaffold. Eventually, the scaffold completely dissolves, and the defect is filled with the patient's own bone.[110]

The most widely studied calcium phosphate (CaP) ceramics for bone TE include tricalcium phosphate (TCP, either α or β), tetracalcium phosphate (TTCP), octacalcium phosphate (OCP) and $Ca_{10}(PO_4)_6(OH)_2$ which is better known as Hydroxyapatite[115]. The rational for using calcium phosphate derived ceramics is that CaP is found naturally in the body and it shows important characteristics such as biocompatibility, osteoconductivity and biodegradability[107].

2.6.2. Organic components

(i) Synthetic materials: Synthetic materials commonly used in the development of scaffolds include polylactic acid (PLA)[116], polyglycolic acid (PGA)[117], polycaprolactone (PCL)[118], oligo(poly(ethyleneglycol)fumarate) (OPF)[119]. Many are produced from renewable sources (with the exception of PCL, which is obtained from crude petroleum, although new composites using innovative natural additives are being explored[120]) and they are biodegradable[121,122,123,124].

However, in general, biocompatible synthetic materials do not provide natural sites for cell adhesion, leading to poor cell attachment, proliferation and matrix deposition. In addition, the *in vivo* hydrolytic degradation of this polymers may cause local pH reductions, which in turn can lead to a decrease in matrix production and/or cellularity[43,44] or the triggering of an inflammatory response[45]. It has been shown that the number of MSCs, implanted with PLA scaffolds in an osteochondral defect, appear to decrease over time[116]; and that PGA scaffolds do not fully integrate with the host cartilage[117] (Figure 2-8).
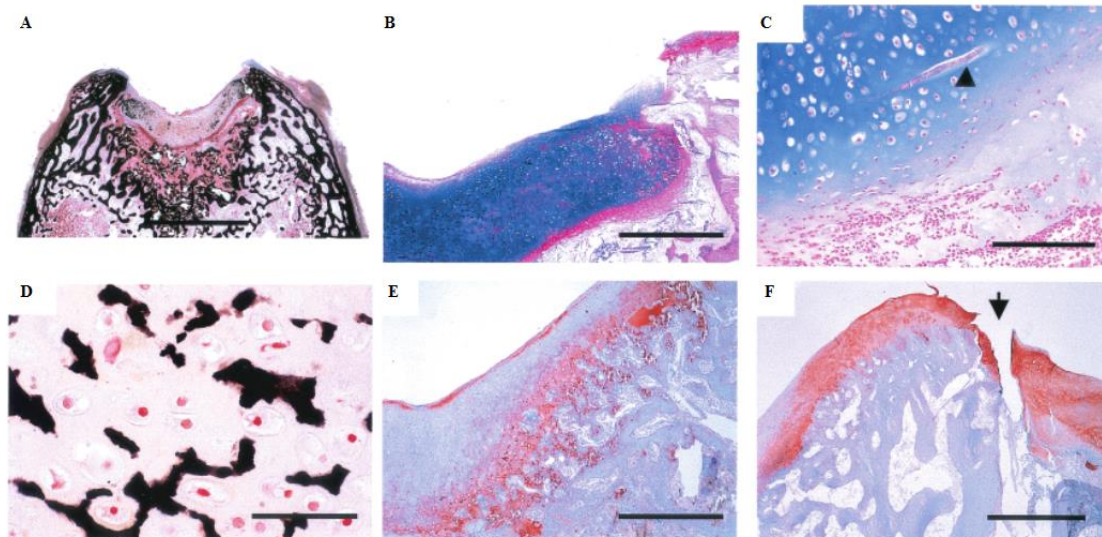
Figure 2-8. Six-week repair of OC defect implanted with PGA derived engineered cartilage. Von Kossa satained for calcium deposition (A, D); alcian blue stained (B, C); type II collagen stained (E), type X collagen stained (F). Bars = 5.0 mm in A; 800 μm in B, E and F; 100 μm in C; and 50 μm in D. Arrowhead (C) indicates a PGA fiber. Arrow (J) indicates a fissure, with host cartilage to the left and engineered cartilage to the right.

Current approaches aim to combine synthetic materials with biological materials, such as gelatine or fibrin, to form composites that provide cell binding sites in order to improve the construct bio-interactivity or the conjugation of peptides with polymers for single-step fabrication of spatially functionalized scaffolds[128]. On top of that, synthetic materials such as PCL are very attractive from a personalized medicine point of view as they can be relatively easy 3D printed[129,130] to produce anatomically accurate implants (Figure 2-9).
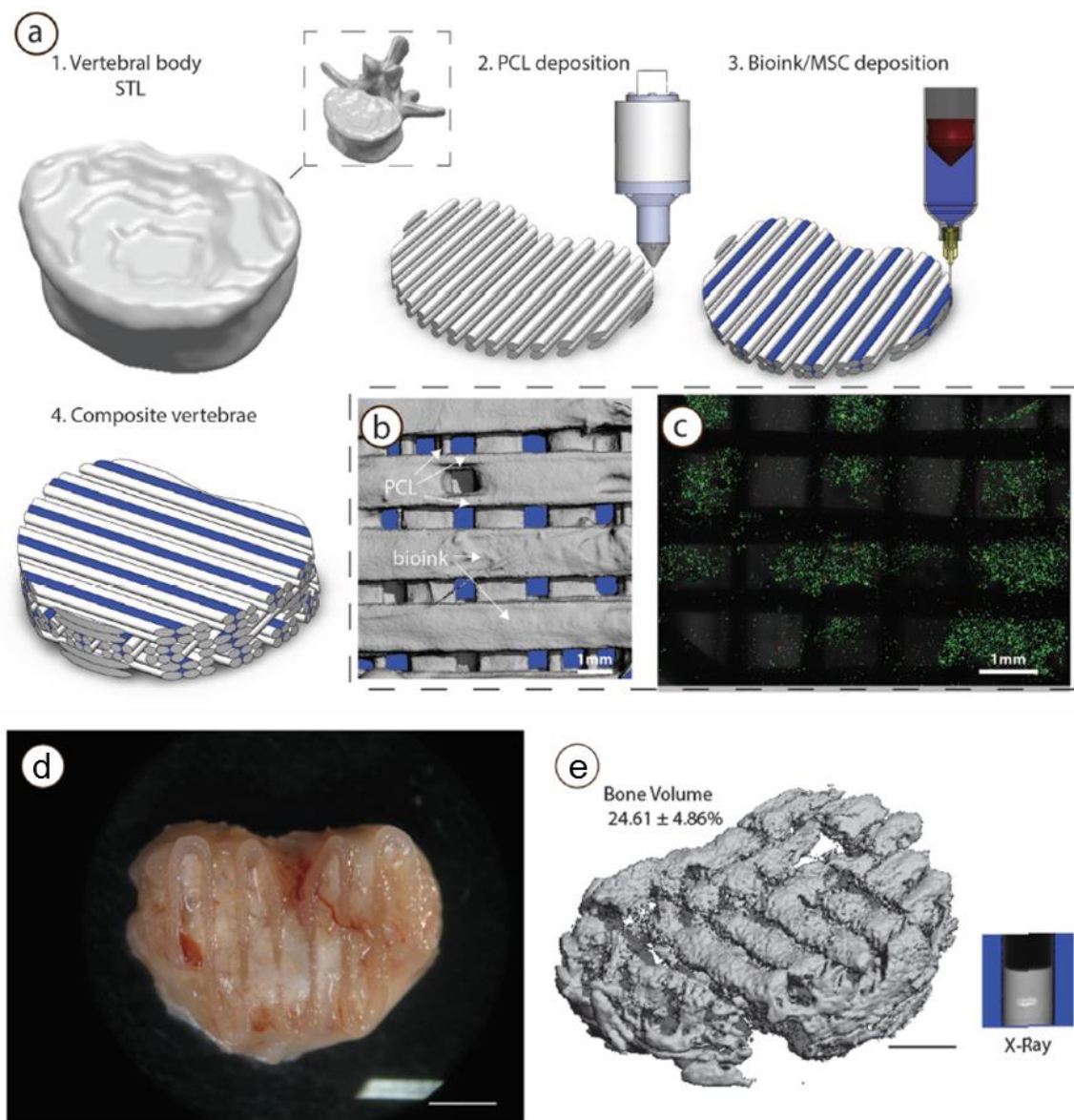
Figure 2-9*. 3D Bioprinting of vertebrae shaped mechanically reinforced bioinks and its development into a vascularized bone organ in vivo following inmplantation of cartilage rudiment. a) Description of multi-tool 3D bioprinting process, 1) The outer geometry of a human vertebral body was scanned and next layers of 2) PCL filaments*

were deposited followed by deposition of the 3) MSC laden bioink this was repeated in an orthogonal fashion to create a 4) composite vertebrae structure. b) μCT analysis demonstrated the distribution of bioink and PCL within the composite vertebrae. Bioink + PCL filaments isolated using μCT, indicating the presence of bioink free channels conduits (blue regions) post-printing. c) Live/dead images of cells within the deposited bioink 1 h post-printing, scale bar 1 mm. d) Macroscopic image of anatomically shaped vertebrae constructs 12 weeks post-implantation scale bar 2 mm. b) μCT reconstruction and X-ray of whole construct, scale bar 2 mm.[129]

(ii) Natural biomaterials: these include fibrin[131], hyaluronic acid[132], collagen[133], gelatin[134], chitosan[135], chondroitin sulphate[136], alginate[137] or the extracellular matrix. They are commonly used in osteochondral tissue engineering as they overcome the lack of biological interaction. The mechanical properties of natural biomaterials are typically lower and less controllable than synthetic biomaterials. This is a major drawback when looking for an implant that can provide some level of mechanical support within the defect while regeneration of the tissue is taking place. Due to the lack of mechanical support, natural biomaterials are often combined with biocompatible synthetic materials. For instance, Gao *et al.*[132] explored a hyaluronic acid derived scaffold in combination with an injectable calcium phosphate (ICP) to provide the mechanical support that mimics subchondral bone. Also, Guo *et al.*[134] designed a crosslinkable OPF, as a scaffold combined with gelatin microparticles that were used to deliver chondrogenic or osteogenic factors.

(iii) Bioactive factors: tissue engineering strategies increasingly involve the functionalization of materials surface with either covalently coupled, electrostatically adsorbed or self-assembled molecules, such as adhesive proteins like functional collagens, fibronectin, RGD peptides[138] and growth factors like bFGF, EGF, insulin, TGF-β[30,31]; to develop brand new materials[52,139] that will facilitate and enhance cell and tissue interactions with the biomaterial.

Growth factors within tissue engineering scaffolds may be presented or released in different manners (Figure 2-10):

- Soluble form: factors loaded into constructs with modulated degradation or diffusive properties in order to tailor the release rate, and which may be combined into systems releasing multiple factors with distinct kinetics[140]. The exposure of cells to different growth factors with time may therefore mimic developmental pathways and healing responses.

- Bound form: factors are attached to a surface in either random or specific orientations, with the possible use of a spacer molecule. Non-covalent associations with matrix components, particularly GAGs, can effect slow release and in some cases may potentiate binding to membrane receptors[141].

Cell-demanded release is typically based on the presence of protease-sensitive peptide sequences within the growth factor protein[142,143]. Due to our inability to recapitulate the complexity of naturally occurring factor spectrum, recent studies have explored the extraction of the soluble fraction from ECM and its incorporation into natural biomaterial derived scaffolds[141].
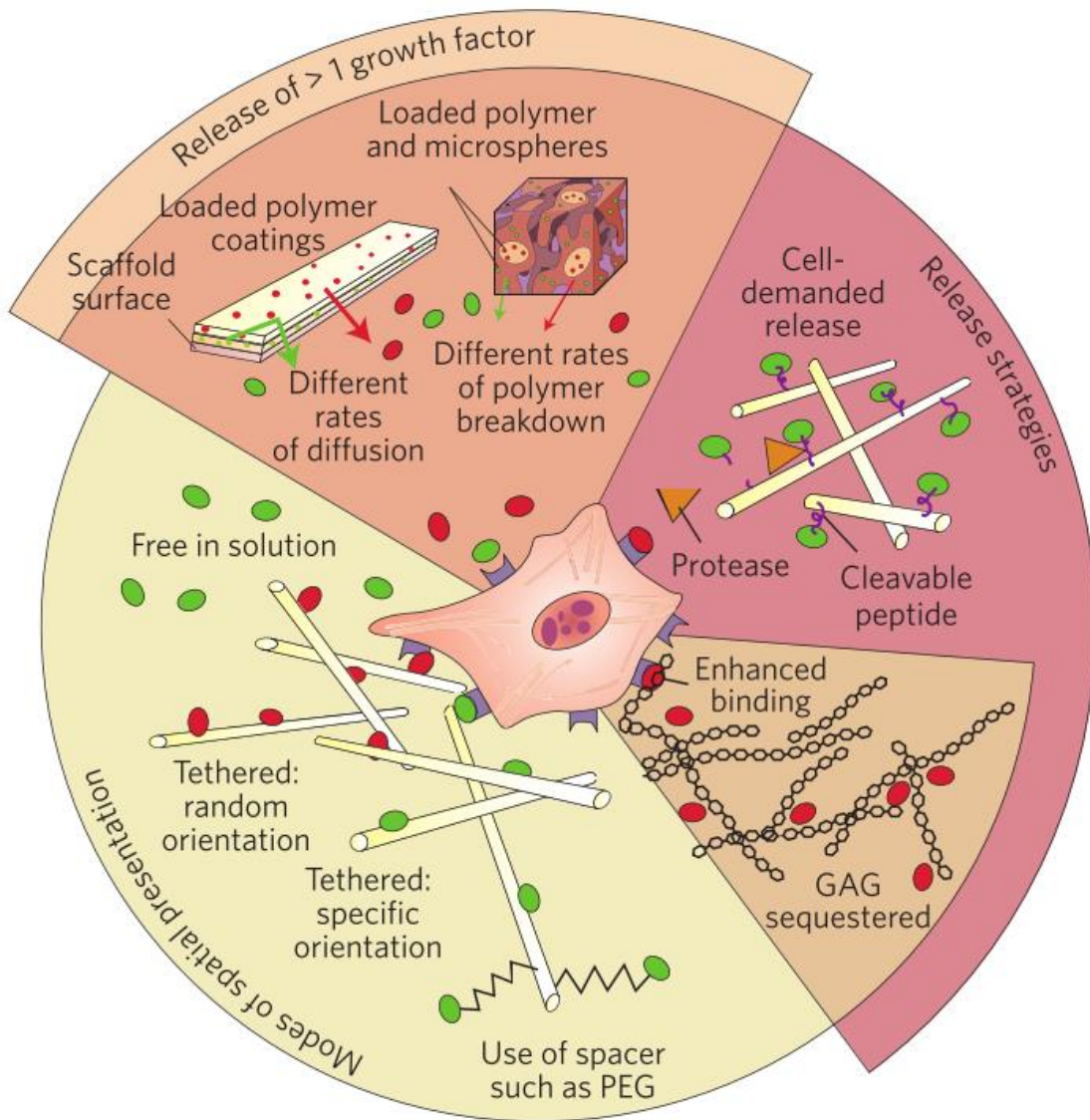
Figure 2-10. Presentation and release of growth factors from tissue engineering scaffolds[141].

2.6.3. Extracellular matrix (ECM) and tissue-specific ECM

In the recent years there has been an increased interest in the use of the extracellular matrix (ECM) of mammalian tissues as natural biomaterials for tissue regeneration as they may contain both the soluble (*e.g.* growth factors) and structural (*e.g.* collagen) molecules[11]. Such molecules can (i) function as cell-adhesive ligands, (ii) release or sequester functional factors, (iii) regulate enzymatic degradation, (iv) incorporate appropriate microstructure and (iv) drive the desired differentiation of progenitor cells that are either seeded onto such constructs prior to implantation[13] or are recruited into the scaffold post-implantation[8–10]. ECM derived scaffolds have been shown to facilitate the repair of many tissues in preclinical studies and in human clinical

42

applications including trachea, muscle, heart valves and abdominal walls[11,12,14–16]. Most commercial scaffolds are derived from soft tissues such as dermis, urinary bladder or small intestinal submucosa (SIS), although their use has been extended to the repair of many different tissue types[11].

Despite their widespread use, it is unlikely that a single tissue source will be the optimal for the regeneration of all organ systems. The ECM contains the molecules secreted by resident cells of each organ system[26,27]. Thus, it is reasonable to assume that the composition and structure of a specific tissue ECM is uniquely suited to maintaining the phenotype and biological function of its resident cells. In the recent years, there has been an increased evidence to support the use of tissue-specific ECM derived materials[144–151]. In particular, regeneration of osteochondral tissues has been improved when using bilayered systems containing components of the cartilage and developing bone (growth plate) ECM in each layer[32].

One of the major advantages of using tissue-specific ECM is that it provides cells with the complex microenvironment of the target native tissue and therefore it contains molecules not found in other tissues that encourage a so-called constructive remodelling, *i.e.*, it supports specific tissue formation at the implantation site rather than forming inferior and less functional scar tissue[20]. When a defect is being regenerated, the environment is not static but dynamic and it responds to external influences such as biomechanical triggers and hormonal actions. For cartilage, the most basic known chondrogenic factors are collagen type II, hyaluronic acid, TGFb, FGF and IGF[152]. In addition, cartilage ECM also contains other factors such as chondromodulin or gremlin-1[153], which inhibit cartilage hypertrophy and mineralization, hence potentially offer a protective role by stopping subchondral bone progressing into the cartilage layer. For bone, most well-known factors include BMPs[154], however other ECM components[155] such as collagen type I, collagen type X, MMPs or VEGF can enable or enhance bone tissue remodelling and avoid hypermineralization[156], which may increase susceptibility to fracture in the long run, despite short-term gains in bone mass[157].

Given the high complexity of these events and the multiple roles that the ECM plays, scaffolds based on natural ECMs are likely better prepared to face the task of providing an appropriate environment than those built from artificial compounds. In fact,

some of the previous mentioned materials are compounds derived from ECM such as collagen, a major component of articular cartilage. Other biomaterials mimic components of articular cartilage, such or chitosan whose structure is similar to glycosaminoglycans (Figure 2-11).

| Chitosan | Chondroitin sulfate | Dermatan sulfate | Hyaluronic acid |
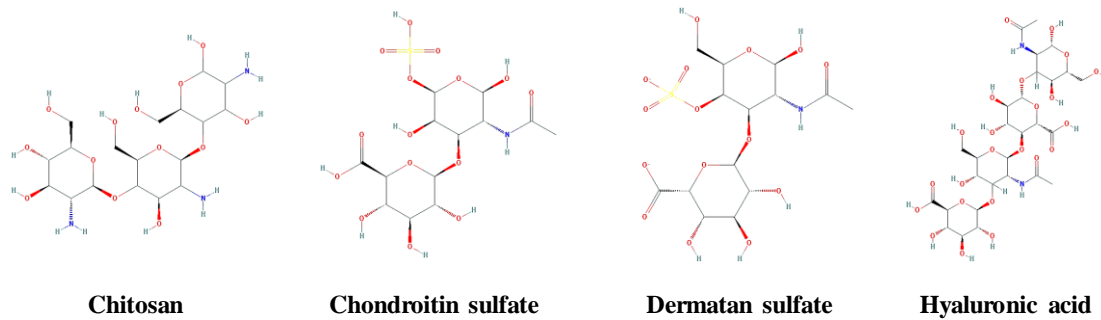
Figure 2-11. Chemical structure of chitosan and most common glycosaminoglycans: chondroitin sulfate, dermatan sulfate and hyaluronic acid. Source: PubChem.

It is important to establish some classification criteria for the different types of ECM used in tissue engineering (Figure 2-12). First, to delineate between the sources of ECM, either derived from native tissue (autologous, allogenic or xenogeneic), or derived from matrix produced by cultured cells *in vitro*. Secondly, to characterise the ECM based on the processing method, *i.e.*, untreated (for instance, small intestine submucosa, retaining naturally fibrous and porous nature of ECM had been originally used untreated for preclinical studies[158–160]), devitalised (when cell death occurs as result of the application of physical methods, such as freeze-thaw cycles, without actively removing DNA or immunogenic antigens) or decellularized (to actively removed DNA and other immunogenic antigens). Last but not least, to define the ECM depending on the presentation or form method: particulate, solubilised (*e.g.* injectable hydrogels), as scaffold (*e.g.* lyophilised constructs) or unmodified (except for possible decellularization).
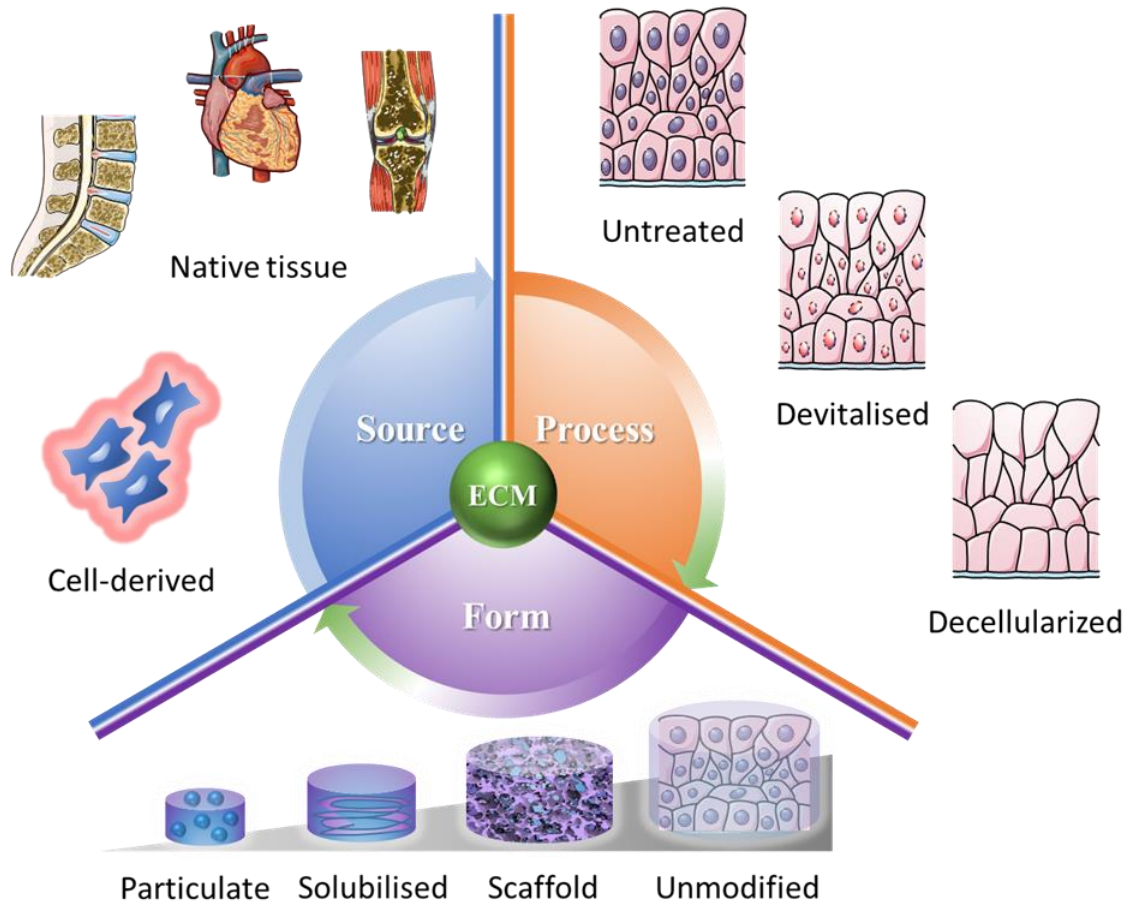
Figure 2-12. Classification of ECM depending on (i) source: native tissue or cell-derived matrix; (ii) process method: untreated, devitalised or decellularized; and (iii) form: particulate, solubilised, in scaffold form or unmodified.

The repair of articular cartilage defects that have progressed into the subchondral bone poses additional challenges. First, bone regeneration should not pass beyond the osseous phase, thus different biomaterials may be needed for each phase. Second, integration between AC and subchondral bone depends on simultaneous maturation of both tissues, which is influenced by the chosen biomaterial in each phase. Based on the previous classification, various possibilities for matrix-based approaches can be found. The three main types of (osteo)chondral ECM derived biomaterials are:

(i)   Osteochondral plugs, taken either from a non-load bearing region of the joint (mosaicplasty) or from a donor (allogenic osteochondral grafting), are used to fill the defect and offer the direct implementation of cartilage and bone matrices[161].

(ii)   Processed ECM: Non-decellularized AC particles, usually combined with a degradable biomaterial (such as fibrin[162,163]) and/or with cells, have led to great promises, improving current techniques such as ACI or MACI[164] to match the outcomes for microfracture. Even particles from osteoarthritic patients have been implanted in subcutaneous pockets in mice leading to better shape fidelity[20]. Although, OA patient-derived ECM may contain undesired pro-inflammatory cytokines[39].

Cartilage matrix can be harvested from allogenic or xenogeneic sources and processed in order to fabricate cartilage derived scaffolds[165]. Devitalisation and decellularization of xenogeneic ECM derived biomaterials is one of the main prerequisites to clinical translation. Regenerative medicine approaches based on decellularized scaffolds derived from biological tissues are rapidly expanding[10,17–19]. The process consists of physically and/or chemically removing cells from a tissue, leaving behind the complex mixture of structural and soluble biomolecules that constitute the ECM, *i.e.* it overcomes the disadvantage of ECM containing cellular antigens (*e.g.* membrane proteins, nucleic acids) recognized as foreign by the host that may trigger an adverse inflammatory response against the scaffold[20]. Some preclinical studies underscore the benefits of devitalized/decellularized ECM material over live ECM. It has been suggested that the processed ECM leaves newly accessible bioactive sites and enhances the release of trapped growth factors, thus encouraging a more homogenous and rapid synthesis of new tissue in cartilage[21] and bone[22,23,166]. However, there are other studies reporting opposite outcomes[24,25]. The inability to point out specific indications where decellularized products have added or not value in trauma reconstruction may be due to the lack of a standard treatment to decellularize ECMs, which varies extensively the composition and amount of tissue-inductive factors.

In addition, decellularization efficiency depends on the physical or chemical properties of the tissue. Due to the dense nature of cartilage ECM in which cells are embedded, more vigorous protocols are required to

achieve the standard of < 50 ng DNA per dry tissue[20,26,27] proposed in literature by Badylak. The disadvantages associated with a harsher decellularization treatment are the destruction of ECM components (GAGs are specially affected by detergents used during washing steps) as well as loss of biomechanical resilience of the collagen structure and mechanical behaviour of the remaining ECM[28]. On the other hand, the decellularized ECMs can also be rebuilt into a scaffold through lyophilisation and crosslinking of the construct[29–31]. Alternatively, the ECM derived material can be combined with other materials to achieve the desired mechanical properties.

Similar to decellularized cartilage, decellularized bone promotes the generation of newly deposited bone-like tissue, even outperforming the bioactivity of established biomaterials such as bioactive glass[167]. Other ECMs can also be used for the regeneration of bone. For example, scaffolds derived from decellularized growth plate ECM have been shown to promote large bone defect healing in cranial[29] and femoral defects[168].

(iii)   The ECM to fabricate scaffolds for osteochondral tissue repair can also be harvested from cells, also known as cell-derived ECM[169,170]. Cell-derived ECM overcomes the issues of potential diseases transfer and allows producing ECM with the patient's own cells in order to avoid any tissue rejection complications. In addition, different cell types can be used in order to synthesize the appropriate ECM for the regeneration of complex tissues such as the osteochondral unit. The fabrication of thin sheets allow for easier decellularization[171]. One of the main challenges in using cell-derived ECM is scaling up the process in a way that can be clinically applied for human regenerative medicine.

Most bones develop and heal by endochondral ossification, the replacement of a hypertrophic cartilaginous intermediary with bone. Thus, it has been demonstrated that a cell-derived hypertrophic cartilage ECM can be used to generate scaffolds for bone repair[172].

47

2.7. Architectures in tissue engineering: microstructure of the scaffold

A central component of osteochondral tissue engineering is designing appropriate 3D environments with the capacity to induce or maintain chondrogenesis or osteogenesis. As previously mentioned, there is a number of techniques available to control scaffold porosity, stiffness and specific-3D architecture. The most common strategies used for osteochondral tissue engineering are described below:

2.7.1. Solvent casting and particulate leaching

A polymer is dissolved in an organic solvent and particles with a specific size are added to the solution. The mixed solution is shaped into a desired geometry by casting it onto a plate to make a membrane or a 3D mould to make a scaffold. When the solvent evaporates, it creates a structure of composite material made of particles and polymer. Finally, the composite is then washed to dissolve the particles, leaving a porous structure. In the porogen-leaching technique, the idea of removing one of the components is the same. In this case, the scaffolding material is not dissolved in a solvent, but casted into a mould and crosslinked. The benefit of this technique is that controlling the particle size will control the pore size of the final product. Recent improvements combining shaking of regular sized spherical porogens can produce well-defined scaffolds[173]. On the other hand, this technique has some associated disadvantages[174], such as the difficulty to maintain a uniform distribution of the porogens within the polymer, because of the difference in densities between the liquid polymer and the solid salt. Moreover, when mixing the components, the polymer solution can wrap completely the porogens particles. Thus, the particles cannot be washed out with water easily. Additionally, most of the time, a dense solidified layer will be formed on the outer layer of the polymer after the solvent of the polymer is removed or the solution has been crosslinked. This layer inhibits the removal of the inside porogen particles. Thus, most of the porous materials prepared by solvent casting and particulate leaching method are limited to 2D thin wafers or membranes (500-2000 µm) or constructed by layering such films into a laminated structure.

2.7.2. Gas foaming

A synthetic polymer such as PCL or PLGA is compressed into a heated mould. Then, the material is placed in a chamber and exposed to high pressure CO_2. After several days the pressure inside is gradually restored to atmospheric levels. During this process CO2 "leaks" from the polymer and forms pores, leaving behind a sponge-like structure. This technique was developed to avoid the use of organic solvents and solid porogens. However, the excessive heat used during compression moulding eliminates the possibility of incorporating any temperature labile element, such as cells or growth factors, into the polymer matrix. In addition, the pores generated do not form a well interconnected structure[175], which is necessary for efficient nutrient and oxygen diffusion and cell mobility through the scaffold.

2.7.3. Thermally induced phase separation (TIPS)

TIPS uses thermodynamics and the different kinetic behaviour of a mixture solution. Basically, a defined binary solution will have a crystallization temperature (commonly known as freezing point) and it will have a phase separation temperature. If the crystallization temperature is higher than the phase separation, by lowering the temperature, a solid-liquid separation takes place. On the other hand, if the crystallization temperature is lower than the phase separation temperature, a liquid-liquid separation occurs. By altering the types of polymer and solvent, polymer concentration and phase separation temperature, different types of porous scaffolds can be produced. For instance, nanofibrous gelatin scaffolds have been created by TIPS technique[176]. Briefly, paraffin spheres of a selected size and preheated to ensure interconnection were prepared onto a Teflon mold. After, a gelatin solution (5% gelatin in 1:1 water:ethanol) was casted onto the paraffin and allowed for phase separation. The construct was freeze-dried and finally submerged into hexane to remove the paraffin. This approach offers the possibility to decide level of porosity and nanofibers fabrication[177]. However, it is a long process fabrication technique and it still needs the use of certain organic solvents that are not ideal for some tissue engineering applications.

2.7.4. Electrospinning

Electrospinning can be used to produce polymeric fibres with diameters ranging from micro to nanometres. The fibres are obtained using an electric force that draws charged thread of polymer solutions or melts that will solidify – by solvent evaporation or cooling down – onto a target or collector (Figure 2-13). It is a very versatile technique as it allows the creation of random and aligned fibres at both the micro and nanoscale. It has been used for many different tissues in the field of orthopaedic tissue engineering[178,179]. However, limitations include (i) the fact that most of the solvents used for electrospinning can be toxic, (ii) for ECM derived biomaterials the technique can denature important molecules, (iii) it is challenging to obtain scaled-up 3D structures and (iv) there can be significant batch to batch variation.
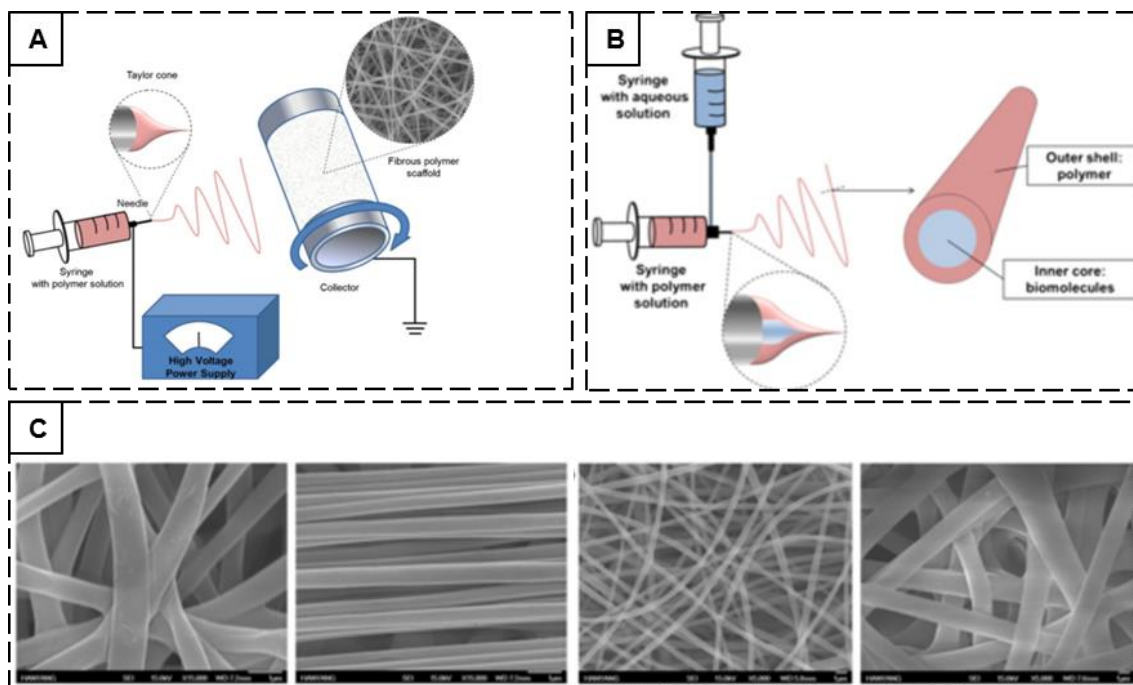
Figure 2-13. *A) Scheme of the electrospinning system with major components. B). Core-shell structure conceptual diagram. C) Various fibrous structures fabricated via an electrospinning technique: random/align directional fibre and micro-/nano-sized fibre, left to right.*

2.7.5. Fibre bonding

This technique involves the formation of an interconnected fibre mesh by combining polymer fibres with a continuous polymer in solution. After the solvent has been evaporated, there is a heat treatment to support bonding of the fibres. Finally, the continuous polymer is dissolved leaving a bonded fibre structure. This technique was first

used in tissue engineering applications by Mikos and colleagues[180] using PGA as a fibre mesh and PLLA as dissolvable matrix to create structures for cell attachment and transplantation. It also has been used for cartilage tissue engineering using starch-polycaprolactone based fibres, but levels of chondrogenesis obtained were not promising when comparing with other materials. The main disadvantages are poor mechanical integrity, lack of stability, residual organic solvents and difficulty to control membrane porosity or morphology[181].

2.7.6. Self-assembly

Nature tends to self-organize its basic structural molecules in order to create more complex tissues. Research has been focused on using this feature in order to engineer scaffolds for regenerative medicine. For example, at physiological temperature and pH, a solution of collagen monomers can self-assemble into a network of fibres surrounding a hydrated solution and presenting a biomimetic appearance to the natural topography of ECM[182]. Another approach is the electrostatic self-assembly (ESA) widely extended for the fabrication of 2D biomaterials. However, more development needs to be conducted in order to extend this idea to 3D environments[183]. In addition, the controlled process only occurs under a complex laboratory procedure that is restricted to only a few polymer configurations, limiting the technique as a large-scale option.

2.7.7. Additive manufacturing (AM)

Most of the techniques described above require relatively long process time until the end product is obtained. Furthermore, the ability to generate a specific three-dimensional construct (such as an anatomically accurate tissue) is challenging at best and mould-dependent. A solution to this problem was born with the rapid prototyping AM techniques, also known as three-dimensional printing (3DP) and the combination of computer aided design software (CAD). These 3D printing techniques include: stereolithography (SLA), selective laser sintering (SLS), fused deposition modelling (FDM), 3D bioprinting and membrane lamination. Perhaps, due to the recent significant development and the large attention from the media, the two most well-known techniques for tissue engineering applications are FDM and 3D bioprinting.

(i) FDM: fused deposition modelling technology is based on the melt processing described above and it consists of the melting and extrusion of a thermoplastic material, such as PCL or PLA, used to 3D print an object. Due to the lack of bioactivity of these materials, FDM is used to build support structures for the bioactive components. This way, it has been possible to print specific architectures to serve as moulds that will be removed[184] or to create adequate reinforcements to increase the mechanical properties of scaffolds for osteochondral tissues and others[130]. A derived technique works with a continuous filament instead of pellets of the material to print. In this case, the technology is named fused filament fabrication (FFF).

(ii) 3D bioprinting: typically involves the deposition of cell-free or cell-laden hydrogels. Some examples of hydrogels that have been successfully used in 3D printing are alginate, agarose, PEGMA and GelMA[185]. Generally, 3D bioprinting utilizes the layer-by-layer method to create tissue-like architectures that can be further crosslinked to increase structural stability. Alternatives to layer-by-layer include microinjection or drop-on-demand inkjet and laser-assisted printing (although the later one requires very expensive equipment). 3D bioprinting is based on three central approaches: (1) biomimicry, aka. biologically inspired engineering, focuses on the reproduction of specific cellular functional components such as mimicking the branching patterns of the vascular tree[186]; (2) autonomous self-assembly, which relies on the cells as the primary driver of histogenesis and requires a deep knowledge of the microenvironment during developmental mechanisms of organogenesis[187]; and (3) mini-tissue building blocks, concept relevant to both of the previous approaches, that can be assembled into larger constructs by rational design, self-assemble or a combination of both[188].

(iii) Hybrid systems: such bioprinters combine either FDM or FFF systems with 3D bioprinting technology. This approach opens a range of new applications that resolves their individual disadvantages due to the lack of bioactivity of the synthetic materials and the lack of mechanical strength

of the bioinks. The synergistic approach overcomes previous limitations on the size, shape, structural integrity and vascularization of bioprinted tissue constructs[130]. Such strategies commonly involve the following steps: First of all, a framework made up of synthetic biomaterials such as PCL and PLGA is fabricated to support the entire mechanical stability of 3D tissue or organ. Second, the hydrogel which is able to encapsulate cells and growth factors is dispensed into the pores. The sequential dispensing of synthetic biomaterials and hydrogel is repeated and stacked to build a 3D tissue or an organ (Figure 2-14)[189].
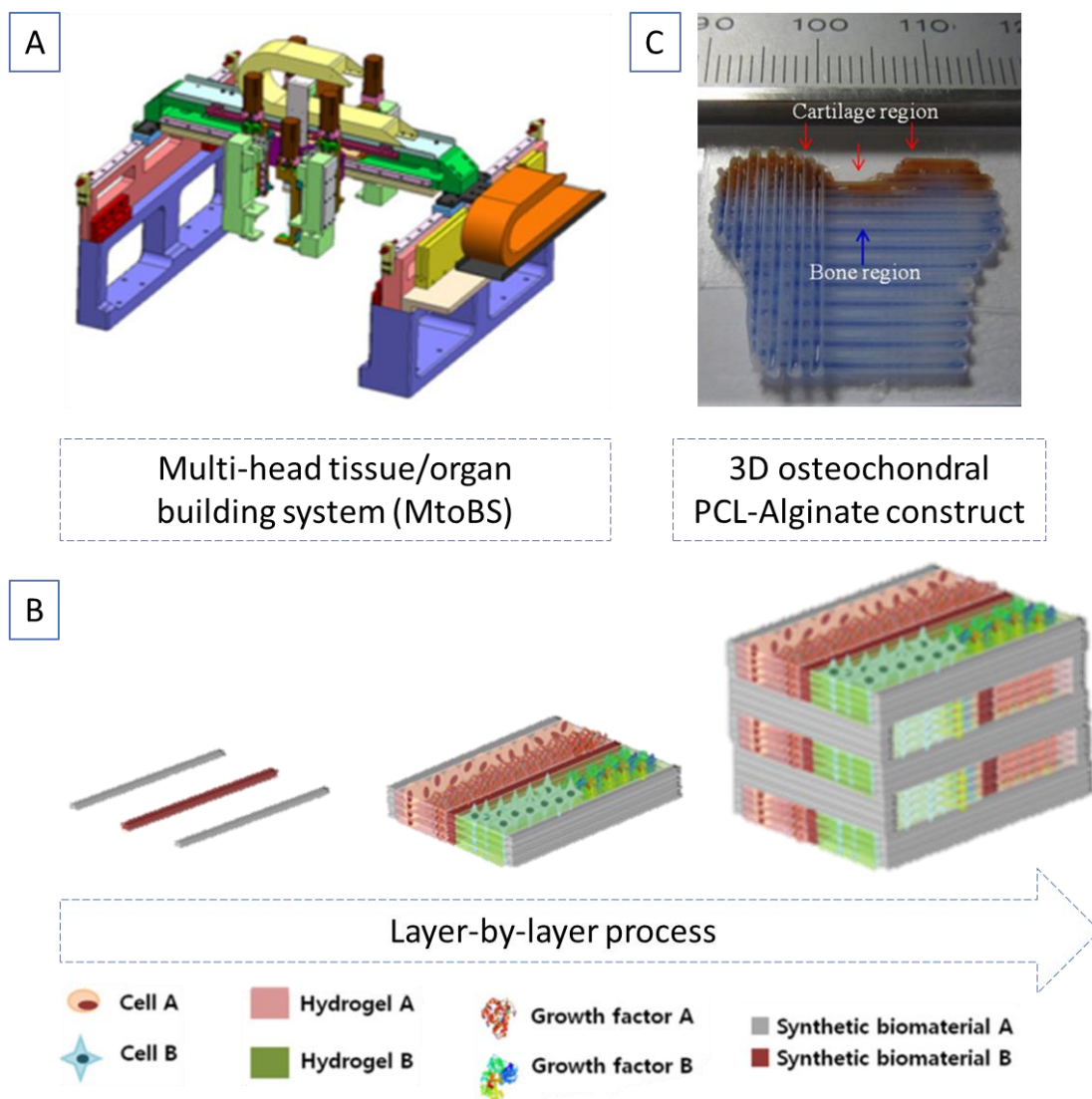
Figure 2-14. *Overview of the bioprinting process. A) Multi-head tissue/organ building system (MtoBS). B) Schematic pictures illustrating the layer-by-layer process and the different components options. C) A conceptual 3D osteochondral structure made up of PCL and two different alginates for osteochondral defect repair. Cartilage and bone*

Nowadays, several options are available in the market that achieve high quality and reproducible printability combining both FDM and bioprinting into one single approach such as the 3D bioplotter from RegenHU-3D Discovery (FDM based) or the desktop 3D bioprinter from Allevi (previously BioBots).

2.7.8. Freeze-drying

Freeze-drying, also known as, lyophilisation, is a dehydration technique which involves the freezing of a wet product (such as collagen slurry) and its subsequent drying (by solvent sublimation) under vacuum. Freeze-drying has many applications: from the food industry to the drug industry and tissue engineering. In terms of scaffolds for tissue engineering, the process (1) enables the fabrication of porous structures to allow cell infiltration into the biomaterial, (2) provides preservation of temperature sensitive biological products, such as growth factors; (3) improves the material storage life, essential for the development of an off-the-shelf product. An extended version of the principles of freeze-drying can be found in CHAPTER - APENDIX: 10.1

Generally, the freeze-drying cycle is divided in 3 phases:

(i) Initial freezing phase: a biomaterial derived slurry is frozen into a mould with a desired shape. The bulk structure cannot be altered as it depends on the recipient or mould (unless is a crosslinked 3D printed hydrogel). On the other hand, the microstructure and pore size can be tailored during the process depending on the heat transfer direction or freezing rate, respectively. Heat transfer can be controlled by mould design, while freezing rate can be controlled by the shelf of the freeze-drier. In this phase, the product is frozen below its glass transition or collapse temperature, which tends to be a few degrees below melting temperature for biological products.

(ii) Primary drying (sublimation) phase: after the product is frozen, pressure in the chamber is reduced by turning the vacuum on, which causes the frozen water to sublimate (transition directly from solid to gas phase). Sublimation characteristics are greatly dependent on the achieved frozen

structure in the first phase. Typically, thicker samples will impede sublimation. On the other hand, interconnected frozen solution or big water crystals will enhance it. In order to accelerate the process, there are two approaches that complement each other. (1) A "condenser" helps deposit chamber vapour. (2) Energy in form of heat is supplied to the product. This energy must remain lower than the product's collapse temperature (the highest allowable product temperature during the conditions of sublimation).

(iii)   Secondary drying phase: shelf temperature is raised to eliminate the final traces of unfrozen water which remain attached to the product due to adsorption. In this phase, the product is not part of a solution anymore but a solid with a higher glass transition temperature (a temperature which is approached but not exceeded in order to avoid compromising product stability).

Once the process is completed, the treated product will have retained its form, volume and original structure, as well as all its physical, chemical and biological properties. It can then be stored (provided packaging is effective to the reduction of moisture migration) for an almost indefinite period.

In traditional freeze drying, products are subjected to a random freeze with no intended gradient of temperatures within the product. This allows for random nucleation points which results in random shaped pores. Directional freeze-drying incorporates an isotropic heat transfer in the initial freezing step to allow for a gradient of temperatures which results in a unidirectional growth of the water crystals and thus longitudinal aligned shaped pores. Freeze-drying technique has been successful in developing collagen derived scaffolds with such microarchitectures for different tissue engineering applications, such as tendon[190], muscle[191], peripheral nerve[192] and articular cartilage[193].

2.7.9. Architectures beneficial for osteochondral tissue engineering

Nature has adopted anisotropic structures for specialized load bearing functions. For instance, tendon's crimped and aligned collagen bundles are nature's optimized anisotropic design for the tissue to bear high tensile loads along the direction of fibre

alignment[194]. In articular cartilage, the arcade-like collagen organisation helps dissipating the high loads passing through our joints. Fibrous or fibrocartilaginous repair tissues, that lack this native tissue organisation, are unable to bear the challenging loads that pass through the joint in the long-term, and eventually degenerate, incapable to withstand the daily wear and tear from the joint movements. Recent studies have demonstrated the importance of both the scaffold pore anisotropy and pore size on the quality and organization of engineered tissues, and hence their long term success[195,196].

It has long been known that cell organization in soft media is strongly influenced by the topography and mechanical properties of the environment[197–201]. Cells have been shown to align themselves in the direction of maximal stiffness sensed in their surrounding environment[202] (**Figure 2-15**) and align along the direction of pull between fixed points[203]. In turn, this environment-controlled orientation leads to the production of an oriented matrix. It has been demonstrated that scaffold architecture can determine the organization of the deposited collagen network by fibroblasts, with a fibre orientation parallel to the major cell axis[204,205]. In addition, cellular and neo-matrix alignment within decellularized cartilage explants appears to be influenced by the underlying collagen architecture of the decellularized tissue[206]. The newly deposited organised tissue has been demonstrated to play a role in further events. It has been seen that the *de novo* deposited aligned matrix of a scaffold made of collagen type I influenced mineral particles to align in the direction of the fibre orientation[207] after inducing an endochondral healing in a rat femoral defect.

Scaffolds with aligned architecture have also been tested for other tissues with an anisotropic nature, such as tendon or ligament[208]. A tissue engineered construct that matches the hierarchical structure of the native anterior cruciate ligament (ACL), has sufficient mechanical properties and encourages the production of ligamentous tissue deposition, will likely improve the clinical treatment of ACL injuries[209]. In addition, scaffolds containing cylindrical tubular conformations result in a higher compressive moduli, compared to constructs with uniform pores, regulating the cell-mediated contraction and enabling the maintenance of complex three-dimensional structures[210] with stabilised mechanical properties[211,212]. Anisotropic structures may also provide further benefits, such as encouraging cell infiltration[195] or facilitating the transport of nutrients and the exchange of metabolites in the porous scaffolds[196].
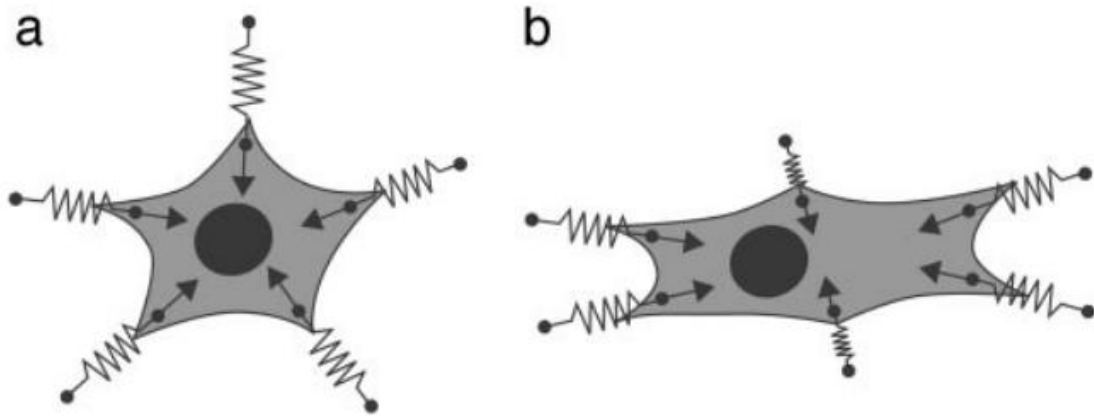
Figure 2-15. *An adherent cell actively pulls on its soft environment through cell–matrix contacts. Experimentally, one finds that cells orient themselves in the direction of maximal stiffness of the environment. In this cartoon, it is presented one possible mechanism by which active mechanosensing in an elastically anisotropic medium might lead to cell orientation. The local elastic environment is represented by linear springs with different spring constants. **a,** In an isotropic environment, all spring constants are the same, growth at different contacts is similar, and the cell does not orient. **b,** If spring constants are largest in one specific direction, the corresponding contacts outgrow the others and the cell orients in the direction of maximal stiffness of the environment[202].*

Moreover, based on early studies, the minimum requirement for pore size for osteochondral tissue engineering is considered to be ~80 µm due to enable rapid cell migration through the scaffold[213–215]. Small pores (80-200) have been shown to favour hypoxic conditions and induced cartilage formation[31,216], while large pores (300-400 µm) that can be well-vascularized and avoid stem cell condensation have been shown to enhance new bone formation by direct osteogenesis[217,218].

2.8. Cells in tissue engineering: identification of a cell source

In osteochondral tissue engineering, different cell types or combinations of cell types have been explored for regenerating this complex interface[219]. These strategies can be broadly split into two different groups. (i) The first strategy involves the use of a cell sources having only a chondrogenic capacity, i.e. chondrocyte progenitors or chondrocytes. (ii) The second strategy involves the use of a single cell source having both chondrogenic and osteogenic differentiation competence, *i.e.*, pluripotent or multipotent stem cells[220].

2.8.1. Chondrocytes

Chondrocytes were long believed to be the exclusive cell residing in cartilage, being responsible for the turnover and maintenance of the tissue. Chondrocytes have an average diameter of 10-13 µm. Due to the avascular condition of the cartilage, chondrocyte cells survive in an anaerobic environment receiving nutrients from the synovial fluid. The logic behind using chondrocytes for cartilage tissue applications is clear, as the cells can produce cartilage tissue. However, harvest of these cells from the joint requires an additional surgery/hospital stay and causes donor-side morbidity, which makes their use costly and not without its problems. Two cell types can be isolated from articular cartilage:

(i) Chondrocyte progenitors, also known as chondroprogenitors, are predominantly found at the surface of articular cartilage[56,221–223]. They have high proliferation capacity and commitment to their differentiation programme[224]. To date, only a limited number of studies have examined their use for tissue engineering, hence conclusive isolation or culture protocols are not available and further validations of their phenotypic stability are required[225].

(ii) Differentiated chondrocytes: they have high chondrogenic capacity and competence to deposit cartilage-like matrix. As chondrocytes are expanded in monolayer they dedifferentiate into a more fibroblastic-like cell, lowering their production of type II collagen and proteoglycans[71]. Adult articular chondrocytes are the most used differentiated cells, however there are some age or disease-related differences across donors making their efficiency/efficacy unpredictable. Other type of chondrocytes that are being explored for cartilage and bone tissue engineering applications include adult nasal chondrocytes[226,227] and juvenile or neonatal articular chondrocytes[228,229].

2.8.2. Stem cells

(i) Pluripotent stem cells: includes embryonic stem cells (ESCs) as well as induced pluripotent stem cells (iPSCs). These cells imply potentially an

unlimited source of desired differentiated cell types, such as chondrocytes or osteoblasts. Pluripotency is very attractive from a personalised medicine perspective. Yet their use is affected by ethical concerns due to implications of using human embryos[230]. Moreover, both ESCs and iPSCs are associated with tumour formation[231], an unacceptable complication for the treatment of a non-life-threatening disease. Thus, the possible approval of the pluripotent stem cell-based therapies for osteochondral tissue regeneration applications remains unanswered.

(ii)   Multipotent mesenchymal stromal/stem cells (MSCs): self-renewal and multipotent progenitor cells able to differentiate into several mesenchymal lineages[91,232,233,234], see Figure 2-16. MSCs are the most used cells in tissue engineering due to large availability and high proliferation capacity. In addition, MSCs have been shown to secrete a variety of cytokines and growth factors that have both paracrine and autocrine effects. Some of these biomolecules have immunomodulatory activities that can suppress the local immune system which could otherwise potentially aggravate the damage occurred or affect the regeneration capacity of an injury. Other bioactive factors have a trophic effect which can inhibit fibrosis and apoptosis or enhance angiogenesis, mitosis, differentiation and tissue-intrinsic cell's reparative behaviour[92]. Mesenchymal stem cells can be obtained from adult and from foetal tissues. Adult tissues include bone marrow, synovium and adipose tissues; while foetal tissues include the placenta, umbilical cord or the umbilical cord blood. MSCs have high proliferation capacity and so they can be expanded *in vitro* enabling the growth of a large number of cells, essential for scaling up procedures.
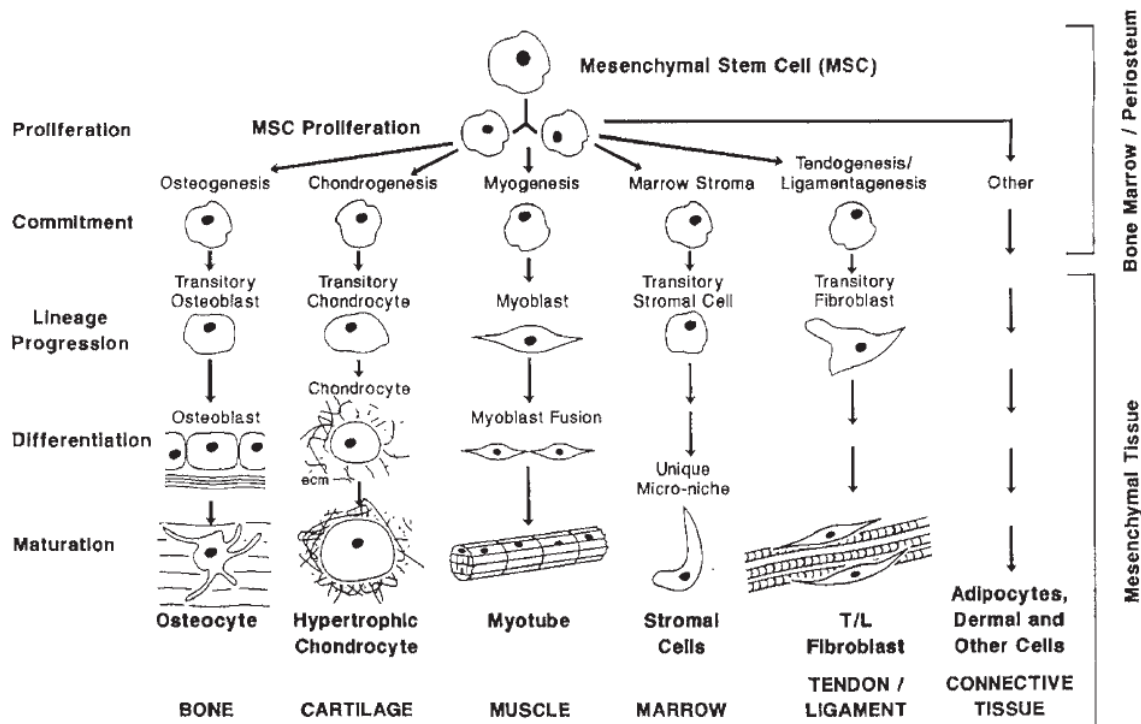
Figure 2-16. The mesengenic process[95]

2.9. Developmental tissue engineering

Successful tissue engineering relies on the integration of cells, signals and scaffolds to create functional tissues. It is important to realize that carbon-life, as we know it, is a few million years ahead of us in development of tissues and corresponding functionality. Thus, even if biomimetic approaches may not be always the best solution for every problem, it is important to give them special attention. With this in mind, we can look at the final and functional structure of the tissue to try to mimic its native components or structure (as described above in previous sections), or we can study how a specific tissue was formed and try to mimic its natural development.

2.9.1. Normal limb development – a template for tissue engineering

Limb development follows a controlled and well-known pattern[235]. The limbs comprise the appendicular skeleton, which is composed of 126 bones in the human body. Limb buds become visible at the end of the fourth week of development, first the forelimb and then 2 days later, the hind (lower) limb. Initially, the limb buds consist of a

mesenchymal core covered by a layer of ectoderm (one of the three primary germ cell layers in the very early embryo), which thickens and forms the apical ectodermal ridge (AER). The AER influences the adjacent mesenchyme, causing it to remain as a population of undifferentiated, rapidly proliferating cells. As the limb grows, when the cells within are no longer under the influence of the AER, and they begin to differentiate into cartilage and muscle. In this manner, development of the limb proceeds proximodistal, *i.e.* running from the centre of the body out towards the distal ends of appendages.

At week 6 of embryonic development, the terminal part of the limb buds flattens and form the hand and footplates. Fingers and toes are formed when cell death in the AER separates it into five parts. Then, further development depends on their continued outgrowth under the influence of the five segments of ridge ectoderm, condensation of the mesenchyme to form cartilaginous digital rays, and the death of intervening tissue between the rays. Development of the upper and lower limbs is similar except that morphogenesis in the lower limbs is delayed 2 days and the limbs rotate in opposite directions. The upper limb rotates 90° laterally whereas the lower limb rotates 90° medially.

While the external shape is being formed, mesenchyme in the buds start to condense and differentiate into chondrocytes, which form the first hyaline cartilage models (Figure 2-17A). When chondrogenesis is arrested and the cells start to increase in number and density, joints are formed in these cartilaginous condensations (Figure 2-17B). Factors regulating the positioning of joints are not clear, but the secreted molecule WNT14 appears to be a key inductive signal[235].

By the end of the embryonic phase (week 12 of development), the cartilaginous limbs become a template for bone formation through endochondral ossification. This process occurs gradually in the so called primary ossification centre of the diaphysis or shaft (the middle tubular section of a long bone composed of compact bone surrounding the bone marrow) and ends up in the development of bones that lead to the extremities (Figure 2-17C). The diaphysis is usually completely ossified at day of birth, but the two ends of the long bones, the epiphyses, are still cartilaginous. Shortly thereafter, however, ossification centres arise in the epiphyses, the secondary ossification centres. This secondary centre takes more time to ossify and a cartilage plate remains between the

diaphyseal and epiphyseal ossification centres. This plate, the growth plate or epiphyseal plate, plays an important role in the growth in length of the bones. Indeed, as previously mentioned, decellularized growth plate ECM derived scaffolds have been shown to accelerate large bone defect healing[29,168], suggesting that mimicking aspects of the structure and composition of this tissue in biomaterial scaffolds might represent a promising strategy for regenerating bone defects or the subchondral region of osteochondral defects.
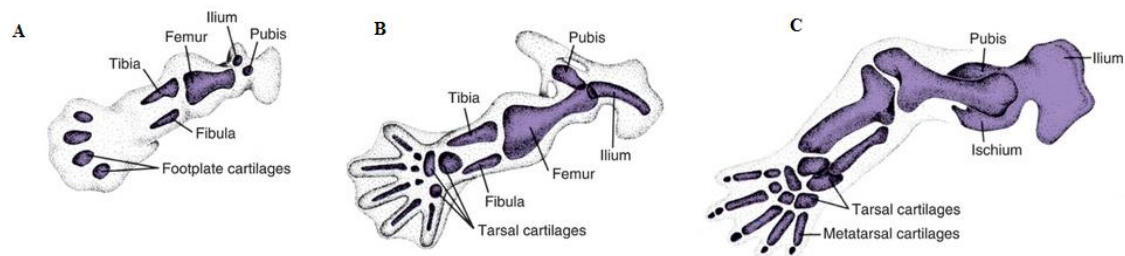
Figure 2-17. Limb development: first hyaline models in a lower extremity of human embryo (A), chondrogenesis arrest and joint development (B), primary ossification centers formation and start of endochondral ossification (C).[235]

Endochondral ossification proceeds on both sides of the growth plate and when the bone has acquired its full length, the epiphyseal plates disappear, and the epiphyses unite with the shaft of the bone (Figure 2-18). The growth plate localization varies depending on the type of bone. For instance, in long bones, the epiphyseal plate is found in each extremity; however, in smaller bones (*e.g.,* phalanges), it is found only at one extremity; and in irregular bones (*e.g.*, vertebrae), one or more primary centres of ossification and usually several secondary centres are present.

Synovial joints between bones, such as the knee or hip, begin to develop at the same time that mesenchymal condensations initiate the process of forming hyaline cartilage and in this case the condensed mesenchyme differentiates into dense fibrous tissue, which ends up forming different structures, such as the articular cartilage, covering the ends of the two adjacent chondrifying bones; the synovial membranes; and the menisci and ligaments within the joint capsule (*e.g.*, the anterior and posterior cruciate ligaments in the knee). In the case of the sutures in the skull, the area between the bones remains as a dense fibrous structure.
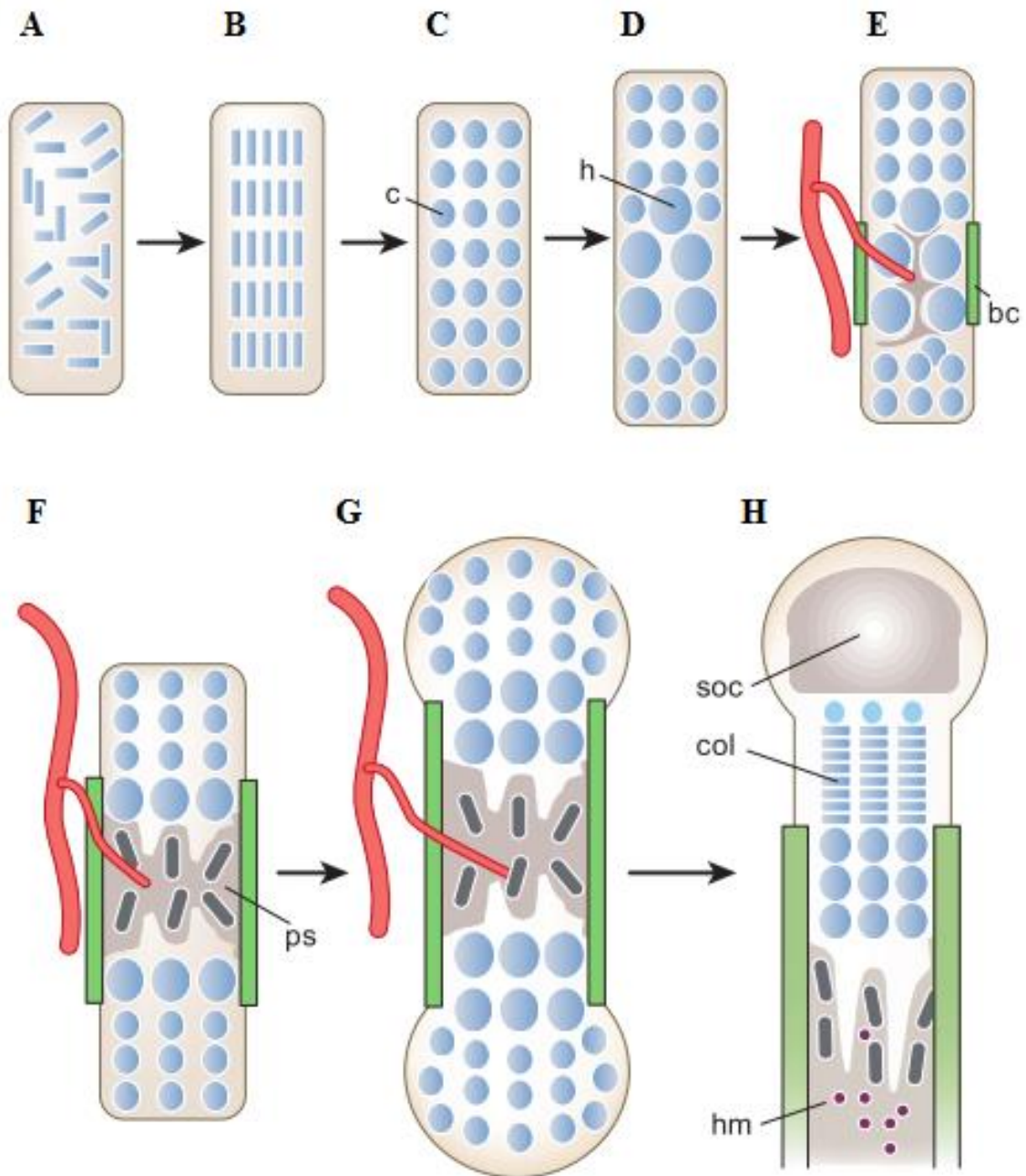
Figure 2-18. *Endochondral bone formation: mesenchyme (A), mesenchymal cells condense (B), cells of condensations become (c) chondrocytes (C), central chondrocytes stop proliferating and become (h) hypertrophic (D). perichondrial cells adjacent to hypertrophic chondrocytes become osteoblasts forming (bc) bone collar and hypertrophic chondrocytes direct the formation of mineralised matrix, attract blood vessels, and undergo apoptosis (E), osteoblasts of primary spongiosa accompany vascular invasion, forming the (ps) primary spongiosa or primary ossification centers (F), chondrocytes continue to proliferate, lengthening the bone, osteoblasts of primary spongiosa are precursors of eventual trabecular bone and osteoblasts of bone collar become cortical bone (G); at the end of the bone, the (soc) secondary ossification centre forms through cycles of chondrocyte hypertrophy, vascular invasion and osteoblast activity. The growth plate below the secondary centre of ossification forms orderly*

2.10. Overall objective: bottom-up biomimetic design of scaffolds for osteochondral tissue engineering

As previously discussed, a large number of materials have (and are currently being) explored for osteochondral TE, suggesting that the ideal scaffold composition, to restore normal joint function, has yet to be identified. The overall objective of this thesis is to develop a new biomimetic scaffold for osteochondral defect regeneration, where the structure and composition of the scaffold was inspired by the ECM of the articular cartilage, growth plate and bone.
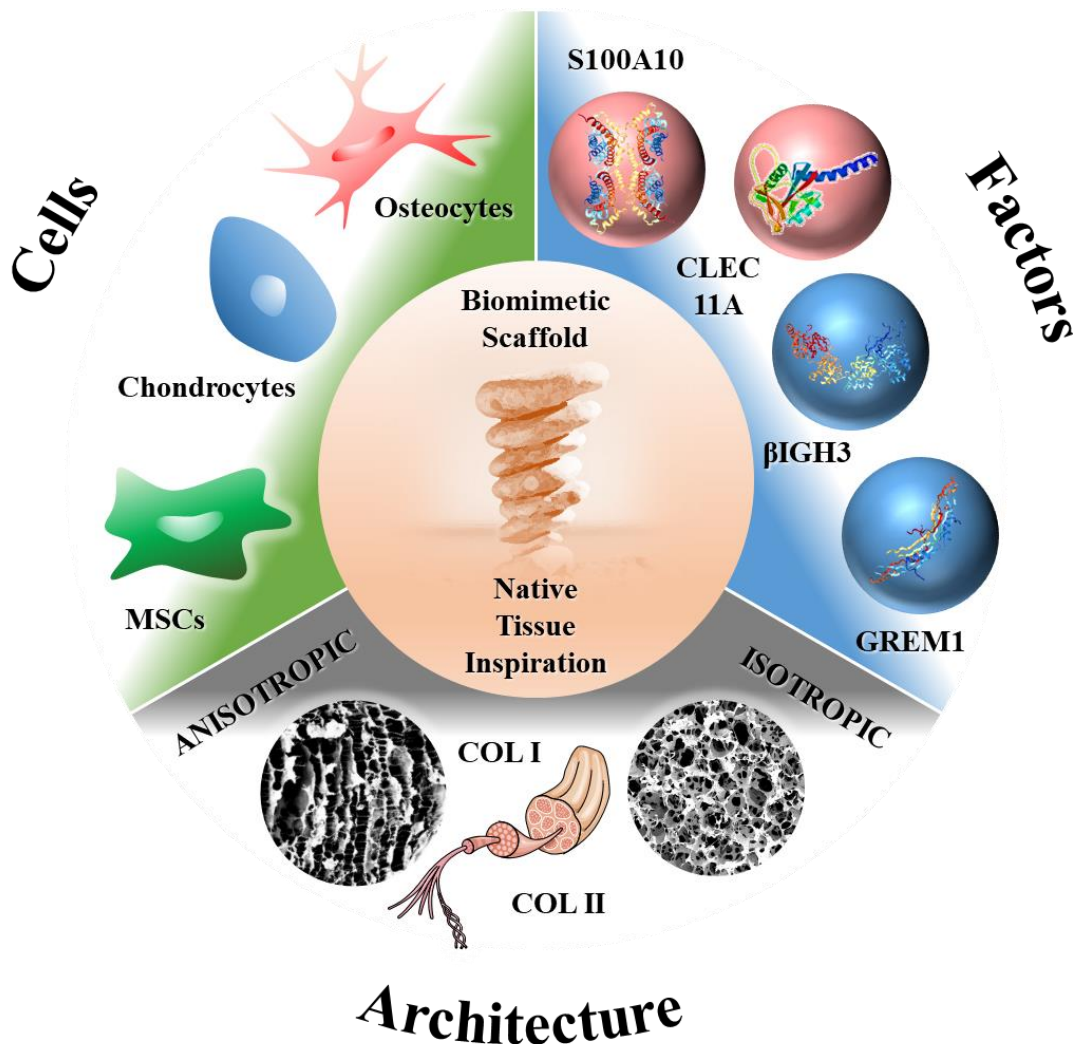
Figure 2-19*. Bottom-up biomimetic tissue engineering. Strategy combining the specific aims of this thesis: (i) identification of the microenvironment key factors, (ii) assessment of the effect of the chosen key factors on chondrogenesis or osteogenesis of MSCs (iii)*

recapitulation of aspects of the native microarchitecture of osteochondral tissue. (iv) assessment of the pore morphology on MSC differentiation. (v) Fabrication of a biomimetic ECM derived scaffolds for osteochondral tissue engineering. The factor protein structures were obtained from Protein Data Bank, except for CLEC11A, which was obtained by structure prediction of the aminoacid sequence with (PS)² (Molecular Bioinformatic Centre, National Chiao Tung University). Collagen cartoon was obtained from Servier Medical Art.

The overall objective will be achieved by addressing the following specific aims:

Specific aim 1: To characterise the ECM proteome of Growth Plate and Articular Cartilage in order to identify osteo- and chondro-inductive factors

ECM derived scaffolds that maintain native tissue complexity have been under investigation for more than 25 years, since Badylak and others started exploring the regenerative potential of small intestinal submucosa[158], and, during that time, ECM derived scaffolds have been implanted in millions of patients[237]. However, the complexity and diversity of biomolecules present in tissue or organ-derived ECMs is not yet fully characterized, hence their mechanism of therapeutic action remains poorly understood[33].

In order to shed some light on this complex topic, and to potentially identify bioactive factors that could be used to functionalise scaffolds and/or used as soluble factors to enhance the development of *in vitro* engineered tissues, the first objective of this thesis is to undertake a proteomic characterization of the extracellular matrix of two different musculoskeletal tissues, which our lab have previously demonstrated to promote tissue-specific differentiation, both *in vitro* and *in vivo*[29,34]. These tissues are porcine articular cartilage and growth plate (hypertrophic cartilage). The goal is to identify soluble factors within these tissues that may impart specific chondroinductivity or osteoinductivity.

Specific aim 2: To assess the effect of soluble factors identified in the ECM of articular cartilage and growth plate on stabilising chondrogenesis and enhancing osteogenesis of MSCs

MSCs seem a particularly attractive cell source for osteochondral tissue engineering. They can be easily extracted using standardized procedures and they are largely available. However, MSC derived chondrocytes tend to become hypertrophic and

progress along an endochondral pathway, ultimately forming bone *in vivo*. We hypothesise that there are proteins in AC ECM that can regulate this process and help engineer phenotypically stable cartilage. The second aim of this thesis is to examine the effect of regulatory factors predominantly identified in the ECM of articular cartilage (from Aim 1 of the thesis) on the phenotypic stability of cartilage engineered using bone marrow derived MSCs both *in vitro* (pellet and scaffold culture) and *in vivo* (subcutaneous implantation into nude mice).

Despite the negative outcome of chondrocyte hypertrophy for cartilage tissue engineering, recapitulating the developmental process of endochondral ossification has become an attractive strategy to engineer bone. However, little is known about this complex process and the role that ECM proteins play. This thesis aims to evaluate the effect of growth plate-specific ECM factors on osteogenesis of MSCs. To this end, MSCs in monolayer model will be cultured in osteogenic media in the presence of GP ECM-specific factors and analysed for mineral deposition after 3 weeks.

Specific aim 3: To optimise the pore morphology (size and microarchitecture) and mechanical properties of ECM derived scaffolds for musculoskeletal tissue engineering

The field of osteochondral tissue engineering has extensively investigated how the composition and bulk mechanical properties of scaffolds determine their efficacy[35,36]. While it is also well established that scaffold architecture is a key determinant of scaffold success[37], the ideal microarchitecture of ECM derived scaffolds targeting osteochondral defect repair has yet to be identified.

Scaffold pore microarchitecture and mechanical properties are believed to play a key role in determining the biological functionality and long-term efficacy of ECM scaffolds. Freeze-drying has been successfully used to produce scaffolds for tissue engineering with porous anisotropic structures and to tailor scaffold pore size. Moreover, 3D printing techniques have been used to generate implantable constructs with robust mechanical properties.

Thus, the second objective of this thesis involves (i) developing a directional freeze-drying protocol in order to fabricate ECM derived scaffolds with aligned pores,

(ii) optimising a freeze-drying protocol to control pore size, and (iii) exploring the design and 3D printing of synthetic polymeric reinforcements for ECM scaffolds with the ultimate aim of optimising their mechanical properties for musculoskeletal applications.

Specific aim 4: To assess the effect of pore morphology on chondrogenesis and endochondral ossification of MSCs seeded onto ECM derived scaffolds

Mesenchymal stem cells (MSCs) seem a particularly attractive cell source for osteochondral tissue engineering. They can be easily extracted from bone marrow aspirates using standardized procedures and they are largely available[238]. The fourth objective of this thesis is to determine the effect of ECM scaffold pore size, pore microarchitecture and composition on chondrogenesis of MSCs and the tendency of such engineered tissues to progress along an endochondral pathway. To this end, MSCs will be seeded onto AC ECM derived scaffolds and the resulting engineered tissue evaluated after 4 weeks in culture.

Specific aim 5: To develop a biomimetic bilayered ECM derived scaffold for osteochondral tissue engineering

Regenerating the complex composition and microarchitecture of the osteochondral unit is essential for the functional repair of damaged joints. The final objective of this thesis is to integrate its key findings in order to develop a bilayered scaffold for osteochondral defect regeneration that recapitulates certain key aspects of the osteochondral tissue. To this end, a scaffold with an optimised anisotropic pore size structure, composed of two different tissue-specific ECMs with chondroinductive (AC ECM) and osteoinductive (bone ECM) properties will be produced using an iterative freeze-casting technique during the freeze-drying process. The capacity of this bilayered ECM scaffold to support spatially defined tissue development will be next assessed *in vitro*, followed by a large animal model study to assess its potential as an 'off-the-shelf' scaffold for osteochondral tissue regeneration.

3. CHAPTER: Identification of tissue-specific factors in the unique ECMs of Growth Plate and Articular Cartilage for improving osteochondral tissue engineering

3.1. Introduction

The repair of critical size cartilage and bone defects still remains a significant clinical challenge[56,68]. Putative tissue engineering solutions require the development of compliant biomaterials to actively modulate adhesion, proliferation, migration and differentiation of seeded cells. There have been very different models proposed by various groups around the world for tissue engineering of osteochondral grafts. In part, this reflects the fact that our understanding of the requirements to restore normal joint function remains poor[96,97]. ECM derived scaffolds that maintain native tissue complexity have been under investigation for more than 25 years[158] and, during that time, they have been implanted in millions of patients[237]. However, the complexity and diversity of biomolecules present in tissue or tissue-derived ECMs are not yet fully characterized to understand material composition, specific interactions with cells and their therapeutic action[33].

Quantitative tandem mass spectrometry (MS/MS) based proteomics has become a very powerful tool used to analyse and comprehend proteomes in different animal tissues and other organisms[239]. For decades, structure and function of selected proteins have been studied in isolation or small groups. MS/MS brings the opportunity to study proteomes as an integrated system so as to provide unprecedented insights into the composition, structure and function of a given tissue[240].

To this end, the first objective of this chapter focuses on the label free MS/MS proteomic characterization of the extracellular matrix of two different musculoskeletal related tissues, which have been previously demonstrated to promote differential tissue deposition by mesenchymal stem cells, both *in vitro* and *in vivo*[29,34]. These tissues are porcine articular cartilage and growth plate. The goal is to identify soluble factors within these tissues that may impart specific chondroinductivity or osteoinductivity to the ECM.

In order to refine the protein list obtained from the MS raw data, all identified protein gene names from each sample group were searched against the Matrisome[241,242] and STRING[243,244] database platforms.

Matrisome database (from *matrix* and *-ome*, where all constituents are considered collectively) is a bioinformatic effort to compile a list with all the proteins in any given matrix and proteins that can be associated or can contribute to matrices in different situations. Using the characteristic domain-based organization of ECM proteins, it has been possible to predict bioinformatically the ensemble of genes encoding extracellular matrix and ECM-associated proteins, *i.e.* the "matrisome", in various model organisms (human, mouse and zebra fish). The database clusters proteins in two groups: core matrisome proteins (including ECM glycoproteins, collagens, and proteoglycans) and matrisome-associated proteins (including ECM-affiliated proteins, ECM regulators, and secreted factors).

STRING (*Search Tool for the Retrieval of Interacting Genes/Proteins*) is a database of known and predicted protein-protein interactions. The interactions include direct (physical) and indirect (functional) associations; they stem from computational prediction, from knowledge transfer between organisms, and from interactions aggregated from other (primary) databases, such as Uniprot. Protein–protein interaction networks are important to understand cellular processes. Such networks can be used for filtering and providing an intuitive platform for functional annotations. Exploring the predicted networks can suggest new directions for future experimental research.

The second objective of this chapter focuses on selecting 2 AC-specific and 2 GP-specific proteins and evaluating their effect on chondrogenesis and osteogenesis of MSCs, respectively.

Gremlin1 (GREM1), previously known as Drm, is a highly conserved cystine-knot-secreted glycoprotein of 184 aa (~20.7 kD) and a member of the differential screening-selected gene aberrant in neuroblastoma (DAN) family. The lack of GREM1 has been clearly linked to limb malformations during development, leading to digit loss, polydactyly and other skeletal disorders, hence earning the 90's movie name[245–247]. Recent research has shown that heparin-bound GREM1 can activate VEGFR2[248], implying that GREM1 could also be involved in the regulation of angiogenesis[249] in appropriate microenvironments. However, a more musculoskeletal-specific role has been

associated to this protein since its discovery. GREM1 is a BMP antagonist that inhibits the BMP/Smad signalling pathway by binding to BMP ligands, particularly BMP2, BMP4 and BMP7[154,250–254]. In addition, GREM1 has been shown to inhibit Wnt/β-catenin signalling[255,256], probably due to inhibition of BMP2-mediated upregulation of Wnt1 and Wnt3 expression[257]. Recent studies have shown that GREM1 expression is upregulated in hypoxic conditions which promote higher levels of chondrogenesis[258]. Taken together, these inhibitions result in a decrease of osteoblast differentiation capacity, indirectly regulating bone formation and acting to stabilise hyaline cartilage homeostasis[259].

TGF-β induced gene human clone 3 (βIGH3), also known as transforming growth factor β-induced protein (TGFβi), is a C-terminal RGD-containing protein of 683 aa (~68 kD). It was originally identified in adenocarcinoma cells as a potential mediator of the TGF signalling cascade, due to its 20-fold mRNA upregulation upon growth arrest by treatment with TGFβ1[260]. Later it was found to bind to and interact with a number of ECM proteins (probably related to its bivalent 4D protein structure), such as type I, II and IV collagens (but not gelatine), fibronectin, biglycan and decorin[261,262]. It also acts as a ligand for several integrins, including α3β1, αVβ3, αVβ5 and αMβ2[263]. βIGH3 is a secreted factor that plays a major role in cell-matrix interaction by regulating cell adhesion[264], enhancing cell spreading[265] and regulating cell proliferation and migration[266]. In humans, this protein has been associated mainly to corneal dystrophies, gaining the name of kerato-epithelin[267,268]. However, during cartilage formation and osteogenesis, βIGH3 is highly expressed in pre-cartilage condensation and in pre-hypertrophic chondrocytes and functions as a negative regulator of mineralization[269,270]. In zebrafish, βIGH3 has been shown to be upregulated in fin regeneration[271].

Unlike the AC, the ECM of GP contained CLEC11A and S100A10. C-type lectin domain family 11 member A (CLEC11A), also known as osteolectin or stem cell growth factor (SCGF), is a secreted sulphated glycoprotein. It was first identified in the bone marrow and has been shown to promote colony formation by human hematopoietic progenitor cells. The plasma levels of CLEC11A correlate with haemoglobin levels and increases in patients after bone marrow transplantation. As a result, CLEC11A was considered a hematopoietic growth factor[272]. However, CLEC11A is also expressed in skeletal tissues[273] and it has been shown to upregulate bone formation by promoting differentiation of mesenchymal progenitors into mature osteoblasts and to maintain the adult skeleton. Knock out mice models of the osteolectin gene results in a phenotype with

lower bone volume and bone density[274]. Hypertrophic chondrocytes can also transdifferentiate into osteoblasts and osteocytes during endochondral ossification[275,276]. Thus, in addition to promoting the differentiation of mesenchymal progenitors into mature osteoblasts, Clec11a might also promote the transdifferentiation of hypertrophic chondrocytes into osteoblasts[274].

S100 calcium-binding protein A10 (S100A10), also known as P11, is a member of the s100 protein family containing two EF-hand calcium-binding motifs (although in P11, one of the motifs is afunctional). P11 forms a heterotetrameric complex with annexin II, which enables it to play an integral part of cellular structural scaffolding and trafficking of matrix vesicles (MVs) by interacting with plasma membrane proteins[277,278]. There are three main functions associated to P11-annexin II complex, depending on which protein binds, accumulating it where P11 is secreted and enhancing its activity. (i) P11 complex interacts with the serotonin receptor proteins, 5-HT receptors such as 5-HT1B, modulating the receptor signal transduction pathways activated by the binding of serotonin[279]. P11 also recruits the cell surface expression of the 5-HT4 receptor, increasing its concentration at the synapse[280]. This results in more rapid serotonin-dependent activities which are associated to depression and mood regulation[281,282]. (ii) P11 complex binds to plasminogen activator (tPA), promoting tPA-dependent plasmin production localized at the cell surface[283]. This plasmin activation can contribute to a variety of different biological process, such as regulation of fibrinolysis, angiogenesis[283]. Moreover, in response to inflammatory stimuli, P11-tPA activates pro-MMP9, which promotes plasmin-dependent macrophage recruitment[284,285]. (iii) The S100A10–annexin 2 complex is crucial in routing of TRPV5 and TRPV6 to plasma membrane[286]. TRPV5 and 6 mutants that do not bind to this complex have been associated with osteopenia due to reduction of calcium uptake and upregulation of osteoclast activity[287]. In mineralization-competent Saos-2 cells and in osteoblasts, it has been shown that secreted MVs are selectively enriched with annexins and P11[288,289]. Taken together there is enough evidence to suggest that P11 may be involved in regulation of MVs-mediated mineralisation.

3.2. Methods

3.2.1. ECM harvest

Articular cartilage (AC) and growth plate (GP) used in the fabrication of ECM-derived scaffolds were harvested, in aseptic conditions, from the femoral condyles of female pigs (3-4 months old), shortly after sacrifice. The cartilage tissue was obtained using a biopsy punch to remove all articular cartilage from the head of the femoral joint. Following this, the head of the bone was sawed in half and sectioned through the epiphyseal line to gain access to the growth plate, which was scrapped with a scalpel (tissue location shown in Figure 3-1). The two distinct tissues (AC and GP) were first broken up into small pieces ($\sim$1mm^3) using a scalpel and cryomilled in order to get a fine powder.
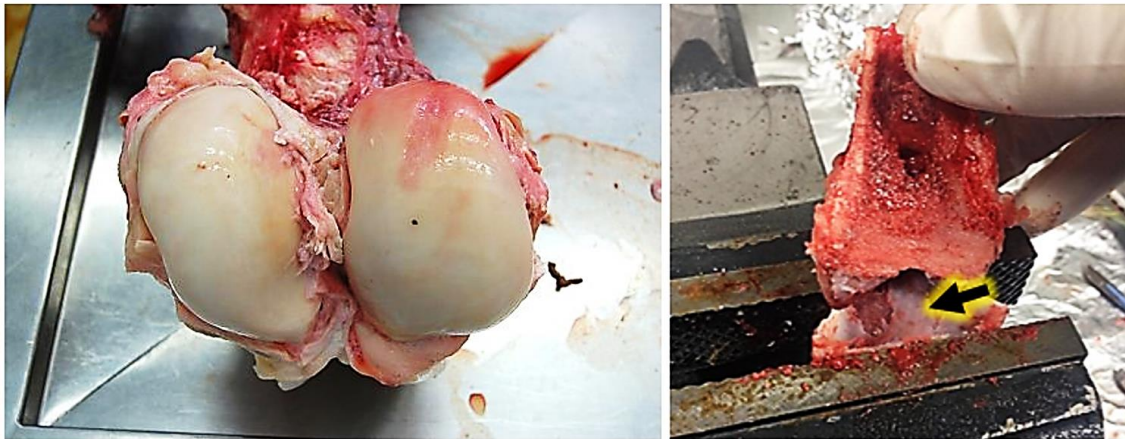
Figure 3-1*. Harvested articular cartilage (left) and growth plate (right) from the femoral condyle of 4-month-old pigs.*

3.2.2. Non-collagenous soluble ECM extraction

In order to characterize the factors and other proteins present in harvested AC or GP ECM, pulverized ECM (n = 3 for each tissue) was processed for mass spectrometry analysis. First, ECM proteins were extracted with 6 M Guanidine-hydrochloride for 2 days at 4 ℃ in rotation. Then, the mixture was centrifuged at 14,000 x g for 10 min at 4 ℃. Supernatant was poured into another tube and pellet containing insoluble material was stored at -80 ℃. Supernatant was incubated with 1:4 volume tricholoracetic (TCA):protein solution for 10 min at 4 ℃ so as to precipitate the soluble ECM proteins. The tube was centrifuge at 14,000 rpm for 5 min. Then, the supernatant was carefully

discarded to avoid pellet disruption. The pellet, was washed with 200 µl acetone and centrifuged again at 14,000 rpm for 5 min. This washing step was repeated another time for a total of 2 washes. Next, the pellet was dried by placing the tube in 95 ℃ heat block for 5-10 min to drive off acetone. Finally, the pellet was carefully re-suspended in 50 µl 6M urea in 50 mM ammonium bicarbonate (ABC).

3.2.3. Protein quantification

After ECM extraction, Nano-drop technology was used to quantify protein levels in order to prepare a sample for mass spectrometry. BCA colorimetric assay was used to validate these results.

3.2.4. Protein preparation and digestion for mass spectrometry

After quantifying protein levels with a nano-drop, a sample volume containing 25 µg of protein was treated with 100 mM dithiothreitol (DTT:sample, 1:20) to get a final concentration of 5 mM DTT. The solution was vortex and incubated at 60 ℃ for 30 min. This should remove disulphide bonds in proteins. Next, the sample was alkylated with 200 mM of iodoacetamide (IAA:sample, 1:20), vortexed and incubated in the dark for 30 min at room temperature. This should permanently inhibit reformation disulphide bonds, which would affect enzyme digestion for mass spectrometry characterization. Then, the sample was diluted with 50 mM ABC to ensure that the 6M urea was diluted to less than 2M before the addition of the trypsin enzyme. Next, 50 µl of the reduced and alkylated sample was added to 1 vial of trypsin singles proteomic grade (T575, Sigma). The sample was vortexed and incubated overnight at 37 ℃ at 350 rpm. To stop the trypsin digestion, 1:60 (HCl:sample) 8.8 M HCl was added to the digested solution.

3.2.5. Ziptip protocol

The samples were prepared by centrifugation at 10,000 rpm for 5 min. Then, the samples were aspirated and dispensed 10 cycles with a previously equilibrated tip (washed with 50% acetonitrile – ACN – in 0.1% trifluoroacetic – TFA – and equilibrated with 0.1% TFA). After, the samples were washed twice with 0.1% TFA and eluted onto

a clean vial with 10 µl of 50% ACN in 0.1% TFA. The samples were allowed to dry during 10-15 min on a vacuum concentrator before resuspending in 20 µl of 0.1% TFA and centrifuging at 15,000 rpm for 5 min. Finally, 16 µl of sample were used to carry out mass spectrometric analysis. This step was performed by trained personnel in the proteomic centre of University College Dublin (UCD).

3.2.6. Mass spectroscopy analysis

Protein identification was done by high performance liquid chromatography–tandem mass spectrometry (HPLC-MS/MS) analysis. The samples were run on a Thermo Scientific Q Exactive mass spectrometer connected to a Dionex Ultimate 3000 (RSLCnano, ThermoFisher Scientific, MA, USA) chromatography system. Tryptic peptides were resuspended in formic acid. Each sample was loaded onto a fused silica emitter (75 µm inner diameter, pulled using a laser puller from Sutter Instruments P2000, CA, USA), packed with UChrom C18 (1.8 µm) reverse phase media (nanoLCMS Solutions LCC, CA, USA) and was separated by an increasing acetonitrile gradient over 45/60 minutes at a flow rate of 250 nL/min. The mass spectrometer was operated in positive ion mode with a capillary temperature of 320 °C, and with a potential of 2300V applied to the frit. All data was acquired with the mass spectrometer operating in automatic data dependent switching mode. A high resolution (70,000) MS scan (300-1600 m/z) was performed using the Q Exactive to select the 8 most intense ions prior to MS/MS analysis using Higher-energy collisional dissociation (HCD) technique. Three different samples from each tissue, either AC or GP, were analysed (biological replicas) and run twice (technical replicas). This step was performed by trained personnel in the proteomic centre of University College Dublin (UCD).

MS/MS derived raw data was analysed using Maxquant software. In order to identify proteins, raw data was searched against a combination of *sus scrofa* reviewed and unreviewed database downloaded from Uniprot. Search parameters included a maximum of one missed trypsin cleavage, cysteine carbamidomethylation as a fixed modification, and methionine oxidation as a variable modification. The precursor mass tolerance was 20 ppm, the fragment mass tolerance was 0.05 Da, and the maximum peptide length was specified as 5 amino acids (default standard parameters of the

software). Peptides that passed the 1% false discovery rate threshold (FDR = 0.01) were used for protein identification[290].

Proteins identified by Maxquant[291] were processed with Perseus[292] in order to elucidate differences across the two tissues. Matrisome[293] and STRING databases[243] were used to cluster proteins into subgroups in order to find protein-protein interactions and to identify enriched biological pathways with key molecules of interest.

In order to reduce the protein list to 4 proteins of interest to use in further studies, the matrisome and string database analysis were focused only on the significantly different proteins between AC and GP. The associated information for each protein in String was then manually curated with different keywords such as "chondrogenesis", "osteogenesis", "cartilage", "bone", "mineralization", "phosphorylation", "collagen" to select proteins that could be related to chondrogenesis or osteogenesis. A more exhaustive literature review of the four proteins selected: GREM1, βIGH3, CLEC11A, S100A10 can be found in the introduction.

3.2.7. Bone marrow derived MSCs isolation and expansion

Bone marrow-derived stem cells (BMSCs) were isolated from the femora of porcine donors (3-4 months, >50 kg) within 3 hours of sacrifice as previously described[294]. The femur was opened under sterile conditions and the marrow was transferred, using a spatula, into a 50 ml Falcon tube containing pre-warmed expansion medium. The marrow was triturated to break the clumps and homogenized, followed by centrifugation using lymphoprep (Axis-Shield, Scotland) in order to separate mononuclear cells, which reside at the interface, from the rest of marrow material. Mononuclear cells were isolated from the femora and plated at a seeding density of 5 x 10^3 cells/cm² in high-glucose Dulbecco's modified eagles medium + GlutaMAX™ (4.5 mg/mL D-Glucose, 200 mM L-Glutamine; hgDMEM) supplemented with 10% foetal bovine serum (FBS). All Gibco®, Biosciences, Dublin, Ireland. Cells were expanded to passage 2 in a humidified atmosphere at 37 ⁰C and 5% CO2.

Bone marrow stem cells (BMSCs) were harvested from 4-month-old porcine bone marrow following a standard protocol. Cells were seeded at a suitable density (2.5x106cells per 58cm2 petri dish) based on previous experiments of my laboratory and monitored daily to assess colony formation. Finally, the mesenchymal progenitor cells were split and expanded for use or frozen in liquid nitrogen for long term storage.

3.2.8. Analysis of AC-specific proteins in pellet model in vitro

Pellets were formed by placing 250,000 BMSCs in a 1.5 ml conical microtube and centrifuged at 650 g for 5 min. The pellets were cultured in normoxic conditions (20% pO_2) at 37 ºC, for 21 days in a chemically defined chondrogenic medium (CM): Dulbecco's modified Eagle's medium (DMEM) + GlutaMAX^{TM} (Gibco$^®$), 1 mM sodium pyruvate, 350 μM L-proline, 1.5 mg/ml bovine serum albumin (BSA), 1 nM dexamethasone, 300 μM ascorbic acid, 17 μM linolenic acid, 10 ng/ml transforming growth factor β3 (TGF-β3, R&D Systems$^®$), 1X insulin-transferrin-selenium. Experimental groups were designed as followed: CM (positive control), CM - TGFβ3 (negative control), CM + 20 ng/ml GREM1, CM + 200 ng/ml GREM1, CM + 20 ng/ml βIGH3, CM + 200 ng/ml βIGH3.

3.2.9. Analysis of GP-specific proteins in monolayer culture

The BMSCs were used at passage 2 for the experiment and were seeded onto 24 well plates at a density of 10^3 cells/cm^2. Cells were allowed to proliferate for 24 hours in expansion medium. Then, wells were divided into experimental groups as per table below and cultured for 21 days in the following media: Osteogenic media as positive control (+OM): DMEM + GlutaMAX^{TM}, 10% foetal bovine serum (Gibco$^®$), 10 mM β-glycerophosphate, 1 nM dexamethasone, 0.09 mM ascorbic acid. Negative control (-OM): osteogenic medium without β-Glycerophosphate. -OM or +OM were supplemented with 10, 50, 100 ng/ml of CLEC11A or S100A10. All media were supplemented with 100 units/ml Penicillin, 100 units/ml Streptomycin (Gibco$^®$) and 0.25μg/ml amphotericin B. After 21 day of culture, monolayers were stained for calcium analysis. Briefly, wells were washed twice with PBS, samples were fixed with 500 µl of iced 100% ethanol for 2 min and washed again with distilled water. Then, 500 µl of alizarin red stain solution were added to each well and allowed to react for 2 min. Finally, excess of solution was washed with distilled water. Samples were fixed with ethanol and pictures were taken with a brightfield microscope.

Table 3-1. Experimental set up for the monolayer assay in order to study the effect of growth plate-specific factors in osteogenesis of MSCs.

1	2	3	4	5	6	7	8

A	Control	Control	10	10	10	10	10	10	
B	Control	Control	50	50	50	50	50	50	**-OM**
C	Control	Control	100	100	100	100	100	100	
D	Control	Control	10	10	10	10	10	10	
E	Control	Control	50	50	50	50	50	50	**+OM**
F	Control	Control	100	100	100	100	100	100	
			CLEC11A (ng/ml)			**S100A10 (ng/ml)**			

3.2.10.   *Statistical analysis of pellet and monolayer biochemical data*

Results are presented as mean ± standard deviation. Graphical results and statistical analysis were performed with GraphPad Prism 5.01 software. Experimental groups were analysed for significant differences using a general linear model for analysis of variance (ANOVA) with factors including different ECM materials and culture conditions. Tukey's multiple comparison test was used to compare different conditions (media *vs.* material). Significance was accepted at a level of $p < 0.05$. GraphPad was also used to calculate outlier datapoints. A significance level of 0.01 was used to determine the removal of a data point.

3.3. Results

3.3.1. *Guanidine hydrochloride treatment results in higher protein extraction from articular cartilage ECM than urea treatment*

Two common denaturant extraction buffers, 8M urea or 6M guanidine hydrochloride, were used to extract soluble proteins from AC ECM. Measurement of extracted supernatant solution with nanodrop served to compare the two treatments and demonstrated that guanidine hydrochloride was 5 times more efficient extracting soluble proteins than urea (Figure 3-2).
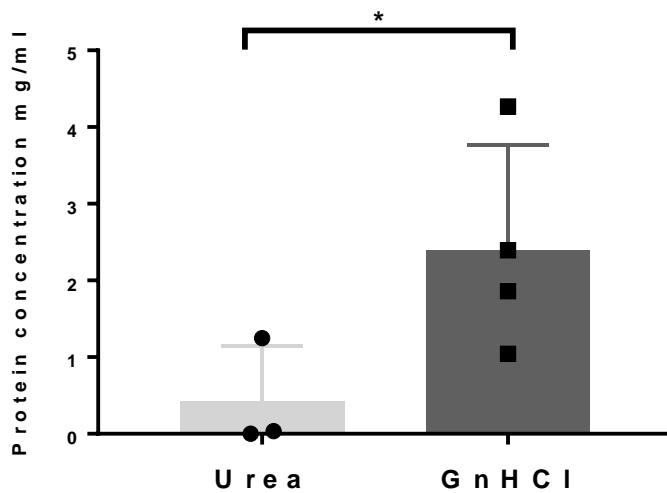
*Figure 3-2. Comparison of urea and guanidine hydrochloride (GnHCl) extracted protein concentration from articular cartilage ECM. *P = 0.04, n ≥ 3.*

3.3.2. Guanidine hydrochloride treatment results in higher protein extraction from growth plate ECM than articular cartilage ECM

Guanidine hydrochloride treatment resulted in extracted supernatant with higher protein concentration in growth plate than in articular cartilage ECM by nanodrop quantification. BCA assay was used to validate nanodrop results.
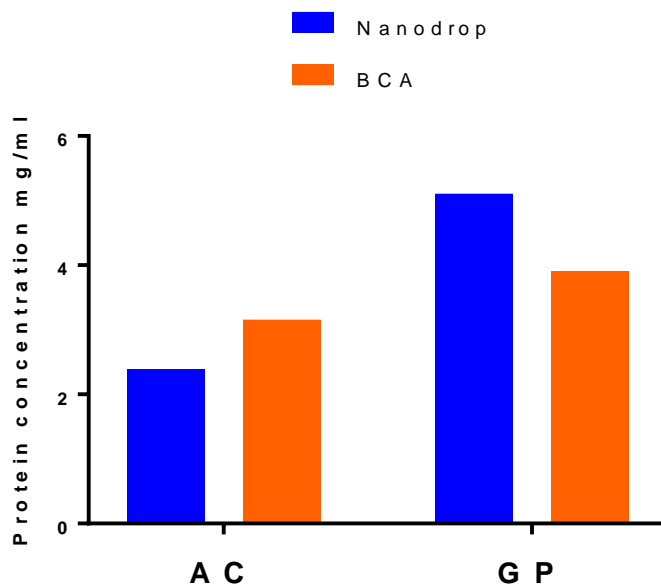
Figure 3-3. Comparison of protein concentration in articular cartilage (AC) and growth plate (GP) ECM extracted supernatant by nanodrop and BCA assay.

3.3.3. MS/MS analysis identifies different proteins within articular cartilage and growth plate ECM

Extracted supernatants from AC and GP ECMs were analysed by MS/MS to identify protein differences between the two tissues. Maxquant software was used to process the raw data. Perseus matrices and plots were used to analyse Maxquant data. Only proteins present in at least two out of three of the replicas were considered for further analysis. Full protein list can be found in CHAPTER: Supplementary data: 9.1.

GP and AC ECM were found to contain a range of shared and distinct proteins (Figure 3-4). Principal component analysis (PCA) and multiscatter-plot confirmed that there was no major differences among the biological replicas within each sample group (Figure 3-4a,b). However, PCA showed there was greater variation within AC biological replicas than within GP biological replicas. A scatter or volcano plot analysis (Figure 3-4c), showing the correlation between protein and intensity in each sample, demonstrated that there were more proteins belonging to the GP (proteins farther to the left) than to the AC (proteins farther to the right).

Significant differences in protein quantification between the AC and GP samples were plotted in a heat map (Figure 3-4d). Similar to the volcano plot, the heat map analysis demonstrated the presence of more proteins in GP compared to AC. Similar to PCA, heat map showed more consistency of protein levels in GP sample than in AC, especially with proteins of low intensity levels in AC.

A Venn diagram was used to illustrate the table list with the amount of proteins in each tissue (Figure 3-4e,f). Of the 297 proteins identified within AC, 89% of these were also detected within GP, however, of the 603 proteins detected in the GP tissue, the majority (56%) were not found in AC.
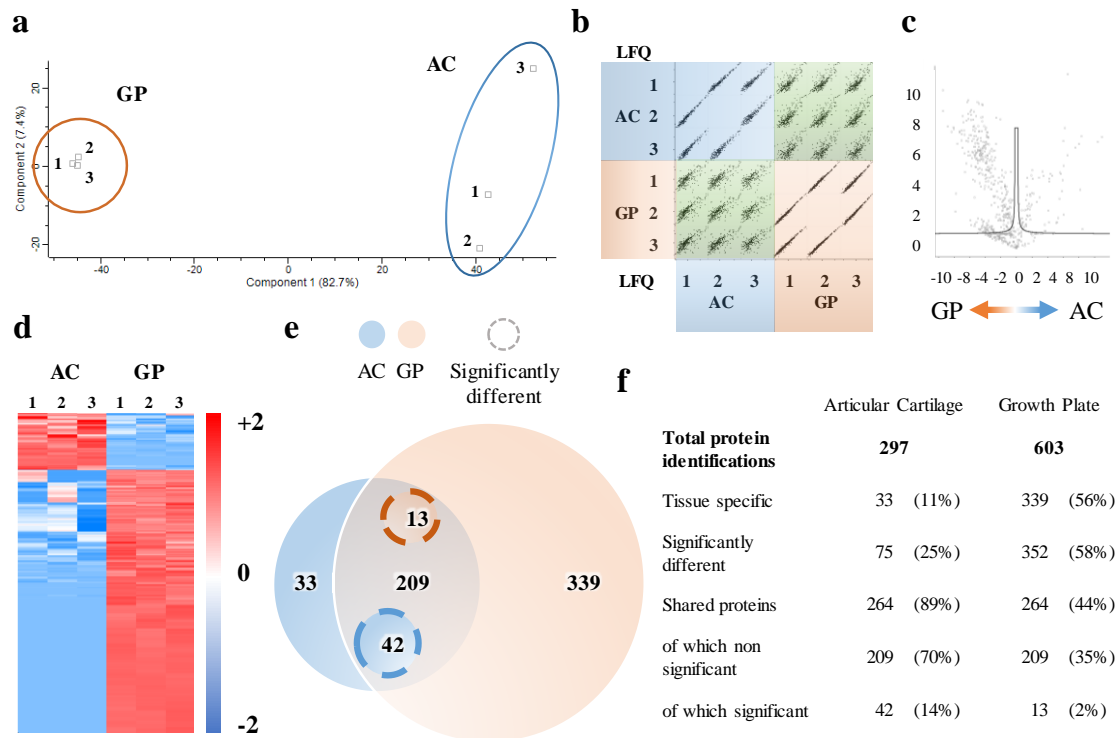
Figure 3-4. *Perseus analysis of Maxquant processed data from mass spectroscopy of extracted Articular Cartilage (AC) and Growth Plate (GP) ECMs (n=3). **a**, Principal component analysis (PCA) plotting emphasized variation and strong patterns in the analysed data. Orange circles clustering the 3 biological replicas of GP and Blue circle clustering AC samples. **b**, Multi scatter plot comparing the LFQ intensity from the 2 tissues. **c**, Volcano graph plotting significance (Y axis) versus fold-change in label free quantification (LFQ) intensities of the samples (X axes) featuring GP or AC-like proteins towards left or right, respectively (FDR = 0.01; s0 = 0.1). **d**, Heat map of the z-score statistical measure of the significantly different proteins based on LFQ intensities within the 2 ECMs groups (FDR = 0.01). **e**, Venn diagram showing the tissue-specific proteins (blue for AC and orange for GP), the shared proteins (grey) and significantly different shared proteins (surrounded by dashed circles). **f**, Table showing the count of identified proteins in both ECMs visualised in **e**.*

3.3.4. Characterization of the ECM matrisome of growth plate and articular cartilage

Further bioinformatics analysis and filtering, through Matrisome database[293], was used to refine the protein list obtained from the Perseus analysis. All identified protein gene names from each sample group were searched against the Matrisome database (Figure 3-5) to cluster proteins into two different ECM related categories (core matrisome and matrisome-associated) and six subgroups (collagens, ECM glycoproteins, proteoglycans, ECM-affiliated, ECM regulators and secreted factors).

The analysis revealed that the two tissues contained a similar number of core matrisome proteins, including: collagens, ECM glycoproteins and proteoglycans. The GP tissue, however, contained more abundant matrisome-associated proteins such as ECM-affiliated, ECM regulators, and secreted factors. The most notable difference in protein number count was found in the matrisome-associated proteins (Table 3-2 and Figure 3-5).

Table 3-2. Matrisome analysis of the proteins identified in Maxquant. Count of Articular Cartilage (top) and Growth Plate (bottom) ECM identified proteins clustered in two groups: (1) core matrisome, including three subgroups (i) collagens, (ii) ECM glycoproteins and (iii) proteoglycans; and (2) matrisome-associated, including three subgroups (i) secreted factors, (ii) ECM regulators and (iii) ECM-affiliated proteins. Percentage of total proteins in each ECM is shown beside the number of proteins.

Matrisome categories	Matrisome subcategories	Articular Cartilage		Growth Plate	
		Number of proteins	% of total matrisome	Number of proteins	% of total matrisome
Core Matrisome	Collagens	17	17.71 %	18	14.88
	ECM Glycoproteins	36	37.50 %	33	27.27
	Proteoglycans	13	13.54 %	13	10.74
Matrisome-associated	ECM-affiliated	13	13.54 %	15	12.40
	ECM regulators	13	13.54 %	34	28.10
	Secreted factors	4	4.17 %	8	6.61
Total Matrisome		96	100 %	121	100 %

Articular Cartilage Matrisome

Secreted Factors

Frzb
Ccl16

ECM Regulators

Loxl3
Serpinb9
Htra1

ECM-affiliated

C1qc
C1qb
C1qa
Clec3a
Grem1

Collagens

Col XIV   Col XI a2
Col VI   Col XVI
Col IX a1

ECM Glycoproteins

Smoc2
Fbn1
Cilp2
Srpx2
Tnc
Matn1,3,4
Fbln7
Thbs1
Mfap2
Vit
Comp
Tgfbi
Thbs4
Cthrc1
Cpxm2
Pcolce

Proteoglycans

Epyc	Chad	Hapln1,3
Fmod	Acan	Ogn
Chadl	Vcan	Bgn
Dcn	Hspg2	

Matrisome Associated — Core Matrisome

17 18%
4 4%
13 14%
13 14%
13 13%
36 37%

Growth Plate Matrisome

Secreted Factors

Angptl2,5
S100a8,9,10,12
Il17b

ECM Regulators

A2m	Ctsd
Hrg	Htra3
Serpin	Elane
c1,h1	Pamr1
F13a1	F2
Plod3	P4ha1
F10	Plod1
Itih1,2,4	Cd109
Ctsk	P3h1
Mmp9,13	
Loxl4	
Ctsg	

ECM-affiliated

Clec11a
C1qtnf3
Lman1
Anxa1,2,5,8
Cspg4

Collagens

Col III
Col X
Col I
Col IX a2
Col XI a1

ECM Glycoproteins

Vtn
Efemp2
Hist1h4a
Ibsp
Lama4
Fibb
Fn1
Lamb2
Sparc
Fgb
Edil3
Fgg
Thbs3

Proteoglycans

Prg3

Matrisome Associated — Core Matrisome

8 7%
18 15%
34 28%
33 27%
15 12%
13 11%

Figure 3-5. *Matrisome analysis of the proteins identified in Maxquant. Pie charts of Articular Cartilage (top) and Growth Plate (bottom) ECM identified proteins clustered in two groups: (1) core matrisome, including three subgroups (i) collagens, (ii) ECM glycoproteins and (iii) proteoglycans; and (2) matrisome-associated, including three subgroups (i) secreted factors, (ii) ECM regulators and (iii) ECM-affiliated proteins. List of protein beside each subcategory correspond to significantly expressed proteins in each ECM.*

3.3.5. STRING database reveals different enriched biological pathways between articular cartilage and growth plate matrisomes

Significantly different proteins between the two samples were searched against the Matrisome database in order to obtain the matrisome related proteins. This newly generated gene list (see listed proteins in Figure 3-5) was searched against the STRING database to investigate protein-protein interaction and enriched regulatory pathways of interest. The combination of Matrisome and STRING databases was used to filter the protein list and to find (i) functional annotations and (ii) individual proteins that could play a key role in cartilage and tissue development.

(i) STRING database revealed that proteins present in both articular cartilage and growth plate extracellular matrix were associated with certain biological process, such as tissue development, cartilage development, bone development, endochondral bone morphogenesis, ossification and angiogenesis.

(ii) Of interest was the finding that the GP contained proteins that are believed to play a role in angiogenesis, such as CSPG4[295,296] and ANGPTL2[297,298]; and osteogenesis, including CLEC11A[274], MMP13[299,300] and S100A10[277,289]. In contrast, AC contained factors known to inhibit hypertrophy and to promote chondrogenesis, such as GREM1, FRZB[153] and TGFβi[265,270]. The differential presence of some of these proteins detected using mass spectrometry was also verified using western blots (this analysis was performed by Olwyn Mahon) (Figure 3-8).
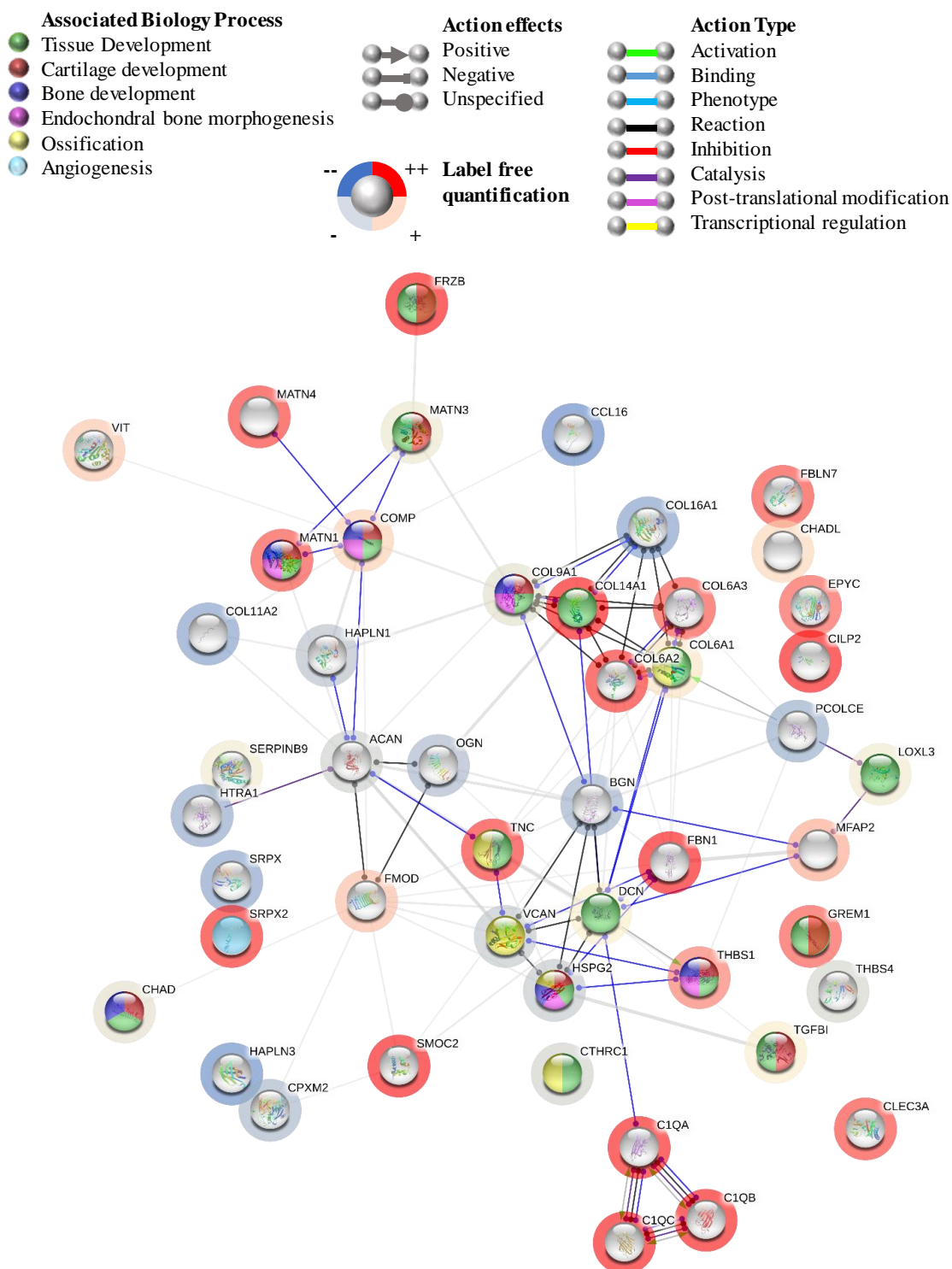
Figure 3-6. *STRING network view of the proteins found in the AC Matrisome (significantly different from the GP Matrisome). Each node represents a protein. The legend shows (i) node colour, indicating the associated biological process; (ii) coloured lines between proteins, indicating the protein-protein interaction: action type and effect; and (iii) color-coded label free intensity, indicating protein abundance ("payload"- dataset added from Maxquant results). P ≤ 0.04.*

StringDB connecting GP Matrisome
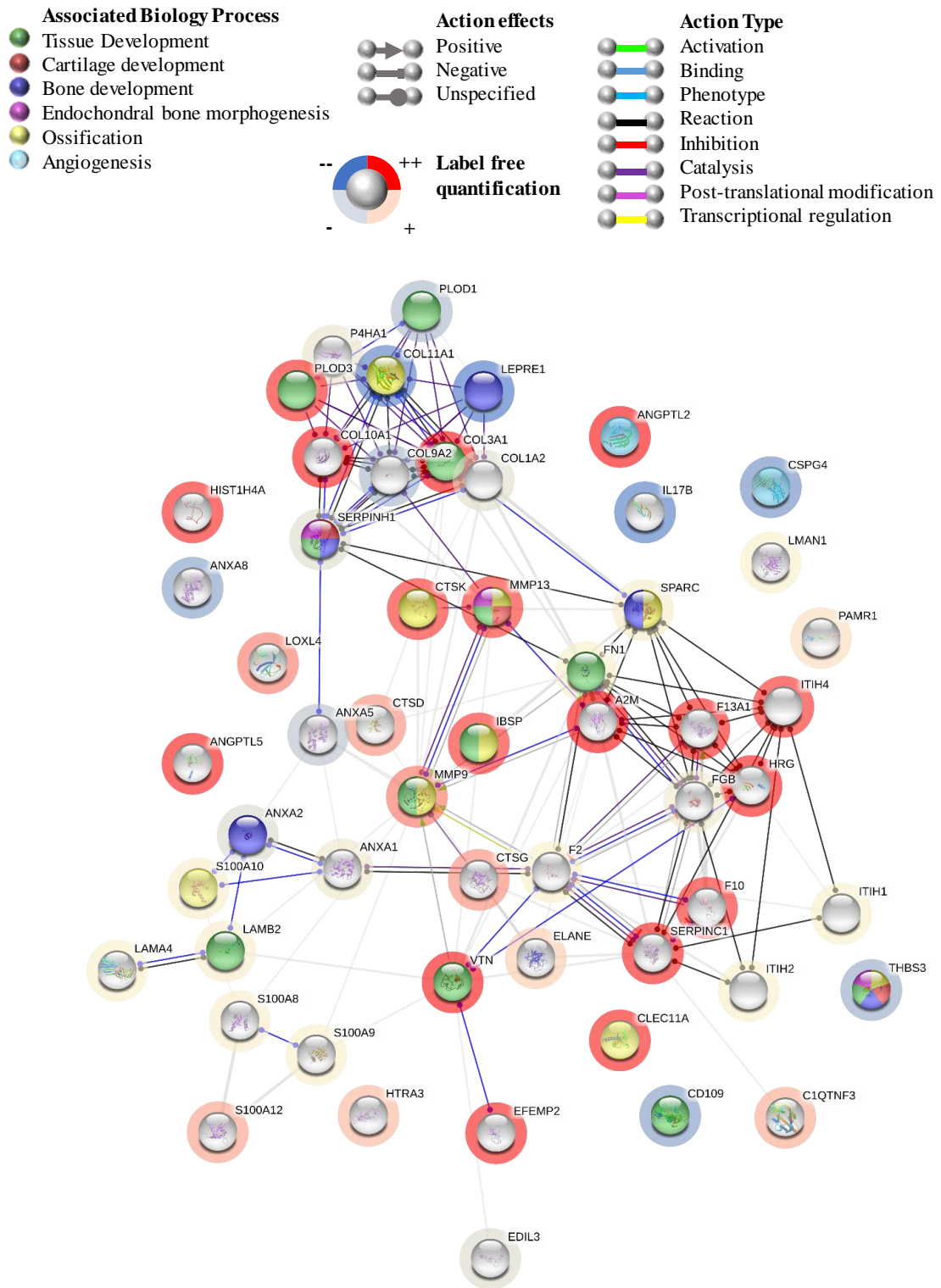
Figure 3-7. *STRING network view of the proteins found in the GP Matrisome (significantly different from the AC Matrisome). Each node represents a protein. The legend shows (i) node colour, indicating the associated biological process; (ii) coloured lines between proteins, indicating the protein-protein interaction: action type and effect; and (iii) color-coded label free intensity, indicating protein abundance ("payload"- dataset added from Maxquant results). P ≤ 0.04.*
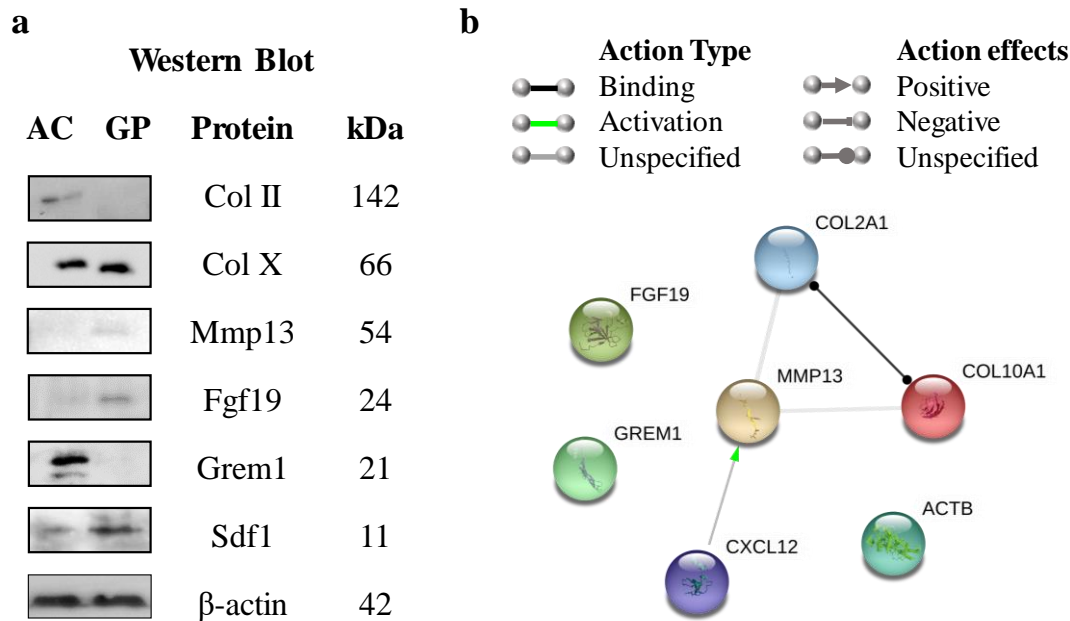
*Figure 3-8. Comparison of Articular Cartilage (AC) and Growth Plate (GP) ECM proteome. **a**, Western blot (WB) analysis of key proteins differentially detected in either tissue type. **b**, STRING network view of the proteins analysed in the WB. Node colour comes from STRING database predetermined colours and not related to colour legend from previous figures. WB data obtained by Olwyn Mahon.*

3.3.6. Matrisome subcategories and STRING can be used as filters to target proteins of interest

In the first results chapter, all identified proteins from both AC and GP were searched against the Matrisome database. In this case, the matrisome analysis was focused only on the significantly different proteins between AC and GP. In this analysis, the number of proteins was reduced from 242 to 51 for AC (blue circle in figure **Figure 3-9**a) and from 548 to 60 for GP (red circle). The matrisome proteins were subdivided into the same subcategories mentioned in the previous chapter: collagen, ECM glycoproteins, proteoglycans (core matrisome), ECM-affiliated, ECM regulators and secreted factors (matrisome-associated). In this case, heat map associated to the label free quantification (LFQ) was incorporated (**Figure 3-9**b). The analysis revealed further differences between the two tissues. The AC tissue contained more collagens, proteoglycans and ECM glycoproteins than the GP. In contrast, the GP tissue contained more ECM regulators, ECM-affiliated and secreted factors than the AC tissue. The combination of these proteins found in the matrisome of both AC and GP tissues was

searched in the STRING database. Only 91 proteins of 111 (51+60) were found in STRING. The generated protein network (**Figure 3-9**c) helped (i) to spatially arrange the proteins from each tissue (blue for AC and red for GP) so as to predict interactions between them. Associations are meant to be specific and meaningful, *i.e.,* proteins jointly contribute to a shared function; this does not necessarily mean they are physically binding each other. (ii) The string database also offers brief information of the input proteins (supplementary data) that was manually reviewed looking for key words such as: collagen, chondrogenesis, bone, mineralisation. These two features were critical to target the four proteins of interest that have been described in the introduction and highlighted in (**Figure 3-9**): GREM1, βIGH3, CLEC11A, S100A10.

For instance, part of the information found in STRING regarding GREM1 was: "inhibits BMP2-mediated differentiation of osteoblasts". This makes it an ideal candidate to reduce hypertrophy. Information on βIGH3 was: "Plays a role in cell adhesion and cell-collagen interactions". In addition, the network linked it to heparan sulfate (HSPG2), which is essential in cartilage development[301,302]. Information on CLEC11A: "promotes osteogenesis", making it an ideal candidate for potential endochondral ossification. Information on S100A10: "regulator of ANXA2" and the network also linked it to ANXA5, which have been shown to regulate matrix vesicle-mediated mineralization[288,289,303].
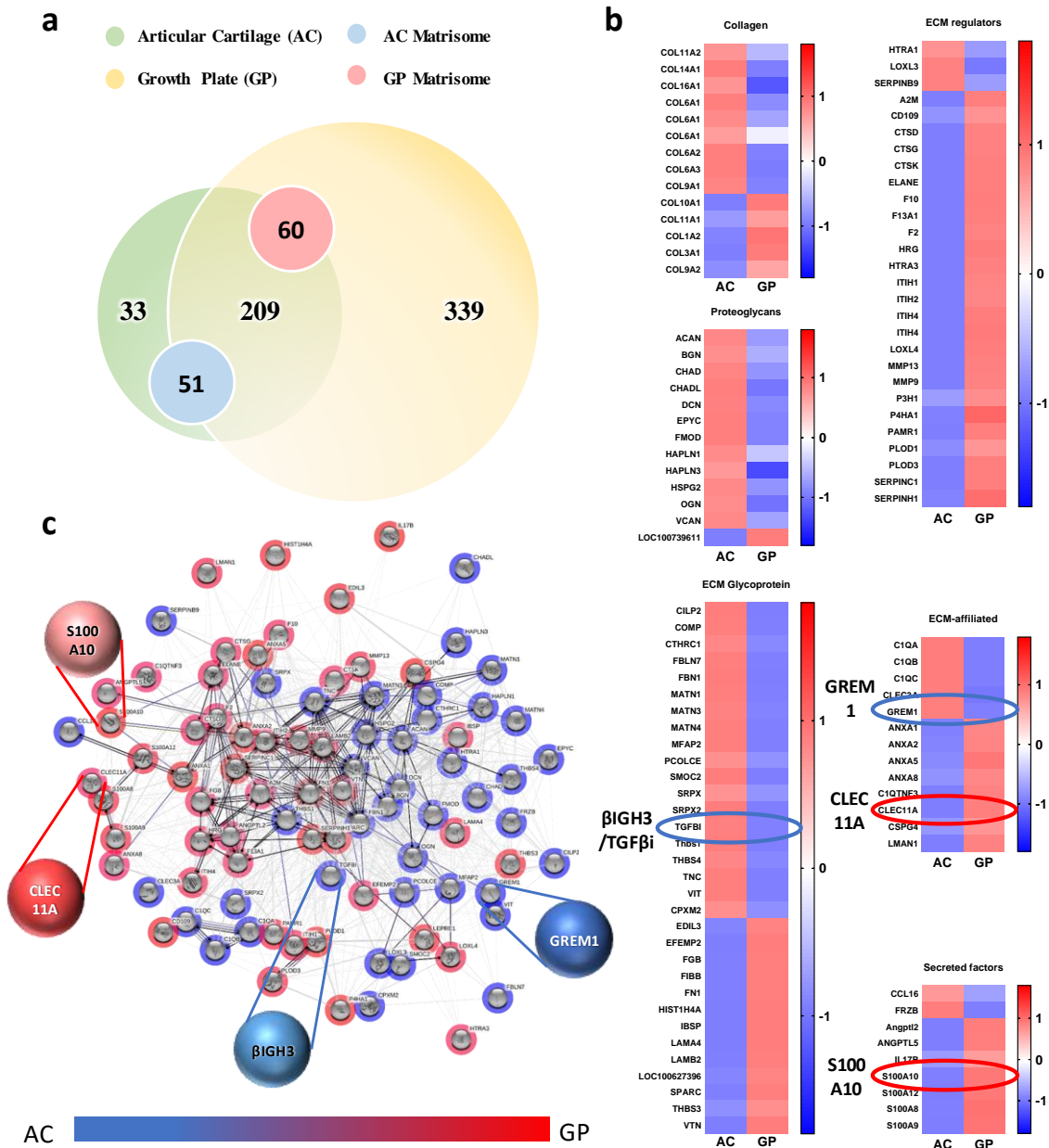
Figure 3-9. *Refinement of Matrisome analysis from first result's chapter. **a**, Venn diagram showing the tissue-unique proteins (dark green for AC and yellow for GP), the shared proteins (light green) and significantly different proteins found in the matrisome of each tissue (blue for AC matrisome and red for GP matrisome). **b**, String network of all the significantly different proteins found in the matrisome, including a payload to differentiate each tissue (blue for AC and red for GP). Four proteins of interest have been highlighted with large spheres. **c**, Heat map of the z-score statistical measure of the significantly different proteins found in the matrisome and divided in 6 subcategories: collagen, proteoglycans, ECM glycoproteins, ECM-regulators, ECM-affiliated and secreted factors. The four proteins of interest have been highlighted with a circle. Significantly different proteins are based on LFQ intensities within the two tissues (FDR = 0.01).*

Table 3-3. *MSMS information summary of the proteins of interest, selected from Matrisome and String database analysis.*

LFQ intensity AC_1	LFQ intensity AC_2	LFQ intensity AC_3	LFQ intensity GP_1	LFQ intensity GP_2	LFQ intensity GP_3	Score	Gene name	Division Matrisome	Category Matrisome
29.52707	28.75344	28.47104	NaN	NaN	NaN	151.35	GREM1	Matrisome-associated	ECM-affiliated Proteins
34.2187	34.00605	32.4233	27.76421	28.29754	28.00421	289.22	TGFBI/ βIGH3	Core matrisome	ECM Glycoproteins
NaN	NaN	NaN	29.93649	30.0177	30.14601	112	CLEC11A	Matrisome-associated	ECM-affiliated Proteins
NaN	NaN	NaN	29.14664	28.26222	28.29255	38.991	S100A10	Matrisome-associated	Secreted Factors

3.3.7. AC-specific proteins can modulate chondrogenesis and hypertrophy of MSCs

Having identified two AC-specific proteins of interest, it was next sought to study their effect on chondrogenesis of MSCs. MSC derived pellets were fabricated by centrifuging 250,000 cells per Eppendorf tube. Pellets were cultured for 21 days in chondrogenic media (CM) or CM plus the AC-specific factors GREM1 or βIGH3 at two different concentrations (20 or 200 ng/ml). All pellets stained positive for alcian blue and picrosirius red, indicative of cartilage matrix synthesis (**Figure 3-10**a). The most robust staining for sGAG deposition was observed in pellets supplemented with βIGH3 at both concentrations. The most robust staining for collagen was the group supplemented with standard CM. To confirm the development of hyaline cartilage, the deposition of collagen type II and type X within the pellets was next analysed by immunohistochemistry. Robust type II collagen deposition was observed in all groups. Pellets supplemented in standard CM alone also showed strong staining for type X collagen deposition, with lower levels observed in the two βIGH3 groups. Pellets stimulated with GREM1 stained weakly for collagen type X.

Quantitative biochemical analysis was also undertaken to supplement the histological results, which revealed similar trends in terms of tissue deposition (**Figure 3-10**b). DNA, sGAG and hydroxyproline (HxP) levels at day 21 were similar across all the groups (ns).

After the effect on chondrogenesis was evaluated, the effect of AC-specific proteins on osteogenesis of MSCs was studied. MSCs were grown in monolayer culture and supplemented with osteogenic media (OM; 5mM β-glycerophosphate) with or without the highest concentration (200 ng/ml) of either GREM1 or βIGH3. After 14 days of culture, alizarin red staining revealed that βIGH3 stimulation had no noticeable effect on mineralization, while it was dramatically supressed by GREM1 stimulation (**Figure**

3-10c). Image analysis provided semi-quantification of these observations, demonstrating significant differences between standard OM and OM+βIGH3 cultures compared to the negative control (OM without β-glycerophosphate) and OM+GREM1.
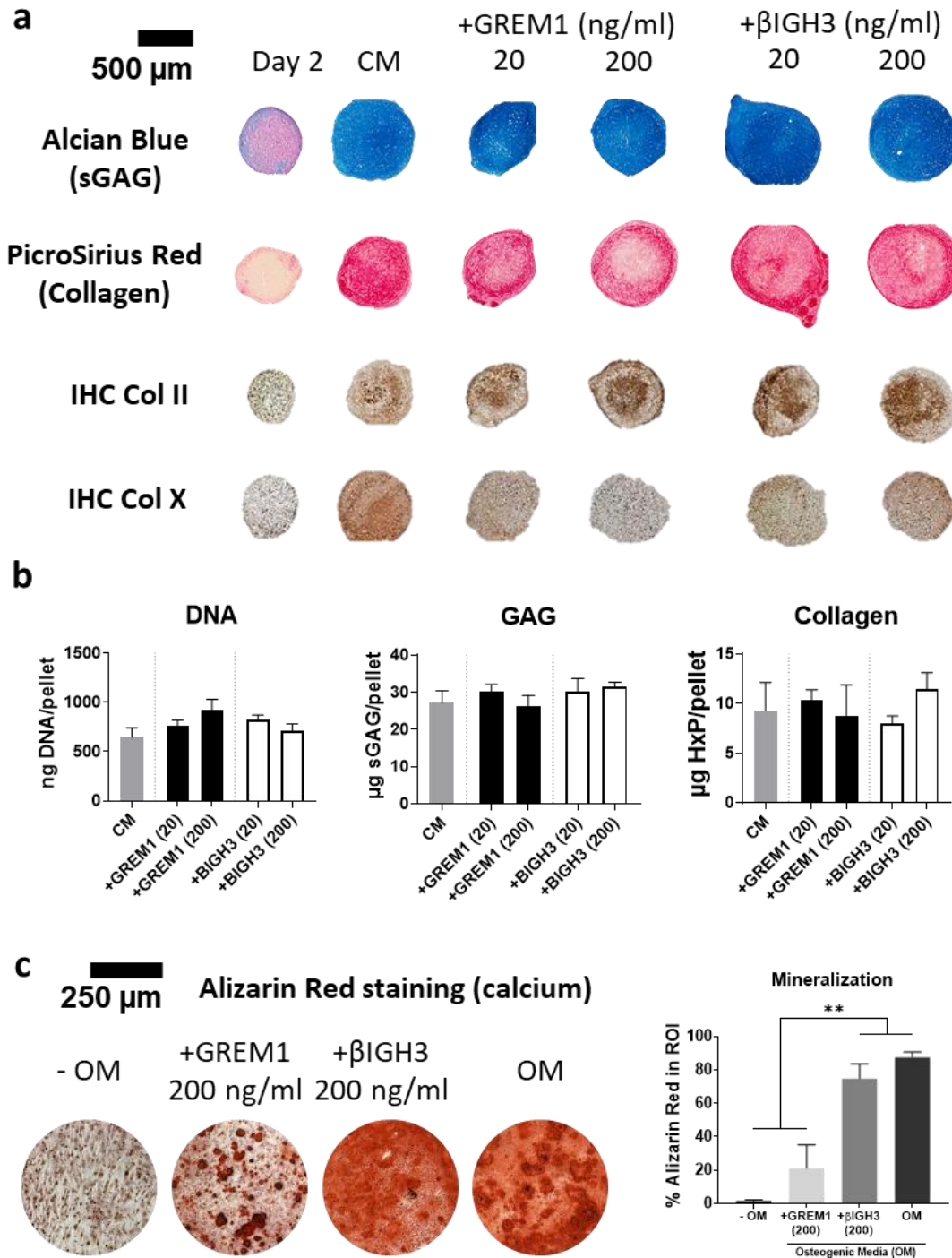
Figure 3-10. Effect of AC-specific proteins in scaffold-free MSC chondrogenesis and osteogenesis. a, Histological analysis of the pellet study cultured for 21 days in chondrogenic media showing alcian blue for gag staining, picrosirius red for collagen staining and immunohistochemistry (IHC) for the chondrogenic marker collagen type II and for the hypertrophic marker collagen type X. Experimental groups are: day 2 control,

*standard chondrogenic media (CM), chondrogenic media supplemented with either 20 or 200 ng/ml of either GREM1 or βIGH3 (n ≥ 2). **b**, Biochemical analysis showing DNA, sGAG and HxP levels per pellet for all groups after 21 days of culture (n ≥ 4). **c**, Left: alizarin red staining representative images of monolayer model. Experimental groups: osteogenic media without β-glycerophosphate and standard osteogenic media supplemented with or without 200 ng/ml of either GREM1 or βIGH3 for 14 days. Right: semi-quantification analysis of the amount of red staining in the region of interest (ROI) of all groups in percentage. (**p ≤ 0.01; n ≥ 2).*

3.3.8. GP-Specific proteins enhance osteogenesis of MSCs in vitro

MSCs were cultured at a density of 10^3 cells/cm^2 in negative control medium (osteogenic medium without β-Glycerophosphate, BGP) for 2 weeks (**Figure 3-11a**) or standard osteogenic medium (OM) for 2 (**Figure 3-11b**) and 3 weeks (**Figure 3-11c**). Samples were supplemented with either 10, 50, 100 ng/ml of CLEC11A or S100A10. Alizarin red staining was performed on the samples after 2 and 3 weeks to analyse calcium deposition.

Samples in negative control medium did not show any mineral deposition after 2 weeks in culture. Semi-quantification of stained samples after 2 weeks demonstrated a dose-dependent mineral deposition for all experimental groups. The highest values were observed with the CLEC11A protein (**Figure 3-11b1**). After 3 weeks, alizarin red quantification revealed that all groups reached a maximum mineral deposition (**Figure 3-11c1**), characterised by intense red staining throughout the sample.
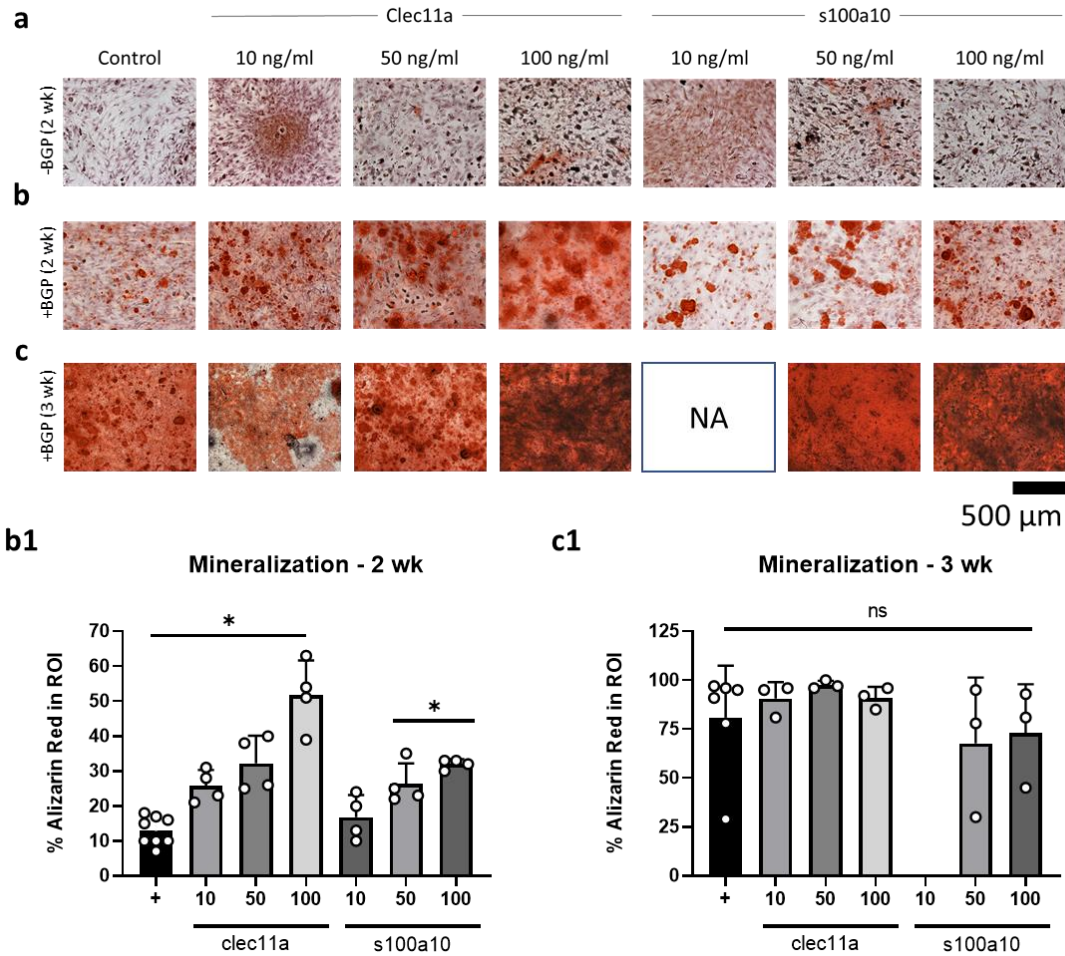
Figure 3-11. *Effect of GP-specific proteins in MSC osteogenesis cultured in monolayer model. **a**, Alizarin red staining of well containing cells after 14 days in negative control medium (osteogenic medium without BGP) supplemented with either CLEC11A or S100A10 at three different concentrations: 10, 50 and 100 ng/ml. **b**, Alizarin red staining of the same groups with positive control medium (standard osteogenic medium) after 14 days of culture. **b1**, Semi-quantification of red staining in **b**. **c**, Alizarin red staining of the same groups in standard OM for 3 weeks. Representative images of monolayer model. **c1**, Semi-quantification of red staining in **c** (*p < 0.05; n ≥ 2).*

3.4. Discussion and conclusion

The complexity and diversity of biomolecules present in tissue or tissue-derived ECMs are not yet fully characterized. In order to shed some light on this complex topic, this study focused on the proteomic characterization of the soluble extracellular matrix of two different musculoskeletal tissues, articular cartilage and growth plate, which we have previously demonstrated to promote differential tissue deposition by mesenchymal

stem cells, both *in vitro* and *in vivo*[29,34]. This can be directly correlated to the unique composition of AC and GP ECM, which were determined based on an in-depth analysis of the less abundant non-collagenous proteins in this tissue. Taken together, the results indicated that the proteomic characterization of soluble ECMs of interest can help us to understand material composition, specific interactions with cells and therapeutic action[33] in tissue engineering.

Guanidine hydrochloride was more efficient than urea for total extraction of soluble proteins from ECMs. This has also been observed for other musculoskeletal tissues such as bone[304]. Recovery of soluble proteins it is essential for proper characterization of pathways regulating each tissue.

The protein composition of GP ECM was more consistent than the composition of AC ECM among the different biological replicas. Our tissue source was randomly selected from a pooled cryomilled sample, which includes a non-homogenous distribution of proteins within the different layers of each tissue. However, different proteins have different stabilities and degradation[305] rates that could explain this sample to sample variability.

AC shared almost 90% of its proteins with GP (264 out of 297 for AC). Thus, only 10% of articular cartilage proteins were tissue-specific. This suggests that only a small number of proteins may be responsible for the suppression of hypertrophy and endochondral ossification within stable articular cartilage. Growth plate identified proteins accounted for roughly 70% of matrisome-associated category as opposed to 50% in AC. Despite this difference, it is noteworthy that the actual number of identified proteins in the core matrisome remained constant for both tissues. It is only the matrisome-associated protein number that changed, suggesting that tissue regulation by matrisome-associated proteins in the growth plate lies in a more complex system than articular cartilage. In these results, it was observed that the number of identified proteins in the core matrisome (collagens, proteoglycans and glycoproteins) remained the same between the two tissues. However, after comparing the label free quantification values, it is noteworthy that the AC had a higher expression than GP of the overall core proteins, which may be related to the need of those proteins to fulfil the structural function of AC. On the other hand, GP, which is a more dynamic tissue, had a higher expression of matrisome associated proteins (regulators, affiliated and secreted factors). In turn, this

suggests that, without neglecting core matrisome proteins, the main focus to find GP proteins of interest that will have an effect on bone tissue development, may lie on the matrisome-associated proteins.

The combination of Matrisome and STRING databases was used to identify functional annotations and individual protein-proteins interactions that could play a key role in cartilage and bone regeneration. Among the many different biological process associated, we focused on those ones with more relevance for osteochondral tissue engineering and demonstrated that both articular cartilage and growth plate extracellular matrices contain proteins associated with chondrogenesis, osteogenesis and angiogenesis.

The proteins detected in the GP ECM using mass spectrometry analysis are in agreement with previous studies, confirming that hypertrophic chondrocytes resident in the GP express a number of angiogenic factors, including CSPG4[295,306], ANGPT2[297,307] and MMPs[308,309], as well as osteogenic factors such as S100A10[289,310], osteolectin (CLEC11A)[274] as well as BMP[311] and FGF related proteins[152,155]. In contrast to the GP, AC ECM was rich in type II collagen, which is known to be chondro-inductive[312], and the presence of hypertrophic inhibitors and cartilage homeostasis regulators such as GREM1[153,246] and TGFβi/βIGH3[265,270]. Previous mass spectrometry studies of AC have also revealed the presence of these proteins at different depths in human articular cartilage and other cartilaginous tissues[39,313].

Despite the interesting findings, this study had two main limitations. First, ECM tissues were harvested from only one donor. Donor to donor variability is always present within biological samples. However, mass spectroscopy of extracted ECM has never been done comparing articular cartilage and growth plate tissue before, thus this study gives a clear idea of the level and number of proteins expected. The second limitation involved characterization of porcine proteins. Mass spectroscopy analysis is essentially based on the comparison of the peptides identified against a protein database. *Sus scrofa* protein database is not yet as characterized (<70,000 uniprot entries) as other species such as *homo sapiens* (> 1 million uniport entries) or *mus musculus* (~90,000 uniprot entries). A practical solution would be to search the identified peptides against a more complete protein database, however, there would be still the problem that unique peptides from distinct species than the database won't be recognised.

After reviewing the information gathered from STRING (see CHAPTER: Supplementary data-9.2 for more details), 4 proteins were chosen to analyse their effect on either chondrogenesis or osteogenesis of MSCs. These proteins are GREM1 (ECM-affiliated) and βIGH3 (ECM glycoprotein) from AC and CLEC11A (ECM-affiliated) and S100A10 (Secreted factor) from GP.

The supplementation to MSC cultures undergoing chondrogenesis with AC-specific proteins led to the development of a more hyaline-like cartilage, as evident by a reduction in the hypertrophic marker collagen type X. This is in agreement with previous studies showing similar results for GREM1 in pellet culture of MSCs[153]. In addition, GREM1 overexpression have also been shown to suppress BMP-derived bone formation[252,314,315]. This was the first time that the AC-protein, βIGH3, was shown to reduce hypertrophy of engineered cartilage without altering chondrogenesis, resulting in high levels of gag and collagen type II. Previous studies have highlighted that the overexpression of βIGH3 negatively function on mineralization of hypertrophic chondrocytes[270]. In this study, GREM1, but not βIGH3, was able to reduce β-glycerophosphate derived mineralisation in a monolayer model. This demonstrates that AC contains multiple proteins that play a role in supressing endochondral ossification of the tissue through different pathways and has a more complex functional composition than traditionally considered. Due to the more potent influence of GREM1 on reducing hypertrophy and MSC-derived mineralisation in osteogenic medium, it was decided to further characterise the potential use of this protein in AC tissue engineering in the next chapter.

The supplementation of GP-specific proteins in the monolayer model led to the improvement of mineralisation by enhancement of osteogenesis in MSCs. However, in this study, without the presence of β-glycerophosphate (BGP), neither CLEC11A nor S100A10 were observed to promote osteogenesis. These results suggest that, at this dosage, the proteins are not enough to promote osteogenesis, however, they can act in combination with osteogenic factors (BGP) to enhance the osteogenic phenotype. Alternatively, due their role in the maintenance of the adult skeleton[274] and vesicle derived matrix ossification (mature matrix)[288], their effect may be more evident in an endochondral bone model. Future studies should evaluate the effect of GP proteins in the enhancement of hypertrophy of MSCs in a scaffold model similar to the described previously in this chapter.

In conclusion, ECM proteomic characterization can help elucidate the complexity and the diversity or uniformity of proteins across different tissues and can be useful for identifying tissue-specific growth factors. Taken together, the results of this study demonstrated the ability to extract and characterize soluble ECM proteins from different musculoskeletal tissues and their clustering into developmental pathways of interest. This information was used to improve osteochondral tissue engineering strategies. It was demonstrated that AC-specific proteins and GP-specific proteins have enhancing effects on stable chondrogenesis and osteogenesis of MSCs *in vitro.*

4. CHAPTER: The effect of AC-specific protein, GREM1, on chondrogenesis of MSCs in a scaffold model *in vitro* and the engineered construct development *in vivo*

4.1. Introduction

Current clinical gold standards to repair damaged articular cartilage (AC) can result in a fibrotic or hypertrophic cartilaginous tissue with poor long-term outcomes[316]. This motivates the development of new tissue engineering strategies to regenerate phenotypically stable AC. Extracellular matrix (ECM) derived biomaterials have become well established tools in tissue engineering and regenerative medicine[11,20,317]. Such biological tissues naturally contain proteins that function as cell-adhesive ligands, release or sequester growth factors, participate in enzymatic degradation, or incorporate appropriate microstructure. These inherent properties can be leveraged to produce biomaterial scaffolds capable of supporting functional regeneration of damaged tissues.

Most commercial ECM scaffolds are derived from soft tissues such as dermis, urinary bladder or small intestinal submucosa (SIS), although they have been used in the repair of many different tissue types[11]. In spite of their widespread use, it is unlikely that a single tissue source (e.g. SIS) will be the optimal for the regeneration of all tissues or organ systems. The ECM contains the molecules secreted by resident cells of each tissue/organ[26,27]. Thus, it is reasonable to assume that the composition and structure of a specific tissue ECM is uniquely suited to maintaining the phenotype and biological function of its resident cells. In the recent years, there has been an increased evidence to encourage the use of tissue-specific ECM derived materials to support the defined differentiation of stem cells[144–151]. For example, it has been demonstrated that bilayered scaffolds derived from the ECM of articular cartilage and growth plate (GP; an ossifying cartilage) promote tissue-specific differentiation of MSCs *in vitro* and enhance the regeneration of osteochondral defects in a large animal model[32]. If the specific signalling proteins (present in different ECMs) that contribute to tissue specific differentiation could be identified, it would help inform the design of new tissue engineering strategies.

In the previous chapter, we identified AC-specific protein, GREM1, to have potential for engineering hyaline-like cartilage *in vitro*. Gremlin1 (GREM1), previously known as Drm, is a highly conserved cystine-knot-secreted glycoprotein of 184 aa (~20.7 kD) and a member of the differential screening-selected gene aberrant in neuroblastoma (DAN) family. The lack of GREM1 has been clearly linked to limb malformations during development, leading to digit loss, polydactyly and other skeletal disorders, hence earning the 90's movie name[245–247]. Recent research has shown that heparin-bound GREM1 can activate VEGFR2[248], implying that GREM1 could also be involved in the regulation of angiogenesis[249] in appropriate microenvironments. However, a more musculoskeletal-specific role has been associated to this protein since its discovery. GREM1 is a BMP antagonist that inhibits the BMP/Smad signalling pathway by binding to BMP ligands, particularly BMP2, BMP4 and BMP7[154,250–254]. In addition, GREM1 has been shown to inhibit Wnt/β-catenin signalling[255,256], probably due to inhibition of BMP2-mediated upregulation of Wnt1 and Wnt3 expression[257]. Recent studies have shown that GREM1 expression is upregulated in hypoxic conditions which promote higher levels of chondrogenesis[258]. Taken together, these inhibitions result in a decrease of osteoblast differentiation capacity, indirectly regulating bone formation and acting to stabilise hyaline cartilage homeostasis[259].

The aim of this chapter (illustrated in **Figure 4-1**) was to analyse the effect of human recombinant versions of tissue-specific proteins, selected from the significantly different proteins between the ECM of AC and GP, on chondrogenesis and osteogenesis of MSCs. The specific objectives were i) to fabricate ECM derived scaffold from solubilised articular cartilage ii) to analyse the effect of the AC-specific proteins GREM1 on chondrogenesis of MSCs in a 3D scaffold model; and iii) to evaluate the ability of cartilage engineered within these scaffolds in the presence of such factors to resist hypertrophy *in vivo*.
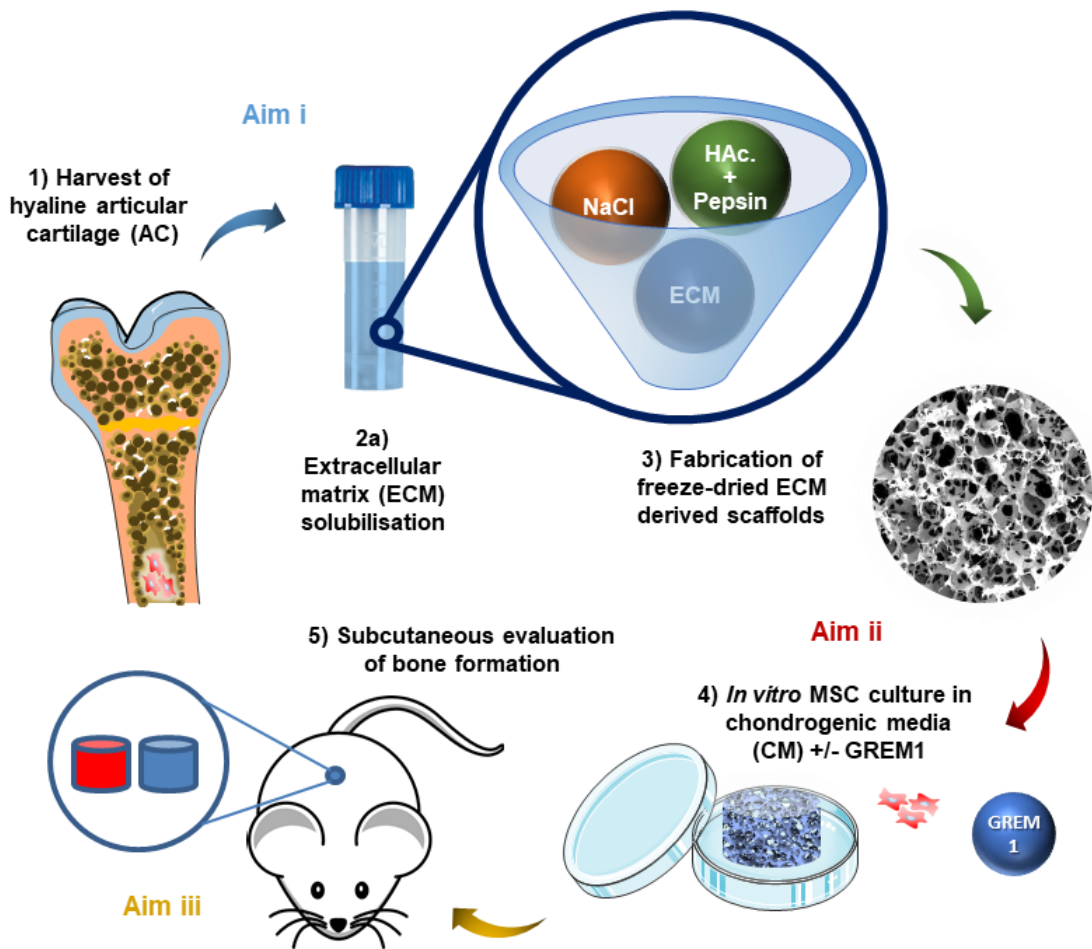
Figure 4-1. *Graphical abstract*

4.2. Methods

Note: all material obtained from Sigma-Aldrich® unless stated.

4.2.1. ECM solubilisation

Four musculoskeletal related tissues, articular cartilage (AC), bone (BN), growth plate (GP) and ligament (LG) were solubilised to obtain the collagenous fraction of the ECM of each tissue, used to later fabricate the ECM derived scaffolds. AC and GP were harvested as described in the previous chapter. Bone ECM was harvested from cow tibiae. LG was harvested from pig posterior cruciate ligament, medial collateral ligament and the lateral collateral ligament. In order to aid in the solubilisation, the BN ECM was first decellularized as previously described[318] (this was not needed for the other tissues). Briefly, BN fragments were blasted with water to remove all the bone marrow. Then, the bone fragments were placed in a series of four detergent washes: 0.1 %

ethylenediaminetetraacetic acid (EDTA) for 1 h, 0.1 % EDTA/10 mM Tris for 12 h, 0.5 % sodium dodecyl sulphate (SDS)/10 mM Tris for 24 h and 50 U/mL DNase, 1 U/mL RNase, 0.1 % EDTA/10 mM Tris for 5 h (all from Sigma-Aldrich). Following the washes, the bone was rinsed with phosphate-buffered saline (PBS) and lyophilised, obtaining demineralised bone matrix (DCB).

AC, DCB, GP and LG were cryomilled with a Spex 6870 Freezer Mill to form a powder. Then, the material was processed by following a standard protocol developed in the laboratory[319]. (i) The tissue was pre-treated with 1 ml per 50 mg original wet tissue of 0.2 M NaOH for 24 h at 4 ºC to solubilise most of the proteoglycan content. The material was centrifuged at 2500 g for 10 min and washed twice with UPW to eliminate the proteoglycans remaining in the supernatant. (ii) The collagen-rich pellet was digested with 1 ml per 50 mg wet tissue pepsin enzyme solution for 24 h at room temperature (RT). Pepsin enzyme solution was made by mixing 1500 units of pepsin in 1 ml of 0.5 M acetic acid. (iii) The digested material was separated by 2 cycles of fractional salt precipitation in order to extract the collagenous portion. This was done by incubating the crude extract in a volume of 5 M NaCl (final concentration of 0.9, 0.8, 2.5 and 0.8 M for AC, BN, GP and LG, respectively; see **Figure 4-2**) for 6 h at 4 ºC and solubilizing the precipitated material in 10 ml of 0.5 M acetic acid overnight at RT. Then, the material was centrifuged at 2500 g for 1 h at 4 ºC. (iv) Once solubilised, the material was dialysed in order to inactivate the pepsin enzyme and eliminate residual salt or proteoglycans. Briefly, the solubilised tissue was transferred into a permeable membrane and dialysed against 0.02 M Na2HPO4 (pH 9.4) for 24 h at 4 °C with change of buffer every 12 h. (v) Finally, the dialysed solubilised ECM was freeze-dried and stored at -20 until needed.

Calculations of 5M NaCl volume

$V_{NaCl-5M} * C_{NaCl-5M} = V_F * C_F;$ (V_F: final volume; $V_F = V_{SN} + V_{NaCl-5M}$)

$V_{NaCl-5M} * C_{NaCl-5M} = (V_{SN} + V_{NaCl-5M}) * C_F;$ (V_{SN}: supernatant volume)

$V_{5M-NaCl} = V_{SN} * C_F/(C_{NaCl-5M} - C_F)$ C_F: final concentration of NaCl.
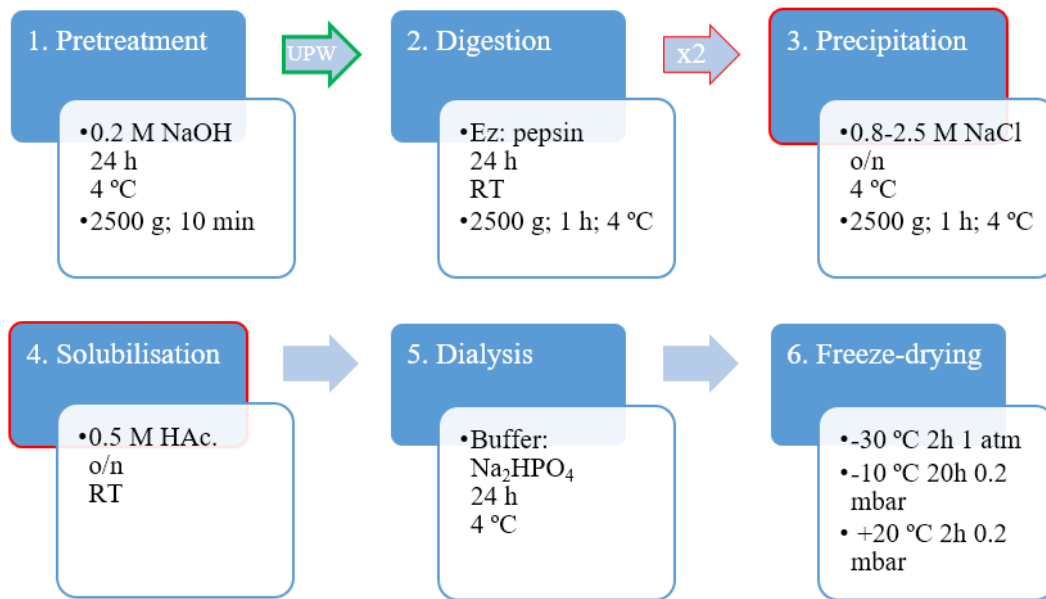
Type	Molecular formula	Relative molecular mass of α-chain	NaCl (M)	
			Precipitation at acidic pH	Precipitation at neutral pH
I	$[\alpha_1(I)]_2\alpha_2$	95	0.7–0.9	2.6
I trimer	$[\alpha_1(I)]_3$		0.7–0.9	4.0
II	$[\alpha_1(II)]_3$	95	0.7–0.9	3.5–4.0
III	$[\alpha_1(III)]_3$	100– 95	0.7–0.9	1.5–1.7
IV	$[\alpha_1(IV)]_3$ $[\alpha_1(IV)]_3[\alpha_2(IV)]_3$	180– 75	1.2	1.7–2.0
V	$[\alpha_1(V)]_2\alpha_2(V)$ $[\alpha_1(V)]_3$	200–130	1.2	3.6–4.5
VI	$\alpha_1(VI)\alpha_2(VI)\alpha_3(VI)$	240–140	2.0	
VII	$[\alpha_1(VII)]_3$	> 170		
VIII	$[\alpha_1(VIII)]_3$	61		
IX	$\alpha_1(IX)\alpha_2(IX)\alpha_3(IX)$	85	2.0	
X	Unknown	59	2.0	
XI	$[\alpha_1(XI)]_2\alpha_2(XI)$	95	1.2	
XII	Unknown			

Figure 4-2. Survey of molecular properties and precipitation conditions of different collagen types[320].

4.2.2. ECM scaffold fabrication

In order to fabricate solubilised articular cartilage (AC), bone (BN), growth plate (GP) or ligament (LG) ECM derived scaffolds, the freeze-dried solubilised collagenous material was mixed to a final concentration of 20 mg/ml (2%) in 0.02 M acetic acid with phenol red chemically modified medium (CDM). CDM was used as pH visual control so as to be able to neutralize the collagenous mixture with small volumes of 0.1 M NaOH. Then, the solution was partially crosslinked with 5 mM glyoxal.

Glyoxal is a linear aliphatic dialdehyde (OCHCHO) containing two aldehyde groups that reacts with NH_2-R groups from amino acids such as lysine (K) and arginine (R). Analysis of the main component in AC, collagen type II, has shown that it contains approximately 1.5% K and 5% R[321,322], which enable the glyoxal to crosslink collagen fibres[323–327] to form a gel[319,328,329]. The most probable reaction between glyoxal and collagen is the formation of Schiff's base type compounds[324].The reaction needs to be done in alkaline buffer (>pH 7) to be reactive. Above pH 10, crosslinking was almost immediate, however this did not change apparent mechanical properties after freeze-drying (data not shown). Therefore, working solution was kept at neutral pH 7 (< pH 10), so as to have time to transfer the solution to custom made moulds.

The AC ECM + glyoxal solution was transferred to custom-made moulds containing wells of 5 mm diameter (volume/well = 60 µl → final scaffold dimension ~ 5Φx3h mm), placed in the oven at 37 ℃ and allow to partially crosslink for 30 min. The moulds made of ertalyte enable for homogenous heat distribution in pre-crosslinking phase and freezing step of subsequent freeze-drying. The material was then freeze-dried following an optimised protocol to obtain random pores of an increased size (~100-200 µm) (described in next chapter). Briefly, the material was frozen to -30 at 1 ℃/min, then annealed at -10 ℃ for 3 hours, re-frozen at -30 ℃ and maintained at this temperature for 1 hour to ensure dropping product temperature below collapse temperature. Primary drying (lyophilisation) was done at -10 ℃ under vacuum (0.2 mbar) for 18 hours. Secondary drying was done at +25 ℃ for 2 hours. Finally, freeze-dried scaffolds were subjected to physical crosslinking with dehydrothermal treatment (DHT) at +115 ℃ for 24 hours. From this point, scaffolds were considered sterile.

4.2.3. Bone marrow derived MSCs isolation and expansion

Bone marrow-derived stem cells (BMSCs) were isolated from the femora of porcine donors (3-4 months, >50 kg) within 3 hours of sacrifice as previously described[294]. The femur was opened under sterile conditions and the marrow was transferred, using a spatula, into a 50 ml Falcon tube containing pre-warmed expansion medium. The marrow was triturated to break the clumps and homogenized, followed by centrifugation using lymphoprep (Axis-Shield, Scotland) in order to separate mononuclear cells, which reside at the interface, from the rest of marrow material. Mononuclear cells were isolated from the femora and plated at a seeding density of 5 x

10³ cells/cm² in high-glucose Dulbecco's modified eagles medium + GlutaMAX™ (4.5 mg/mL D-Glucose, 200 mM L-Glutamine; hgDMEM) supplemented with 10% foetal bovine serum (FBS). All Gibco®, Biosciences, Dublin, Ireland. Cells were expanded to passage 2 in a humidified atmosphere at 37 ºC and 5% CO_2.

Bone marrow stem cells (BMSCs) were harvested from 4-month-old porcine bone marrow following a standard protocol. Cells were seeded at a suitable density (2.5x10⁶cells per 58cm2 petri dish) based on previous experiments of my laboratory and monitored daily to assess colony formation. Finally, the mesenchymal progenitor cells were split and expanded for use or frozen in liquid nitrogen for long term storage.

4.2.4. In vitro 3D scaffold model

The BMSCs were used at passage 2 for the experiment and were seeded onto the scaffold at a density of 500,000 cells per scaffold. Before supplementing the media, the cells were allowed to attach to the scaffolds for 2 hrs in the incubator at 37 ºC. Stem cells need about 10 to 14 days to differentiate into chondrogenic and osteogenic lineages[233] and so the constructs were cultured for 28 days to allow for differentiated cell-derived tissue deposition. The constructs were cultured in normoxic (20% pO_2) or hypoxic conditions (5% pO_2) at 37 ºC, in 3 ml of CM, CM + 20 ng/ml GREM1 or CM + 200 ng/ml GREM1.

4.2.5. Subcutaneous in vivo mouse model

Following 4 weeks *in vitro* priming, MSC-seeded scaffolds were implanted subcutaneously into the back of nude mice (Balb/c; Harlan, UK). Briefly, two subcutaneous pockets were made along the central line of the spine, one at the shoulders and the other at the hips, and into each pocket 2 constructs of the same group were inserted. 8 constructs were implanted per each experimental group. Mice were sacrificed at 4- and 6-weeks post-implantation by CO_2 inhalation. The animal protocol was reviewed and approved by the ethics committee of Trinity College Dublin and Health Products Regulatory Authority (HPRA). See experimental set up in summary figure below (**Figure 4-3**).
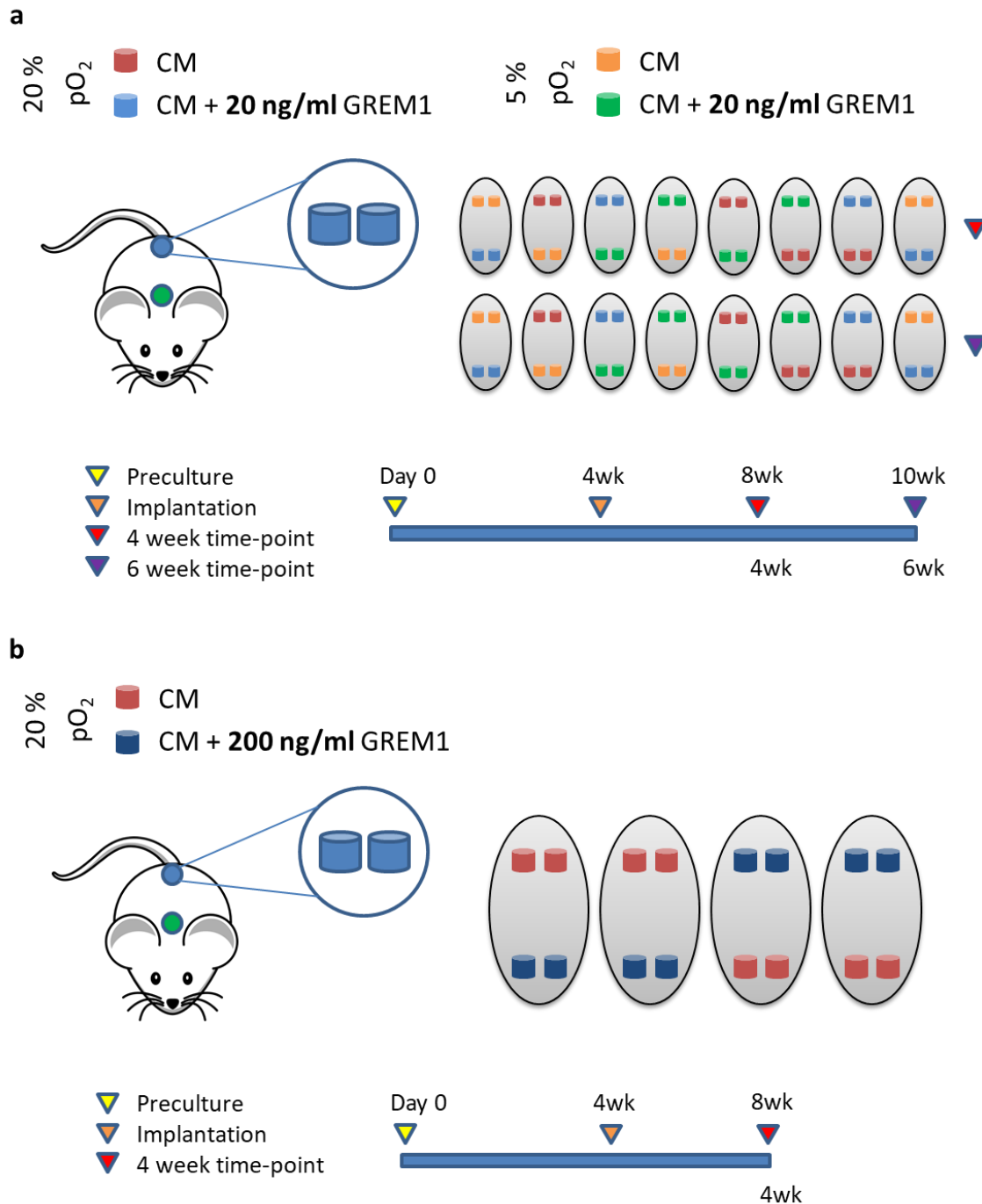
Figure 4-3. *Experimental set up for subcutaneous mouse model. **a**, Comparison of precultured BMSCs in AC scaffolds supplemented with either CM or CM + 20 ng/ml GREM1 in either normoxic (20 % pO₂) or hypoxic conditions (5 % pO₂) at 4- and 6-weeks post-implantation. **b**, Iteration of the same study with a higher concentration of GREM1 during preculture (CM + 200 ng/ml GREM1), only in normoxic conditions.*

4.2.6. Biochemical analysis

The pellets or engineered constructs were biochemically analysed at day 0 (after cell seeding) and day 28 for DNA, sulphated GAG (sGAG), collagen content and calcium deposition (3 scaffolds at each time point). On removal from culture, samples were freeze-dried, and dry masses of the samples were recorded for normalization. All samples were subsequently frozen at -85 ℃ for later analysis. The scaffolds were either enzymatically digested by incubating the constructs in 125 μg/ml papain, 0.1 M sodium acetate, 5 mM cysteine HCl, 0.05 M ethylendiaminetetraacetic, pH 6.0 at 60 ℃ under rotation (10 rpm) for 18 hr for DNA, sGAG and collagen analysis or chemically digested by incubating the constructs in 1M HCl at 60 ℃ under rotation (10 rpm) for 18 hr for calcium analysis. The DNA content was estimated by Bisbencimide Hoechst assay. The proteoglycan content was estimated by quantifying the sGAG in the scaffolds using the dimethylmethylene blue dye-binding assay (Blyscan, Biocolor Ltd, Northern Ireland), using bovine chondroitin sulphate as standard. Collagen content was indirectly determined by measuring the hydroxyproline content after acidic hydrolysis of the samples at 110 ℃ for 18 hr in 38% HCl. Samples were assayed using a cholarime-T assay, assuming a hydroxyproline/collagen content ratio of 1:7.69[330]. Calcium content was determined using the o-cresolphthalein complexone (oCPC) method where a violet colored complex is formed between calcium ions reacting with oCPC[331] (Sentinel Diagnostics). All samples were run in triplicate ($n \geq 3$).

4.2.7. Histological analysis

At each time point (0 and 28 days) ECM derived constructs (2 scaffolds at each time point) were fixed overnight at 4 ℃ in a 4% paraformaldehyde solution. After being washed in PBS, the samples were dehydrated in serial increasing gradient alcohol solutions and xylenes and finally embedded in paraffin. The wax-embedded constructs were sectioned (6 μm slices) and mounted onto microscope slides. Sections were rehydrated and stained with 1% alcian blue 8GX in 0.1 M HCl for sGAG, with picrosirius red for collagen, with alizarin red for calcium and with hematoxylin & eosin for differences in new tissue formed.

Immunohistochemical analysis was performed on 6 μm sections made with a microtome. Samples were first rehydrated by dipping three times in xylenes for 5 min (to remove the wax), in 100% alcohol 3 times for 1 min and in running tap water for 5 min. Then the samples were washed in PBS for 5 min before treating them with 0.5 mg/ml

pronase at 37 ℃ for 5 min as the antigen retrieval method, washed with PBS for 5 min and then treated with 3% H_2O_2 at room temperature (RT) for 20 min to block endoperoxide activity. After rinsing with PBS for 5 min, the slides were blocked with 10% goat serum at RT for 1 hr and incubated with the primary antibody at 4 ℃ overnight. See table below for antibody information. The next day incubation with the secondary antibody was performed, at RT for 1 h. By using VectastainABC reagent (VectastainABC kit, Vector Laboratories©, UK) for 5 min in peroxidase DAB substrate kit (Vector laboratories, UK), it was possible to observe a colour alteration. Samples were dehydrated with graded ethanol and xylenes and mounted with Vectamount medium (Vector Laboratories©, UK), which is an optically clear and odourless solution for permanently preserving histochemical stains.

Table 4-1. *List of antigens, primary and secondary antibodies used for immunohistochemistry analysis, including working dilutions for each antibody and catalogue number.*

Antigen	Primary antibody	Secondary antibody
Collagen type I	1:400, mouse monoclonal IgG ab90395 (Abcam®, UK)	1:200, anti-mouse IgG B7151 (Sigma)
Collagen type II	1:100, mouse monoclonal IgG ab3092 (Abcam®, UK)	1:200, anti-mouse IgG B7151 (Sigma)
Collagen type X	1:100, mouse monoclonal IgM ab49945 (Abcam®, UK)	1:200, anti-mouse IgM ab49760 (Abcam®, UK)

4.2.8. PCR analysis

RT-PCR was performed using a similar protocol to those previously described[332]. TRI Reagent® (Sigma) was used to lyse the cells. Briefly, 1 ml of Trizol was added to each construct in RNAse-free tubes before snap-freezing it in liquid nitrogen and stored at -80 ℃ until further use. When ready to be used, the solution was placed on ice to allow it to thaw slowly. While thawing, samples were homogenised (IKAT10, IKA® Works Inc., NC, USA) for 2 min. mRNA was extracted according to the manufacturer's protocol. Briefly, 200µl of chloroform were added to each tube and centrifuged at 12,000g at 4°C. RNA located in the upper phase was transferred to a new RNAse free tube, isopropanol was added at the same volume as well as 4µl glycoblue to allow visualisation of the RNA in the following steps. The tubes were stored at -20°C overnight

and again placed on ice to allow the solution to thaw and centrifuged at 12,000g at 4°C for 15 min. A visible blue RNA pellet was formed, supernatant was discarded, and the tubes dried. 1ml of 70% ethanol (in RNAse free water) was added to wash the pellet. Another centrifugation step was performed at 12,000g at 4°C for 15 min, ethanol was removed and the pellet air dried. RNAse free water (30 µl) was used to dissolve the pellet. A NanoDrop-1000 spectrophotometer (Thermo Fisher Scientific) was used to quantify RNA yield. Sample purity was checked via 260/280 (>1.8) absorbance ratio. Transcription of mRNA to cDNA was performed using a high capacity cDNA reverse transcription kit (Invitrogen). A mastermix was added to 500 ng of RNA and placed in a thermocycler. The following temperature sequence was applied: 10 min at 25 °C, 2 hrs at 37 °C, 5 min at 85 °C, 1 min at 4 °C. cDNA was quantified using Qubit ssDNA assay kit (Q10212 – Life Technologies) following manufacturer's instructions. Then, quantitative polymerase chain reaction (qPCR) was prepared for all samples (~30 ng cDNA) using SYBR Select Master Mix with ROX passive dye (Applied Biosystems, 4472920). The expression of glyceraldehyde 3-phosphate dehydrogenase (GAPDH), sex-determining region Y-related high mobility group-box 9 (SOX9), collagen type II (COL2), runt-related transcription factor 2 (RUNX2), matrix metalloproteinase 13 (MMP13) and collagen type X (COL10) were quantified using primers detailed below. The amplification was performed with the ABI 7500 Fast Real-time PCR machine (Applied Biosystems). All samples were run in duplicate (n ≥ 4). The relative quantity of each sample was calculated with reference to GAPDH (RPL4 was assessed as potential house-keeping gene but was not considered stable enough for the current experimental set up) and expressed as fold change normalized to the control group (ΔΔCt method).

Table 4-2. Forward and reverse primers used in qPCR for each gene and its associated role (Sigma).

Function	Gene	Forward primer (5'-)	Reverse primer (5'-)
House-keeping	GAPDH	TTTAACTCTGGAAAGTGG	GAACATGTAGACCATGTAGTG
House-keeping	RPL4	GTAACTACAATCTTCCCATGC	GGTCTTTGCATATGGGTTTAG
Chondrogenesis	SOX9	CAGACCTTGAGGAGACTTAG	GTTCGAGTTGCCTTTAGTG
Chondrogenesis	COL2	CGACGACATAATCTGTGAAG	TCCTTTGGGTCCTACAATATC
Hypertrophy	RUNX2	CCAACAGAGGCATTTAAGG	CCAAAAGAAGTTTTGCTGAC
Hypertrophy	MMP13	GACCAAATTATGGAGGAGATG	AAACAAGTTGTAGCCTTTGG
Hypertrophy	COL10	CCAACATCCAGAATCCATC	GTAGGTGTTTGGTATTGCTC

4.2.9. In vivo evaluation

Harvested samples from subcutaneous mice model were fixed in a formalin solution for 24 hours and the levels of mineralization within the tissue were quantified using μCT (Scanco Medical, Switzerland) at a threshold of 210, corresponding to a density of 399.5 mg hydroxyapatite/cm^3. Total volume per sample was calculated from reconstructed μCT.

Demineralized wax-embedded constructs were sectioned at 6 μm and stained with safranin-O for cartilage matrix evaluation. Safranin O staining was also used in combination with Photoshop CS6 to quantify the area of positively stained cartilage within the sample. Protocol developed can be found in CHAPTER - APENDIX: 10.5.

4.2.10.   Statistical analysis

Results are presented as mean ± standard deviation (n ≥ 3 at each time point). Graphical results and statistical analysis were performed with GraphPad Prism 5.01 software. Experimental groups were analysed for significant differences using a general linear model for analysis of variance (ANOVA) with factors including different ECM materials and culture conditions. Tukey's multiple comparison test was used to compare different conditions (media *vs.* material). Significance was accepted at a level of $p < 0.05$. GraphPad was also used to calculate outlier datapoints. A significance level of 0.01 was used to determine the removal of a data point.

4.3. Results

4.3.1. Composition of the solubilised ECM derived material used for the scaffold fabrication

In the previous chapter, it was stablished that GREM1 was enough to suppress collagen type X (a marker of hypertrophy) in a pellet model and reduce mineralisation (a marker of osteogenesis) in a monolayer model, the next step was to assess its influences on chondrogenesis in a more translationally relevant 3D scaffold. In order to fabricate a relevant cartilage-specific scaffolding material, AC ECM was pepsin solubilised in acetic acid and salt (NaCl) precipitated to obtain the structural collagenous fraction of the ECM.

Solubilised AC ECM composition was then compared to other musculoskeletal relevant solubilised ECMs.

In the previous mass spectrometry analysis, the samples analysed consisted of the GnHCL-extracted supernatant of AC and GP tissues. In this case, mass spectrometry analysis was performed on the collagenous fraction (material used to fabricate the scaffolds) of four different musculoskeletal related tissues: articular cartilage (AC), bone (BN), growth plate (GP) and ligament (LG). Proteomic analysis was performed as described in the previous chapter. Maxquant software in combination with a *sus scrofa* uniport database were used to process the raw data from the MS/MS. Perseus matrices and plots were used to analyse maxquant data. Only proteins present in at least two out of three of the replicas were considered for further analysis. Principal component analysis (PCA) was used to cluster the solubilised ECMs according to their composition, based on the 11 different proteins and their amount (established by label free quantification, LFQ) found in each tissue. AC and GP ECM were found to have a similar composition, while both tissues differed from BN or LG ECM (**Figure 4-4**a). Differences in protein LFQ between the four ECMs were plotted in a heat map. Similar to the PCA per protein plot (**Figure 4-4**b), the heat map analysis demonstrated the presence of several proteins in each ECM, however each tissue was characterised by the presence of only a few main proteins (**Figure 4-4**c). The main protein in the solubilised ECM of AC was COL2 (PGC, progastricsin is most likely a retained pepsin enzyme from digestion step). The main proteins in BN were COL1 and COL3 with some COL14 and COL2. The main proteins in GP were COL2 and COL1 (no COLX was found; the precipitation of such relatively small collagen from a complex matrix may need further optimisation). The main protein in LG was COL1.

Quantitative biochemical analysis revealed that the mean quantity of DNA remaining in all the scaffolding materials post processing was closer to or lower than the 50 ng/mg dry weight threshold established for effective decellularization[27] (**Figure 4-4**d). The lowest levels of DNA were found in the BN ECM, probably due to the additional decellularization protocol before solubilisation[318]. The analysis also demonstrated the almost complete removal of sGAG from all the matrices (**Figure 4-4**e). Collagen content was quantified by hydroxyproline (HxP) assay and determined that GP had the lowest values of HxP per dry weight compared to AC or LG ECMs (**Figure 4-4**f). Overall levels

of calcium present in the ECMs were low, with the highest levels found in the BN ECM (**Figure 4-4**g).
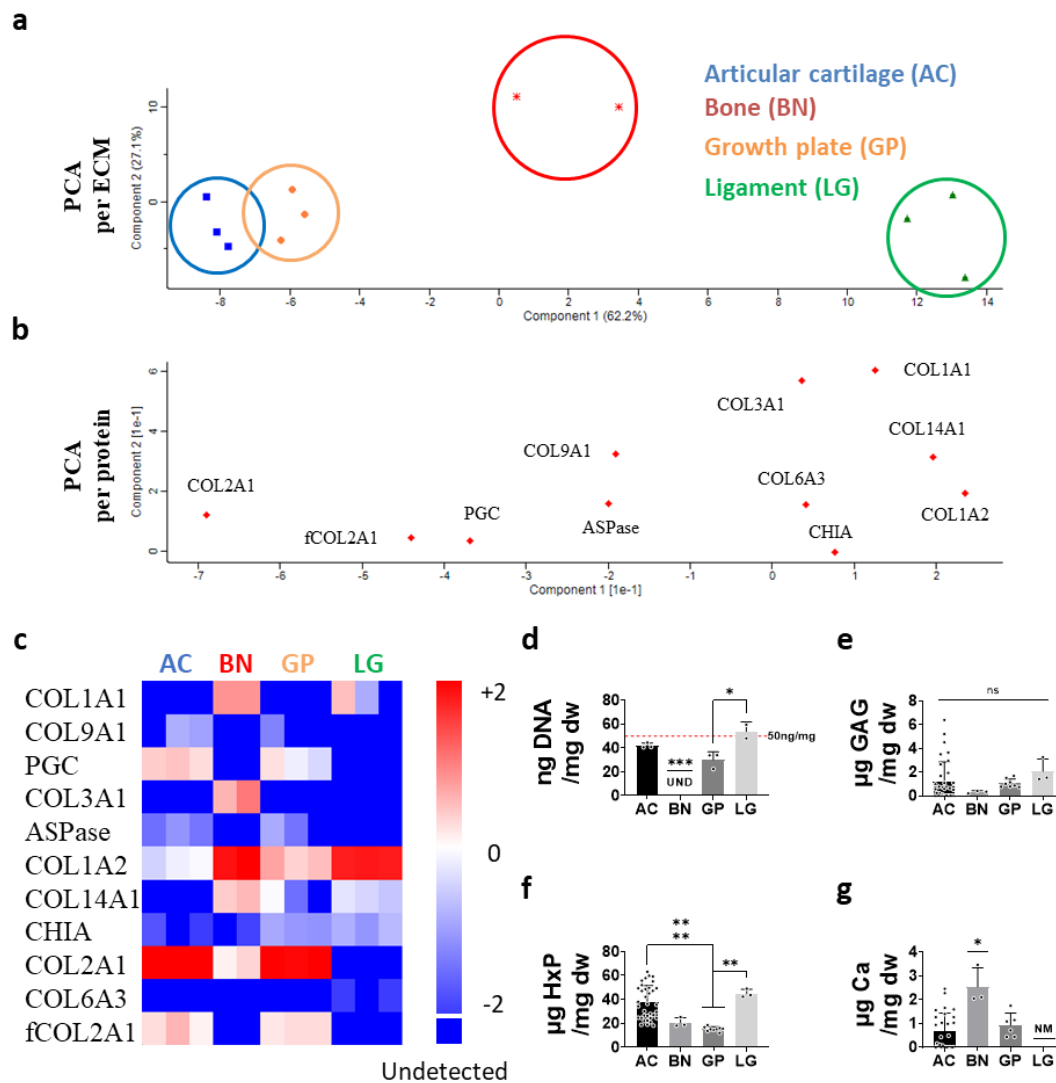
*Figure 4-4. Composition of solubilised musculoskeletal ECM. **a,** Principal component analysis (PCA) per ECM: articular cartilage (AC) in blue, bone (BN) in red, growth plate (GP) in orange or ligament (LG) in green. **b,** PCA per protein showing a pattern distribution based on composition of each ECM. **c,** Heat map of the z-score statistical measure of the different proteins based on LFW intensities found in all the tissues. Biochemical analysis showing levels of **d,** ng DNA per mg dry weight; **e,** μg GAG per mg dry weight; **f,** μg HxP per dry weight; and **g,** μg calcium per dry weight (*P<0.05, **P<0.001, ****P<0.00001; n ≥ 2 with pooled data from different batches). DNA values were obtained by Dr. Dave Browe and Dr. Fiona Freeman (UND: Undetected. NM: Not measured). Solubilisation of BN ECM was performed by Dr. Dave Browe and Dr. Fiona Freeman.*

4.3.2. GREM1 can supress hypertrophy of cartilaginous tissues engineered in ECM derived scaffold

Having stablished the basal composition of the solubilised AC ECMs (mainly collagen type II), the next step was to fabricate freeze-dried solubilised AC ECM derived scaffolds (5Φx3h mm). These scaffolds were seeded with 500,000 BMSCs and used to assess the influence of GREM1 on MSC chondrogenesis in a more translationally relevant 3D model. Constructs were maintained at 20% pO$_2$ in media supplemented with 20 ng/ml of GREM1.

After 28 days in culture, all engineered tissues stained strongly for alcian blue and picrosirius red, indicating robust sGAG and collagen deposition in both groups (**Figure 4-5**a). Tissues engineered using standard CM stained positive for type II collagen, but some type I and type X collagen deposition was also observed. On the contrary, constructs additionally stimulated with GREM1 stained negative for type I and type X collagen deposition, while still stained strongly for collagen type II. In addition, alizarin red staining demonstrated the presence of small calcified deposits in tissues engineered using standard CM, which was not observed in constructs additionally stimulated with GREM1.

Biochemical analysis was used to validate histological results and it showed similar trends in terms of tissue deposition (**Figure 4-5**b). DNA levels (normalised per dry weight, dw) on the scaffolds at day 28 were similar across both groups. Similar levels of sGAG/DNA and HxP/DNA ratios were observed in all scaffolds. Overall levels of calcium accumulation were low, with a trend towards lower levels of accumulation in tissues engineered in the presence of GREM1.

Quantitative real-time PCR was also performed on constructs after 28 days of culture (**Figure 4-5**c). MSCs seeded on the scaffolds and stimulated with CM + GREM1 (20 ng/ml) expressed comparable levels of SOX9, COL2 (chondrogenic markers) and RUNX2 (osteogenic marker) to cells cultured in standard CM only. On the contrary, cells supplemented with GREM1 expressed significantly lower levels of MMP13 and COL10 (hypertrophic marker) than cells cultured in CM.
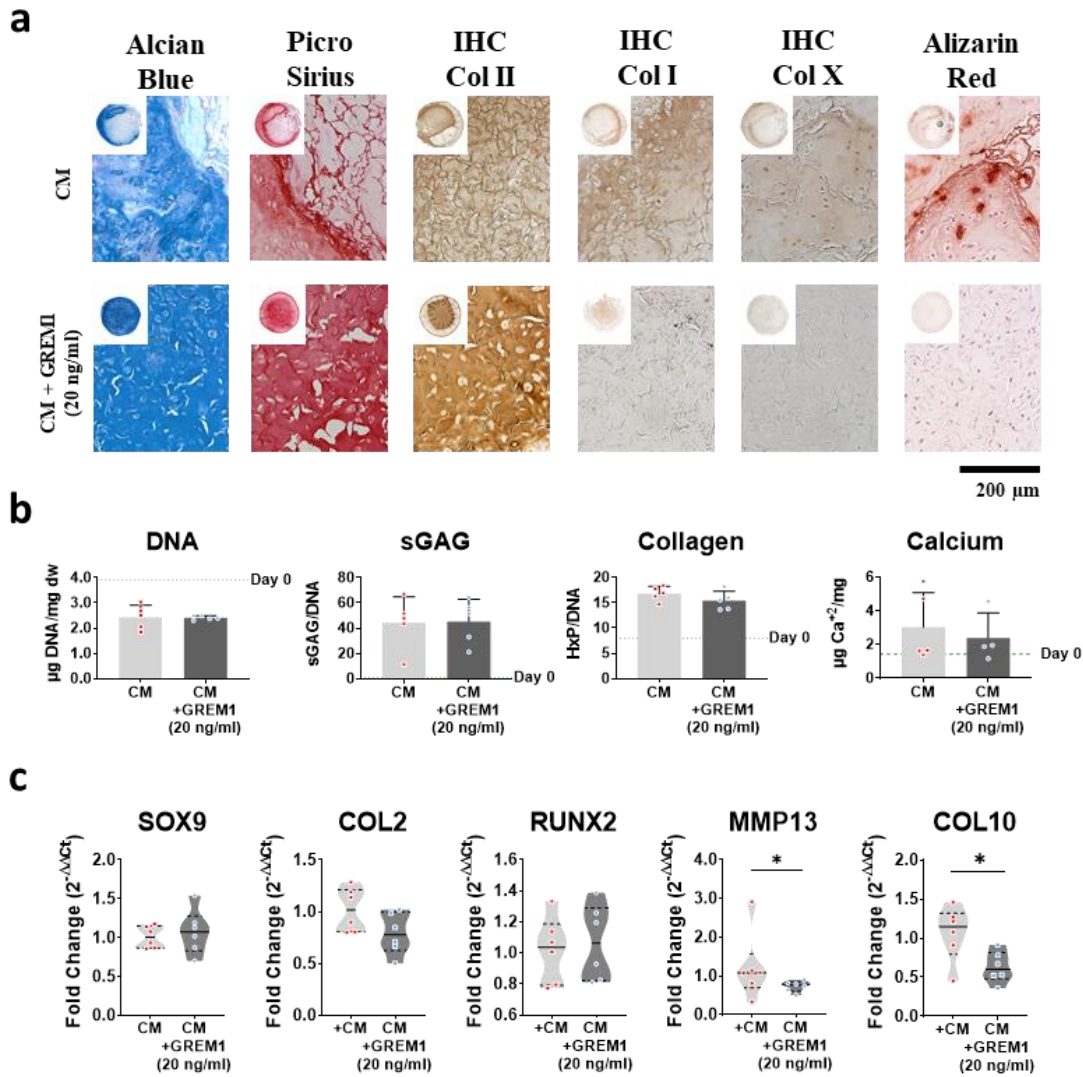
***Figure 4-5**. Effect of 20 ng/ml GREM1 on MSC seeded on solubilised AC derived scaffold. **a**, Representative histological images of constructs after 28 days of culture in chondrogenic media supplemented with or without 20 ng/ml GREM1. The figure shows alcian blue for gag staining, picrosirius red for collagen staining, immunohistochemistry for the chondrogenic marker collagen type II, for the fibrotic marker collagen type I and for the hypertrophic marker collagen type X; and alizarin red for calcium staining (n = 2). **b**, Biochemical analysis showing levels of µg DNA/mg dry weight (dw), sGAG/DNA, HxP/DNA and calcium/mg dw for control and experimental groups after 28 days of culture (n ≥ 4). Day 0 levels are indicated by a green dash line in each graph. **c**, Quantification of SOX9, COL2, RUNX2, MMP13 and COL10 gene expressions after 28 days of culture. Expression is relative to the control (CM). Graphs illustrate violin plots with median and quartiles (*P ≤ 0.05 unpaired t-test; n = 6).*

4.3.3. Pre-treatment with GREM1 alters the remodelling of engineered cartilage in vivo

MSC seeded scaffolds were cultured for 28 days in normoxic conditions (20 % pO$_2$), in either standard chondrogenic medium (CM) or CM supplemented with 20 ng/ml GREM1, and then implanted subcutaneously in the back of mice to assess whether GREM1 could promote the development of more phenotypically stable cartilage tissue *in vivo*. After 4 weeks the mice were sacrificed, and samples retrieved. Macroscopically the explanted tissues appeared heterogenous, with areas retaining a gloss cartilage-like appearance, while other areas had a bone-like appearance (**Figure 4-6**a). Surface vascularization was apparent in some constructs. Next, samples were fixed, and x-ray scanned. Reconstructed images obtained from μCT showed bone-like mineral deposition in all groups, with higher levels observed in constructs pre-treated with 20 ng/ml GREM-1 (**Figure 4-6**b).

Histological analysis was also performed after decalcification of the samples. Safranin-O staining was analysed semi-quantitatively to determine the levels of residual cartilage within the engineered tissues. This analysis revealed that GREM1 treated constructs retained a significantly higher level of sGAG-rich, cartilage-like tissue post-subcutaneous implantation (**Figure 4-6**c).

A similar analysis was performed at 6 weeks post-implantation. μCT quantification demonstrated an increase in new bone deposition between week 4 and 6. No increase in mineralisation were observed between weeks 4 and 6 in engineered tissues precultured with GREM1 (**Figure 4-7**a). Semi-quantification of safranin-O stained histological sections revealed a significant reduction in the levels of residual cartilage matrix from week 4 to 6 in tissues precultured in CM only. In contrast, no such temporal reduction in the levels of cartilage matrix was observed in GREM1 pre-stimulated constructs from 4 to 6 weeks (**Figure 4-7**b).
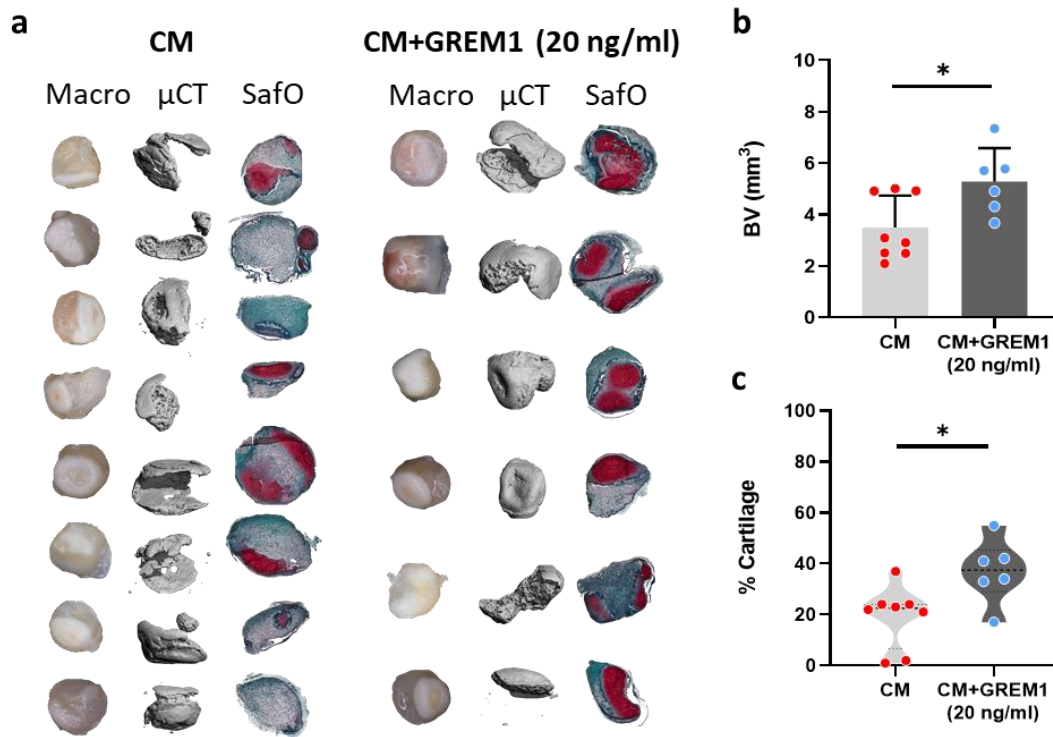
Figure 4-6*. Analysis of cartilage engineered development in mouse subcutaneous model 4 weeks post-implantation. **a**, All macroscopic, reconstructed micro x-ray computed tomography and histological safranin-o staining (cartilage in red) images of both control and experimental groups 4 weeks post-subcutaneous implantation in mice. Before implantation. the groups were precultured for 28 days in control (CM) and experimental medium (CM + 20 ng/ml GREM1) as in previous result figure. **b**, Quantification of the total bone volume. **c**, Semi-quantification of the amount of red staining per total area from histological section in percentage. (*P < 0.05; n ≥ 6).*
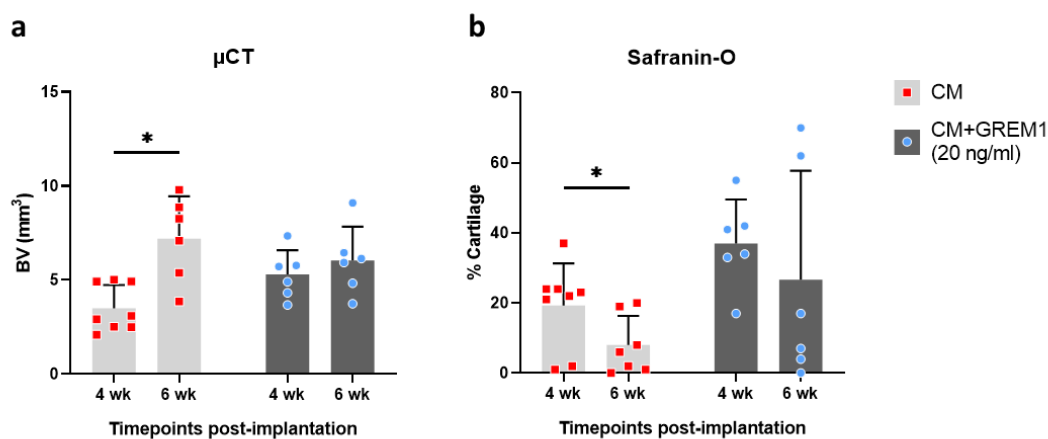
Figure 4-7. *Comparison of the cartilage engineered development in mouse subcutaneous model between 4- and 6-weeks post-implantation. **a**, Quantification of the total bone volume, based on x-ray microcomputed tomography. **b**, Semi-quantification of*

114

4.3.4. *Increasing the concentration of GREM1 (200 ng/ml) does not alter the remodelling of engineered cartilage in vivo*

While higher levels of residual cartilage were observed *in vivo* within engineered tissues pre-treated with GREM1, high amounts of bone were still observed after subcutaneous implantation. From this outcome, it was hypothesized that higher concentrations of GREM1 might be required to supress endochondral ossification. It was previously observed (**Figure 3-10**a) that higher concentration of GREM1 (200 ng/ml) could potentially supress collagen homogenous deposition in pellet culture. Thus, before starting a new subcutaneous study, an *in vitro* assessment of the 3D scaffold model with a higher concentration of GREM1 (200 ng/ml) was performed.

The results using a higher dosage of GREM1 during preculture on the scaffold model demonstrated a similar trend to the previous study. After 28 days un culture, all engineered groups stained strongly for alcian blue and picrosirius red, indicating robust gag and collagen deposition, respectively (**Figure 4-8**a). Tissues engineered using standard CM stained positive for collagens type II, type I and type X. On the contrary, constructs stimulated with CM supplemented with 200 ng/ml GREM1 stained weakly for collagen type I and X, while still stained strongly for collagen type II.

Quantitative biochemical analysis was also undertaken to supplement the histological results, which revealed similar trends in terms of tissue deposition. DNA, sGAG, hydroxyproline (HxP) and calcium levels at day 28 were comparable in both groups (**Figure 4-8**b).

Quantitative real-time PCR was also performed on constructs after 28 days of culture (**Figure 4-8**c). MSC seeded on the scaffolds and supplemented with CM + 200 ng/ml GREM1 expressed comparable levels of SOX9, COL2, RUNX2, MMP13, COL10 to cells cultured in standard CM alone. However, regulation of the expression of the hypertrophic markers MMP13 and COL10 followed a similar trend to the previous study.
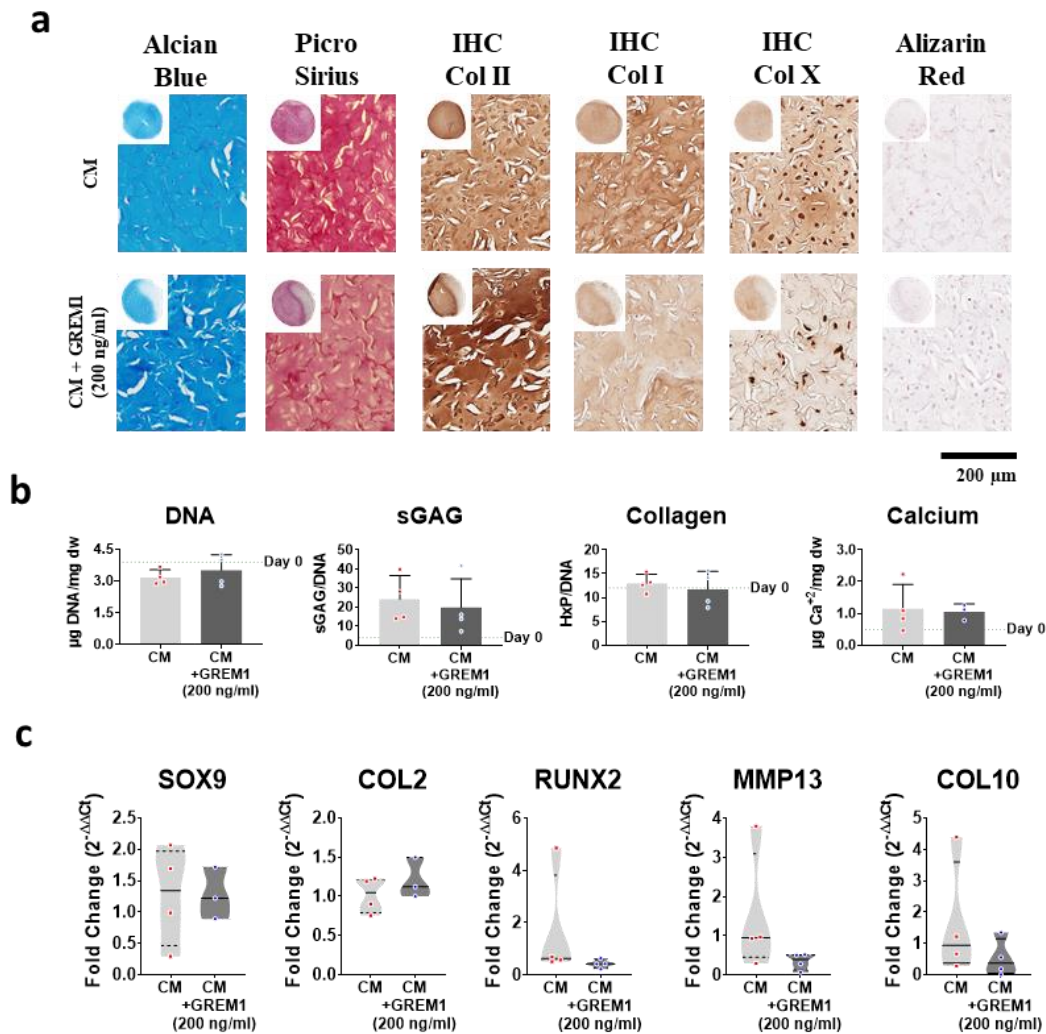
Figure 4-8*. Effect of 200 ng/ml GREM1 on MSC seeded on solubilised AC derived scaffold. **a**, Representative histological images of constructs after 28 days of culture in chondrogenic media supplemented with or without 20 ng/ml GREM1. The figure shows alcian blue for gag staining, picrosirius red for collagen staining, immunohistochemistry for the chondrogenic marker collagen type II, for the fibrotic marker collagen type I and for the hypertrophic marker collagen type X; and alizarin red for calcium staining (n = 2). **b**, Biochemical analysis showing levels of µg DNA/mg dry weight (dw), sGAG/DNA, HxP/DNA and calcium/mg dw for control and experimental groups after 28 days of culture (n = 4). Day 0 levels are indicated by a green dash line in each graph. **c**, Quantification of SOX9, COL2, RUNX2, MMP13 and COL10 gene expressions after 28 days of culture. Expression is relative to the control (CM). Graphs illustrate violin plots with median and quartiles (n ≥ 3).*

Having established that the increase of GREM1 concentration to 200 ng/ml was not detrimental for chondrogenesis nor its antihypertrophic effect, the precultured constructs were next implanted in a subcutaneous mouse model. MSC seeded scaffolds

were cultured for 28 days in either chondrogenic media (CM) or CM supplemented with 200 ng/ml GREM1. The constructs were then implanted in the back of mice to study cartilage tissue development in an angiogenic environment. After 4 weeks the mice were sacrificed, and samples retrieved.

Macroscopic pictures were taken shortly after sacrifice. As seen in the previous iteration of the study, heterogenous tissue development was observed with areas where the glossy-like cartilage still remained and areas resembling bone-like tissue (**Figure 4-9**a). Surface vascularization was apparent in some constructs. Next, samples were fixed, and x-ray scanned. Reconstructed images obtained from μCT showed high mineral content in all groups. In this study, the bone volume quantification demonstrated that constructs pre-treated with 200 ng/ml GREM-1 was similar to the control group (**Figure 4-9**b).

Histological analysis was performed after decalcification of the samples. Safranin-O staining was used to evaluate the remodelling of deposited cartilaginous tissue during pre-culture. Semi-quantification of the histological sections demonstrated that there was no significant difference for retention of GAGs post-subcutaneous implantation, with a trend (*p=0.053) towards higher GAG retention in the 200 ng/ml GREM1 treated group compared to control (**Figure 4-9**c).
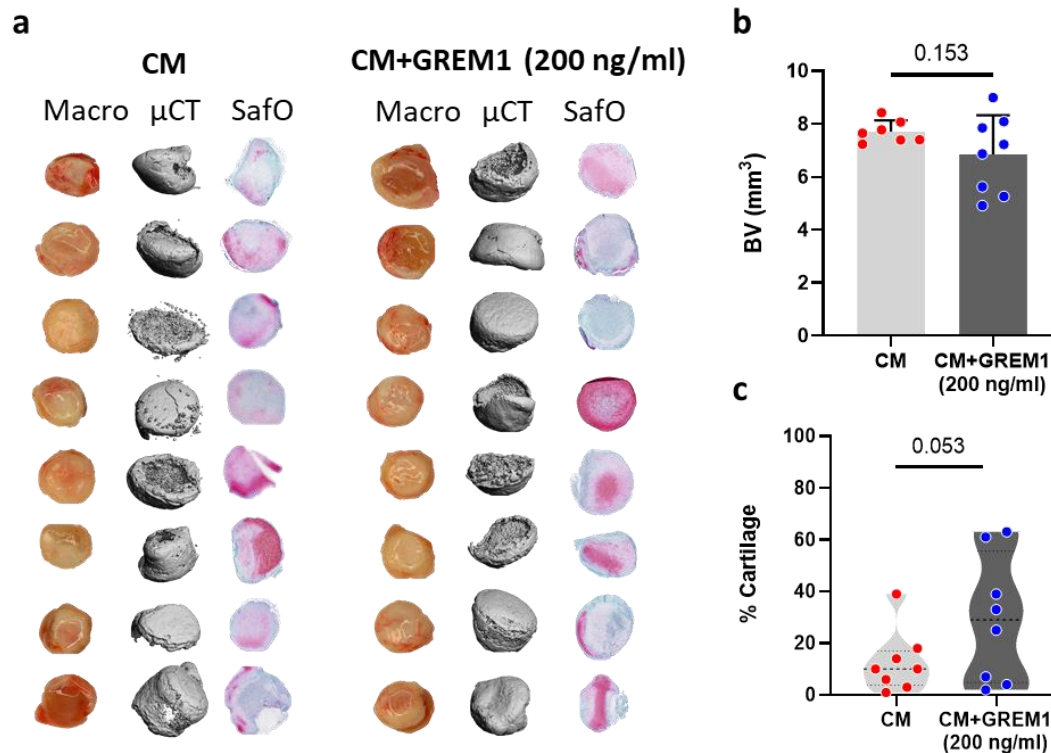
Figure 4-9. *Analysis of cartilage engineered development in mice subcutaneous model.* ***a****, All macroscopic, reconstructed micro x-ray computed tomography and histological safranin-o staining (cartilage in red) images of both control and experimental groups 4 weeks post-subcutaneous implantation in mice. Before implantation. the groups were precultured for 28 days in control (CM) and experimental medium (CM + 200 ng/ml GREM1) as in previous result figure.* ***b****, Quantification of the total bone volume.* ***c****, Semi-quantification of the amount of red staining per total area from histological section in percentage. (n = 8).*

4.3.5. The combined effect of hypoxia (5% pO₂) and GREM1 on chondrogenesis in vitro and endochondral ossification in vivo

Having established that pre-treating constructs with a higher concentration of GREM1 does not inhibit mineralisation, this thesis next investigated if the combination of GREM1 (20 ng/ml) stimulation and hypoxia (a known regulator of cartilage homeostasis[333,334]) could have a synergistic effect on chondrogenesis *in vitro* and further mineralisation *in vivo*.

Biochemical analysis of the pre-treated constructs before implantations revealed that combined hypoxia and GREM1 supplementation resulted in higher sGAG deposition

(**Figure 4-10**b). Similar levels of DNA, collagen (HxP) and calcium were observed in all the conditions (**Figure 4-10**a,c,d).
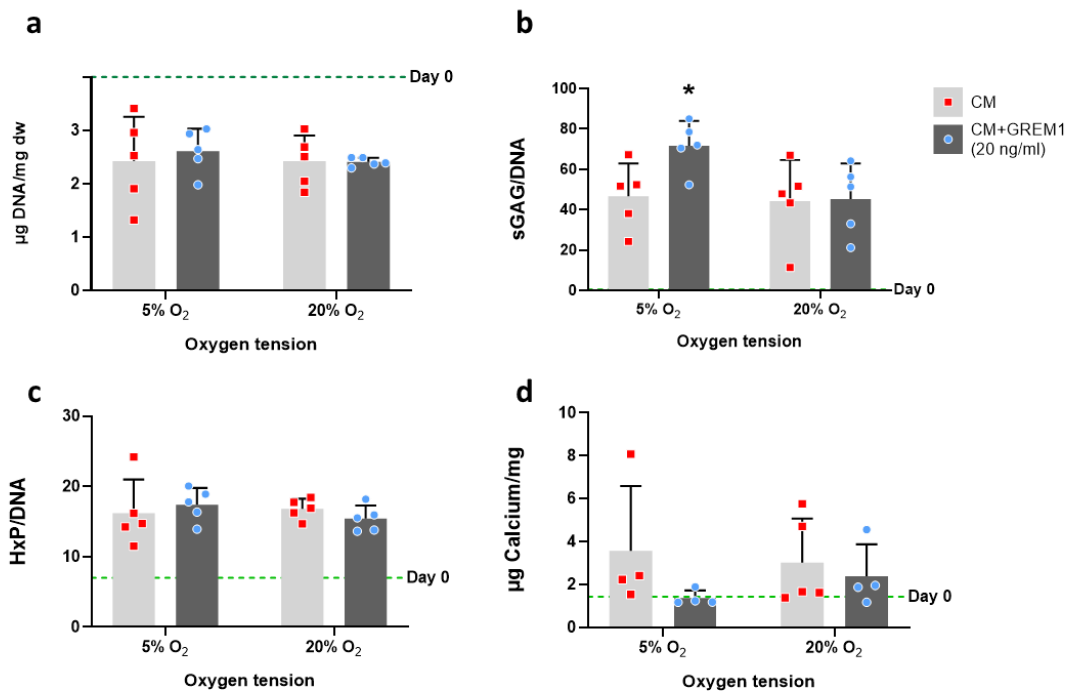
*Figure 4-10. Combination of hypoxia and GREM1 treatment. Biochemical analysis showing levels of **a**, µg DNA/mg dry weight (dw), **b**, sGAG/DNA, **c**, HxP/DNA and **d**, calcium/mg dw for control and experimental groups after 28 days of culture (n ≥ 4) in either hypoxia (5% pO$_2$) and normoxia (20% pO$_2$) conditions. Day 0 levels are indicated by a green dash line in each graph.*

Constructs pre-treated with standard CM or CM + GREM1 (20 ng/ml) and maintained in either normoxic or hypoxic conditions were implanted subcutaneously in the back of mice to assess the endochondral bone development *in vivo*. After 4 and 6 weeks, the constructs were fixed and x-rayed. Reconstructed images obtained from µCT showed bone-like mineral deposition in all groups. Hypoxic preconditioning had no significant effect on implant mineralisation (**Figure 4-11**a).

Histological analysis was also performed after decalcification of the samples. Safranin-O staining was analysed semi-quantitatively to determine the levels of residual cartilage within the engineered tissues. This analysis revealed that all groups preconditioned in hypoxia (5% pO$_2$) followed a comparable pattern to groups preconditioned in normoxia (20% pO$_2$) in terms of matrix degradation (**Figure 4-11**c,d). A significant reduction in the levels of residual cartilage matrix from 4 to 6 weeks was observed for constructs pre-treated with standard CM. In contrast, no such temporal

reduction in the levels of cartilage matrix was observed in GREM1 pre-stimulated constructs from 4 to 6 weeks leading to significantly higher levels of retained cartilage matrix at 6 weeks (**Figure 4-11**c).
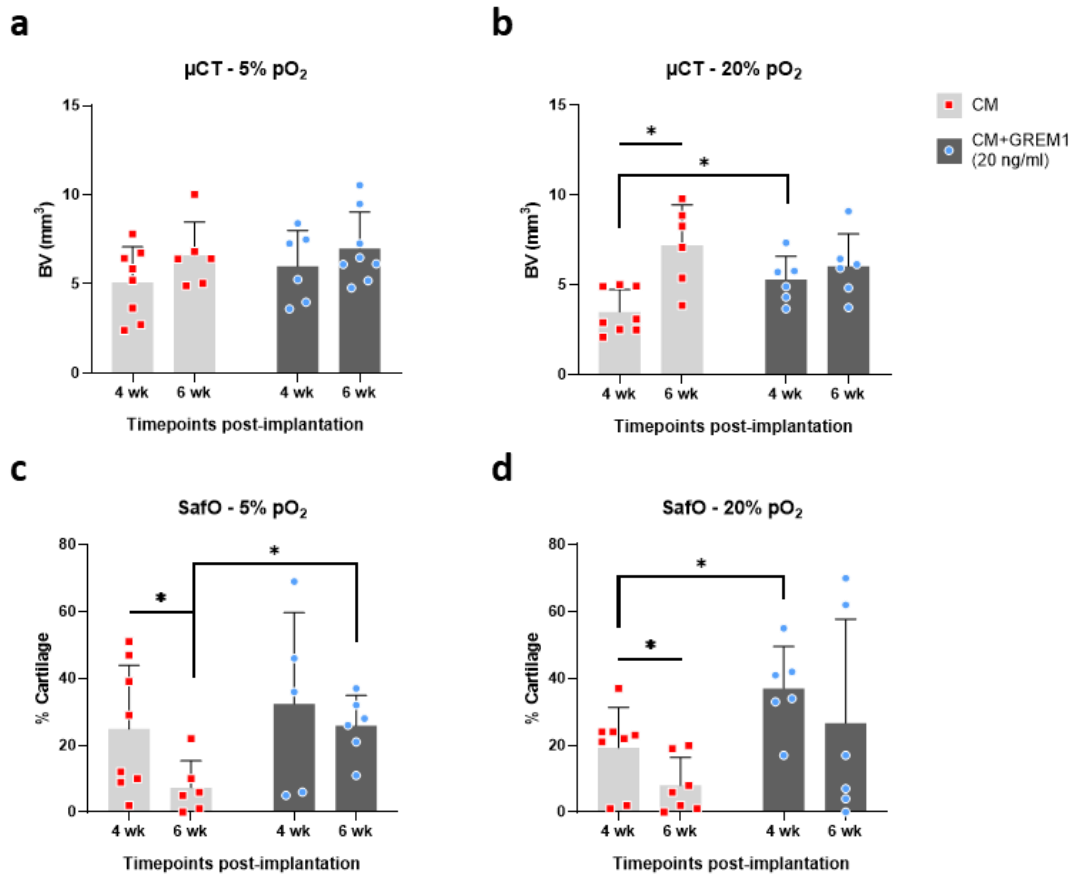
*Figure 4-11. Hypoxia and GREM1 pretreated engineered cartilage development in mouse subcutaneous model between 4- and 6-weeks post-implantation. **a**, Quantification of the total bone volume, based on x-ray microcomputed tomography. **b**, Semi-quantification of the amount of red staining per total area from safranin-o histological section in percentage. (*P < 0.05; n ≥ 5).*

4.4. Discussion

In the recent years, there has been an increased evidence to support the use of ECM derived materials[144–151] for tissue engineering applications. However, it is unlikely that a single tissue source will be the optimal for all organ systems. The advantage of using tissue-specific ECMs for tissue engineering and regenerative medicine is that it contains the functional and structural molecules secreted by resident cells of the specific

tissue or organ system[26,27]. It is reasonable to assume that the composition and structure of such matrices is uniquely suited to maintaining the cell phenotype of the specific tissue, and in particular that proteins that are more expressed in a specific tissue may play particularly important roles. The aim of this study was to determine the effect of AC-specific protein, GREM1, on the chondrogenesis of MSCs in a 3D scaffold model and the *in vivo* development of such *in vitro* engineered cartilage in the presence of GREM1. Taken together, the results indicated that AC-specific protein, GREM1, can be used as soluble cues to help engineer more hyaline-like cartilage *in vitro* that inhibits matrix degradation *in vivo*.

In the previous chapter, GREM1 effect on chondrogenesis was evaluated in a pellet model. In order to develop a more complex 3D model, a solubilised matrix derived from AC was chosen to fabricate freeze-dried scaffolds. Mass spectrometry was used to confirm that the solubilised material consisted mainly of collagen type II, with very low remnants of sGAG or DNA. This enabled the establishment of a porous scaffold that is pro-chondrogenic[319,335], but which also facilitated an assessment of the role of other regulatory factors in a model system that was relevant for cartilage tissue engineering.

As hypothesized, the antihypertrophic effect of GREM1 was also maintained in a more complex 3D scaffold model, as demonstrated by the lower expression of key hypertrophic markers. However, constructs precultured with GREM1 did not inhibit the mineralisation of the implanted constructs. It was observed that constructs primed with CM only, had an increase of bone levels from 4 to 6 weeks, while GREM1 primed constructs had similar levels at both time points. This suggests that GREM1 pre-treated constructs may mineralise faster than the control group. Assuming that some GREM1 is retained in the matrix during the priming, the faster mineralisation could be explained by a higher vascularisation due to the angiogenic role of GREM1. As previously mentioned, GREM1 is a proangiogenic ligand of VEGFR2 ligand, which is independent of VEGF canonical pathway[336].

Interestingly, both the low (20 ng/ml) and high (200 ng/ml) concentrations of GREM1 engineered constructs were able to resist the degradation of the deposited ECM upon implantation and help maintain a cartilage phenotype through the ossification process. Although, this was less evident in the high GREM1 treatment. This is in agreement with a recent study demonstrating that higher concentrations of GREM1 (>500

ng/ml) exert dose-dependent catabolic effects *in vitro* through the NF-κB pathway leading to cartilage degradation[337].

In the lower GREM1 treated group, this matrix "protection" was prolonged even after 6 weeks, while decrease of cartilage-like tissue over time is evident in CM primed constructs. During endochondral ossification, the process of ECM degradation is a key feature of the subsequent bone remodelling. This ECM degradation is mainly driven by the metalloproteinases produced by hypertrophic chondrocytes[338]. The *in vitro* results supported the conclusion that GREM1 inhibits the MSC hypertrophic phenotype. This suggests that constructs primed with GREM1 are able to inhibit matrix degradation because maybe there are less metalloproteinases. However, this is not enough to stop host-mediated bone formation.

In vivo results suggested that optimum concentration for GREM1 is yet to be found, or it may be that the presence GREM1 is not sufficient to supress endochondral bone formation and that other regulators of cartilage homeostasis are needed for stable cartilage tissue engineering applications[248]. Previous research has demonstrated that hypoxia will supress hypertrophy of MSCs[339–341]. However, other studies also point to the differential effect of hypoxia in MSCs and conclude that hypoxia alone doesn't reduce expression of COL10[342]. Research investigating scaffolds made of variable hyaluronic acid (HA) concentration, observed that hypoxia only had a beneficial effect for MSC chondrogenesis in constructs with low HA concentrations[342]. In addition, when culturing explanted tibiae in hypoxia, the length of the growing bone was reduced, but higher mineral density was observed in the bone regions[343]. In this thesis, the combinatory effect of GREM1 with a hypoxic environment was further studied. Although these factors were observed to have a synergistic effect *in vitro*, this effect did not translate into a reduction in endochondral bone formation *in vivo*. Moreover, in this scaffold system, hypoxia pre-treatment did not reduce mineral formation after subcutaneous implantation and matrix degradation was evident from 4 to 6 weeks post implantation in constructs primed in standard CM only, similarly to constructs cultured in normoxia.

On the other hand, it is important to consider that the mouse subcutaneous model is a highly vascularised environment[344]. It is, however, a challenging but efficient strategy in which to discard experimental groups in a timely manner. The results above demonstrate a promising role for GREM1 in engineering stable cartilage matrix that resists degradation during *in vivo* remodelling. Future studies should look at GREM1

engineered cartilage in a chondral or osteochondral defect site to evaluate clinically relevant response of this AC-specific protein.

5. CHAPTER: Tailoring scaffold microarchitecture

5.1. Introduction

Scaffold pore size and shape plays a key role in long term outcomes of tissue engineering strategies[195]. It has been suggested that the minimum pore size required for successful osteochondral tissue engineering is ~80µm, as this allows for cell migration throughout the scaffold and adequate nutrient transport[213–215]. Small pores (80-200 µm) have been shown to favour hypoxic conditions and induced cartilage formation[31,216], while large pores (300-400 µm), that can be well-vascularized and limit stem cell condensation, enhance new bone formation by directing osteogenesis[217,218]. In addition to pore size, pore structure is also critical. It has been shown that underlying scaffold orientation will lead to the production of an oriented matrix[207]. Moreover, cellular and neo-matrix alignment within decellularized cartilage explants appears to be influenced by the collagen architecture of the decellularized tissue[206]. This suggests that scaffold pore architecture will play a key role in engineering tissues that mimic spatial complexity of the osteochondral unit, although the ideal scaffold design for such applications has yet to be identified.

A number of different approaches have been proposed to modify the internal architecture of porous scaffolds. These include electrospinning, 3D printing and freeze-drying. Electrospinning allows the development of fibrous scaffolds that span the nanometre to micrometre scale, however the materials that can be processed using this technique typically lack inherent osteo/chondro-inductivity and therefore typically require further biofunctionalization[209]. In addition, the dimensional scaling-up of electrospun scaffolds is challenging[177]. 3D printing strategies, such as fused deposition modelling, broadens the material of choice and easily allows the production of complex tissue-like shapes, however, it requires significant parameter optimization (pressure, temperature and rate extrusion) to achieve high reproducibility at nano- and micrometre dimensions[188]. Nevertheless this technology can be very useful in cartilage[345] and bone[129] tissue engineering to reinforce softer biomaterials, by improving the overall construct's mechanical properties.

Different freeze-drying techniques can be used to obtain biologically active scaffolds with tailorable interconnected pores of defined shape[190,191,193] and size[346,347].

Freeze-drying has been previously used to fabricate scaffolds with defined pore architectures with different biomaterials, such as gelatin[348], type I collagen[182,190,195,349,350], alginate[351], silk[352], chitin[353] and chitosan[354]. However, these materials have some inherent limitations and disadvantages, such as promoting fibrotic tissue deposition[355,356] or creating ossification centres for mineralisation[357], that may not be the optimum for articular cartilage tissue engineering. In this chapter, a tissue-specific ECM derived material from articular cartilage will be used to fabricate scaffolds with natural chondroinductive and chondrogenic properties[319].

The aims of this chapter were (i) to characterise the mechanical properties of a solubilised articular cartilage ECM derived scaffold, (ii) to develop a directional freeze-drying protocol to fabricate ECM derived scaffolds with aligned pores mimicking aspects of the aligned collagen network in articular cartilage, (iii) to modify the freeze-drying protocol to produce scaffolds with increased pore size, and (iv) to design and 3D print a synthetic polymeric reinforcement for ECM derived scaffolds in order to increase the overall stiffness of the resulting composite biomaterial.

5.2. Methods

Note: all material obtained from Sigma-Aldrich® unless stated.

5.2.1. Fabrication of scaffolds with random or aligned pores

The ECM material was harvested and solubilised as described in previous chapters. Briefly, AC ECM was dissected from porcine femoral heads and solubilised in pepsin and acetic acid. Solubilised AC ECM was salt precipitated and dialysed before freeze-drying to obtain working material. ECM derived scaffolds were fabricated as previously described[319]. Briefly, the freeze-dried collagenous material was mixed to a final concentration of 20 mg/ml (2%) in 0.02 M acetic acid. The solution was neutralized with NaOH and partially crosslinked with 5-10 mM glyoxal.

The solution was transferred to custom-made moulds, placed in the oven at 37 ºC and allow to partially crosslink for 30 min. Two moulds were used to fabricate the scaffolds in order to obtain random or aligned pores in the freeze-dried cake as explained

in the CHAPTER - APENDIX: 10.2 (see Figure 10-4). In order to generate random or aligned pores, the heat transfer direction had to be optimized for each case. The heat transfer direction at which this temperature is achieved are important as can influence ice crystal structure, defining how the product dries, and final pore shape of the dried structure. Multidirectional heat transfer will lead to an isotropic porous structure (random pores), while unidirectional heat transfer will lead to an anisotropic porous structure (aligned pores).

The two different protocols chosen to fabricate the scaffolds were:

Random pores

(i)   -30 °C (1 °C/min) hold for 1 h; atm pressure
(ii)   -10 °C (1 °C/min) hold 20 h; 0.200 mbar
(iii)   +25 °C (1 °C/min) hold 2 h; 0.200 mbar

Aligned pores

(i)   -190 (Liquid N_2) hold for 2 min; atm pressure
(ii)   +25 °C hold for 10 min; atm pressure
(iii)   -30 °C hold for 1 h; atm pressure
(iv)   -10 °C (1 °C/min) hold 20 h; 0.200 mbar
(v)   +25 °C (1 °C/min) hold 2 h; 0.200 mbar

After freeze-drying, the scaffolds then underwent dehydrothermal (DHT) crosslinking. The DHT process was performed in a vacuum oven (VD23, Binder, Germany), at 115 °C, in 2 mbar for 24 hr, as previously described in the literature[358].

5.2.2. Fabrication of scaffolds with random pores of an increased pore size

In order to generate scaffolds with increased pore size, an annealing step was included in the freeze-drying process. Annealing is a technique that comprises warming a product following initial freezing step. It is important to consider that slower cooling rate leads to larger ice crystals and better ice "networking" (useful for making scaffolds with big and interconnected pores), while rapid cooling can give a more even distribution of solutes to control homogeneity. Annealing, can help achieve the advantages of both slow and rapid cooling[346].

The solubilised ECM material described above was transferred to custom-made moulds, placed in the oven at 37 ℃ and allow to crosslink for 30 min. Then the samples were freeze-dried following the steps listed below:

(i)   -30 °C (1 °C/min); hold for 30 min; atm pressure

(ii)   -10 °C (5 °C/min); hold for 3 h; atm pressure*

(iii)   -30 °C (1 °C/min); hold for 1h; atm pressure

(iv)   -10 °C (1 °C/min), hold 20 h; 0.200 mbar

(v)   +25 °C (1 °C/min), hold 2 h; 0.200 mbar

*Annealing step
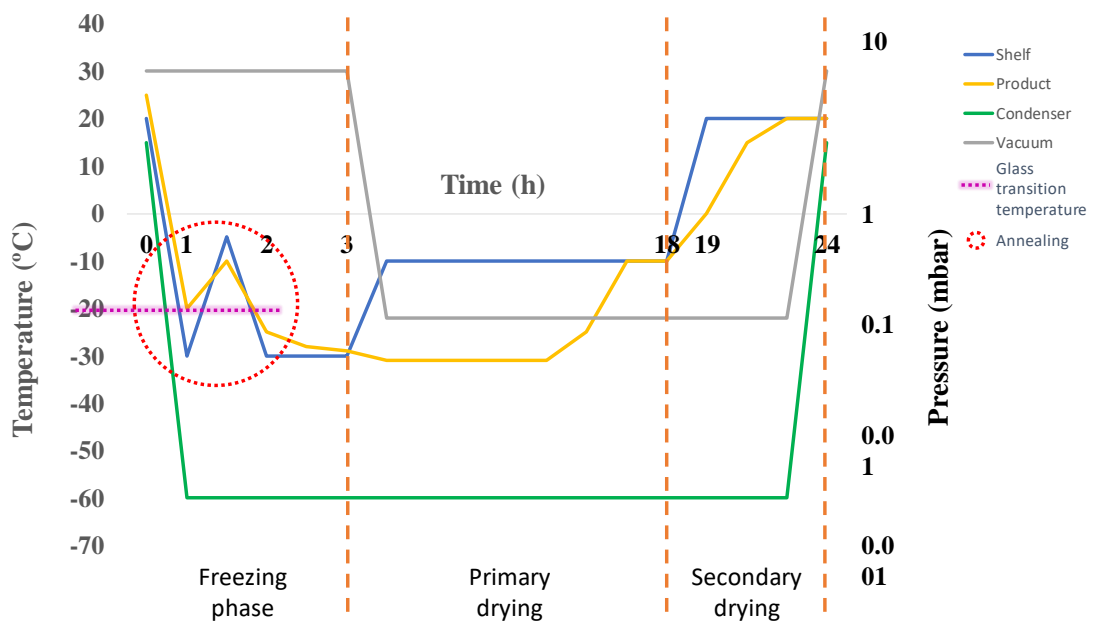
Figure 5-1. Typical process of freeze-drying divided in its three phases: initial freezing step, primary drying (sublimation) and secondary drying. For simplification purposes, time scale intervals are not constant.

5.2.3. Pore morphology characterization

Pore size: Scanning electron microscope images of the freeze-dried scaffolds were used to quantify pore size using Fiji (Fiji Is Just ImageJ).

Alignment: Macroscopic images of the freeze-dried scaffolds were taken after DHT crosslinking to assess level of pore anisotropy. 'OrientationJ' and 'Directionality' plugins, from Fiji, were used to create the colour maps of the pore orientation and to generate data to plot the direction curves, respectively. An extended version of the protocol can be found in CHAPTER - APENDIX: 10.3.

5.2.4. 3D printing of a synthetic polymeric reinforcement framework

PCL framework were fabricated using the 3D Discovery multi-head bioprinting system purchased from Regen Hu, Switzerland. The 3D Discovery was set up to allow the deposition of melted PCL (Sigma, Mn 45 000), which was melted at 60° and 3D printed in strands at a pressure of 0.5 MPa with a 25 Gauge needle (0.260 mm nominal inner diameter). Layer thickness was set up at 0.2 mm to allow a fusion between consecutive layers. The feed rate was set up at 4 mm/s.

The solubilised ECM was poured onto the 3D printed PCL framework and casted into a mould before freeze-drying using standard parameters to obtain random pores.

5.2.5. Mechanical testing

ECM scaffold samples (Φ5 mm x h 3 mm, n = 4) were subjected to a uniaxial unconfined compression test in phosphate-buffered saline (PBS, pH 7), using a single column mechanical tester (Zwick/Roell Z2.5, Herefordshire, UK) with a 5N load cell. Briefly, constructs were kept hydrated in PBS bath maintained at room temperature. A preload of 0.01N was applied for 60 seconds to ensure that top and bottom construct surfaces were in direct contact with the impermeable loading platens. Force was zeroed after preload, then followed by a cyclic compression test consisting of 6 compressive cycles with increasing strain amplitude of 10, 20, 30, 40, 50 and 60% in sequence at a rate of 2.22% strain per second. A holding time of 10 seconds between each cycle was added to allow full height recovery of the samples. The load versus displacement data were recorded throughout. The apparent stress and strain were calculated by dividing the load value with the initial cross-sectional area of each sample and the displacement value with the initial sample height, respectively. The apparent Young's modulus was determined from the slope of the initial linear region of the plotted stress-strain curves obtained from the second cycle. Cumulative percentage of the total height loss and height

loss per cycle was calculated to characterize super-elastic properties of the constructs. Scaffold permanent deformation (PD) at each cycle was calculated as follows: $PD = (\text{Test Speed}*\Delta t_n)/h_0$, where Δt_n is the interval of time at the start of the nth cycle in which no force is applied to the sample, while h_0 is the initial height of the sample.

5.2.6. Cell culture

Bone marrow stem cells (MSCs) were harvested and seeded at a density of 500,000 cells per scaffold (1,000,000 MSCs per bilayer scaffold), as described in previous chapter. Before supplementing the media, the cells were allowed to attach to the scaffolds for 2 hrs in the incubator at 37 ℃.

To assess cell infiltration, the constructs were kept for 7 days in normoxic conditions (20% O_2 and 5% CO_2) at 37 ℃ supplemented with 5 ml of expansion media: DMEM + GlutaMAX^{TM}, 10% fetal bovine serum (Gibco$^®$), 100 units/ml Penicillin, 100 units/ml Streptomycin (Gibco$^®$) and 0.25μg/ml amphotericin B.

5.2.7. Live/dead confocal microscopy

After 7 days in culture, live/dead assay was performed on the constructs in order to assess the cell viability, cell expansion and cell distribution of PBMSCs in the sECM derived scaffolds. It is a two-color fluorescence assay that simultaneously determines: (i) Live cell number: undamaged and metabolically active cells have intracellular esterases that convert non-fluorescent, cell-permeable calcein acetoxymethyl (calcein AM) to the intensely fluorescent calcein. Cleaved calcein is retained within cytoplasm of living cells and produces intense green fluorescence. The excitation wavelength used was ~495 nm and the emission wavelength recorded was ~515 nm. (ii) Dead cell number: the ethidium homodimer-1 (EthD-1) enters damaged cells membranes and is fluorescent when bound to nucleic acids. EthD-1 produces a bright red fluorescence in damaged or dead cells. The excitation wavelength used was ~495 nm and the emission wavelength recorded was ~635 nm.

The scaffolds were transferred to a 24 well plate and washed thoroughly in PBS, since the presence of serum from the media where they were cultured can increase

extracellular fluorescence by hydrolysing calcein (AM). The constructs were sliced in longitudinal direction (so the microscope imaging can take place in the middle of the construct). Then 1 ml of the freshly prepared Live/Dead solution was added. Briefly, the solution is prepared by mixing 20µL EthD-1(2 mM) + 4µL Calcein (5mM) + 10mL PBS in a 15ml Falcon tube (Molecular Probes Product Information; Il Keun Kwon 2005). After incubation for 1 hr, the scaffolds were washed three times with PBS. Finally, the constructs were imaged in the confocal microscope. The percentage of live/dead cells was obtained using Image J to count the green (alive) or red (dead) cells.

5.3. Results

5.3.1. Solubilised articular cartilage ECM derived scaffolds demonstrate shape-memory properties

Constructs were fabricated with 2% (20 mg/ml) of solubilised articular cartilage (AC), crosslinked with either 5 or 10 mM Glyoxal and freeze-dried following a standard protocol[319]. A decellularized cryomilled AC scaffold crosslinked with EDAC, previously used in our laboratory[30,32], was used as control to compare their mechanical properties. Upon rehydration, the scaffolds were subjected to 20% compression test at a rate of 2.22%/s. Increases in glyoxal concentration produced a marginal (but not significant) increase in scaffold stiffness (Figure 5-2a). Increasing the amount of glyoxal crosslinking resulted in the development of less elastic scaffolds, with higher levels of permanent deformation observed after the application of 20% strain (Figure 5-2b).

The solubilised ECM derived scaffolds had superior elastic properties, compared to the traditional cryomilled scaffolds (F250). The stiffness of the solubilised scaffold was not modified after 10 cycles at 80% compression and the scaffolds did not undergo any apparent macroscopic morphological changes, unlike the F250 scaffolds whose gross structure was noticeably influenced by the application of such cyclical loading (Figure 5-2c,d).

Scaffolds were subjected to cyclic compression testing, consisting of 6 compressive cycles with increasing strain amplitude of 10, 20, 30, 40, 50 and 60% in sequence at a rate of 2.22% strain per second, in order to further characterise this apparent

shape-memory behaviour. Minimal reduction in mechanical properties was observed after the test (Figure 5-2e). Permanent deformation of the scaffolds was observed only after the 3rd cycle (Figure 5-2f), with a total permeant deformation under 10% of the initial height after the test was completed. When mechanically compressed using tweezers, the solubilised ECM scaffolds recovered their original shape on unloading (Figure 5-2g).

a Young modulus

b Permanent deformation (20% strain)

No permanent deformation

c Elasticity (80% strain)

d Before   After

2/5

F250

2 mm

e Scaffold 2/5

f Strain
- 0.5-0.6 (Cycle 5)
- 0.4-0.5 (Cycle 4)
- 0.3-0.4 (Cycle 3)
- 0.2-0.3 (Cycle 2)
- 0.1-0.2 (Cycle 1)

g 0s   0.5s   1s   1.5s   5 mm
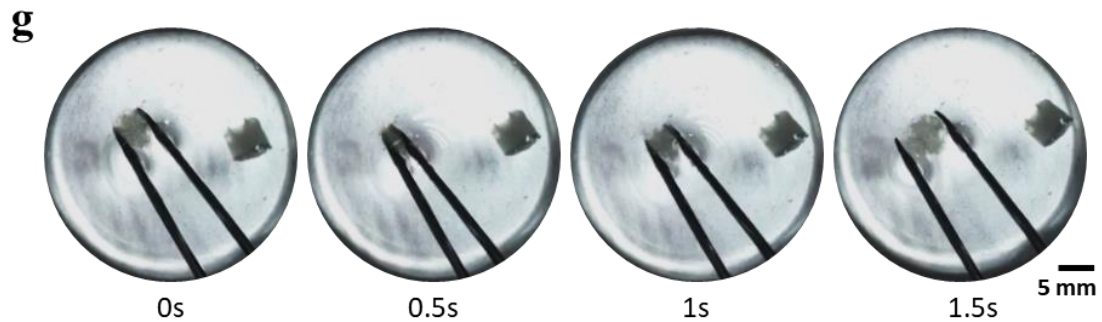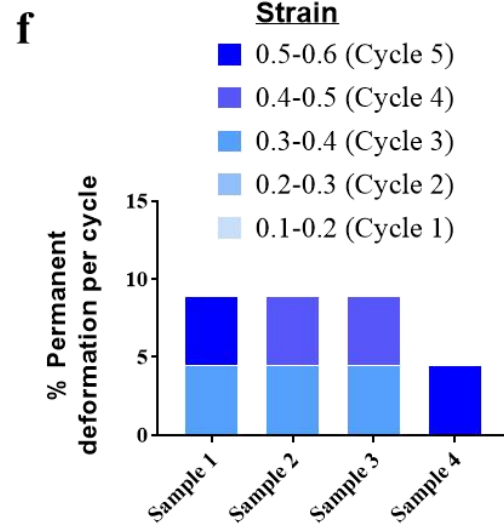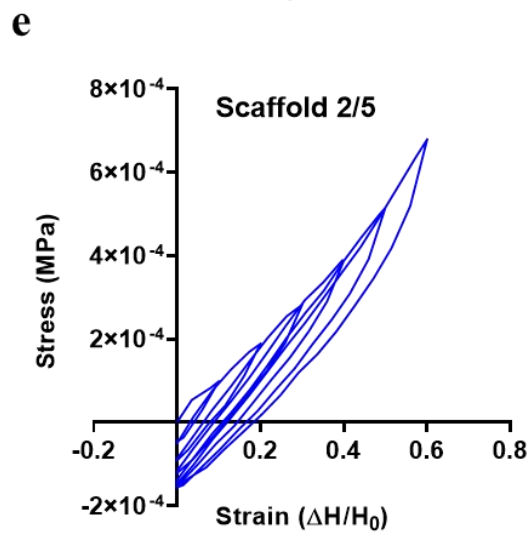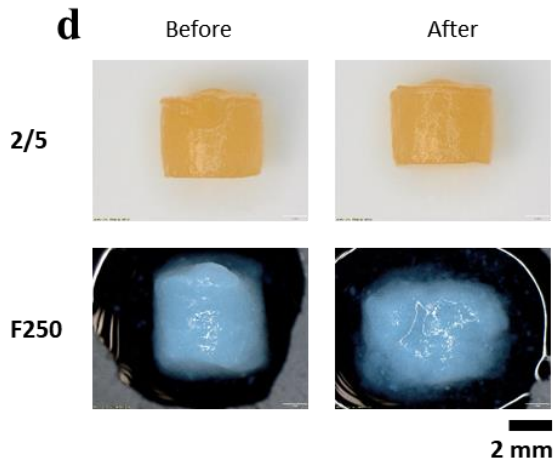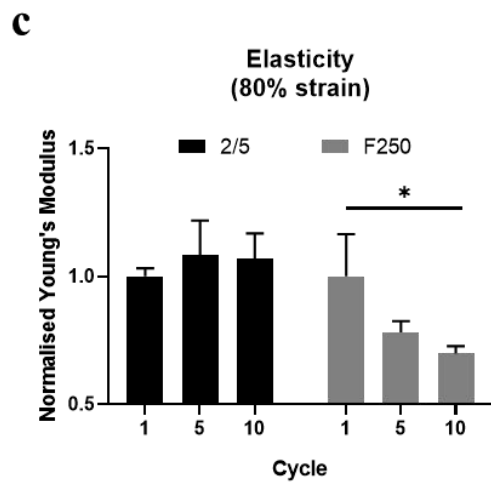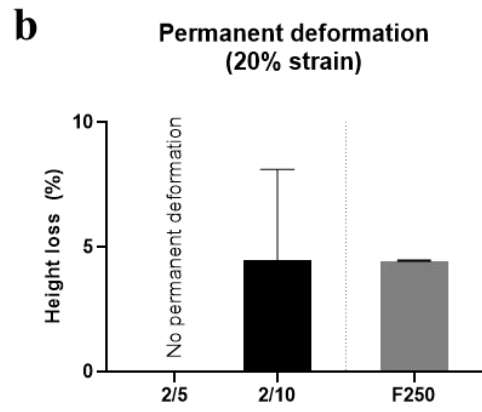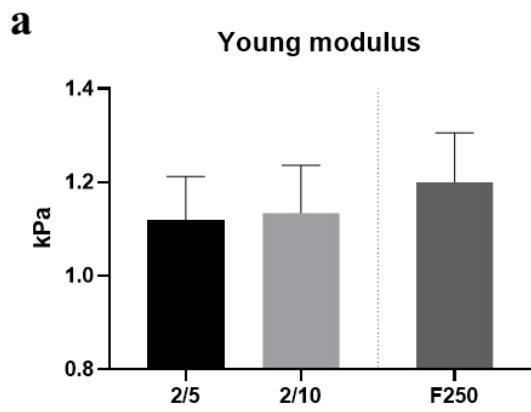
Figure 5-2*. Comparison of the mechanical properties of solubilised vs cryomilled AC ECM derived scaffolds.* ***a****, Young modulus (kPa) of two different solubilised AC ECM scaffolds and one cryomilled AC ECM scaffold: (i) 2% ECM crosslinked with 5 mM Glyoxal (2/5), (ii) 2% ECM crosslinked with 10 mM Glyoxal (2/10) and (iii) 250 mg(ww)/ml of fine cryomilled AC ECM scaffold crosslinked with EDAC (F250).* ***b****, Permanent deformation calculated from the height loss seeing after 20% compression of the material for the five groups.* ***c****, Comparison of the elasticity between 2/5 and F250 scaffolds after 10 cycles at 80% compression. Young modulus has been normalised to the first cycle young modulus of the corresponding scaffold.* ***d****, Macroscopic pictures of the 2/5 and F250 scaffolds after 10 cycles at 80% compression.* ***e****, Representative Stress Vs Strain curves of a 2/5 scaffold after cyclic compression test consisting of 6 compressive cycles with increasing strain amplitude of 10, 20, 30, 40, 50 and 60% in sequence at a rate of 2.22% strain per second.* ***f****, % Permanent deformation (height loss) per cycle of 2/5 scaffolds.* ***g****, Video frames of the super-elastic properties of a representative AC sECM derived scaffold sample in wet conditions (time-frame in seconds). (*P < 0.05; n=4). Nina Cassidy, Dr Dave Browe and Dr. Henrique Almeida were involved in the fabrication of the scaffolds for this analysis. All mechanical testing was performed on hydrated scaffolds.*

5.3.2. Increasing the ECM concentration of the scaffold increases the scaffold stiffness

In an attempt to increase the mechanical properties of the scaffolds, 2 different approached were taken: (i) increase glyoxal crosslinking from 5 to 10 mM and (ii) increase ECM concentration. As seen in the previous figure, scaffolds crosslinked with different glyoxal concentrations were shown to have a similar stiffness. In contrast, increasing ECM concentration had a significant effect on stiffness. Scaffolds with 2, 3, 4 and 6 % solubilised material were fabricated. SEM images show how increasing the ECM concentration significantly reduce the scaffold pore size (**Figure 5-3**a). In addition, prior to freeze-drying process, the increase of ECM concentration also increased the viscosity of the solution, with the 6 % material being difficult to pipette (data not shown). The diameter (theoretical 5 mm) and height (theoretical 3 mm) of the scaffolds were recorded, demonstrating that the scaffold fabrication process was reproducible when changing viscosity of the material (**Figure 5-3**b,c).

The Young modulus of the scaffolds was calculated from the slope of the strain vs stress curve at 20% strain. Increasing the ECM concentration had a significant effect on the scaffold stiffness, with the Young's modulus increasing with increases in ECM concentration (**Figure 5-3**d). In addition, mechanical testing after 7 compressive cycles of increasing strain amplitudes, demonstrated that scaffolds fabricated with higher ECM

concentration had less permanent deformation than scaffolds fabricated with lower ECM concentrations (**Figure 5-3**e).
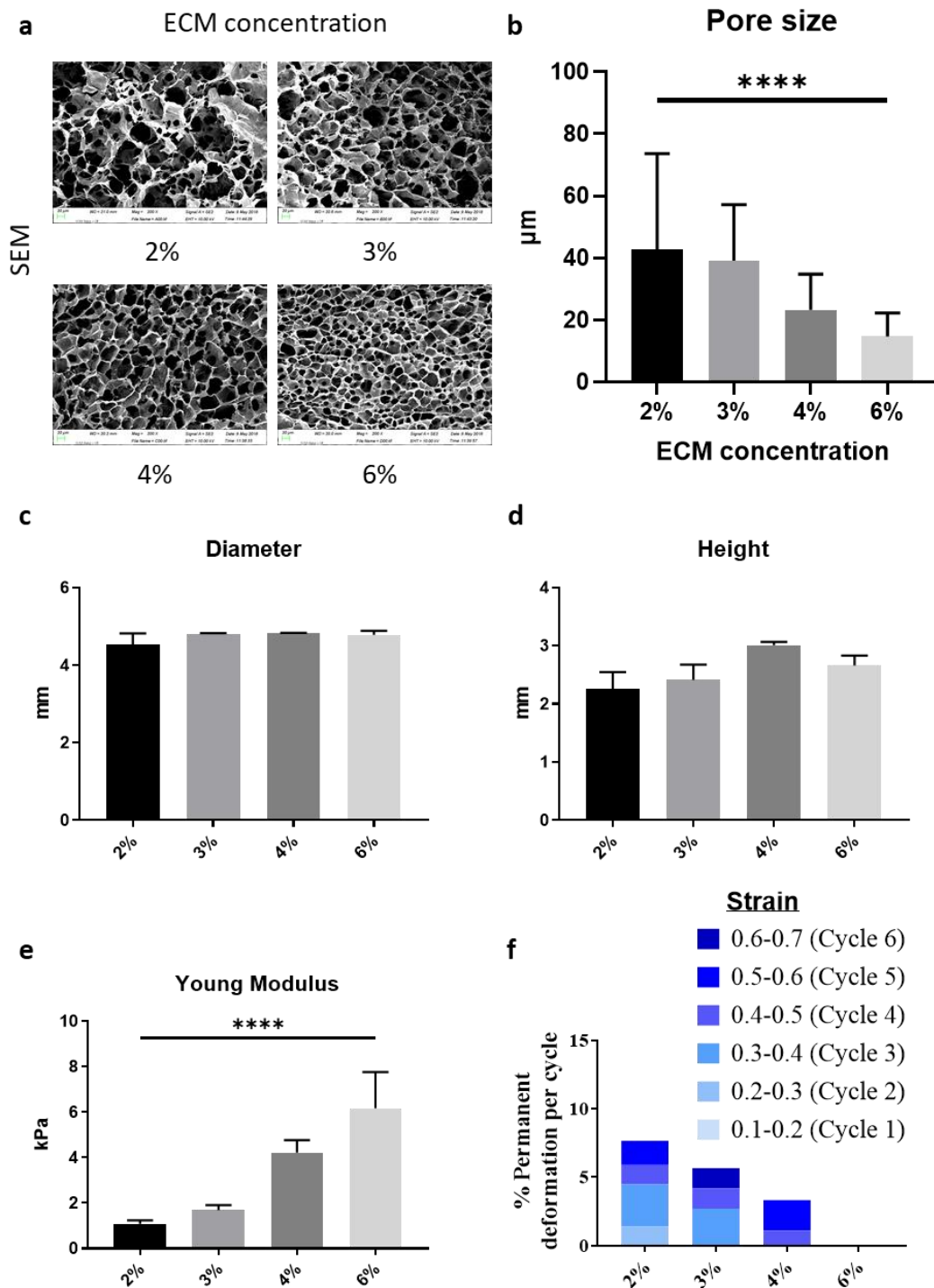
Figure 5-3. Comparison of the mechanical properties of scaffolds with different ECM concentration. a, Scanning electron microscopy images of scaffolds made with 2, 3, 4 and 6% and crosslinked with 5mM glyoxal. b, Quantification of the scaffold pore size in μm. c, Diameter of the scaffolds measured in mm. d, Height of the scaffolds calculated from the mechanical test plate distance in mm. e, Stiffness calculated from the young

5.3.3. Directional freeze-drying can be used to fabricate ECM derived scaffolds with an aligned architecture

Porous anisotropic structures of solubilised AC ECM can be produced by controlling the direction of heat transfer during the freezing step before freeze-drying (**Figure 5-4**). The Young's Modulus at 20% compressive strain (in the longitudinal direction) of acellular aligned scaffolds (2.27 ± 0.25 kPa) was significantly higher than the random scaffolds (0.97 ± 0.27 kPa), see **Figure 5-4**b. Both crosslinked scaffolds (random and aligned) possessed shape-memory characteristics (data not shown). Scanning electron microscopy (SEM) was used to characterize the morphology (size and alignment) and distribution of the channels/pores in both scaffold types (**Figure 5-4**c). The mean pore diameter for the random scaffolds was 54 ± 13 µm, while the mean pore/channel diameter for the aligned scaffolds was 44 ± 11 µm (**Figure 5-4**d). OrientationJ and directionality plugin were used to quantify degree of pore anisotropy (**Figure 5-4**e,f). There was no obvious preferred pore alignment in the scaffolds fabricated using the traditional mould (random scaffolds). Conversely, an aligned honeycomb-like pore architecture was observed in the scaffolds fabricated by directional freeze-drying (aligned scaffolds).
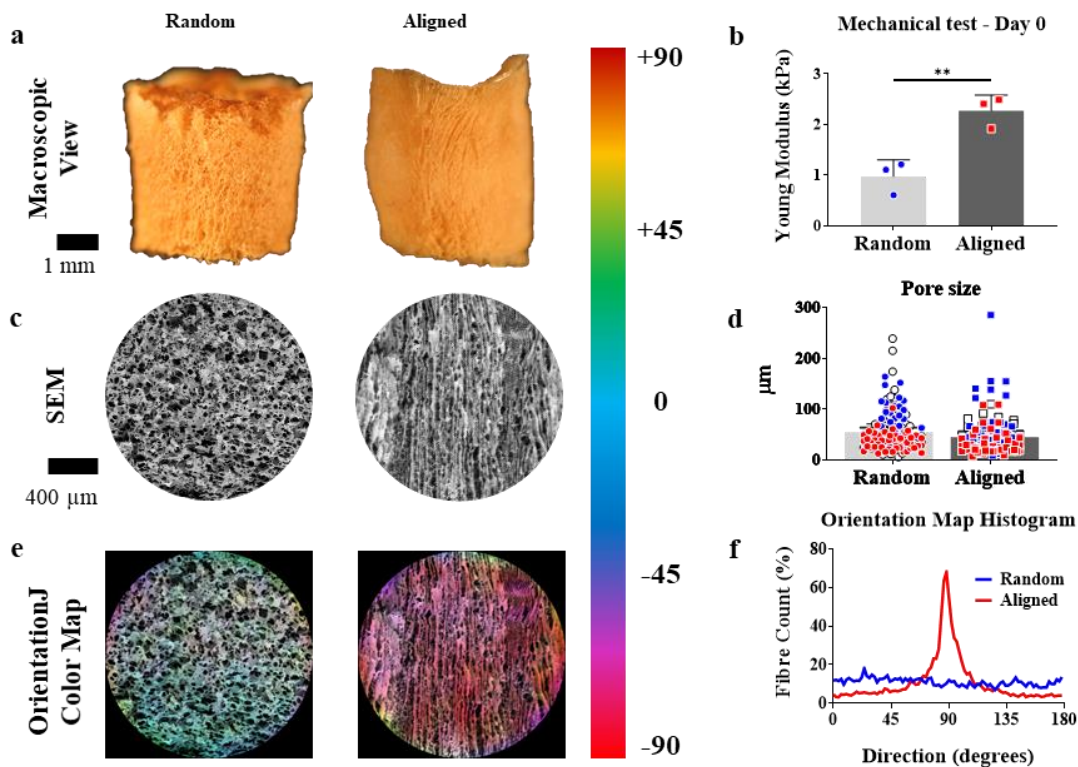
Figure 5-4. *Characterization of pore anisotropy in 20/5 scaffolds.* ***a****, Representative macroscopic images of the multidirectional (left) or directional (right) freeze-drying based scaffolds.* ***b****, Compression test (20% strain) of acellular ECM derived scaffolds with either isotropic pore architecture (random) or anisotropic pore architecture (aligned).* ***c****, Scanning electron microscopy images of the corresponding scaffolds showing random (left) or aligned (right) pores.* ***d****, Mean pore/channel diameter comparison between random and aligned scaffolds (columns represent the mean of 3 pooled samples, while dots corresponds 50 measurements from the 3 different samples in white, red and blue).* ***e****, Overlaying fibre orientation colour map showing the degree of anisotropy in the solubilized ECM derived scaffolds.* ***f****, Representative histogram curve of the orientation shown in the colour map images. **P < 0.001; n ≥ 3. All mechanical testing is performed on hydrated scaffolds.*

5.3.4. Controlling temperature during iterative freeze-casting can be used to fabricate bilayered ECM derived scaffolds with different anisotropies

In order to fabricate bilayered scaffolds, the material for the bottom layer is first casted into a mould. The material is then frozen following desired parameters. The anisotropy of the bottom layer can be controlled using the protocols discussed previously. Then the material for the top layer is added and frozen again. The anisotropy of the top layer can be controlled depending on the temperature of the bottom layer when the second

layer is added. As a result, three different scaffolds can be fabricated: (i) random bottom and top layers, (ii) random bottom and aligned top layer and (iii) aligned bottom and top layers (**Figure 5-5**).
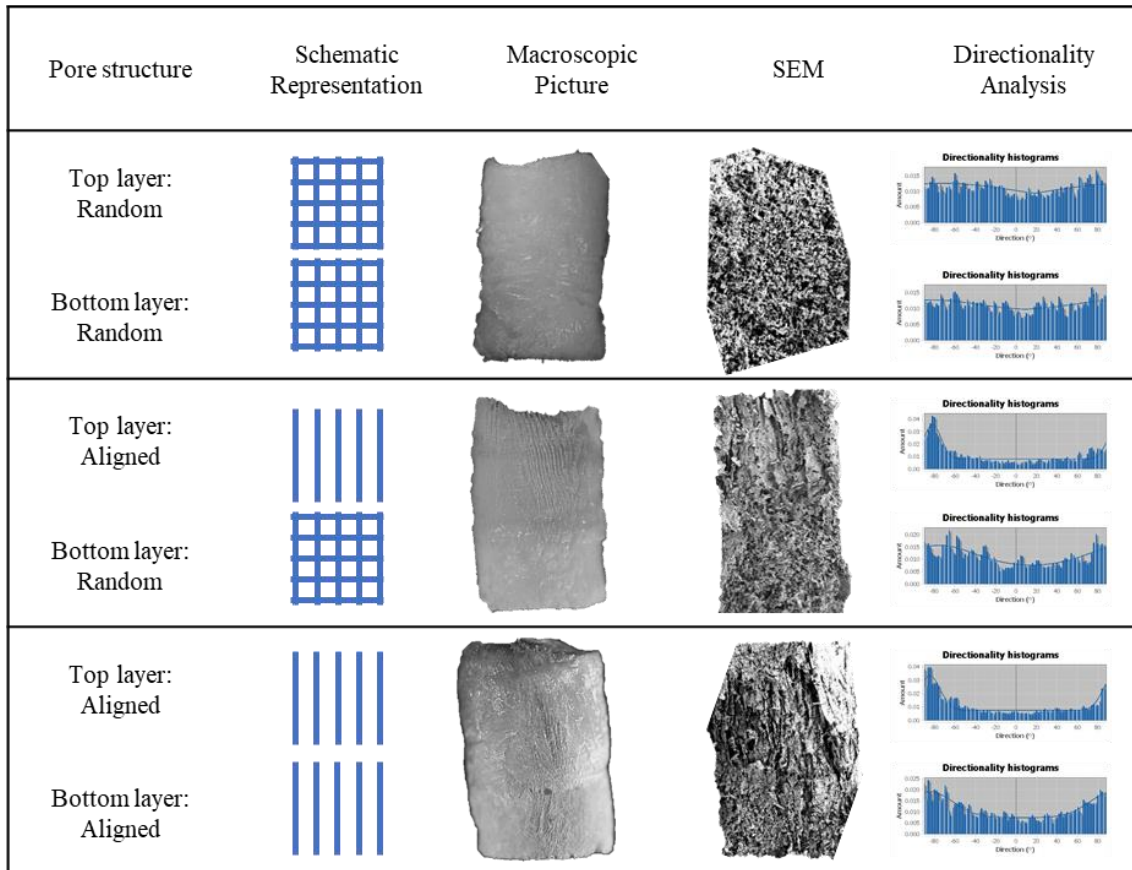
Figure 5-5. *Microarchitecture of bilayer scaffolds showing the pore anisotropy, schematic representation, macroscopic picture of the scaffold, scanning electron microscopy picture and representative histogram curves of the orientation calculated by directionality plugin from ImageJ.*

5.3.5. *Cell attachment/infiltration is enhanced in scaffolds with aligned pores*

Bone marrow derived MSCs were seeded on these scaffolds to evaluate cell viability and cell spreading after 7 days in culture. Similar levels of DNA were measured on both scaffolds at day 0 (**Figure 5-6**a), indicating a similar seeding efficiency for all groups. However, more cells (green, stained with calcein) were observed within scaffolds with aligned pores compared to scaffolds with random pores after 7 days of culture in

expansion media (**Figure 5-6**b). This trend was observed for both AC and GP sECM derived scaffolds (data only presented for AC), although in general more cells could be seen in sAC compared to sGP ECM derived scaffolds. Fewer cells were observed within the centre of the scaffold than on the outside. Cells aligning along the longitudinal axis of the scaffold fibres were observed in anisotropic scaffolds (**Figure 5-6**c,**d**). Low numbers of dead cells (labelled red) were observed in all groups.
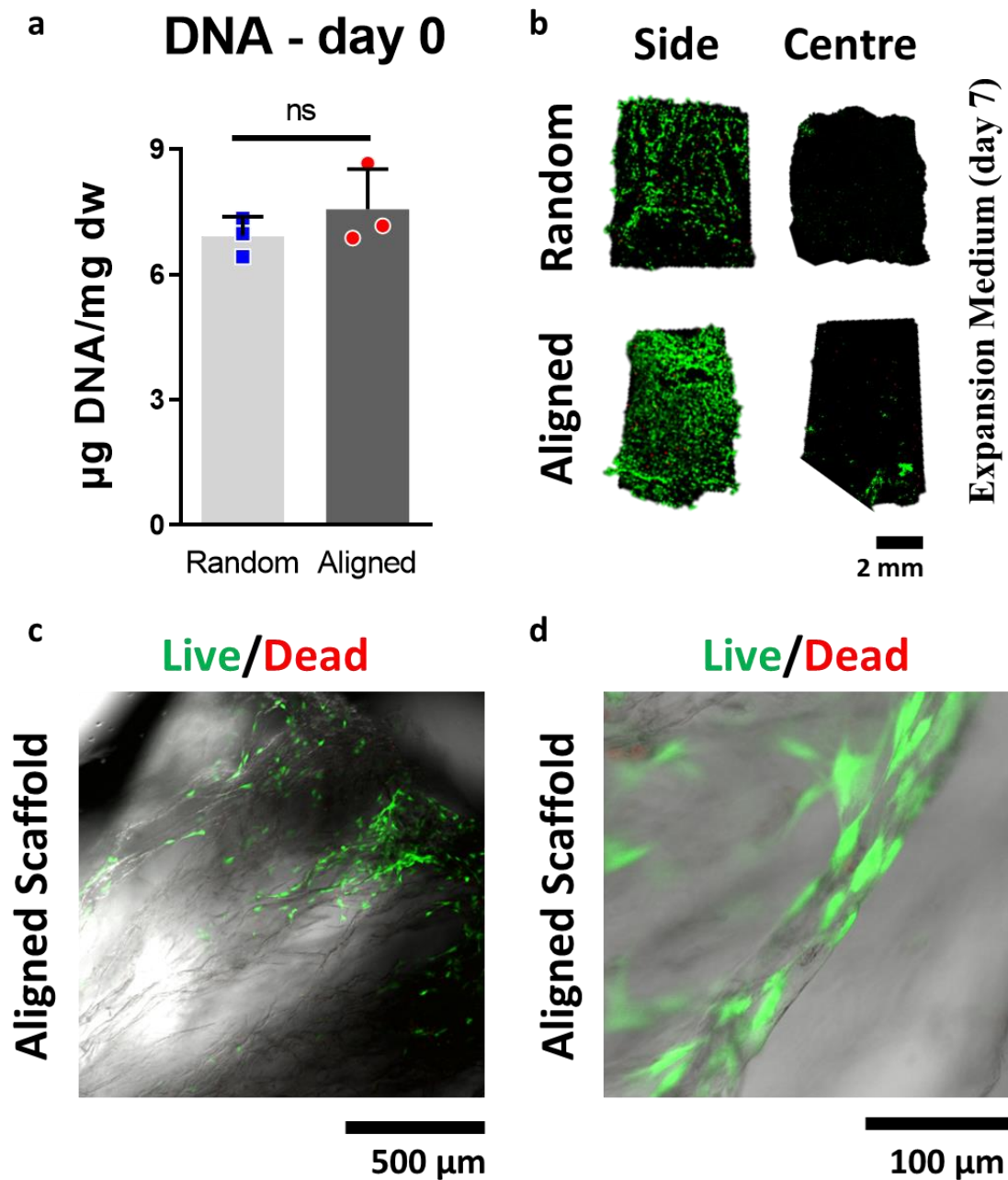
*Figure 5-6. Influence of scaffold microarchitecture on cell seeding. **a**, DNA levels of seeded MSCs solubilised articular cartilage (sAC) scaffolds with different microarchitectures, either random or aligned (n = 3). **b**, Live/dead confocal images performed after 7 days culture in expansion medium (n =2). **c and d,** higher magnification confocal images of the centre of an aligned scaffold from (**b**).*

5.3.6. *Annealing during freeze-drying can be used to tailor scaffold pore size and increase cell infiltration*

The pore size of solubilised ECM scaffolds can be tailored by adding an annealing step during the freeze-drying process. Scanning electron microscopy (SEM) and Image J were used to characterize the pore size in both scaffold types (without and with an annealing step). Scaffolds fabricated without an annealing step had smaller pores than the scaffolds fabricated with an annealing step. The mean pore diameter for the non-annealed scaffolds was 54 ± 13 µm, while the mean pore/channel diameter for the annealed scaffolds was 133 ± 40 µm (**Figure 5-7**a,c). There was no significant difference in stiffness between the two scaffolds (**Figure 5-7**d). Both scaffolds (non-annealed and annealed) kept the shape-memory characteristics previously mentioned.

Bone marrow derived MSCs were seeded on these scaffolds to evaluate cell viability and cell spreading after 7 days in culture. Immediately after cell seeding, the DNA levels were comparable in both scaffolds (Figure 7e), suggesting similar cell seeding efficiencies. Larger numbers of cells (green, stained with calcein) were observed in the middle of annealed scaffolds compared to non-annealed scaffolds after 7 days of culture in expansion media (**Figure 5-7**b). Low cell death was confirmed by the low number of cells staining positive for ethidium bromide homodimer (red cells).
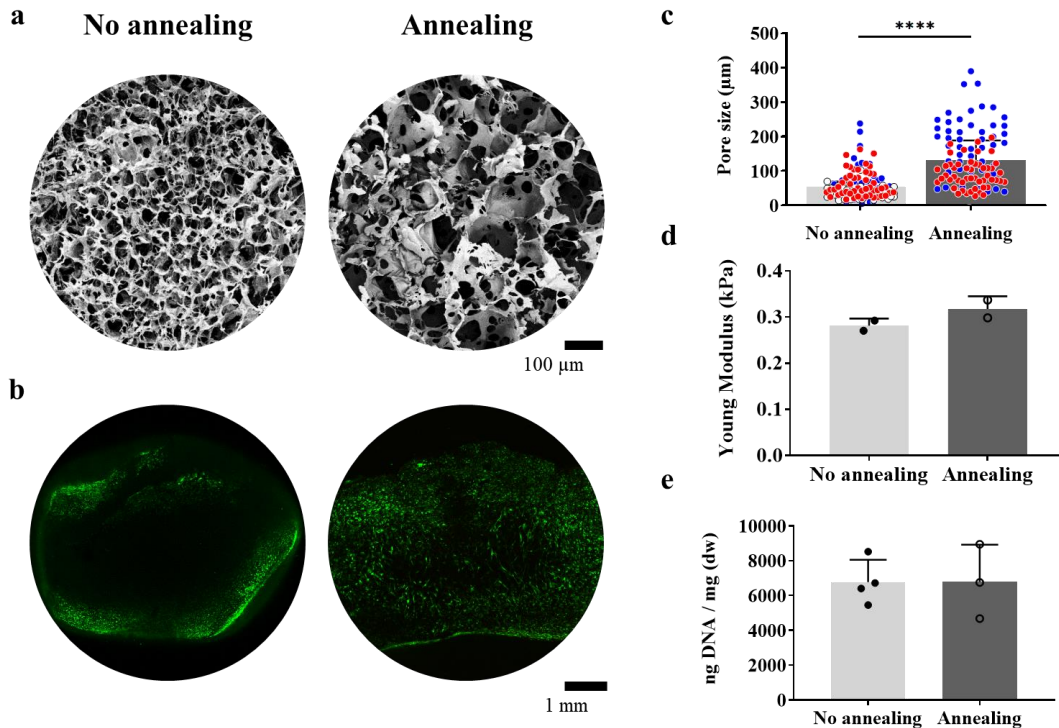
Figure 5-7. *Influence of annealing on scaffold pore size, stiffness and cell infiltration.* ***a****, Representative scanning electron microscopy images of the non-annealed scaffolds (left) and the annealed scaffolds (right).* ***b****, Live/dead confocal images of seeded MSCs on solubilised articular cartilage (sAC) scaffolds with different pore sizes (non-annealed and annealed), performed after 7 days culture in chondrogenic media.* ***c****, Mean pore/channel diameter comparison between random and aligned scaffolds (columns represent the mean of n ≥ 2 pooled samples, while dots corresponds 50 measurements from the n ≥ 2 different samples in white, red and blue; *P < 0.0001).* ***d****, Compression test of acellular non-annealed and annealed ECM derived (n = 2).* ***e****, DNA levels at day 0, post seeding. (n = 4).*

5.3.7. *Development of 3D printed synthetic reinforcements for ECM derived scaffolds*

While highly elastic, the compressive modulus of the ECM derived scaffolds was significantly lower than that of native cartilage and bone. To address this, this thesis aimed to mechanically reinforce the ECM scaffolds with PCL networks fabricated by fuse deposition modelling (FDM). Briefly, the solubilised ECM was poured onto a well in which the PCL reinforcement was placed, before freeze-drying to achieve the reinforced ECM derived scaffold (**Figure 5-8**). PCL reinforcement dramatically increased the Young's modulus of composite scaffolds (**Figure 5-8**b). Scanning electron microscopy (SEM) was used to characterize the material morphology and distribution of

140

the ECM within the PCL framework (**Figure 5-8**c). There were no obvious changes in the pore structure of the freeze-dried ECM scaffolds with the inclusion of PCL (**Figure 5-4**), and all PCL fibres seemed to be homogeneously covered by ECM. MSCs were seeded onto the PCL reinforced scaffolds and cultured in expansion media for 7 days. Confocal microscopy was used to assess biocompatibility and cell interaction with the PCL fibres (**Figure 5-8**d and e). The presence of PCL did not appear to have any negative effect on migration of MSCs through the scaffold or their viability after 7 days of culture.
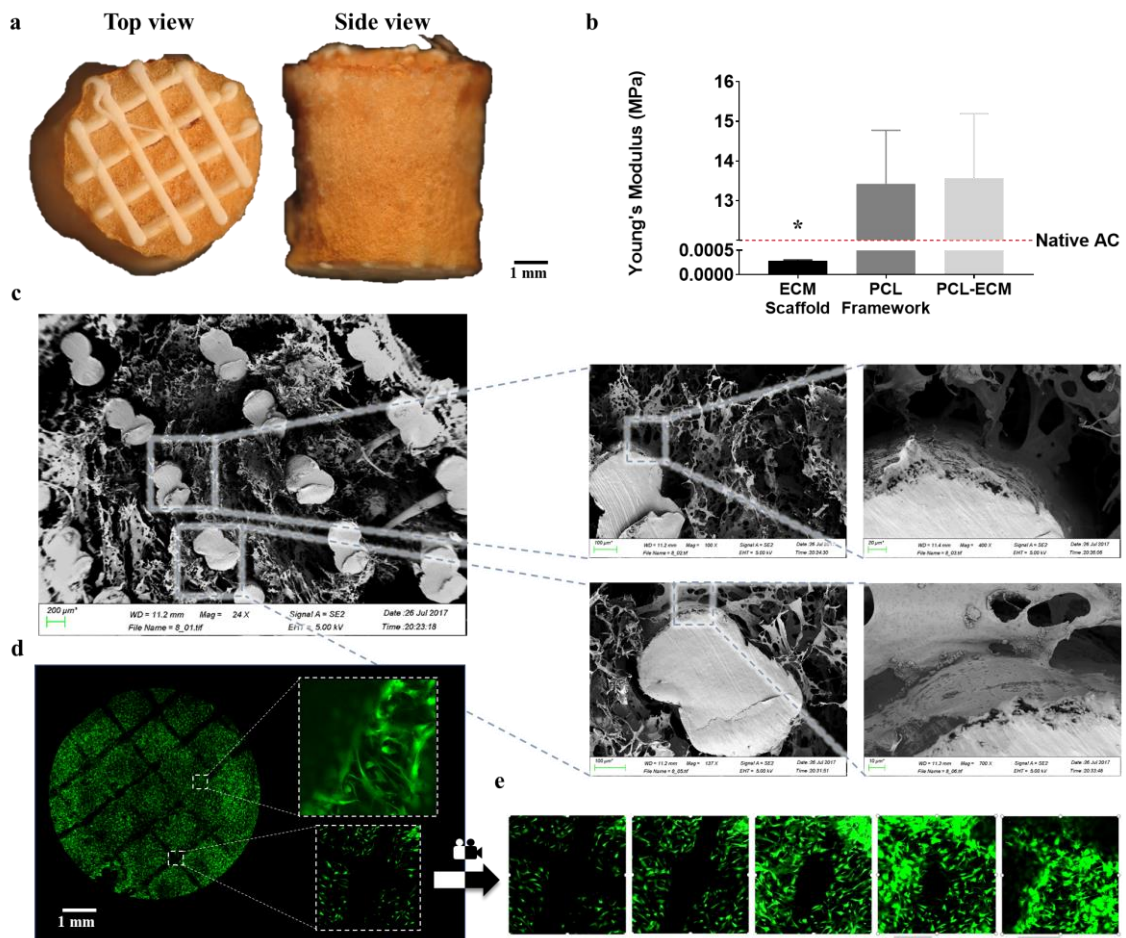
Figure 5-8. Synthetic reinforcement of ECM derived scaffolds. *a*, Top and side macroscopic views of the PCL reinforced AC ECM scaffold. *b*, Compression test of ECM derived scaffolds, PCL framework alone and the PCL reinforced ECM scaffold (*$P = 0.001$, $n \geq 3$). *c*, Scanning electron microscopy images of the inside of the acellular construct at different magnifications. *d*, Live/dead confocal images of seeded MSCs on the PCL reinforced scaffold, performed after 7 days culture in expansion media at different magnifications. *e*, Z-stack reconstructed confocal image of the 3D construct, showing the seeded MSCs surrounding one of the PCL fibres. PCL reinforcements were 3D printed by Pierluca Pittaco and mechanical testing was performed by Nicholas Betts.

5.4. Discussion and conclusion

Recapitulation of the native structure of AC has become one of the main challenges in joint regeneration. Thus, there are currently no tissue engineering strategies that consistently regenerate hyaline cartilage with structure, composition and biomechanics similar to native AC. New strategies, such as directional freeze-drying, 3D printing or electrospinning aim to address this problem by producing scaffolds with pre-defined architectures capable of directing the growth and organization of engineered tissues. Directional freeze-drying has been demonstrated to enable the manufacturing of tailorable anisotropic structures in lyophilised scaffolds. The aims of this chapter were (i) to characterise the mechanical properties of an AC ECM derived scaffold, (ii) to develop a directional freeze-drying protocol to fabricate ECM derived scaffolds with aligned pores mimicking aspects of the native cartilage structure, (iii) to optimise the fabrication of scaffolds with increased pore size to enhance cell infiltration and potential tissue deposition, and (iv) to design and 3D print a synthetic polymeric reinforcement for ECM derived scaffolds in order to increase their mechanical properties. The results of this chapter indicate that shape-memory scaffolds with a tailored pore size and anisotropic architecture can be used to enhance MSCs infiltration. Furthermore, 3D printed PCL reinforcements can be used to improve the mechanical properties of ECM derived scaffolds.

The concentrations of ECM and glyoxal were chosen based on preliminary basic optimization experiments, which examined cell infiltration and glyoxal toxicity[319]. Glyoxal was chosen as a cross-linker due to the fact that it results in relatively low levels of cytotoxicity when compared to other aldehyde crosslinkers[359]. Glyoxal cross-linking of the solubilized ECM produced elastic scaffolds exhibiting shape-memory properties. The solubilization process removed the majority of sGAGs from the ECM, leaving behind a collagen rich solution[319]. During the scaffold fabrication process, this solution is brought to neutral pH and 37 °C, leading to collagen fibril formation and gelation. Exposure to the dialdehyde glyoxal subsequently crosslinks this physical network by crosslinking free amine groups in the collagen[324–326,328]. A standard protocol for freeze drying then produces a porous network of collagen struts, displaying elastic properties at the macroscopic scale. Scaffolds not crosslinked with glyoxal dissolve upon rehydration, however stable glyoxal crosslinked hydrogels lack superelasticity. It is hypothesized that

during the freeze-casting before lyophilising, the glyoxal crosslinked collagen fibres are cryogelated, fixing the structure in a deformable shape-memory construct[360]. Previous mechanical tests on individual collagen fibrils has demonstrated that while they do not behave as homogenous materials, they commonly display linear behaviour, and can withstand tensile strains of up to 100% without fracturing[361,362]. The fibrils also exhibited time-dependent recoverable residual strains. Hence, the elastic behaviour of these ECM-derived scaffolds can be expected based on what is known about the mechanical properties of collagen itself. All scaffold variations demonstrated high elasticity when rehydrated with shape-memory properties.

A directional freeze-drying technique was used to fabricate ECM derived scaffolds with anisotropic pore geometry, improving the scaffold mechanical properties without compromising its shape-memory properties. Similar methodologies, used to design aligned architectures have been shown to produce stiffer scaffolds compared to those with uniform pores[182,210,351,363]. A further advantage of modifying pore architecture is that it can provide structural cues to resident cells, which in turn can facilitate the engineering of complex tissue/organs[212,364–366]. In the context of AC tissue engineering, such biomimetic approaches can potentially facilitate the engineering of cartilage tissues that recapitulate the native tissue architecture[367]. Introducing aligned pores was found to enhance cell infiltration into the scaffold. Moreover, the fabrication process allows for the assembly of different layers, with compositions and morphologies can be tailored for the tissue of interest. Whether such architectural cues enable the engineering of biomimetically organised AC will be further addressed in the next chapter of this thesis.

The addition of an annealing step during isotropic freeze-drying was used to control the pore size of ECM derived scaffolds. As expected, scaffolds with larger pore size enabled improved cell infiltration compared to smaller pores, without affecting the stiffness and shape-memory properties of the scaffolds. This is in agreement with previous studies showing that increasing pore size in collagen-gag scaffolds promotes greater cell infiltration 48 hours post seeding[215]. Here it was observed that such differences are maintained after 7 days of culture. This suggests that tissue deposition will potentially be more homogenous in scaffolds with bigger pores.

In their current iteration, the scaffolds should be capable of sustaining mechanically challenging environments due to their highly elastic properties but will not

initially contribute to load bearing until sufficient *de novo* tissue has formed. To improve the mechanical properties of these scaffolds (i.e. their stiffness), different approaches could be employed, such as increasing the ECM (material) concentration. However, this will lead to a decrease in pore size which in turn will limit cell infiltration. Another alternative is to reinforce the softer ECM derived scaffold with a stiffer material. It was possible to reinforce the ECM derived scaffold with PCL microfibres, thereby increasing the average stiffness of the composite construct without negatively impacting the porous nature of the ECM scaffold itself. This is in agreement with many studies in the literature, showing that the addition of synthetic polymers to "soft" biomaterials creates more robust constructs[129]. This improvement in mechanical properties could potentially provide a level of mechanical functionality, compatible with the loading environment of native tissues such as articular cartilage[367]. It should be clarified that no attempt was made to pre-treat the PCL before addition of the solubilised ECM. This may be a potential limitation when scaling up to higher constructs as PCL hydrophobicity may impede ECM distribution throughout the PCL framework. Preliminary work has been undertaken to pre-treat the PCL with NaOH as it is been shown to make its surface more hydrophilic[368,369]. Importantly, the capacity of the ECM scaffold to support cell infiltration was not compromised at the expense of the added PCL reinforcement. Indeed, the cells remained viable and were homogeneously distributed through the fibre reinforced ECM scaffold.

In conclusion, the freeze-casting conditions during freeze-drying are of critical importance to the design of biomimetic scaffolds as they enable the tailoring of pore morphology. Pore size and architecture regulate cell infiltration and morphology in ECM scaffolds and thus may play a major role in regulating new tissue deposition and organization. The next chapters of this thesis will assess the potential of such pore-tailorable scaffolds to modulate chondrogenesis and osteogenesis of MSCs, and ultimately their utility in engineering tissues that recapitulate the complex microarchitecture of articular cartilage.

6. CHAPTER: Effect of scaffold pore microarchitecture on MSC chondrogenesis and progression towards endochondral ossification

6.1. Introduction

Articular cartilage (AC) has a complex structure consisting of an arcade-like collagen fibre network that enables it to withstand the high loads passing through synovial joints[367]. Cartilage and osteochondral defect repair still remains a significant challenge[56,68], with current clinical approaches failing to recapitulate the native structure of AC. This motivates the development of novel tissue engineering strategies to recapitulate the complexity of such biological tissues. Recent studies have pointed to the importance of scaffold/biomaterial architecture in directing successful cartilage tissue engineering. For example, cellular and neo-matrix alignment within decellularized cartilage explants is influenced by the underlying collagen architecture of the decellularized tissue[206]. The architecture of porous scaffolds has been shown to influence multiple factors that are integral to successful tissue engineering such as cell infiltration[195], matrix deposition[37], scaffold mechanical properties[211] and the transport of nutrients and waste products into and out of the scaffold[196]. The role of scaffold pore architecture in engineering phenotypically stable AC that mimics the complex organization of the native tissue remains poorly understood.

Previous research has demonstrated that anisotropic fibres can guide the morphology, orientation and phenotype of cells, such that the resulting engineered tissue emulated certain features of native cartilage[370,371]. In spite of these developments, it is still unclear whether such scaffolds can continue to direct neo-tissue organization after long periods of culture[210,365], or more importantly *in vivo* after their implantation into orthotopic defects[195,196]; thus, fundamental questions on the role of biomimetic scaffold architectures for hyaline cartilage tissue engineering remains unanswered. In this chapter, it was hypothesized that, once the pore size had been optimised to overcome differences in cell infiltration between random and aligned porous scaffolds, that pore alignment would still play a role in determining the phenotype of the resulting tissue.

The first aim of this chapter was to determine the effect of pore morphology within AC ECM derived scaffold on chondrogenesis of MSCs. The specific goals were (i) to study the effect of pore size on cell distribution and cartilage matrix deposition, (ii) to analyse the effect of pore anisotropy on chondrogenesis and on recapitulating aspects of the microarchitecture of articular cartilage, and (iii) to assess cartilage matrix deposition within ECM derived scaffolds mechanically reinforced with a 3D printed PCL network.

The second aim of this chapter was (iv) to develop an aligned bilayered scaffold suitable for osteochondral tissue repair. Two different ECM derived materials, articular cartilage and bone ECM, previously used in our lab due to their chondrogenic[30,319] and osteogenic[318] potential, were used to fabricate the bilayered ECM derived scaffold. It was hypothesized that the different biological cues contained within each ECM in combination with the tailored pore size and shape would modulate chondrogenic or osteogenic[366] behaviour of the material *in vitro* and *in vivo* during the repair of an osteochondral defect within a caprine model. Two different media conditions were employed to evaluate cellular behaviour within the bi-layered scaffolds *in vitro*: chondrogenic medium with TGF-β3 as a potent chondrogenic factor and osteogenic medium with β-glycerophosphate as an osteogenic stimulatory factor. The chondrogenic behaviour was assessed using the chondrogenic markers[56] sGAG and type II collagen. The osteogenic behaviour was evaluated based on the mineralization of the scaffold and production of collagen type I and X[372].

6.2. Methods

Note: all material obtained from Sigma-Aldrich® unless stated.

6.2.1. AC ECM Scaffold fabrication

Solubilised ECM derived scaffolds were fabricated as described above in the previous chapter. Briefly, collagenous material was mixed to a final concentration of 20 mg/ml in 0.5 M acetic acid with phenol red chemically modified media (CDM). CDM was used as pH visual control so as to be able to neutralize the collagenous mixture with

small volumes of 0.1 M NaOH. Then, the solution was partially crosslinked with 5 mM glyoxal. The solution was transferred to custom-made moulds, placed in the oven at 37 ºC and allow to crosslink for 30 min. Two different moulds and four different freeze-drying protocols were used to fabricate the scaffolds with tailored pore morphology: (i) random standard, (ii) random annealed, (iii) aligned standard, (iv) novel aligned annealed (**Figure 5-4**a,b).

<u>Random standard</u>

1) -30 °C (1 °C/min) hold for 1 h; atm pressure
2) -10 °C (1 °C/min) hold 20 h; 0.200 mbar
3) +25 °C (1 °C/min) hold 2 h; 0.200 mbar

<u>Random annealed</u>

1) -30 °C (1 °C/min) hold for 1 h; atm pressure
2) -10 °C (5 °C/min) hold for 3 h; atm pressure
3) -30 °C (1 °C/min) hold for 1 h; atm pressure
4) -10 °C (1 °C/min) hold 20 h; 0.200 mbar
5) +25 °C (1 °C/min) hold 2 h; 0.200 mbar
6)

<u>Aligned standard</u>

1) -190 (Liquid N_2) hold for 2 min; atm pressure
2) +25 °C hold for 10 min; atm pressure
3) -30 °C hold for 1 h; atm pressure
4) -10 °C (1 °C/min) hold 20 h; 0.200 mbar
5) +25 °C (1 °C/min) hold 2 h; 0.200 mbar

<u>Aligned annealed (novel)</u>

1) -190 (Liquid N_2) hold for 2 min; atm pressure
2) +25 °C hold for 10 min; atm pressure
3) -10 °C hold for 3 h; atm pressure
4) -30 °C (1 °C/min) hold for 1 h; atm pressure
5) -10 °C (1 °C/min) hold 20 h; 0.200 mbar
6) +25 °C (1 °C/min) hold 2 h; 0.200 mbar

After freeze-drying, the scaffolds then underwent dehydrothermal (DHT) crosslinking in a vacuum oven (VD23, Binder, Germany), at 115 °C, in 2 mbar for 24 hr.
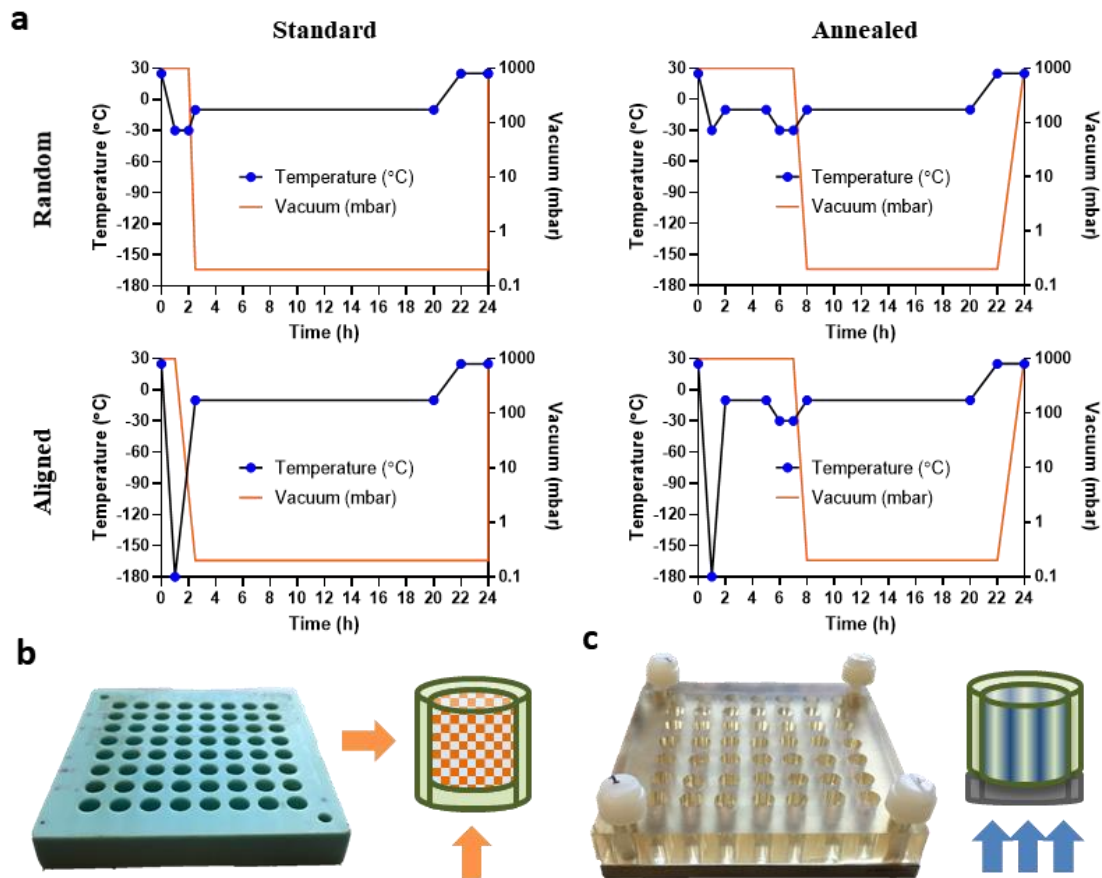
Figure 6-1. Development of novel combined treatments to tailor pore morphology: size and shape. *a,* Graphical output of the temperature and vacuum levels during 4 different freeze-drying (FD) protocols: (i) random standard, (ii) random annealed, (iii) aligned standard, (iv) aligned annealed. *b,* Tufset polypropylene mould used for the fabrication of scaffolds with random pore shape (left) and the main heat transfer directions that affect the moul (right). *c,* Silicon (wells) and metal (base) mould used for aligned pores (left) and main heat transfer direction that affects the mould (right).

6.2.2. Bilayered (AC:BN) ECM Scaffold fabrication

Tissue-specific bilayer scaffolds were made with two distinct layers of solubilised ECM materials: articular cartilage (AC) and bone (BN). Fabrication method was adapted from protocol described above. Briefly, AC ECM and BN ECM slurries were made to a final concentration of 2% in 0.5 M acetic acid with phenol red chemically modified media (CDM). CDM was used as pH visual control so as to be able to neutralize the collagenous

mixture with small volumes of 0.1 M NaOH. Then, the solution was partially crosslinked with 5 mM glyoxal at 37 ℃ for 30 min. The BN ECM slurry was poured onto the mould allowing unidirectional heat transfer (metal base + silicon wells) and frozen for 2 min with liquid nitrogen. Then, the AC ECM slurry was poured on top and allowed to equilibrate for 10 min. The mould was then placed in the freeze-drier and the aligned annealed protocol was further followed. After freeze-drying, the scaffolds then underwent dehydrothermal (DHT) crosslinking in a vacuum oven (VD23, Binder, Germany), at 115 °C, in 2 mbar for 24 hr.

6.2.3. 3D printing of a synthetic polymeric reinforcement framework

PCL framework were fabricated using the 3D Discovery multi-head bioprinting system purchased from Regen Hu, Switzerland. The 3D Discovery was set up to allow the deposition of melted PCL (Sigma, Mn 45 000), which was melted at 60° and 3D printed in strands at a pressure of 0.5 MPa with a 25 Gauge needle (0.260 mm nominal inner diameter). Layer thickness was set up at 0.2 mm to allow a fusion between consecutive layers. The feed rate was set up at 4 mm/s.

The solubilised ECM was poured onto the 3D printed PCL framework and casted into a mould before freeze-drying (FD). The samples were subjected to FD method 4: directional freezing and -10 ℃ for 3 h treatment to obtain aligned annealed pores.

6.2.4. Pore morphology characterization

Pore size: Scanning electron microscope images of the freeze-dried scaffolds were used to quantify pore size using Fiji (Fiji Is Just ImageJ).

Alignment: Macroscopic images of the freeze-dried scaffolds were taken after DHT crosslinking to assess level of pore anisotropy. 'OrientationJ' and 'Directionality' plugins, from Fiji, were used to create the colour maps of the pore orientation and to generate data to plot the direction curves, respectively. An extended version of the protocol can be found in CHAPTER - APENDIX: 10.3.

6.2.5. Cell culture

Bone marrow stem cells (MSCs) were harvested and seeded at a density of 500,000 cells per scaffold (1,000,000 MSCs per bilayer scaffold), as described in previous chapter. Before supplementing the media, the cells were allowed to attach to the scaffolds for 2 hrs in the incubator at 37 ºC.

To assess cell infiltration, the constructs were kept for 7 days in normoxic conditions (20% O_2 and 5% CO_2) at 37 ºC supplemented with 5 ml of expansion media: DMEM + GlutaMAX^{TM}, 10% fetal bovine serum (Gibco®), 100 units/ml Penicillin, 100 units/ml Streptomycin (Gibco®) and 0.25µg/ml amphotericin B.

To assess cell differentiation and tissue deposition, the constructs were cultured in 3 ml of either **(i) chondrogenic media**: Dulbecco's modified Eagle's medium (DMEM) + GlutaMAX^{TM} (Gibco®), 1 mM sodium pyruvate, 350 µM L-proline, 1.5 mg/ml bovine serum albumin (BSA), 1 nM dexamethasone, 300 µM ascorbic acid, 17 µM linolenic acid, 10 ng/ml transforming growth factor β3 (TGF-β3, R&D Systems®), 1X insulin-transferrin-selenium; or **(ii) osteogenic media**: DMEM + GlutaMAX^{TM}, 10% fetal bovine serum (Gibco®), 10 mM β-glycerophosphate, 1 nM dexamethasone, 0.09 mM ascorbic acid. All media were supplemented with 100 units/ml Penicillin, 100 units/ml Streptomycin (Gibco®) and 0.25 µg/ml amphotericin B.

6.2.6. Biochemical analysis

The engineered constructs were biochemically analysed as described in previous chapter. Briefly, samples at day 0 (after cell seeding) and day 28 for DNA, sulphated GAG (sGAG), collagen content and calcium deposition (3 scaffolds at each time point). On removal from culture, samples were freeze-dried and dry masses of the samples were recorded. All samples were subsequently frozen at -85 ºC for later analysis. The scaffolds were either enzymatically digested by incubating the constructs in 125 µg/ml papain, 0.1 M sodium acetate, 5 mM cysteine HCl, 0.05 M ethylendiaminetetraacetic, ph 6.0 at 60 ºC under rotation (10 rpm) for 18 hr for DNA, sGAG and collagen analysis or chemically digested by incubating the constructs in 1M HCl at 60 ºC under rotation (10 rpm) for 18 hr for calcium analysis. The DNA content was estimated by Bisbencimide Hoechst assay. The proteoglycan content was estimated by quantifying the sGAG in the scaffolds using the dimethylmethylene blue dye-binding assay (Blyscan, Biocolor Ltd, Northern Ireland),

using bovine chondroitin sulphate as standard. Collagen content was indirectly determined by measuring the hydroxyproline content after acidic hydrolysis of the samples at 110 ℃ for 18 hr in 38% HCl. Samples were assayed using a cholarime-T assay, assuming a hydroxyproline/collagen content ratio of 1:7.69[330]. Calcium content was determined using the o-cresolphthalein complexone (oCPC) method where a violet colored complex is formed between calcium ions reacting with oCPC[331] (Sentinel Diagnostics).

6.2.7. Histological analysis

The engineered constructs were processed for histology analysis as described in previous chapter. Briefly, at each time point (0 and 28 days) ECM derived constructs (2 scaffolds at each time point) were fixed overnight at 4 ℃ in a 4% paraformaldehyde solution. After being washed in PBS, the samples were dehydrated in serial increasing gradient alcohol solutions and xylenes and finally embedded in paraffin. The wax-embedded constructs were sectioned (6 μm slices) and mounted onto microscope slides. Sections were rehydrated and stained with 1% alcian blue 8GX in 0.1 M HCl for sGAG, with picrosirius red for collagen, with alizarin red for calcium.

Immunohistochemical analysis was performed on 6 μm sections made with a microtome. Samples were first rehydrated by dipping three times in xylenes for 5 min (to remove the wax), in 100% alcohol 3 times for 1 min and in running tap water for 5 min. Then the samples were washed in PBS for 5 min before treating them with 0.5 mg/ml pronase at 37 ℃ for 5 min as the antigen retrieval method, washed with PBS for 5 min and then treated with 3% H_2O_2 at room temperature (RT) for 20 min to block endoperoxide activity. After rinsing with PBS for 5 min, the slides were blocked with 10% goat serum at RT for 1 hr and incubated with the primary antibody at 4 ℃ overnight. See table below for antibody information. The next day incubation with the secondary antibody was performed, at RT for 1 h. By using VectastainABC reagent (VectastainABC kit, Vector Laboratories©, UK) for 5 min in peroxidase DAB substrate kit (Vector laboratories, UK), it was possible to observe a colour alteration. Samples were dehydrated with graded ethanol and xylenes and mounted with Vectamount medium (Vector Laboratories©, UK), which is an optically clear and odourless solution for permanently preserving histochemical stains.

Table 6-1. *List of antigens, primary and secondary antibodies used for immunohistochemistry analysis, including working dilutions for each antibody and catalogue number.*

Antigen	Primary antibody	Secondary antibody
Collagen type I	1:400, mouse monoclonal IgG ab90395 (Abcam®, UK)	1:200, anti-mouse IgG B7151 (Sigma)
Collagen type II	1:100, mouse monoclonal IgG ab3092 (Abcam®, UK)	1:200, anti-mouse IgG B7151 (Sigma)
Collagen type X	1:100, mouse monoclonal IgM ab49945 (Abcam®, UK)	1:200, anti-mouse IgM ab49760 (Abcam®, UK)

6.2.8. Polarised light microscopy

Picro-sirius red stained samples were imaged under polarized light microscopy to investigate collagen fiber orientation. PLM images were further analysed with Image J Directionality and Orientation J plugins to characterise the degree of orientation. An extended version of the protocol can be found in CHAPTER - APENDIX: 10.4.

6.2.9. PCR analysis

RT-PCR was performed using a similar protocol to those previously described[332]. TRI Reagent® (Sigma) was used to lyse the cells. Briefly, 1 ml of Trizol was added to each construct in RNAse-free tubes before snap-freezing it in liquid nitrogen and stored at -80 ℃ until further use. When ready to be used, the solution was placed on ice to allow it to thaw slowly. While thawing, samples were homogenised (IKAT10, IKA® Works Inc., NC, USA) for 2 min. mRNA was extracted according to the manufacturer's protocol. Briefly, 200µl of chloroform were added to each tube and centrifuged at 12,000g at 4°C. RNA located in the upper phase was transferred to a new RNAse free tube, isopropanol was added at the same volume as well as 4µl glycoblue to allow visualisation of the RNA in the following steps. The tubes were stored at -20°C overnight and again placed on ice to allow the solution to thaw and centrifuged at 12,000g at 4°C for 15 min. A visible blue RNA pellet was formed, supernatant was discarded, and the tubes dried. 1ml of 70% ethanol (in RNAse free water) was added to wash the pellet. Another centrifugation step was performed at 12,000g at 4°C for 15 min, ethanol was

removed and the pellet air dried. RNAse free water (30 µl) was used to dissolve the pellet. A NanoDrop-1000 spectrophotometer (Thermo Fisher Scientific) was used to quantify RNA yield. Sample purity was checked via 260/280 (>1.8) absorbance ratio. Transcription of mRNA to cDNA was performed using a high capacity cDNA reverse transcription kit (Invitrogen). A mastermix was added to 500 ng of RNA and placed in a thermocycler. The following temperature sequence was applied: 10 min at 25 °C, 2 hrs at 37 °C, 5 min at 85 °C, 1 min at 4 °C. cDNA was quantified using Qubit ssDNA assay kit (Q10212 – Life Technologies) following manufacture's instructions. Then, quantitative polymerase chain reaction (qPCR) was prepared for all samples (~30 ng cDNA) using SYBR Select Master Mix with ROX passive dye (Applied Biosystems, 4472920). The expression of glyceraldehyde 3-phosphate dehydrogenase (GAPDH), sex-determining region Y-related high mobility group-box 9 (SOX9), collagen type II (COL2), runt-related transcription factor 2 (RUNX2), matrix metalloproteinase 13 (MMP13) and collagen type X (COL10) were quantified using primers detailed below. The amplification was performed with the ABI 7500 Fast Real-time PCR machine (Applied Biosystems). All samples were run in duplicate ($n \geq 4$). The relative quantity of each sample was calculated with reference to GAPDH (RPL4 was assessed as potential house-keeping gene but was not considered stable enough for the current experimental set up) and expressed as fold change normalized to the control group ($\Delta\Delta$Ct method).

Table 6-2. *Forward and reverse primers used in qPCR for each gene and its associated role (Sigma).*

Function	Gene	Forward primer (5'-)	Reverse primer (5'-)
House-keeping	GAPDH	TTTAACTCTGGAAAGTGG	GAACATGTAGACCATGTAGTG
House-keeping	RPL4	GTAACTACAATCTTCCCATGC	GGTCTTTGCATATGGGTTTAG
Chondrogenesis	SOX9	CAGACCTTGAGGAGACTTAG	GTTCGAGTTGCCTTTAGTG
Chondrogenesis	COL2	CGACGACATAATCTGTGAAG	TCCTTTGGGTCCTACAATATC
Hypertrophy	RUNX2	CCAACAGAGGCATTTAAGG	CCAAAAGAAGTTTTGCTGAC
Hypertrophy	MMP13	GACCAAATTATGGAGGAGATG	AAACAAGTTGTAGCCTTTGG
Hypertrophy	COL10	CCAACATCCAGAATCCATC	GTAGGTGTTTGGTATTGCTC

6.2.10. *Osteochondral caprine model*

Surgical procedure in caprine model was carried out as previously described[32,373]. Briefly, the goats were sedated using diazepam (0.3-0 .4 mg/kg IV) and butorphanol (0.2 mg/kg IV). Epidural was administered using morphine (0.2 mg/kg). Following placement of an intravenous catheter, anesthesia was induced with propofol (maximum dose 4 mg/kg IV). Anesthesia was maintained using isoflurane with ventilation to maintain normal end tidal CO_2 between 4.6 and 6 kPa. Isotonic fluids were provided at 10 ml/kg/h. Following induction of anesthesia, the goats were placed in dorsal recumbency and an arthrotomy of each stifle joint was then performed using the lateral para-patellar approach. A critically-sized defect, 6 mm in diameter x 6 mm in depth, was created in each medial femoral trochlear ridge using a hand drill, a flattened drill bit and a depth guide. The joint was flushed with saline fluids (0.9 % NaCl) and the stifle joints were assigned to one of the two treatment groups: 1) Empty control and 2) AC-BN ECM derived bilayered scaffold. The bilayered scaffold was press fit into the defect site cell-free before routine closure of the joint capsule, subcutaneous tissues and skin. Morphine (0.1-0.2 mg/kg IM) and non-steroidal anti-inflammatory drugs [Carprofen (1.5-2.5 mg/kg subcutaneously) (Rimadyl)] were administered at the end of anesthesia. Following surgery, goats were housed in small indoor pens to allow skin incisions to heal and were allowed full weight bearing immediately. During this period the animals were closely monitored to ensure adequate analgesia. Carprofen and antibiotics [Amoxicillin (Noroclav)] were administered for 5 days post-surgery. Two weeks post-operatively, following removal of sutures, animals were let out to pasture for the remainder of the study period. Euthanasia was carried out with an overdose of sodium pentobarbital (Euthatal) administered by IV injection after 6 months post-implantation (n = 8) to permit harvesting of the treated joints. Ethical evaluation and approval were administered by

University College Dublin (AREC-18-17) and the Health Products Regulatory Authority (AE18982/P142).

6.2.11. *Repair tissue evaluation*

Macroscopic evaluation of the joints was performed immediately upon opening the joint (**Table 6-3**)[373]. 1.5 cm^3 sections containing the defect site were harvested, samples were fixed in a formalin solution and the levels of mineralization within the repair tissue (5 mm diameter cylindrical region) was quantified using µCT (Scanco Medical, Switzerland) at a threshold of 210, corresponding to a density of 399.5 mg hydroxyapatite/cm^3. Two regions of interest for calculating bone density (bone volume per total volume) were defined as follow: The subarticular spongiosa (SAS) defined as the bottom 3mm of the bony region of the defect) and the subchondral bone plate (SBP) defined as the upper 1mm of the bony region of the defect. For ongoing histological evaluation, two protocols have been developed to analyze the quality of the repaired tissue of the osteochondral defects[32]. Extended versions of these protocols can be found in CHAPTER - APENDIX: 10.4 and 10.6.

Table 6-3. *Macroscopic scoring system for cartilage repair. Maximum score possible is 12.*

Characteristic for macroscopic scoring	Grading	Score
Edge integration (new tissue relative to native cartilage)	Full	2
	Partial	1
	None	0
Smoothness of the cartilage surface	Smooth	2
	Intermediate	1
	Rough	0
Cartilage surface degree	Flush	2
	Slight depression	1
	Depressed/overgrown	0
Color of cartilage	Opaque	2
	Translucent	1
	Transparent	0
Percentage filling	80 – 100 %	4
	60 – 80 %	3
	40 – 60 %	2
	20 – 40 %	1
	0 – 20 %	0

6.2.12. Statistical analysis

Results are presented as mean ± standard deviation. Graphical results and statistical analysis were performed with GraphPad Prism 5.01 software. Experimental groups were analysed for significant differences using a general linear model for analysis of variance (ANOVA) with factors including different ECM materials and culture conditions. Tukey's multiple comparison test was used to compare different conditions (media *vs.* material). Significance was accepted at a level of $p < 0.05$. GraphPad was also used to calculate outlier datapoints. A significance level of 0.01 was used to determine the removal of a data point.

6.3. Results

6.3.1. Larger pores allow for enhanced cell infiltration and homogenous tissue deposition

AC ECM derived scaffolds were fabricated using either the standard FD process (small pores ~ 63 µm) or with the annealing process (large pores ~ 173 µm) (**Figure 6-2**b). After cell seeding, cell infiltration was more noticeable in the scaffold with larger pores. Histological analysis at day 0 showed all nuclear red stained cells agglomerating along the perimeter of the scaffold with small pores, while there was greater cell infiltration into the centre of the scaffolds with the larger pores (**Figure 6-2**c). Confocal images, after 7 days of culture, demonstrated more green cells (stained with calcein) in the centre of the scaffolds with large pores than in the scaffolds with smaller pores (**Figure 6-2**e)

Polarised light microscopy (plm) of the picrosirius red stained histological samples demonstrated that scaffolds with larger pores were characterised by higher amount of orange fibres (**Figure 6-2**d), suggesting that the annealing step was compacting the material into denser fibres. On the other hand, scaffolds with small pores showed higher amount of fibres in green. In plm, the color orange is characteristic of a high accumulation of collagenous material or due to the type of collagen (compacted fibres of collagen type II will have an orange color, while smaller non fibrillar collagens like collagen type VI will have a green color). However, since both scaffolds are made with the same material source, in this case, it can be assumed that the color change is related to the density of the collagen.

A more homogenous distribution of sGAGs and collagens was observed in the annealed (large pore) scaffolds after 28 days of culture in chondrogenic media (**Figure 6-2** f, g). In addition, sGAG staining was more intense in the annealed scaffolds with the larger pores. Polarised light microscopy was able to detect birefringent fibres in both scaffolds demonstrating mature collagen deposition (**Figure 6-2**h). No mineralization was observed in either scaffold (**Figure 6-2**i).

There was no significant difference in the amount of DNA levels or collagen deposited in the two scaffold types. There was a significant increase in sGAG deposition

in the scaffolds with bigger pores compared to scaffolds with smaller pores, confirming the histological findings. No significant difference were found in calcium levels and it was observed that the levels were overall very low (**Figure 6-2**j).

a Transversal crossection analysis

b Pore size (SEM)

c sGAG (Alcian Blue)

d Collagen (PLM; PR)

e Live/dead (Confocal)

Standard

Annealed

50 μm   100 μm   50 μm   1mm

f sGAG (Alcian Blue)

g Collagen (Picrosirius Red)

h Collagen (PLM)

i Calcium (Alizarin Red)

Standard

Annealed

1 mm

j

ns — μg DNA/mg dw — Standard, Annealed

* — GAG/DNA — Standard, Annealed

ns — HxP/DNA — Standard, Annealed

ns — % Calcium per mg dw — Standard, Annealed

159

***Figure 6-2.** Effect of pore size on chondrogenesis of MSCs (random standard Vs random annealed). **a,** Diagram explaining the transversal cross section cut for analysis of this figure's results. **b,** Scanning electron microscopy images of scaffolds fabricated with standard or annealed protocols. **c,** Histological analysis of day 0 samples with alcian blue for sGAG staining, and **d,** polarised light microscopy image of picrosirius red for collagen staining. **e,** Live/dead images of MSC seeded scaffolds after 7 days in expansion medium. **f,** Histological analysis of day 28 samples cultured in chondrogenic medium (CM) with alcian blue for sGAG staining; **g,** picrosirius red for collagen staining; **h,** polarised light microscopy image of (**g**); and **i,** alizarin red for calcium staining. **j,** Biochemical analysis of day 28 samples cultured in CM, showing µg DNA/mg dry weight (dw), sGAG/DNA, HxP/DNA (collagen) and % Calcium levels per mg dw.*

6.3.2. *Directional freeze-casting and annealing treatment before freeze-drying can be used in combination to tailor pore shape and size*

In the previous chapter, directional freeze casting and annealing was used to modulate pore alignment and size, respectively. In this study, both treatments were combined into one protocol in order to tailor both pore shape and pore size. Scanning electron microscopy (SEM) was used to characterize the morphology and distribution of the channels/pores in the four different scaffolds: (i) random standard, (ii) random annealed, (iii) aligned standard, and (iv) aligned annealed (**Figure 6-3**a). Scaffolds fabricated with a standard process had smaller pores than the scaffolds fabricated with the annealing step. The mean pore diameter for the random standard scaffolds was 54 ± 13 µm, while the mean pore/channel diameter for the aligned standard scaffolds was 44 ± 10 µm (**Figure 6-3**c). The mean pore diameter for the random annealed scaffolds was 132 ± 40 µm, while the mean pore/channel diameter for the aligned scaffolds was 97 ± 3. OrientationJ and Directionality Image J plugins were used to quantify the degree of anisotropy of the pores. There was no obvious preferred pore alignment in the scaffolds fabricated using the traditional mould (random scaffolds), which is illustrated by the wide range of colors shown in the overlapped colormap image, obtained from OrientationJ plugin (**Figure 6-3**b), and the quantification of the aligned structure by Direcionality plugin (**Figure 6-3**d). Conversely, pores were typically aligned at an angle of 90 degrees (to the horizontal) in scaffolds fabricated using directional freeze-drying (aligned scaffolds), which was illustrated by the preferred red color in the overlapped colormap image (**Figure 6-3**b) and by the quantification of the aligned structure (**Figure 6-3**d).
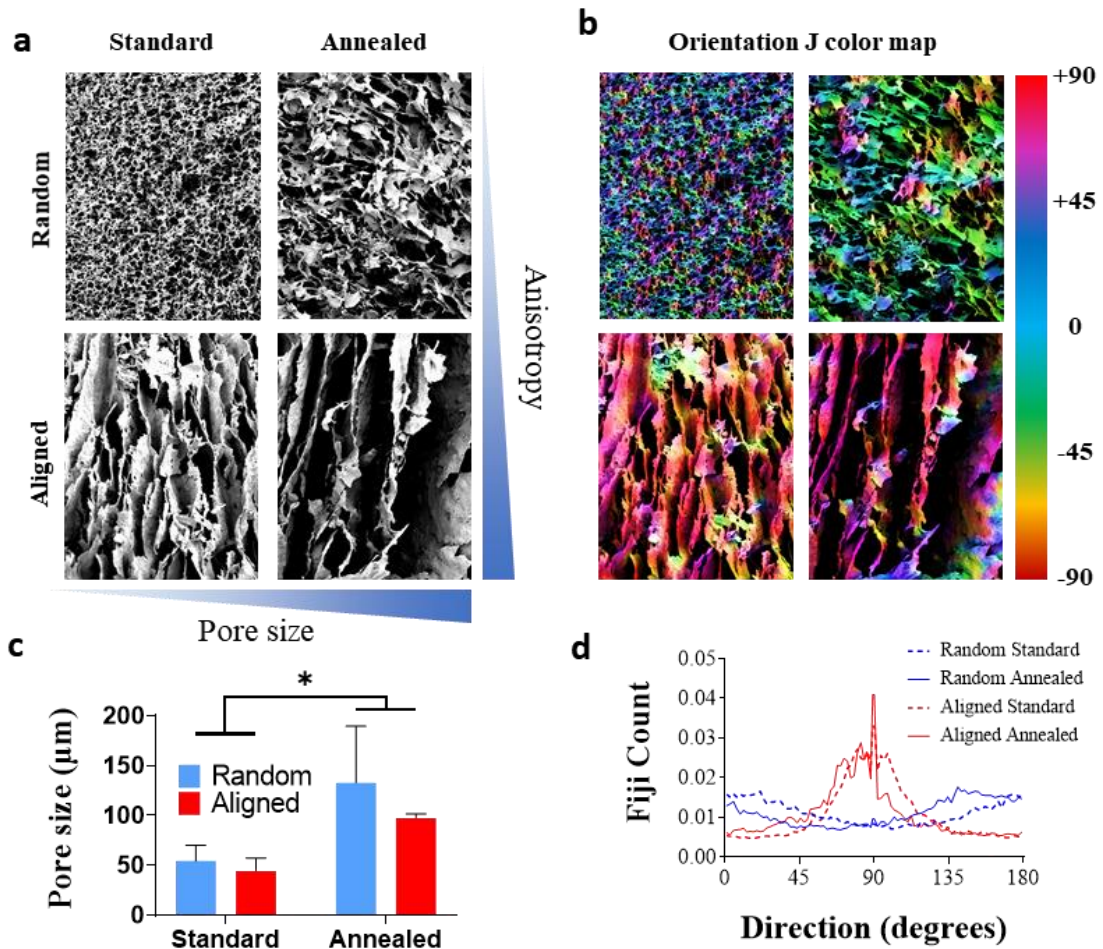
Figure 6-3. *Characterisation of pore morphology in scaffolds fabricated with a novel freeze-drying protocol combining directional freeze-casting and annealing. **a,** Scanning electron microscopy images of the scaffolds corresponding to the 4 different FD protocols. Increase of pore anisotropy and size is indicated beside the images. **b,** Overlapping fibre orientation colour map showing degree of anisotropy in the scaffolds. **c,** Mean/pore/channel diameter for all 4 groups based on SEM images. **d,** Histogram curve of the orientation colour map images.*

6.3.3. Anisotropic pore morphology enables a cartilage-like oriented tissue deposition

MSCs were seeded onto annealed random or annealed aligned scaffolds and cultured in chondrogenic media for 28 days. After 4 weeks, histological analysis demonstrated the homogenous deposition of cartilaginous tissue throughout both scaffolds. Both scaffolds supported the deposition of a tissue rich in sGAGs and type II collagen (**Figure 6-4**e, f, g). Only weak staining for type X collagen type (a hypertrophic marker) was observed in both scaffolds (**Figure 6-4**h).

161

Biochemical analysis validated histological results and demonstrated that there was no significant difference in the DNA, sGAG and collagen content of scaffolds with random and aligned pores (**Figure 6-4**i,j,k). No significant difference in the expression of SOX9, COL2, RUNX2, MMP13 and COL10 was observed in random and aligned scaffolds (**Figure 6-4**l).

Polarised light microscopy was undertaken to characterise collagen alignment in both scaffolds (**Figure 6-5**a). Magnified pictures were taken of two regions of interest (ROI) in the scaffolds: top and middle ROIs (**Figure 6-5**b). While the top of both scaffolds was characterised by the presence of collagen fibres parallel to the surface, collagen alignment differed within the middle of the two scaffolds. Collagen fibres appeared to be randomly distributed within the scaffold with random pores. In contrast, the newly synthesised collagen fibers appeared to be preferentially deposited parallel to the pores within the aligned scaffold. Directionality analysis confirmed very distinct collagen fiber alignments within the top and mid ROIs in the scaffold with aligned pores (**Figure 6-5**c,d).
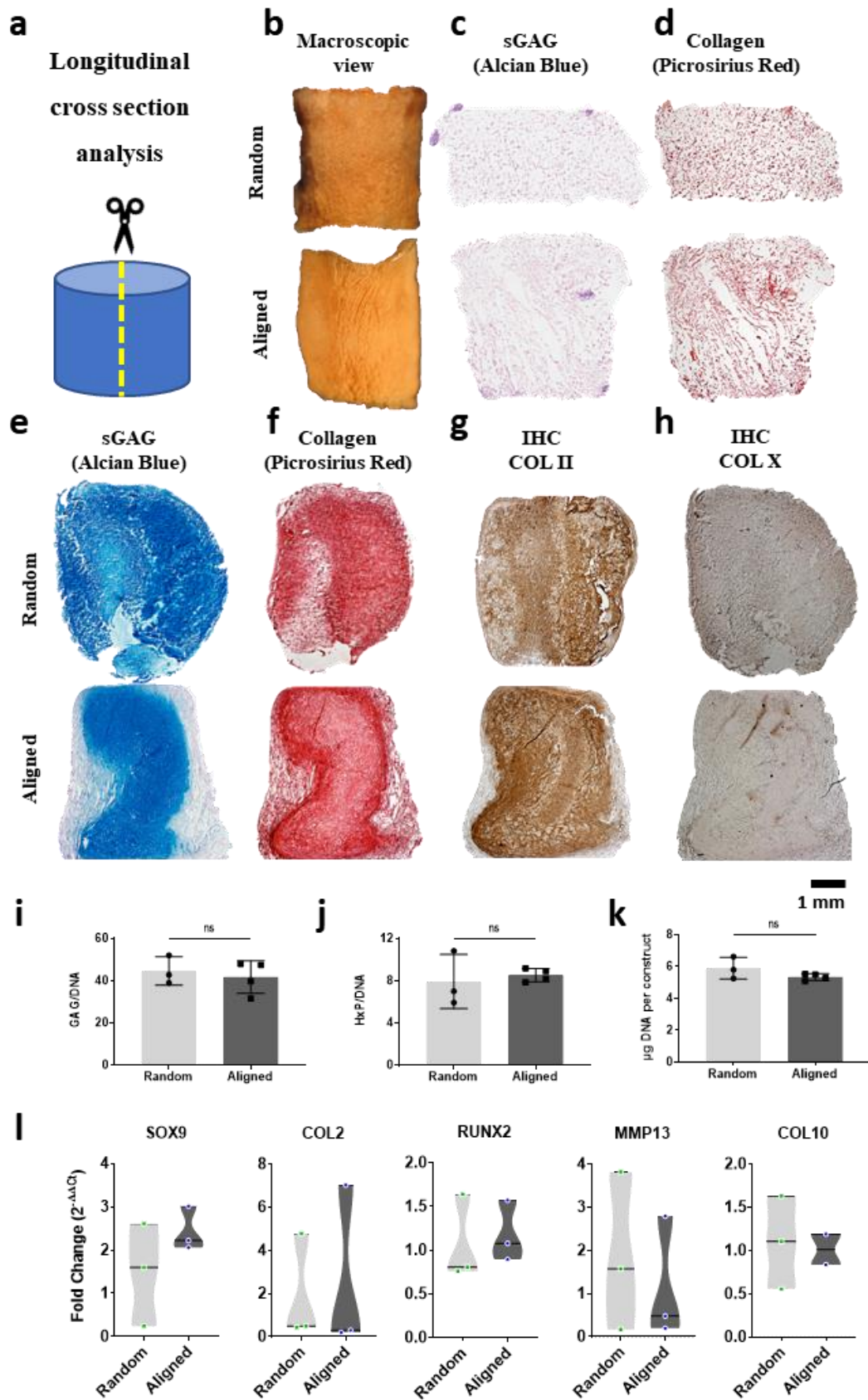
Figure 6-4. *Histological and biochemical analysis of the effect of pore anisotropy on chondrogenesis of MSCs (random annealed Vs aligned annealed).* ***a,*** *Diagram*

*explaining the longitudinal cross section cut for analysis of this figure's results. **b,** Macroscopic picture of random and aligned scaffolds. **c,** Histological analysis at day 0, showing alcian blue for sGAG staining and **d,** picrosirius red staining for collagen staining. **e,** Histological analysis at day 28 samples cultured in chondrogenic medium, showing alcian blue for sGAG staining; **f,** picrosirius red for collagen staining; **g,** immunohistochemistry for collagen type II (chondrogenic marker); and **h,** collagen type X (hypertrophic marker). Biochemical analysis showing **i,** sGAG/DNA; **j,** HxP/DNA (collagen); and **k,** µg DNA per construct of samples cultured in CM for 28 days. **l,** Quantification of SOX9, COL2A1, RUNX2, MMP13 and COL10A1 gene expressions by PCR after 28 days of culture in CM. Expression is relative to the random scaffold group. Graphs illustrate violin plots with median and quartile (n ≥ 2).*
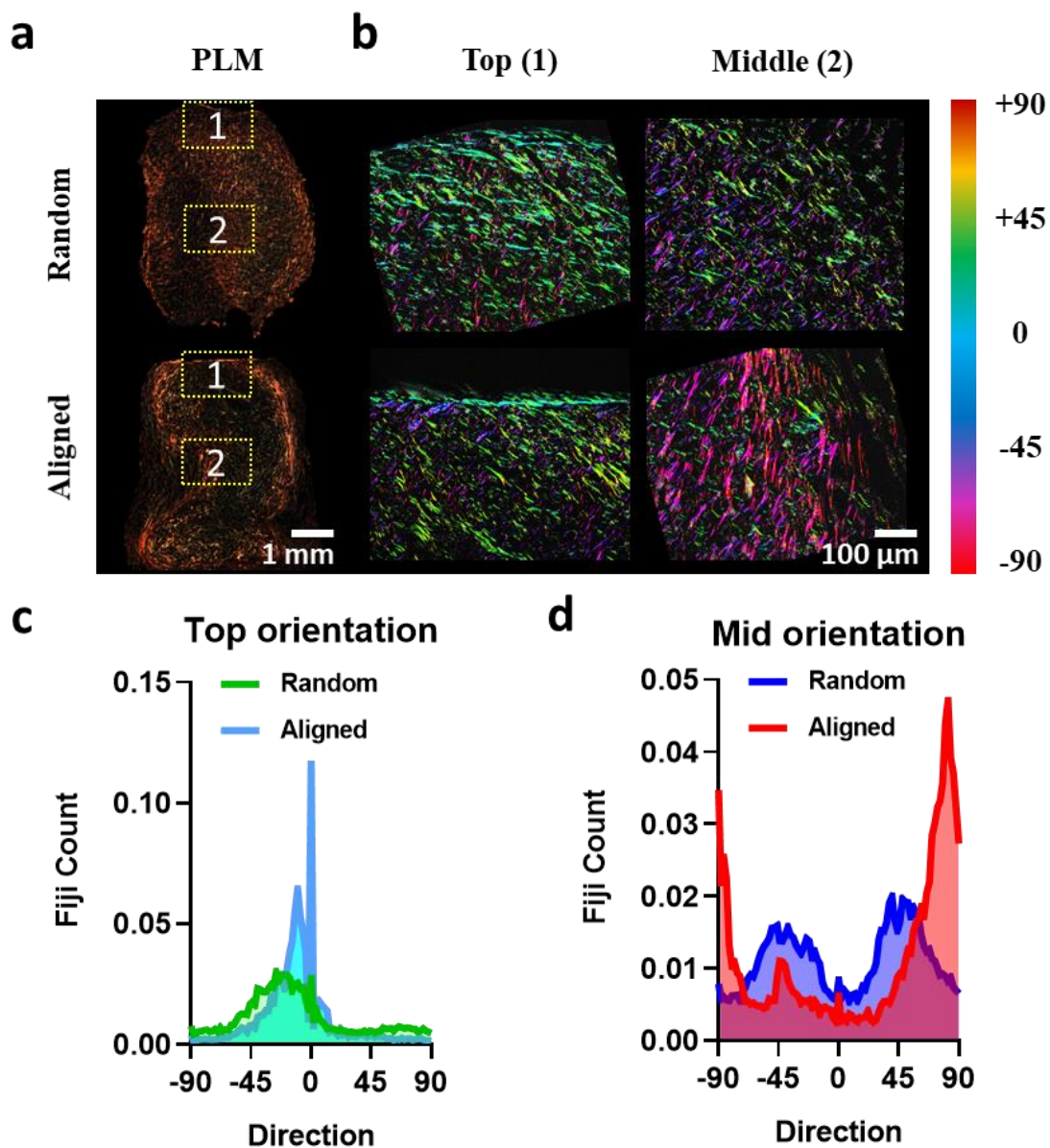
*Figure 6-5. Collagen alignment analysis by polarised light microscopy (PLM). **a,** Representative PLM images (n = 2) of the picrosirius red staining of random and aligned scaffolds after 28 days in culture. Two regions of interest (ROI) are highlighted by dashed yellow square: top and middle of the scaffold. **b,** Orientation J color map overlaying the PLM image for both ROIs showing the degree of anisotropy of the deposited collagen. **c,** Histogram curves showing the quantification of anisotropy by Directionality plugin, for both random and aligned scaffold, in the top **d,** and the middle ROI of the PLM images.*

6.3.4. Anisotropic tissue deposition is supported within PCL reinforced scaffolds

AC ECM material was poured onto the bi-material mould (silicon wells and metal base). PCL scaffolds were place into wells containing AC ECM material before crosslinking. After 30 minutes at 37 ºC, the material was freeze-dried following the aligned annealed protocol. Since the melting point of PCL is 60 ºC, samples were not process through DHT (115 ºC 24 h. ETO was used as sterilization method.

The scaffolds were seeded with MSCs and cultured for 28 days in chondrogenic medium. Both the ECM alone scaffold and the PCL reinforced scaffold stained positive for alcian blue and picrosirius red, indicating the deposition of sGAGs and collagen (**Figure 6-6**b). Aligned collagen deposition is observed in the PCL reinforced scaffolds (**Figure 6-6**c, d)

Higher DNA levels were observed in the PCL reinforced scaffolds at day 0, demonstrating an improved cell seeding efficiency. This difference was less evident after 28 days of culture (**Figure 6-6**e). There was no significant difference in either sGAG or collagen deposition within the two scaffolds after 28 days of culture (**Figure 6-6**f, g).
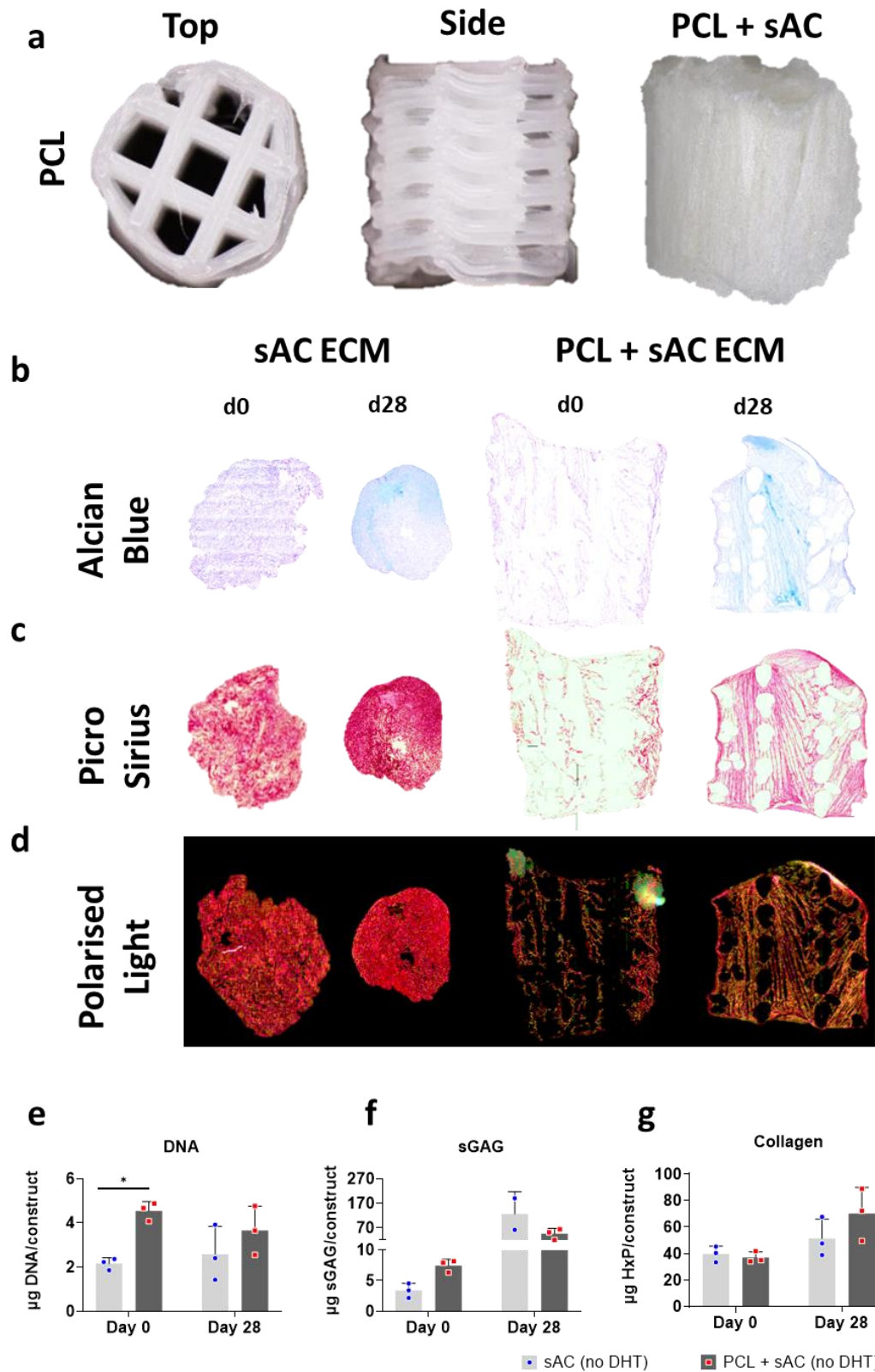
*Figure 6-6. Effect of PCL reinforcement on AC ECM derived scaffolds with aligned pore morphology. **a,** Macroscopic pictures of the top view of PCL frame (left), the side view of the PCL frame (middle) and the side view of a PCL reinforced aligned AC ECM scaffold. PCL scaffolds were fabricated by Dr. Fiona Freeman using RegenHU*

6.3.5. *Development of an aligned ECM-tissue specific bilayer scaffolds results in an osteochondral-like tissue deposition*

It was possible to fabricate a bilayer scaffold made of two ECMs, articular cartilage and bone solubilised ECM, with aligned annealed pores that recapitulate aspects of the osteochondral tissue morphology (**Figure 6-7**a,c,d). Food colorant was used during optimisation process to evaluate the integration between the two layers (**Figure 6-7**b) and ensure the solutions did not mix into each other.

Different tissues were deposited in each layer of the bi-layered scaffolds. In chondrogenic medium, the top layer (AC ECM) stained strongly with alcian blue and picrosirius red, indicating robust sGAG and collagen deposition. On the other hand, only weak staining for collagen deposition was observed in the bottom layer (BN ECM). Both layers stained negative for alizarin red, indicating no mineralisation of the scaffolds. In osteogenic medium, neither layer was shown to stain strongly for sGAG. Both layers stained strongly for collagen and for mineral deposition (**Figure 6-7**e,f,g).

Similar DNA levels were measured in both layers at day 0. After 28 days of culture, DNA levels were significantly higher in the sAC layer than in the sBN layer in both chondrogenic and osteogenic media (**Figure 6-7**h). sGAG deposition was higher in the AC layer in chondrogenic conditions (**Figure 6-7**i). The highest levels of collagen deposition occurred in the AC layer of scaffolds cultured in osteogenic medium (**Figure 6-7**j). Calcium analysis demonstrated very low levels of calcium at day 0 or at day 28 in samples cultured in chondrogenic medium. In contrast, robust calcium deposition was observed in constructs cultured in osteogenic medium, with significantly higher levels measured in the sBN layer.

Immunohistochemistry was used to assess the different types of collagen deposited in each scaffold layer in the different medias. When constructs were cultured in chondrogenic media, the AC layer stained strongly for collagen type II (**Figure 6-8**a).

There was however, weak positive staining for collagen type I (**Figure 6-8**b). Interestingly, collagen type X was localised to the pericellular area, which is typical of articular cartilage, as seen in the control (**Figure 6-8**c). The bone layer did not stain positive for collagen type II or type I deposition, although some weak positive staining for collagen type X was observed.

In osteogenic medium, weak staining for collagen type II was observed in both layers (**Figure 6-8**d). Positive staining for both collagen type I and type X was observed in the AC layer (**Figure 6-8**e,f). The BN layer stained strongly for collagen type I, indicative of supporting direct intramembranous ossification.
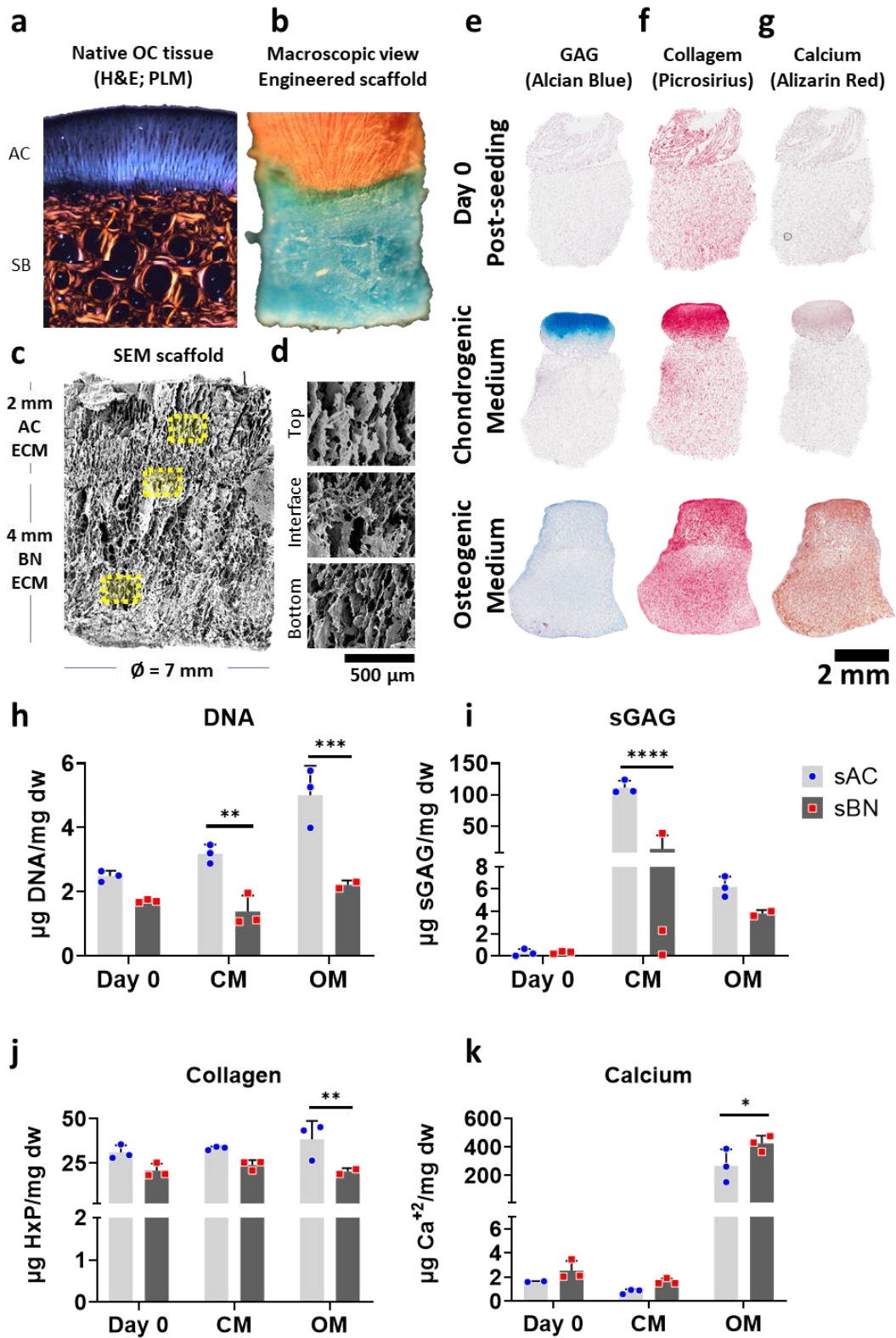
Figure 6-7. *Development of a bilayered ECM derived scaffold for osteochondral tissue engineering.* ***a,*** *Hematoxylin and eosin stained histological section of the native osteochondral goat tissue.* ***b****, Macroscopic view of the bilayer scaffold. ECMs have been dyed before FD to confirm spatial differentiation of both layers.* ***c,*** *Scanning electron*

*microscopy image of the bilayer scaffold. Top layer corresponding to articular cartilage (AC) ECM and bottom layer, to bone (BN) ECM. **d,** SEM zoomed images of top (AC), interface and bottom (BN) areas. **e,** Histological analysis at day 0 and day 28 of culture in either chondrogenic medium (CM) and osteogenic medium (OM), showing alcian blue for sGAG staining; **f,** picrosirius red for collagen staining; **g,** alizarin red for calcium staining. **h,** Biochemical analysis at day 0 and day 28 samples cultured in CM and OM, showing µg DNA/mg dry weight (dw); **i,** sGAG/DNA; **j,** HxP/DNA (collagen); and **k,** µg Calcium per mg dw. The two layers (AC layer: blue dots/light grey bar; BN layer: red dots/dark grey bar) were separated with a scalpel before analysis. (n ≥ 2).*
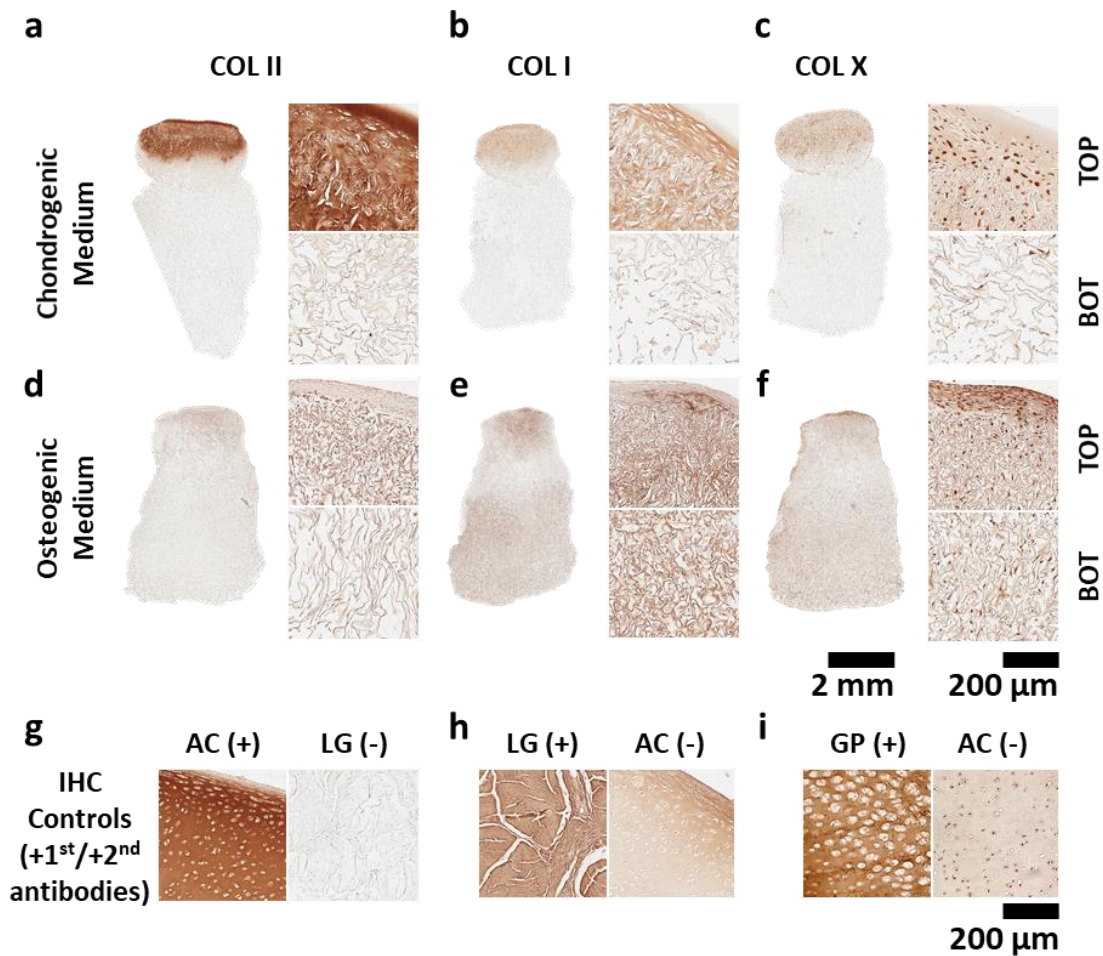
Figure 6-8. *Analysis of the tissue-specific deposition in the bilayer scaffold. **a,** Immunohistochemistry (IHC) analysis at day 28 of samples cultured in either chondrogenic medium (CM) and osteogenic medium, showing **a, d,** collagen type II; **b, e,** collagen type I; **c, f,** collagen type X. Positive and negative controls for each IHC analysis are showed in **g,** col II; **h,** col I; and **i,** col X. Acronym legend: articular cartilage (AC), ligament (LG) and growth plate (GP). (n=2)*

6.3.6. Bilayered scaffold treatment leads to a more consistent repair compared to empty controls

To evaluate the regenerative potential of the bilayered aligned scaffold within a challenging *in vivo* model, AC-BN scaffolds were implanted cell-free into critically-sized osteochondral defects created in the lateral trochlear ridge of goats. Animals were paired so that one stifle was treated with the bilayered scaffold and the other stifle was left empty. Six months after scaffold implantation, the quality of repair was compared to defects left empty.

The macroscopic appearance of defects treated with the bilayered scaffold demonstrated good repair overall with no significant difference in the macroscopic score between scaffold and empty control, although there is a trend towards higher scores in the scaffold treated group (**Figure 6-10**c). Scaffold treated groups lead to a more consistent repair (**Figure 6-9**d), particularly evident in the color of the repaired cartilage and the percentage of defect filled (**Figure 6-10**d,e).

Reconstructed images obtained from micro X-ray computed tomography of the harvested osteochondral sections demonstrated that there was variable regeneration of the bone region. The bone volume within the two regions of interest, either the subchondral bone plate (SBP, defined as the upper 1mm of the bony region) or the subarticular spongiosa (SAS, defined as the bottom 3 mm of the bony region), was similar with no significant difference across the groups. Yet, again, the scaffold treated groups appeared to develop a more consistent bone repair than the defects left empty (**Figure 6-9**e). It was observed that in the cases of poor healers, the scaffold treated groups performed better than the defects left empty. In many cases, the macroscopic healing is correlated with the bone healing of the SAS region (**Figure 6-11**d,e).
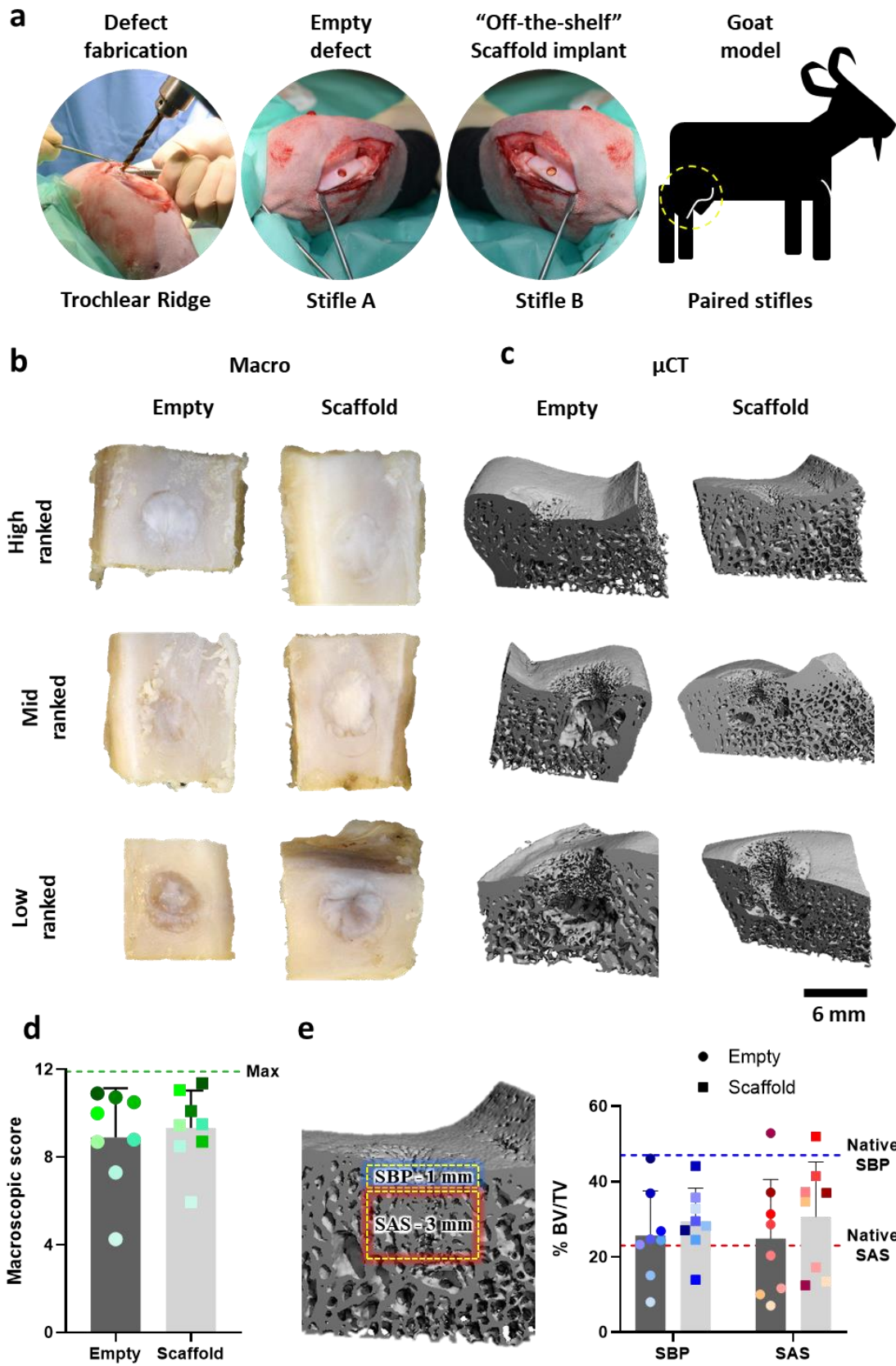
Figure 6-9. *In vivo analysis of the bilayer scaffold repair of an osteochondral defect 6 months post-implantation.* ***a,*** *Trochlear ridge osteochondral model illustrating:*

*defect fabrication with a hand drill, empty defect and implanted scaffold. Animals joints were paired to have an empty defect in one stifle and the implanted scaffold in the other stifle. **b,** macroscopic images for the highest-, mid- and lowest-ranked samples in empty and scaffold-treated defects. **c,** Micro x-ray computed tomography (μCT) of the corresponding samples. **d,** Quantification of the macroscopic appearance of the defects based on the repair tissue edge integration, smoothness, surface appearance, color and filling of the defect. Each animal is represented in one color of the green spectrum and the intensity is based on results from the empty group (n=8). **e,** Quantification of the bone volume per total volume within two regions of the defect, the upper 1mm subchondral bone plate region (SBP) and the lower 3 mm subarticular spongiosa region (SAS). Each animal is represented in one color of the blue (SBP) or red spectrum (SAS) spectrum and the intensity is based on results from the empty group (n=8). Native values for n=1 sample are reported with a dash line for each ROI.*
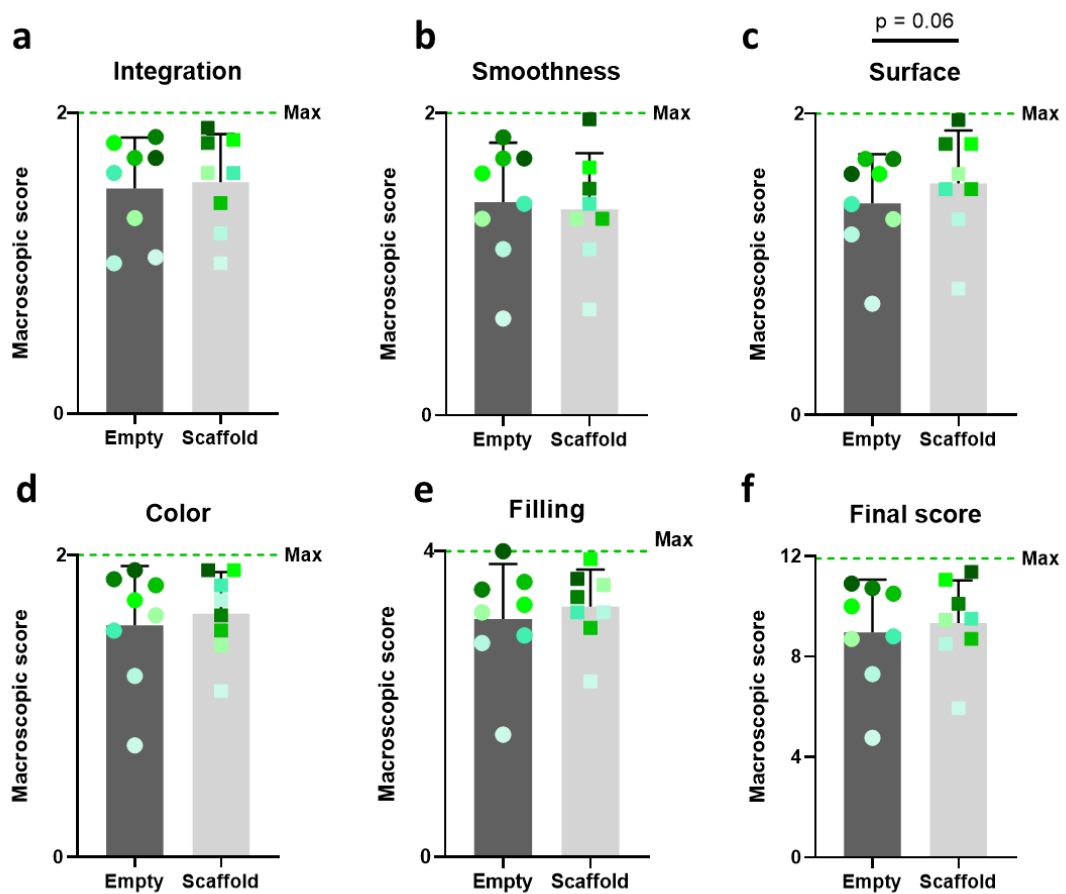
Figure 6-10. *Individual parameters of the macroscopic score system: **a,** Edge integration; **b,** Smoothness; **c,** surface appearance; **d,** color of the repaired cartilage; **e,** filling of the defect; and **f,** combined scores (n=8).*
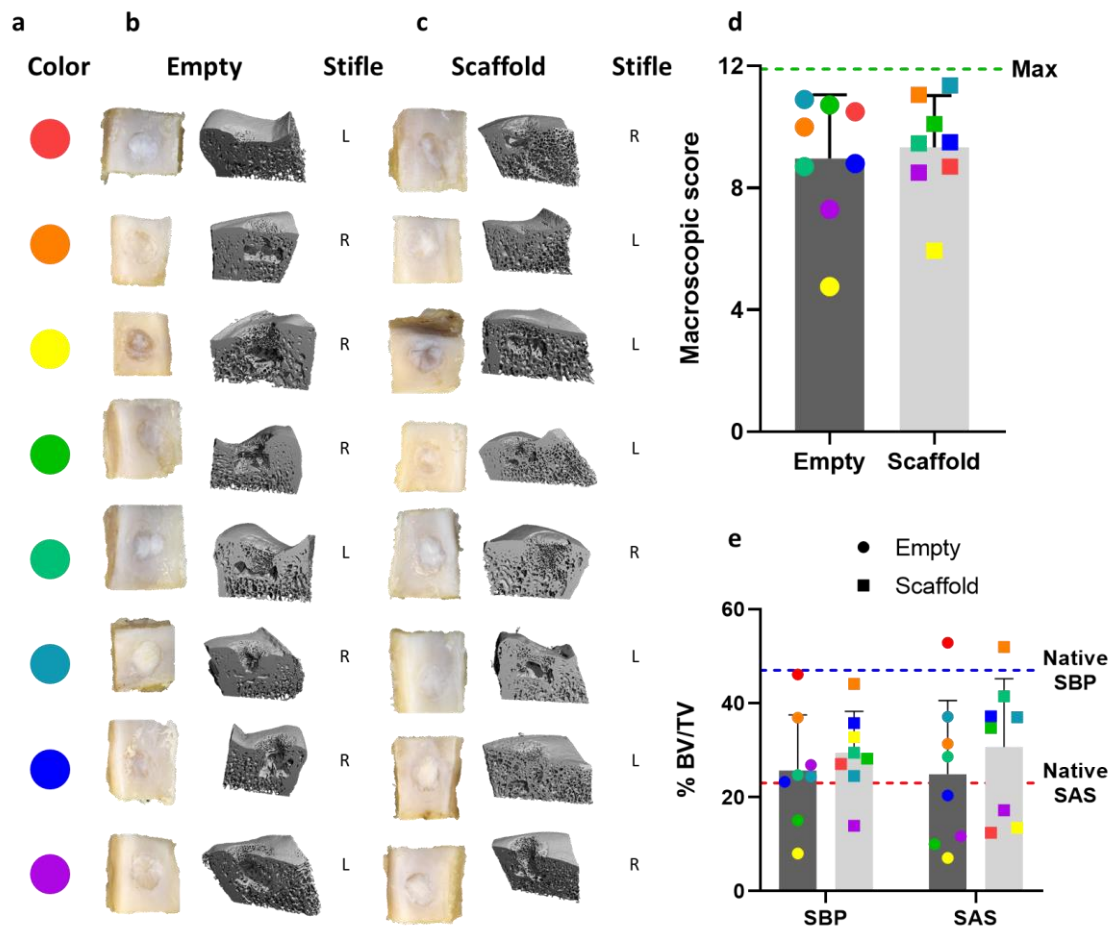
Figure 6-11. *Illustration of all the macroscopic and μCT images and quantified results labelled with the same color for each animal.* ***a,*** *Color legend for each animal.* ***b,*** *Macroscopic and μCT images of defects left empty.* ***c,*** *Macroscopic and μCT images of defects treated with the bilayered scaffold.* ***d,*** *Macroscopic score.* ***e,*** *Percentage of bone volume (n=8).*

6.4. Discussion and conclusion

The aims of this chapter were to determine the effect of pore morphology within AC ECM derived scaffolds on chondrogenesis of MSCs and the development of a bilayered scaffold for osteochondral tissue repair. The results demonstrated that pore size has a positive effect on cell infiltration, distribution and homogenous tissue deposition. In addition, an aligned pore architecture was observed to direct the organisation of the deposited collagen fibres. Finally, a bilayered tissue-specific ECM lead to a spatially different tissue deposition *in vitro* and a more consistent osteochondral defect repair *in vivo*.

The first aim of this chapter was to determine the effect of pore morphology within AC ECM derived scaffolds on chondrogenesis of MSCs. The results demonstrated that, as expected, pore size has a positive effect on cell infiltration. It has been speculated that the aligned nanofibers provides greater spacing or openness by changing the spatial organisation of "pores" between fibres and in turn allow for a more efficient cell migration and infiltration[351,374]. However, as it was demonstrated, this can be solved by increasing pore size[375] (without affecting pore-size mediated differentiation). It may be, that studies comparing aligned vs random architectures, are not giving random structures the best-case scenario for cell infiltration and tissue deposition. This is in agreement with previous studies showing enhanced cell attachment in scaffolds with large pore size[215]. In this study, it was also demonstrated that efficient cell infiltration lead to a homogeneous cell distribution, which in turns supports homogenous tissue deposition throughout the scaffold.

An aligned pore architecture was observed to direct the organisation of the deposited collagen fibres, promoting a more AC-like collagen network and thus, recapitulating aspects of the osteochondral tissue architecture. To the best of our knowledge, this was the first time that such an in-detail tissue characterisation with polarises light microscopy and tissue-specific collagen analysis has been described for cartilage-like tissue engineering *in vitro*. It was demonstrated that an anisotropic structure can provide a basal structure onto which cells can lay out a more architectural biomimetic, and thus a more functional, tissue. This is in agreement with previous studies showing that oriented collagen derived scaffold formed superior biomechanically tissue engineered cartilage constructs to non-oriented scaffolds, after 4 weeks post-implantation subcutaneously[193].

A challenge for tissue engineering is producing scaled-up three-dimensional cellular constructs with clinically relevant structural integrity[130] to treat large defects. This can be achieved by reinforcing the aligned ECM construct with a "tough" polymeric framework that cells cannot deform at the large macroscale. In this study, the 3D printed polymer of choice was a PCL framework. The ECM slurry was poured into the PCL frame before freeze-casting. Once freeze-dried, the construct formed was mechanically stable. For the *in vivo* study, we decided not to reinforce the scaffold with PCL. If larger

osteochondral defects were to be created, PCL reinforcement could be considered to provide further mechanical support.

Anisotropic tissue deposition was supported within PCL reinforced scaffolds. After 28 days of culture, it was confirmed that the PCL network allowed collagen deposition along the aligned ECM fibres. In addition, aligned collagen fibres were also observed along the PCL network. It is possible that cells interacting with the PCL could have aligned themselves in the direction of maximal stiffness sensed in the surrounding environment[202] and thus deposited collagen aligned to the PCL fibres. This is in agreement with previous work demonstrating enhanced collagen fibre organisation along PCL-microchamber wells[187]. It is important to consider that in this study the scaffolds did not undergo DHT treatment to avoid melting the PCL. However, this made the non-reinforced group much softer and compliant to cell-mediated contraction, thus collapsing the initial architecture and showing a different tissue deposition to previous aligned scaffolds.

Despite the interesting findings, these studies had some limitations. It is important to consider that the studies were developed *in vitro* and lacked key chondrogenic cues such as mechanical loading or hypoxic environment. It is well documented that such factors play an important role in the maintenance of chondrogenic behaviour[376,377] and may play a synergistic role with the initial alignment for an organised matrix deposition. A potential approach to address these study limitations would be to incorporate some form of confinement for the recapitulation of the native microenvironment[378], to mechanically stimulate the constructs or to use hypoxic conditions in order to reduce the hypertrophic behaviour. Another limitation from these studies is that the scaffold architecture is resolved in a binary question: either they are aligned or random. However, native tissues are hardly homogenous, and in fact, articular cartilage is characterised by the presence of three layers organised differently, being aligned parallel to the articular surface in the superficial region of the tissue, more disorganised network in the middle region and perpendicular to the articular surface in the deep zone[50,379]. Parallel surface architecture was naturally achieved by self-organisation of the cells at the edge of the scaffold, which has also been reported in other systems containing 3D printed microchambers[187]. However, a more controllable system would incorporate a multi-layered scaffold to recapitulate the different AC microarchitectures, as seen in other

studies combining layers of different anisotropy for top, middle and/or bottom zones[211,363,370,371].

The second aim of this chapter was to develop a bilayer scaffold with oriented microarchitecture for osteochondral tissue repair. Two different solubilised ECM derived materials, articular cartilage (sAC ECM) and bone (sBN ECM), previously used in our lab due to their chondrogenic[30] and osteogenic[318] potential, were used to fabricate the layered ECM derived scaffold with aligned pores by a novel iterative directional freeze-casting combined with annealing treatment before freeze-drying. The hypothesis was that the different biological cues contained within each ECM[29,162,380], would regulate the chondrogenic or osteogenic behaviour of the material *in vitro*.

As expected, in chondrogenic medium, the AC ECM layer supported chondrogenesis of the MSCs, as evident by robust sGAG and collagen deposition. In contrast, in osteogenic medium, the BN ECM layer better supported osteogenesis, as evident by the higher levels of calcium deposition. This correlates with previous studies that have shown the chondroinductivity[20,30,335,356] and osteoinductivity[381–383] of AC ECM and BN ECM, respectively. In addition, AC was shown to promote higher cell proliferation than BN ECM based on DNA levels in both media. The higher levels of mineralization in the BN ECM could be the reason for the significant drop of DNA levels after 28 days of culture. Previous studies have indicated that there is a strong correlation between mineralization and cell death in such scaffold systems[384]. Similar levels of collagen were observed in each layer in all culture conditions. However, IHC demonstrated differential tissue deposition. Care must be taken when extracting conclusions from the hydroxyproline assay results. Hydroxyproline is a non-proteinogenic amino acid synthesised as a post-translational modification and the hydroxyproline levels can vary in different types of collagen[385,386].

Following a detailed analysis demonstrating the capacity of these bi-layered ECM derived scaffolds to support spatially defined stem cell differentiation and organised tissue deposition *in vitro*, they were next implanted in an osteochondral defect and compared to an empty control for their capacity to promote tissue regeneration *in vivo*. After 6 months, the defects treated with the bilayered scaffold treated defects appeared to have a more consistent repair than defects left empty. In general, the cartilage macroscopic scoring was correlated with the subchondral bone healing. This is in

agreement with previous studies highlighting the importance of subchondral bone reconstruction, vital to facilitate a robust cartilage repair[48,387]. Histological examination of the repaired tissue is ongoing work and will reveal more information on the recapitulation of the native microarchitecture and tissue composition.

In conclusion, taken together the results demonstrated that anisotropic architecture of ECM derived scaffolds can influence MSC tissue deposition organisation in an appropriate microenvironment. Incorporation of tailored microarchitecture into a bilayer scaffolds, made up of AC and bone ECMs, demonstrates potential as an effective chondro- or osteoconductive strategy to improve osteochondral tissue engineering.

7. CHAPTER: Final discussion and conclusion

The overall objective of this thesis was to build a new biomimetic scaffold for osteochondral tissue engineering and assess it efficacy both *in vitro* and *in vivo*. Successful tissue engineering relies on the integration of cells, signals and scaffolds to create functional tissues. It is important to realize that carbon-life, as we know it, is a few million years ahead of us in development of tissues with a composition and organization exquisitely suited to its function. Thus, even if biomimetic approaches may not be always the best solution for every problem, it is important to give them special attention. With this in mind, the challenge of developing tissue engineering strategies can be approached from two perspectives: (i) we can study how a specific tissue was formed with a view to mimicking its natural development, or (ii) we can look at the at the final components and functional structure of the native tissue to try to use them or mimic them as appropriate. This thesis focused on the latter approach.

The specific aims of this thesis were (i) to characterise the ECM proteome of cartilage and growth plate (hypertrophic cartilage), in order to identify chondro- and osteo-inductive factors; (ii) to assess the effect of soluble factors identified in the ECM of AC and GP on stabilising chondrogenesis and enhancing osteogenesis of MSCs; (iii) to optimise the pore morphology and mechanical properties of ECM derived scaffolds for musculoskeletal tissue engineering; (iv) to assess the effect of pore morphology on chondrogenesis and progression along an endochondral pathway for MSCs seeded onto these ECM derived scaffolds; and (v) to develop a biomimetic bilayered ECM derived scaffold for osteochondral tissue engineering and assess its efficacy *in vitro* and *in vivo*.

7.1. The ECM proteome of cartilage and growth plate

Proteomic analysis comparing articular cartilage and growth plate (hypertrophic cartilage) was useful in identifying AC and GP-specific proteins with potential for cartilage and bone tissue engineering applications, respectively. The proteins detected in the GP ECM using mass spectrometry analysis are in agreement with previous studies, confirming that hypertrophic chondrocytes resident in the GP express a number of angiogenic factors, including CSPG4[295,306], ANGPT2[297,307] and MMPs[308,309], as well as

osteogenic factors such as S100A10[289,310], osteolectin (CLEC11A)[274] as well as BMP[311] and FGF related proteins[152,155]. In contrast to the GP, AC ECM was rich in type II collagen, which is known to be chondro-inductive[312], and the presence of hypertrophic inhibitors and cartilage homeostasis regulators such as GREM1[153,246] and TGFβi/βIGH3[265,270]. Previous mass spectrometry studies of AC have also revealed the presence of these proteins at different depths in human articular cartilage and other cartilaginous tissues[39,313]. The benefit of the analysis undertaken in this study was that it enabled the identification of proteins which were unique to either AC or GP and which could potentially be applied as soluble cues in articular cartilage or endochondral bone tissue engineering strategies.

7.2. The effect of AC and GP specific proteins on stabilising chondrogenesis and enhancing osteogenesis of MSCs

Once the composition of soluble factors in AC and GP ECM was characterised, tissue-specific factors were assessed for their capacity to promote either osteogenesis or the engineering of phenotypically stable AC. The supplementation of AC-specific proteins, GREM1 and βIGH3 led to the improvement of hyaline-like cartilage by reducing the expression of the hypertrophic marker collagen type X as well as supporting robust chondrogenesis with high levels of sGAG and collagen type II synthesis. Furthermore, it was demonstrated that cartilage engineered constructs in the presence of GREM1 was more resistant to the degradation of the deposited ECM upon subcutaneous implantation and helped to maintain a cartilage phenotype. The results above demonstrate a promising role for GREM1 in cartilage tissue engineering and future studies should look at GREM1 engineered cartilage in a chondral or osteochondral defect sites to assess if there is a clinically relevant role for this AC-specific protein in joint regeneration strategies.

The supplementation of GP-specific proteins in a monolayer model of osteogenesis led to increases in mineralisation by MSCs. It was demonstrated that CLEC11A and S100A10 can act in combination with osteogenic factors (BGP) to enhance the osteogenic phenotype in a dose-dependent response. Due to their role in the maintaining the adult skeleton[274] and vesicle derived matrix ossification (mature matrix)[288], their effect may be more evident in an endochondral bone model. Future

studies should evaluate the effect of GP proteins in the enhancement of hypertrophy of MSCs in a scaffold model similar to the described previously in this chapter.

7.3. Optimising the pore morphology and mechanical properties of ECM derived scaffolds

A novel approach to freeze-cast ECM derived scaffolds was developed. In summary the approach consists of combining directional freeze-casting and annealing treatment before freeze-drying the samples. This technique allows the tailoring pore morphology at micrometre scale in shape (random Vs aligned) as well as in size (ranging from 40-200 µm). Previous studies have managed to tailor pore size by modulating the freezing-rate of the freeze-casting. However, with this approach, in order to create big pores, slow rates are needed. The slow freezing rates can promote the generation of many nucleation points at different times which in turns creates a high standard deviation for final pore size[347]. Combining the high freezing rates provided by liquid nitrogen freezing (needed for alignment) with annealing allows for the development of scaffolds with homogenous larger pores

7.4. The effect of pore morphology on chondrogenesis and progression along an endochondral pathway

In the recent years, there has been an increase interest in the use of anisotropic structures for tissue engineering. In the case of cartilage, such alignment can provide a basal architecture onto which cells can lay out a more biomimetic, and thus a more functional, tissue. Previous studies demonstrated that oriented cartilage derived scaffold formed biomechanically superior tissue engineered cartilage constructs to non-oriented scaffolds 4 weeks post-implantation subcutaneously[193]. In this study, it was demonstrated with polarised light microscopy that an aligned scaffold can promote a more cartilage-like collagen fibre microarchitecture, recapitulating aspects of the native tissue.

7.5. A biomimetic bilayered ECM derived scaffold for osteochondral tissue engineering

It was also possible to create a bilayered scaffold with aligned pores that supported the rapid infiltration of MSCs. The bilayered scaffold was composed of two different tissue-specific ECMs with unique chondroinductive and osteoinductive potential, respectively, as demonstrated by tissue deposition *in vitro*. The bilayer scaffold was implanted *in vivo* to treat a critical osteochondral defect size of 6 mm diameter by 6 mm height, as previously described[32,373]. The results, although preliminary, would appear to demonstrate that the scaffolds can promote more consistent repair of osteochondral defects, particularly in animals with a low endogenous capacity for spontaneous bone regeneration.

7.6. Conclusion

To conclude, the results demonstrate diverse uses for tissue-specific ECM factors in musculoskeletal tissue engineering. These range for the use of soluble factors, identified in the ECM of specific tissues, for modulating the phenotype of skeletal stem cells, to the use of biomimetic architectures in biological ECM scaffolds for directing tissue deposition when engineering functional cartilage or osteochondral tissues.

8. CHAPTER: Future directions

8.1. Off-the-shelf and high-throughput analysis strategies

Based on the characterisation of the ECM, key molecular proteins for cartilage or bone tissue engineering were found. Two proteins from AC ECM, GREM1 and βIGH3, were assessed for promoting a stable hyaline cartilage-like tissue deposition.

Following an *off-the-shelf* strategy, the solubilised ECM derived scaffolds could potentially be functionalised by loading such proteins onto the scaffold for cartilage defect repair. Native ECM has been shown to act as a reservoir for growth factors that can be released upon demand[388]. Thus, as previously demonstrated with other ECM derived scaffolds[30], it is reasonable to expect a controlled release of the loaded proteins that could promote a stable cartilage phenotype without the need of constant supplementation over time *in vitro*. In a preliminary *in vitro* study (**Figure 8-1**), an AC ECM scaffold loaded with TGFβ3 and GREM1 was able to promote chondrogenesis of MSCs, with tissue deposition levels comparable to the scaffold supplemented with both factors in the chondrogenic medium over 28 days of culture.

There are, however, other proteins that may also have potential for cartilage tissue engineering. In this type of single protein assessment, synergistic effects of different proteins remain elusive. Following a high-throughput strategy, micro-pellet arrays in combination with fractional factorial design could be used to find important correlations.

On the other hand, only two proteins from the GP ECM proteomic analysis, CLEC11A and S100A10, were tested for monolayer mineralisation. It would be interesting to see the effect of these proteins on MSCs to study if they can drive a hypertrophic phenotype or an endochondral ossification *in vitro*. In addition, there are other proteins that could have potential for bone tissue engineering.

In addition, it would be interesting to combine such tissue-specific factors with a scaffold containing a tailored pore microarchitecture, to further biomimic the heterogenous components present in complex native tissues such as the osteochondral unit.
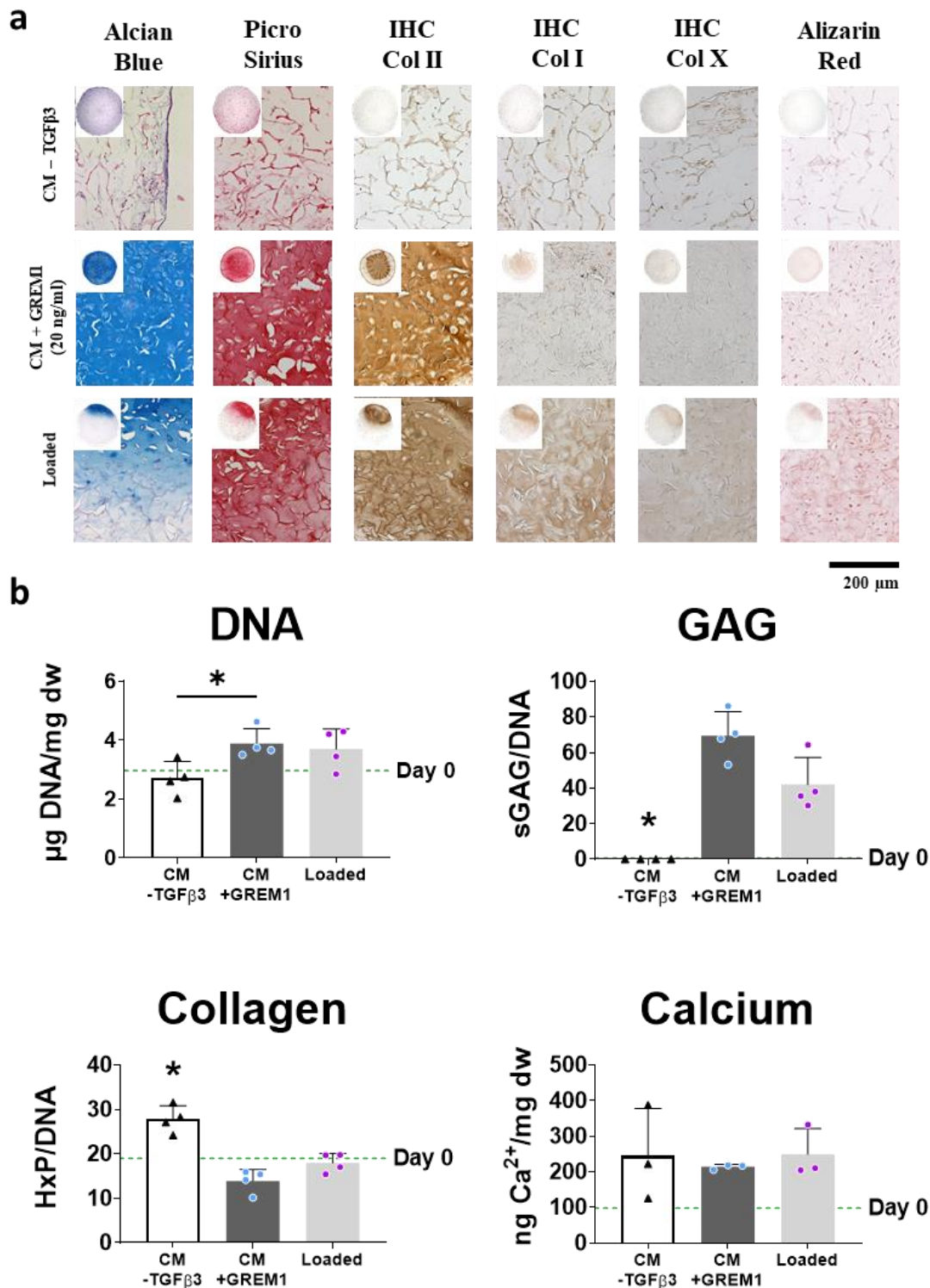
Figure 8-1. *TGFβ3 and GREM1 loaded scaffolds promotes cartilage like tissue deposition. **a,** Histological analysis showing alcian blue for gag staining, picrosirius red for collagens staining, immunohistochemistry of type II, type I and type X collagen and alizarin red for calcium staining of the following three groups: scaffolds cultured for 28 days in deficient chondrogenic medium (without TGFβ3), scaffolds cultured in standard*

*chondrogenic medium (containing TGFβ3) with GREM1 and scaffolds loaded with TGFβ3 and GREM1 cultured in deficient chondrogenic medium. **b,** Biochemical analysis showing µg DNA/ mg dw, sGAG/DNA ratio, HxP/DNA ratio and ng Calcium/mg dw of the three described groups (*P < 0.05, n ≥ 3).*

8.2. Effect of cyclic loading in anisotropic scaffolds and characterisation of the morphology of seeded cells

In chapter IV and V, it was possible to generate scaffolds with aligned architecture that promoted aligned tissue deposition. It has been described before how cyclic loading is important to induce aligned tissue deposition[389]. It would be interesting to test the scaffolds with anisotropic pore architecture in a loading regime to study if this alignment can be improved or to test the importance of the initial tissue deposited in an aligned scaffold and its development in a cyclic loading environment. In addition, characterization of cell shape adopted in scaffolds with different level of microarchitecture anisotropy will help to answer how morphology affects cell differentiation and the resulting deposited tissue in solubilised ECM derived scaffolds.

8.3. Evaluate osteogenesis in anisotropic scaffolds with altered pore sizes

In this thesis, the scaffold pore size was optimised for chondrogenesis. It would be interesting to study the effect of pore morphology and size on osteogenesis of MSCs seeded into bone ECM scaffolds. Once the best microarchitecture for osteogenesis has been determined, a bilayer scaffold with a AC ECM layer with aligned pores optimised for chondrogenesis (pore size < 200 µm) and a layer of bone ECM with either aligned or random pores with a size optimised for osteogenesis could be assembled into a single bilayered scaffold for osteochondral tissue engineering.

8.4. Assessing the phenotypic stability of GREM1 stimulated cartilage in more physiologically relevant *in vivo* models

It was observed that MSCs seeded in ECM scaffolds and cultured in hypoxic conditions and in the presence of GREM1 deposited the highest amounts of sGAG *in*

vitro. When tested in the subcutaneous model in mice, this group also supported the highest amount of ectopic bone formation after 4- and 6-weeks post implantation. It is however unclear if GREM1 stimulated cartilage would form endochondral bone in a model system that is more representative of the joint defect environment. The knee environment it is a very isolated system and so it may be interesting to implant the constructs subcutaneously in osteochondral explants, or in a synovium like membrane to mimic the joint hypoxic environment, with only one side exposed to subcutaneous influence to mimic the angiogenic subchondral bone environment.

8.5. Evaluation of bone defect repair *in vivo*

Previous studies have evaluated the use of scaffolds containing aligned pores for enhancing cell infiltration and endochondral bone formation in a rat femoral defect[207]. However, the promoted tissue did not bridge the gap of the critical defect after 6 weeks post-implantation. Based on the results of the osteochondral goat study from this thesis, in which bone regeneration was highly promoted with an aligned tissue-specific ECM, future studies should evaluate the use of these material following a similar approach to the above-mentioned study, to evaluate if such scaffolds can be used to repair critical femoral defects.

9. CHAPTER: Supplementary data

9.1. Protein list

9.1.1. Articular Cartilage Proteins

LFQ intensity AC_1	LFQ intensity AC_2	LFQ intensity AC_3	Peptides	Unique peptides	Score	Intensity	Gene name	Division Matrisome	Subcategory matrisome
28.35758	28.80888	NaN	15	14	191.17	20304000000	COL11A1	Core matrisome	Collagens
35.40952	34.97002	35.00299	39	38	323.31	2.3936E+11	COL11A2	Core matrisome	Collagens
33.9656	33.75663	34.17027	57	2	323.31	38906000000	COL14A1	Core matrisome	Collagens
30.21917	NaN	29.90455	56	1	11.516	2702800000	COL14A1	Core matrisome	Collagens
30.03131	30.51126	29.03215	8	3	80.797	9189500000	COL15A1	Core matrisome	Collagens
29.82595	31.0949	30.48884	4	4	31.884	10193000000	COL1A1	Core matrisome	Collagens
29.45621	29.78767	30.1966	13	13	93.924	20345000000	COL1A2	Core matrisome	Collagens
26.71882	NaN	27.05497	3	3	19.264	995870000	COL27A1	Core matrisome	Collagens
35.11644	34.73333	34.83295	17	16	323.31	2.6774E+11	COL2A1	Core matrisome	Collagens
32.60205	31.64212	32.57851	12	12	101.03	17787000000	COL6A1	Core matrisome	Collagens
30.19072	30.09093	29.33818	6	6	82.783	2976300000	COL6A1	Core matrisome	Collagens
31.58607	31.47315	31.90483	3	3	39.012	12479000000	COL6A1	Core matrisome	Collagens
33.7797	33.79333	33.70841	29	29	297.87	51108000000	COL6A2	Core matrisome	Collagens
34.93293	34.77254	34.54541	21	21	323.31	1.5189E+11	COL9A1	Core matrisome	Collagens
32.17435	32.00068	32.29655	5	5	82.195	48229000000	COL9A2	Core matrisome	Collagens
30.36953	29.97856	29.76819	9	9	59.91	6513200000	COL16A1	Core matrisome	Collagens
35.63591	35.75494	35.40616	122	122	323.31	1.7419E+11	COL6A3	Core matrisome	Collagens
29.61681	30.02789	28.93646	9	9	103.68	1982200000	AEBP1	Core matrisome	ECM Glycoproteins
27.90552	28.01324	NaN	12	12	77.517	519880000	CILP	Core matrisome	ECM Glycoproteins
33.22116	33.34982	33.67661	49	49	323.31	22944000000	CILP2	Core matrisome	ECM Glycoproteins
37.08738	36.81419	37.31697	41	13	323.31	5.5647E+11	COMP	Core matrisome	ECM Glycoproteins
29.53473	28.71158	NaN	30	2	96.405	2312400000	COMP	Core matrisome	ECM Glycoproteins
31.74523	32.44209	31.64757	6	6	67.35	19448000000	CTHRC1	Core matrisome	ECM Glycoproteins
31.56833	31.92447	31.66043	15	15	153.38	45634000000	EDIL3	Core matrisome	ECM Glycoproteins
28.52765	28.57762	28.0682	12	12	96.492	1429300000	EMILIN1	Core matrisome	ECM Glycoproteins
28.14957	28.08451	NaN	3	3	25.45	811680000	FBLN1	Core matrisome	ECM Glycoproteins
32.55472	32.94576	32.95489	17	17	136.14	21175000000	FBLN7	Core matrisome	ECM Glycoproteins
28.97544	28.8649	29.12943	9	9	58.825	1066200000	FBN1	Core matrisome	ECM Glycoproteins
24.79323	27.12898	26.11856	33	33	323.31	89384000000	FGB	Core matrisome	ECM Glycoproteins
34.73726	34.65874	34.67409	88	88	323.31	3.4305E+11	FN1	Core matrisome	ECM Glycoproteins
37.08074	36.47845	36.92702	39	39	323.31	2.962E+11	MATN1	Core matrisome	ECM Glycoproteins
30.20443	30.55938	29.762	12	12	117.15	10296000000	MATN2	Core matrisome	ECM Glycoproteins
37.14357	36.73568	37.05793	33	33	323.31	5.7601E+11	MATN3	Core matrisome	ECM Glycoproteins
33.79275	33.88231	33.8903	28	28	259.09	36329000000	MATN4	Core matrisome	ECM Glycoproteins
28.79359	28.05092	29.65901	3	3	22.131	1715400000	MFAP2	Core matrisome	ECM Glycoproteins
32.99988	32.80785	32.60373	24	24	274.88	60988000000	MFGE8	Core matrisome	ECM Glycoproteins
29.05876	28.1399	29.16065	8	8	79.437	1390000000	PCOLCE	Core matrisome	ECM Glycoproteins
28.63951	27.73731	NaN	8	8	61.368	1149700000	PCOLCE2	Core matrisome	ECM Glycoproteins
26.36785	NaN	26.58835	2	2	11.684	121600000	RSPO3	Core matrisome	ECM Glycoproteins

29.26578	29.26186	29.11642	4	4	31.414	1248200000	SMOC2	Core matrisome	ECM Glycoproteins
29.69515	29.70154	29.83711	9	9	79.112	17480000000	SPARC	Core matrisome	ECM Glycoproteins
29.57143	30.46314	29.03234	11	11	82.189	3741200000	SRPX	Core matrisome	ECM Glycoproteins
32.20557	31.93484	32.14643	23	23	197.48	9971900000	SRPX2	Core matrisome	ECM Glycoproteins
34.2187	34.00605	32.4233	28	28	289.22	33968000000	TGFBI	Core matrisome	ECM Glycoproteins
35.95359	35.83418	36.12303	62	61	323.31	3.0238E+11	THBS1	Core matrisome	ECM Glycoproteins
25.48195	26.16337	NaN	4	3	22.176	110530000	THBS2	Core matrisome	ECM Glycoproteins
30.387	31.02518	30.66043	18	16	130.19	22253000000	THBS3	Core matrisome	ECM Glycoproteins
30.37306	29.8798	30.4715	13	7	112.21	3060900000	THBS4	Core matrisome	ECM Glycoproteins
35.09926	34.73605	34.71416	64	18	323.31	80969000000	TNC	Core matrisome	ECM Glycoproteins
26.91866	NaN	27.15991	48	2	37.083	147120000	TNC	Core matrisome	ECM Glycoproteins
32.6145	33.06519	32.45405	22	22	323.31	20351000000	VIT	Core matrisome	ECM Glycoproteins
26.12056	26.68405	NaN	4	4	64.28	347450000	VWA1	Core matrisome	ECM Glycoproteins
27.12524	27.05703	NaN	21	21	306.7	75371000000	FGG	Core matrisome	ECM Glycoproteins
38.15304	37.61222	38.59675	58	44	323.31	1.355E+12	ACAN	Core matrisome	Proteoglycans
38.13351	37.11458	37.2389	40	40	323.31	8.169E+11	BGN	Core matrisome	Proteoglycans
34.66681	34.18016	34.82022	28	28	323.31	1.0685E+11	CHAD	Core matrisome	Proteoglycans
31.82092	31.91592	32.16261	22	22	241.79	17083000000	CHADL	Core matrisome	Proteoglycans
35.1541	34.74685	35.72059	35	35	323.31	1.1239E+11	DCN	Core matrisome	Proteoglycans
32.80178	32.10109	32.7333	15	15	148.23	14444000000	EPYC	Core matrisome	Proteoglycans
36.92316	36.52988	37.11206	18	17	323.31	4.5392E+11	FMOD	Core matrisome	Proteoglycans
37.48547	37.41266	37.4916	35	35	323.31	1.1332E+12	HAPLN1	Core matrisome	Proteoglycans
34.53427	34.64431	34.97383	16	16	119.67	1.4593E+11	HAPLN3	Core matrisome	Proteoglycans
34.04669	33.70275	34.25772	43	43	323.31	95011000000	HSPG2	Core matrisome	Proteoglycans
34.92937	34.986	33.65063	25	25	323.31	3.0026E+11	PRELP	Core matrisome	Proteoglycans
28.4305	30.16231	29.84559	10	10	74.382	1862600000	VCAN	Core matrisome	Proteoglycans
31.20362	31.68177	29.87093	12	12	78.173	5350600000	OGN	Core matrisome	Proteoglycans
26.40659	26.69445	NaN	10	10	76.111	3949200000	CD109	Matrisome-associated	ECM Regulators
27.79699	28.27604	28.57442	6	6	41.522	1867200000	HTRA1	Matrisome-associated	ECM Regulators
31.8928	32.0187	32.53362	25	24	238.19	18480000000	LOXL3	Matrisome-associated	ECM Regulators
26.99992	27.83382	NaN	10	10	77.139	1743600000	MMP2	Matrisome-associated	ECM Regulators
31.13057	31.08398	31.15074	20	14	253.75	25164000000	P4HA1	Matrisome-associated	ECM Regulators
29.29228	29.55459	29.19371	14	1	164.71	5652300000	P4HA2	Matrisome-associated	ECM Regulators
28.66942	28.83222	27.57521	19	19	190.8	7962100000	PLOD1	Matrisome-associated	ECM Regulators
31.71166	31.71129	31.91114	30	30	323.31	34482000000	Plod2	Matrisome-associated	ECM Regulators
29.90627	29.92366	29.95975	15	15	122.04	7705000000	SERPINB9	Matrisome-associated	ECM Regulators
29.25149	30.0189	28.7358	14	14	132.22	4556300000	SERPINF1	Matrisome-associated	ECM Regulators
34.33338	33.72862	33.96748	18	18	323.31	3.3455E+11	SERPINH1	Matrisome-associated	ECM Regulators
26.82723	NaN	27.24391	9	9	89.398	1780800000	TGM2	Matrisome-associated	ECM Regulators
29.84833	29.6803	28.98888	13	13	158.01	8819200000	LEPRE1	Matrisome-associated	ECM Regulators
27.34486	27.61316	26.79067	13	13	173.79	7681200000	ANXA1	Matrisome-associated	ECM-affiliated Proteins
27.04396	27.13046	NaN	9	9	70.727	1791400000	ANXA11	Matrisome-associated	ECM-affiliated Proteins
31.33485	31.30128	30.8165	29	29	323.31	35792000000	ANXA2	Matrisome-associated	ECM-affiliated Proteins
29.58135	30.21466	NaN	9	8	103.12	10727000000	ANXA4	Matrisome-associated	ECM-affiliated Proteins
31.59997	31.77643	30.97972	21	20	293.02	46716000000	ANXA5	Matrisome-associated	ECM-affiliated Proteins
29.78793	29.69486	NaN	31	31	242.73	12276000000	ANXA6	Matrisome-associated	ECM-affiliated Proteins
29.40718	29.40288	29.82561	4	4	76.867	1352900000	C1QA	Matrisome-associated	ECM-affiliated Proteins
30.31948	30.5904	30.73627	5	5	106.71	3252400000	C1QB	Matrisome-associated	ECM-affiliated Proteins

188

30.83914	31.02419	31.23438	6	6	60.613	4291200000	C1QC	Matrisome-associated	ECM-affiliated Proteins
32.87992	32.88131	33.0901	11	11	142.19	29212000000	CLEC3A	Matrisome-associated	ECM-affiliated Proteins
28.63457	NaN	28.47588	2	2	87.663	1712600000	CLEC3B	Matrisome-associated	ECM-affiliated Proteins
27.03601	27.01063	NaN	21	21	194.85	4834300000	CSPG4	Matrisome-associated	ECM-affiliated Proteins
29.52707	28.75344	28.47104	8	8	151.35	1179500000	GREM1	Matrisome-associated	ECM-affiliated Proteins
28.28313	28.25966	28.48999	3	3	19.077	2403500000	CCL16	Matrisome-associated	Secreted Factors
31.16327	31.38087	31.4608	7	7	66.002	5736300000	FRZB	Matrisome-associated	Secreted Factors
27.28542	NaN	26.12776	5	5	43.366	2943100000	IL17B	Matrisome-associated	Secreted Factors
26.12825	NaN	27.26901	2	2	11.503	209070000	SFRP5	Matrisome-associated	Secreted Factors
NaN	27.63083	27.01041	32	16	323.31	23890000000	ACL	#N/A	#N/A
29.71076	29.7427	28.31709	10	10	116	18428000000	ACP5	#N/A	#N/A
29.67649	29.35252	NaN	22	1	62.619	18211000000	ACTA1	#N/A	#N/A
33.54697	33.56309	33.69696	28	9	323.31	2.5729E+11	ACTB	#N/A	#N/A
29.37198	29.32034	27.27711	31	23	323.31	11522000000	ACTN1	#N/A	#N/A
26.35864	26.82238	25.92125	4	4	28.648	491890000	AKR1A1	#N/A	#N/A
30.36609	30.38154	30.04049	40	36	323.31	92479000000	ALB	#N/A	#N/A
28.59071	29.15323	NaN	5	4	41.231	2872100000	ALDOC	#N/A	#N/A
27.51209	27.65704	NaN	6	6	52.133	1546600000	ANG	#N/A	#N/A
26.59818	27.03926	NaN	3	3	44.396	1560300000	ARPC3	#N/A	#N/A
30.32549	30.53325	30.3004	23	23	208.38	30242000000	ATP5A1	#N/A	#N/A
29.73875	29.98915	29.03197	15	15	209.77	19781000000	ATP5B	#N/A	#N/A
28.16452	27.72592	28.36499	4	4	56.292	2271600000	CALM1	#N/A	#N/A
30.23843	30.67985	30.46918	12	12	98.089	11352000000	CALR	#N/A	#N/A
28.83358	28.50184	28.01792	9	9	115.77	6296800000	CALU	#N/A	#N/A
26.84589	26.9438	26.70833	10	10	86.254	3408300000	CANX	#N/A	#N/A
25.66611	25.84127	NaN	12	12	98.273	2274400000	CCT3	#N/A	#N/A
27.51232	27.39084	26.93179	10	10	64.906	2755600000	CCT6	#N/A	#N/A
28.73989	29.25487	29.61868	4	4	31.318	2672500000	CDH1	#N/A	#N/A
26.72598	27.33433	NaN	16	16	158.89	4268700000	CERCAM	#N/A	#N/A
27.05331	27.6487	27.3463	6	6	41.07	934250000	PHGDH	#N/A	#N/A
31.85073	31.96013	31.46349	18	18	195.3	7843600000	CHI3L1	#N/A	#N/A
29.9901	29.85039	28.20965	20	20	323.31	27773000000	MAN1A1	#N/A	#N/A
28.46115	28.88951	28.00747	27	27	197.12	7037500000	CLTC	#N/A	#N/A
28.50843	28.10159	28.0018	17	17	323.31	6512300000	CLU	#N/A	#N/A
28.67738	29.12903	NaN	24	24	174.45	5735700000	COPA	#N/A	#N/A
28.30352	28.5386	27.28419	19	19	166.35	4734800000	COPB2	#N/A	#N/A
26.89435	27.68525	NaN	5	5	40.511	2004400000	COPG1	#N/A	#N/A
28.57697	28.98014	28.20494	8	8	80.684	927050000	CPXM1	#N/A	#N/A
29.60256	29.57735	29.59174	8	8	61.47	1630700000	CYTL1	#N/A	#N/A
28.71908	28.85852	28.85881	7	7	49.739	4142300000	DDOST	#N/A	#N/A
27.41836	27.28577	NaN	11	9	88.717	2432700000	DDX17	#N/A	#N/A
30.53353	30.40507	30.0397	32	29	323.31	30683000000	DES	#N/A	#N/A
26.49023	27.87947	26.2029	19	19	154.79	4473500000	DHX9	#N/A	#N/A
27.5969	27.82341	28.1882	5	5	35.43	1499100000	DPYSL2	#N/A	#N/A
32.43204	31.86765	32.4023	19	19	179.55	75663000000	EEF1A	#N/A	#N/A
29.07104	29.25147	28.99375	11	11	84.006	7925800000	EEF1G	#N/A	#N/A
30.44085	31.03151	30.00531	32	31	285.65	23747000000	EEF2	#N/A	#N/A
27.83726	27.37882	27.97136	18	8	182.43	7777200000	EIF4A1	#N/A	#N/A

30.14746	29.97992	30.45248	17	15	312.31	12254000000	ENO1	#N/A	#N/A
28.74577	28.66811	28.96389	4	2	31.89	3502000000	ENO3	#N/A	#N/A
29.47297	29.83855	29.54698	11	10	99.671	16645000000	FKBP10	#N/A	#N/A
28.78469	NaN	28.6513	12	11	87.956	7753900000	FKBP9	#N/A	#N/A
27.68398	28.38989	NaN	4	4	23.905	1576500000	FLNC	#N/A	#N/A
26.91764	27.6401	NaN	7	7	49.994	1953200000	GALE	#N/A	#N/A
29.3138	28.01473	28.29697	23	23	204.23	6940300000	GANAB	#N/A	#N/A
32.67072	33.13063	32.48996	21	19	323.31	78498000000	GAPDH	#N/A	#N/A
26.61765	26.31986	NaN	25	14	205.17	8535100000	GBF1	#N/A	#N/A
26.69737	26.93191	26.72507	9	4	29.635	473930000	GDI1	#N/A	#N/A
28.07989	27.91131	28.97358	10	5	73.41	2562800000	GDI2	#N/A	#N/A
28.54422	29.02707	28.52683	23	1	200.56	8690000000	GFPT1	#N/A	#N/A
28.37065	29.30014	27.58527	13	13	129.3	8457300000	GNB2L1	#N/A	#N/A
27.82857	28.12785	26.84434	10	10	85.308	3169300000	GOT2	#N/A	#N/A
27.32328	27.36836	NaN	9	9	65.849	1277500000	GPI	#N/A	#N/A
30.94433	30.74695	31.33069	29	29	276.11	28153000000	GRP-58	#N/A	#N/A
30.58585	30.40669	30.47305	19	19	202.4	10286000000	GSN	#N/A	#N/A
27.47143	27.38435	NaN	6	6	45.982	1628700000	H1FX	#N/A	#N/A
31.60302	30.56747	32.04013	5	1	104.75	38764000000	H2AFX	#N/A	#N/A
32.83019	32.81027	33.73832	10	10	71.035	1.165E+11	H3F3A	#N/A	#N/A
31.13944	30.53621	31.68119	10	10	155.19	1.0671E+11	HBA	#N/A	#N/A
32.50429	31.7906	32.36497	16	8	323.31	3.1071E+11	HBB	#N/A	#N/A
26.91787	27.15943	27.55618	15	15	115.23	2626600000	HDLBP	#N/A	#N/A
27.40592	27.82633	NaN	9	9	64.93	557920000	HHIPL2	#N/A	#N/A
31.11607	31.10368	32.18255	17	10	92.793	32376000000	HIST1H1B	#N/A	#N/A
33.8561	33.75304	34.88699	20	7	182.26	1.1772E+11	HIST1H1T	#N/A	#N/A
33.91874	33.63168	34.03878	13	3	214.7	2.1713E+11	HIST1H2BA	#N/A	#N/A
34.072	33.42492	33.33338	15	15	167.79	2.4993E+11	HIST1H4A	#N/A	#N/A
29.27886	28.98905	29.92719	13	3	21.645	9990000000	HIST3H2BB	#N/A	#N/A
NaN	27.68325	28.16686	8	4	68.695	2245500000	HNRNPA2B1	#N/A	#N/A
27.60357	27.61947	28.36328	15	15	118.35	4537100000	HNRNPM	#N/A	#N/A
29.31592	29.86586	28.73215	17	17	147.87	8575600000	HNRNPU	#N/A	#N/A
31.07527	31.13357	30.39693	26	17	323.31	30435000000	HSP90AA1	#N/A	#N/A
31.80132	31.80309	31.48779	33	31	323.31	48917000000	HSP90B1	#N/A	#N/A
27.8496	28.33743	26.87173	16	7	115.7	1844000000	HSPA1A	#N/A	#N/A
31.49496	31.29038	31.27042	34	32	323.31	46947000000	HSPA5	#N/A	#N/A
26.78019	28.10225	27.01924	16	16	162.89	10002000000	HSPD1	#N/A	#N/A
27.38311	26.89412	26.59106	9	0	68.35	9845100000	IGHG	#N/A	#N/A
32.98924	32.68288	33.09046	31	31	323.31	20828000000	IL1RAP	#N/A	#N/A
26.81787	27.09476	NaN	13	13	93.836	1090300000	IQGAP1	#N/A	#N/A
28.30691	28.57542	29.12317	8	8	69.481	934570000	K1C9	#N/A	#N/A
29.36317	29.36576	29.68913	12	6	120.81	2112900000	K2C1	#N/A	#N/A
28.07163	27.66085	28.81381	9	8	70.186	991110000	KRT10	#N/A	#N/A
30.6748	30.87884	30.80855	15	13	126.1	17606000000	LDHA	#N/A	#N/A
28.23375	28.52739	28.15649	8	3	44.76	2986600000	LDHB	#N/A	#N/A
32.24181	32.24329	32.19287	5	5	50.349	24717000000	LECT2	#N/A	#N/A
30.74951	30.75031	31.08474	30	1	288.53	13692000000	LMNA	#N/A	#N/A
30.26002	30.13675	29.69765	15	6	45.068	26403000000	LOC100154783	#N/A	#N/A

190

31.53691	31.72716	31.60731	27	27	323.31	86014000000	LOC100156689	#N/A	#N/A
37.36177	36.87062	35.88445	4	4	207.32	7.9947E+11	LOC100302368	#N/A	#N/A
30.66051	31.05381	31.23426	9	9	74.431	9184200000	LOC100510904	#N/A	#N/A
27.24254	27.86938	NaN	23	1	252.87	7078000000	LOC100516776	#N/A	#N/A
28.57924	NaN	29.605	7	7	68.388	11384000000	LOC100517228	#N/A	#N/A
27.34942	28.3598	NaN	11	11	93.326	3713100000	LOC100519984	#N/A	#N/A
30.32012	30.41901	29.65412	5	5	33.773	9254800000	LOC100523846	#N/A	#N/A
31.43847	31.32442	31.9951	12	12	126.82	18367000000	LOC100626701	#N/A	#N/A
31.86784	32.09544	30.96534	10	10	69.362	8739200000	LOC100737120	#N/A	#N/A
31.72501	31.41705	31.47354	15	6	264.78	57354000000	LOC100737887	#N/A	#N/A
26.93764	26.77744	27.07153	2	2	15.113	853750000	LOC100738863	#N/A	#N/A
28.69694	29.25813	27.99026	6	6	70.58	5517200000	LOC102164134	#N/A	#N/A
NaN	30.33127	29.84313	3	3	19.787	2841000000	LOC102165291	#N/A	#N/A
32.04238	31.46884	32.53095	14	14	220.35	22820000000	LOC102165939	#N/A	#N/A
30.09258	30.17176	31.22711	18	5	43.179	9224400000	LOC595122	#N/A	#N/A
28.40941	27.88943	27.11327	27	27	193.17	3279400000	LRP1	#N/A	#N/A
34.89938	34.48388	33.87298	16	4	323.31	64996000000	LYSC3	#N/A	#N/A
27.63277	28.18333	27.78463	9	9	70.856	1455300000	MFI2	#N/A	#N/A
28.46443	27.30382	27.73286	20	11	141.37	8078400000	MSN	#N/A	#N/A
28.40186	27.48577	NaN	5	5	70.046	5327000000	MYL6	#N/A	#N/A
25.35151	26.07063	NaN	4	4	27.518	475620000	MYO1C	#N/A	#N/A
28.84906	28.6102	29.256	8	4	61.131	8499500000	NME2	#N/A	#N/A
27.99156	27.45419	NaN	6	6	39.847	2721500000	NPM1	#N/A	#N/A
28.11709	28.42682	27.23517	16	16	152.03	5872600000	OAT	#N/A	#N/A
26.30172	26.10242	NaN	14	9	142.81	3284900000	PABPC1	#N/A	#N/A
25.93411	26.49881	NaN	8	7	50.692	1043500000	PAPSS1	#N/A	#N/A
30.17355	30.38463	30.57443	25	24	214.19	27433000000	PAPSS2	#N/A	#N/A
29.75774	30.18483	29.09821	31	31	282.8	19455000000	PDIA4	#N/A	#N/A
29.57933	29.32135	30.19202	13	13	184.03	8820900000	PDI-P5	#N/A	#N/A
27.50983	27.4929	26.74689	11	8	76.408	1665000000	PFKL	#N/A	#N/A
28.58068	28.71614	28.40617	13	11	107.3	1649000000	PFKP	#N/A	#N/A
29.11376	29.27673	29.99712	12	12	138.61	7244700000	PGAM1	#N/A	#N/A
30.62767	30.84229	30.54757	22	0	237.22	12687000000	PGK1	#N/A	#N/A
31.5993	31.87595	32.47528	18	18	188.41	29736000000	PKLR	#N/A	#N/A
29.59523	29.21799	30.16159	9	8	89.431	16435000000	PPIA	#N/A	#N/A
28.21127	28.58172	NaN	8	5	49.279	6868200000	PRDX1	#N/A	#N/A
28.13193	28.13001	27.70154	6	6	42.555	2883900000	PRDX2	#N/A	#N/A
29.97254	29.94712	28.60752	10	7	86.057	10038000000	PRDX4	#N/A	#N/A
29.20562	30.11917	28.40402	6	6	40.881	1882500000	PRDX6	#N/A	#N/A
27.81427	26.92343	26.87361	11	11	130.81	3223100000	PRKCSH	#N/A	#N/A
25.67047	25.99624	NaN	4	4	27.646	629210000	PRPS2	#N/A	#N/A
26.81336	NaN	27.11297	3	3	18.715	201080000	PXYLP1	#N/A	#N/A
27.97049	27.31562	27.39067	10	10	74.396	4235300000	RAN	#N/A	#N/A
30.10974	29.69056	29.33208	5	5	45.408	2722700000	RARRES2	#N/A	#N/A
28.50971	28.80698	28.69126	8	8	142.03	8716200000	RCN3	#N/A	#N/A
31.52	30.94196	31.43151	8	8	163.62	10890000000	RNASE4	#N/A	#N/A
29.30917	29.5583	29.59674	11	11	145.69	11088000000	RPL10	#N/A	#N/A
28.3198	NaN	28.78821	7	2	64.965	5413100000	RPL10A	#N/A	#N/A

28.14482	28.43595	29.51788	10	10	108.75	5713200000	RPL11	#N/A	#N/A
29.25163	29.1121	29.71741	8	8	80.759	10270000000	RPL13	#N/A	#N/A
28.71276	29.76387	29.25627	13	13	80.826	8108200000	RPL13A	#N/A	#N/A
29.26915	29.08134	29.2488	9	9	63.036	10171000000	RPL14	#N/A	#N/A
28.44608	29.23569	NaN	8	8	70.409	9378000000	RPL15	#N/A	#N/A
29.43432	29.57744	30.15025	7	7	108.74	15583000000	RPL18	#N/A	#N/A
29.35708	29.03178	NaN	11	11	78.765	10878000000	RPL18A	#N/A	#N/A
26.77718	27.11068	28.16466	5	5	68.931	5758500000	RPL19	#N/A	#N/A
29.51122	29.42946	29.44608	7	6	63.332	8971600000	RPL22	#N/A	#N/A
27.2261	27.07551	NaN	3	3	21.804	2315600000	RPL23	#N/A	#N/A
27.6083	27.71745	NaN	9	9	64.07	7681600000	RPL23A	#N/A	#N/A
27.04635	27.67889	NaN	5	5	36.69	6580800000	RPL24	#N/A	#N/A
27.80329	28.14807	27.92914	8	8	63.301	6320600000	RPL27	#N/A	#N/A
29.61523	29.90067	30.75772	17	17	135.71	12049000000	RPL3	#N/A	#N/A
27.94218	28.26857	28.02512	7	7	60.51	3751600000	RPL30	#N/A	#N/A
29.2184	29.14287	30.14029	9	9	55.756	9409000000	RPL35A	#N/A	#N/A
29.13563	28.23023	30.06021	22	10	186.3	17135000000	RPL4	#N/A	#N/A
28.96097	28.89209	28.90486	10	10	88.252	8693100000	RPL5	#N/A	#N/A
30.43619	30.49629	30.76809	18	18	225.46	40983000000	RPL6	#N/A	#N/A
29.05636	29.64065	27.98506	14	7	108.18	13182000000	RPL7	#N/A	#N/A
29.06992	29.26944	29.17358	6	6	48.737	11490000000	RPL7A	#N/A	#N/A
29.27888	29.63093	29.96884	13	13	98.211	19941000000	RPL8	#N/A	#N/A
28.50764	29.05204	27.04562	6	6	44.379	6601000000	RPL9	#N/A	#N/A
28.44482	28.31207	NaN	8	8	79.191	5270300000	RPLP0	#N/A	#N/A
29.10167	29.41663	28.94053	17	17	134.04	7482500000	RPN1	#N/A	#N/A
29.14029	29.82789	29.52172	14	14	99.938	11454000000	RPS11	#N/A	#N/A
28.23713	28.15393	NaN	6	6	45.377	3466200000	RPS13	#N/A	#N/A
30.0575	30.42832	30.0817	12	12	91.65	14745000000	RPS16	#N/A	#N/A
28.25997	27.65185	NaN	3	3	21.802	5780300000	RPS17	#N/A	#N/A
29.1116	29.54988	NaN	13	13	107.33	11447000000	RPS18	#N/A	#N/A
27.49899	27.41119	28.58978	10	10	90.457	3364900000	RPS19	#N/A	#N/A
29.70197	29.90441	29.80226	12	12	83.13	12547000000	RPS2	#N/A	#N/A
28.51171	28.27799	28.53382	4	4	32.479	4437700000	RPS20	#N/A	#N/A
27.63027	28.1155	NaN	6	6	53.499	11253000000	RPS25	#N/A	#N/A
29.8752	30.33756	28.88792	21	21	172.52	15605000000	RPS3	#N/A	#N/A
30.08512	30.45973	29.99577	18	18	141.28	17611000000	RPS3A	#N/A	#N/A
30.05414	30.09472	30.5538	16	16	157.93	21434000000	Rps4	#N/A	#N/A
28.34621	NaN	28.7024	8	8	86.23	5280900000	RPS5	#N/A	#N/A
28.6804	29.65395	29.0352	15	7	124.15	13145000000	RPS6	#N/A	#N/A
29.34993	29.59295	30.33639	13	13	179.15	11049000000	RPS8	#N/A	#N/A
28.84781	29.30493	27.86744	13	2	85.755	9704400000	RPS9	#N/A	#N/A
28.28065	28.95543	27.68592	11	11	149.77	4991100000	RPSA	#N/A	#N/A
28.74727	28.93787	28.30008	26	26	234.95	9770500000	RRBP1	#N/A	#N/A
28.93019	29.29691	28.81351	13	13	123.39	4748600000	SCIN	#N/A	#N/A
26.26275	26.43111	NaN	5	5	32.853	819690000	SEPT9	#N/A	#N/A
28.3887	28.806	NaN	9	3	60.283	11981000000	SLC25A6	#N/A	#N/A
27.43651	27.33705	28.00667	4	4	25.233	478390000	SRSF1	#N/A	#N/A
27.44237	27.56376	NaN	2	2	11.84	1173800000	SRSF2	#N/A	#N/A

26.9438	27.17217	NaN	2	2	19.876	439790000	SRSF7	#N/A	#N/A
26.94827	27.09456	26.40056	4	4	34.982	3151900000	SSR4	#N/A	#N/A
28.52099	28.37844	29.11317	13	13	98.54	3383500000	TKT	#N/A	#N/A
28.28445	27.4753	28.88256	5	5	39.731	3811200000	TMED10	#N/A	#N/A
28.51009	28.72722	27.99405	9	9	116.04	3631600000	TPI1	#N/A	#N/A
30.73925	30.36328	30.11706	15	0	301.26	28470000000	TUBA1B	#N/A	#N/A
30.72029	30.94942	29.79707	17	2	263.11	33599000000	TUBB	#N/A	#N/A
26.53677	27.09325	26.29365	17	3	36.604	911570000	TUBB1	#N/A	#N/A
29.81317	30.25462	29.45617	20	20	268.3	17166000000	UGDH	#N/A	#N/A
29.10059	29.54955	28.62226	16	16	121.36	2597000000	UGP2	#N/A	#N/A
27.42502	28.21739	NaN	7	7	73.542	4733800000	VDAC2	#N/A	#N/A
26.5077	26.71424	NaN	7	2	42.662	1175400000	YWHAB	#N/A	#N/A
28.10335	28.32006	27.25241	7	5	128.12	1643100000	YWHAZ	#N/A	#N/A
32.97946	32.8334	33.35928	35	35	323.31	1.1865E+11	Uncharacterized	#N/A	#N/A
30.18423	29.72607	30.37067	24	15	247.17	26045000000	Uncharacterized	#N/A	#N/A
31.13479	31.48015	30.9262	12	12	162.18	40411000000	Uncharacterized	#N/A	#N/A
31.36448	31.39703	31.92142	14	14	159.62	40425000000	Uncharacterized	#N/A	#N/A
30.40832	30.05659	30.58388	4	4	38.913	33554000000	Uncharacterized	#N/A	#N/A

9.1.2. Growth Plate Proteins

LFQ intensity GP_1	LFQ intensity GP_2	LFQ intensity GP_3	Peptides	Unique peptides	Score	Intensity	Gene name	Division Matrisome	Subcategory Matrisome
31.86964	31.8814	31.6793	6	6	68.709	22808000000	COL10A1	Core matrisome	Collagens
31.4565	31.47798	31.69839	15	14	191.17	20304000000	COL11A1	Core matrisome	Collagens
34.72243	34.7448	34.49816	39	38	323.31	2.3936E+11	COL11A2	Core matrisome	Collagens
29.84313	29.83189	30.15388	8	3	80.797	9189500000	COL15A1	Core matrisome	Collagens
30.76596	29.71094	29.06856	4	4	31.884	10193000000	COL1A1	Core matrisome	Collagens
31.61048	31.57172	31.32726	13	13	93.924	20345000000	COL1A2	Core matrisome	Collagens
27.16394	26.91354	NaN	3	3	19.264	995870000	COL27A1	Core matrisome	Collagens
34.98261	35.09969	34.65598	17	16	323.31	2.6774E+11	COL2A1	Core matrisome	Collagens
29.22621	28.74942	28.34782	5	5	39.442	3531900000	COL2A1	Core matrisome	Collagens
28.57932	28.54753	28.47022	3	3	20.092	2514200000	COL3A1	Core matrisome	Collagens
31.0922	30.27653	30.12509	12	12	101.03	17787000000	COL6A1	Core matrisome	Collagens
27.7267	27.69929	NaN	6	6	82.783	2976300000	COL6A1	Core matrisome	Collagens
30.08347	29.82488	29.70956	3	3	39.012	12479000000	COL6A1	Core matrisome	Collagens
31.61127	31.85133	31.6842	29	29	297.87	51108000000	COL6A2	Core matrisome	Collagens
33.5103	33.46405	33.56751	122	122	323.31	1.7419E+11	COL6A3	Core matrisome	Collagens
34.08686	34.02952	34.07758	21	21	323.31	1.5189E+11	COL9A1	Core matrisome	Collagens
32.46449	32.7317	32.76129	5	5	82.195	48229000000	COL9A2	Core matrisome	Collagens
28.68949	28.83506	29.62207	9	9	59.91	6513200000	COL16A1	Core matrisome	Collagens
NaN	25.30215	26.3369	5	5	37.135	266920000	AGRN	Core matrisome	ECM Glycoproteins
27.55764	NaN	27.56986	30	2	96.405	2312400000	COMP	Core matrisome	ECM Glycoproteins
35.4087	35.37205	35.21056	41	13	323.31	5.5647E+11	COMP	Core matrisome	ECM Glycoproteins
NaN	27.38755	27.3407	3	3	24.892	658540000	CTGF	Core matrisome	ECM Glycoproteins
30.50076	30.46509	30.83289	6	6	67.35	19448000000	CTHRC1	Core matrisome	ECM Glycoproteins
32.43584	32.43445	32.44285	15	15	153.38	45634000000	EDIL3	Core matrisome	ECM Glycoproteins
27.72605	27.68472	27.82675	3	3	30.724	1966700000	EFEMP2	Core matrisome	ECM Glycoproteins

28.07173	27.05992	NaN	12	12	96.492	1429300000	EMILIN1	Core matrisome	ECM Glycoproteins
29.90999	29.84417	30.00838	17	17	136.14	21175000000	FBLN7	Core matrisome	ECM Glycoproteins
30.35867	30.32539	30.14151	11	6	43.315	7939300000	FGA	Core matrisome	ECM Glycoproteins
33.81373	33.74495	33.73217	33	33	323.31	89384000000	FGB	Core matrisome	ECM Glycoproteins
27.18641	26.78856	26.74484	1	1	20.756	769450000	FGB	Core matrisome	ECM Glycoproteins
35.42264	35.40768	35.37347	88	88	323.31	3.4305E+11	FN1	Core matrisome	ECM Glycoproteins
29.08096	29.25836	29.02675	6	6	46.117	3586700000	IBSP	Core matrisome	ECM Glycoproteins
27.11486	26.84194	26.74881	7	7	47.443	765570000	LAMA4	Core matrisome	ECM Glycoproteins
27.36169	26.73725	26.77994	9	9	61.165	977500000	LAMB2	Core matrisome	ECM Glycoproteins
32.70837	32.74819	32.39922	39	39	323.31	2.962E+11	MATN1	Core matrisome	ECM Glycoproteins
29.93115	30.22986	30.30954	12	12	117.15	10296000000	MATN2	Core matrisome	ECM Glycoproteins
35.80222	35.58212	35.25053	33	33	323.31	5.7601E+11	MATN3	Core matrisome	ECM Glycoproteins
29.42584	29.22568	29.84169	28	28	259.09	36329000000	MATN4	Core matrisome	ECM Glycoproteins
32.78384	32.7243	32.82618	24	24	274.88	60988000000	MFGE8	Core matrisome	ECM Glycoproteins
26.28673	NaN	26.15275	8	8	79.437	1390000000	PCOLCE	Core matrisome	ECM Glycoproteins
26.68097	26.99981	26.5225	8	8	61.368	1149700000	PCOLCE2	Core matrisome	ECM Glycoproteins
31.19712	31.32646	31.02518	9	9	79.112	17480000000	SPARC	Core matrisome	ECM Glycoproteins
28.41183	28.2502	28.56456	11	11	82.189	3741200000	SRPX	Core matrisome	ECM Glycoproteins
25.87488	26.38364	25.86964	23	23	197.48	9971900000	SRPX2	Core matrisome	ECM Glycoproteins
27.76421	28.29754	28.00421	28	28	289.22	33968000000	TGFBI	Core matrisome	ECM Glycoproteins
34.71365	34.62402	34.63011	62	61	323.31	3.0238E+11	THBS1	Core matrisome	ECM Glycoproteins
31.43072	31.24768	31.42397	18	16	130.19	22253000000	THBS3	Core matrisome	ECM Glycoproteins
31.51789	31.43624	31.54954	64	18	323.31	80969000000	TNC	Core matrisome	ECM Glycoproteins
30.44312	30.49123	30.63504	22	22	323.31	20351000000	VIT	Core matrisome	ECM Glycoproteins
29.80852	29.73379	29.88495	11	11	103.91	5737200000	VTN	Core matrisome	ECM Glycoproteins
33.49334	33.61204	33.53612	21	21	306.7	75371000000	FGG	Core matrisome	ECM Glycoproteins
36.81024	36.73618	36.44648	58	44	323.31	1.355E+12	ACAN	Core matrisome	Proteoglycans
36.52052	36.35834	35.9529	40	40	323.31	8.169E+11	BGN	Core matrisome	Proteoglycans
33.35192	33.34863	33.10676	28	28	323.31	1.0685E+11	CHAD	Core matrisome	Proteoglycans
30.44983	30.62706	30.70561	22	22	241.79	17083000000	CHADL	Core matrisome	Proteoglycans
32.34226	32.33103	32.03184	35	35	323.31	1.1239E+11	DCN	Core matrisome	Proteoglycans
28.46205	28.33735	28.20914	15	15	148.23	14444000000	EPYC	Core matrisome	Proteoglycans
34.86092	34.84973	34.79188	18	17	323.31	4.5392E+11	FMOD	Core matrisome	Proteoglycans
37.12328	37.12232	36.78877	35	35	323.31	1.1332E+12	HAPLN1	Core matrisome	Proteoglycans
33.24545	33.3598	33.21752	43	43	323.31	95011000000	HSPG2	Core matrisome	Proteoglycans
27.44624	27.18168	NaN	6	6	43.417	940010000	LUM	Core matrisome	Proteoglycans
35.23292	35.32456	35.24693	25	25	323.31	3.0026E+11	PRELP	Core matrisome	Proteoglycans
27.05051	NaN	27.03297	12	12	78.173	5350600000	OGN	Core matrisome	Proteoglycans
28.08618	28.27177	28.14424	3	3	25.29	1755100000	PRG3	Core matrisome	Proteoglycans
29.30704	29.25476	29.31685	19	1	141.52	4029300000	A2M	Matrisome-associated	ECM Regulators
29.43724	28.78687	29.14972	10	10	76.111	3949200000	CD109	Matrisome-associated	ECM Regulators
27.32406	27.14433	27.43928	4	4	25.405	1035400000	CTSD	Matrisome-associated	ECM Regulators
27.53475	27.34036	27.64334	4	4	28.92	1157500000	CTSG	Matrisome-associated	ECM Regulators
27.66445	27.49823	27.6452	5	5	30.51	1205000000	CTSK	Matrisome-associated	ECM Regulators
28.23361	27.8337	28.13717	5	5	45.202	1763100000	ELANE	Matrisome-associated	ECM Regulators
28.31993	28.51717	28.41639	6	6	64.969	2173500000	F10	Matrisome-associated	ECM Regulators
31.34647	31.15225	31.39872	20	20	137.27	15980000000	F13A1	Matrisome-associated	ECM Regulators
26.61428	26.80993	26.9608	6	6	94.43	649080000	F2	Matrisome-associated	ECM Regulators

26.96521	26.8947	26.86242	5	5	30.383	781010000	HRG	Matrisome-associated	ECM Regulators
27.61723	27.38813	27.41321	6	6	41.522	1867200000	HTRA1	Matrisome-associated	ECM Regulators
26.01822	26.22992	26.23325	5	5	30.835	455390000	HTRA3	Matrisome-associated	ECM Regulators
26.8114	26.79984	27.13878	6	6	40.787	776720000	ITIH1	Matrisome-associated	ECM Regulators
26.4123	26.38237	26.7397	5	5	34.333	574570000	ITIH2	Matrisome-associated	ECM Regulators
27.34765	27.15316	27.24209	8	2	71.405	955180000	ITIH4	Matrisome-associated	ECM Regulators
26.84637	26.86773	26.73337	8	2	14.209	707960000	ITIH4	Matrisome-associated	ECM Regulators
30.5001	30.47711	30.66958	25	24	238.19	18480000000	LOXL3	Matrisome-associated	ECM Regulators
27.53519	27.8259	27.64231	7	6	103.44	1350600000	LOXL4	Matrisome-associated	ECM Regulators
27.8444	27.88116	28.03118	11	11	91.608	1540800000	MMP13	Matrisome-associated	ECM Regulators
27.51676	27.83141	28.05894	10	10	77.139	1743600000	MMP2	Matrisome-associated	ECM Regulators
27.62687	27.61512	27.87085	7	7	43.028	1295800000	MMP9	Matrisome-associated	ECM Regulators
31.67741	31.6751	31.51911	20	14	253.75	25164000000	P4HA1	Matrisome-associated	ECM Regulators
29.12832	29.29872	29.50457	14	1	164.71	5652300000	P4HA2	Matrisome-associated	ECM Regulators
27.75678	27.36695	27.61253	7	7	46.817	1335600000	PAMR1	Matrisome-associated	ECM Regulators
30.02406	29.79129	30.10986	19	19	190.8	7962100000	PLOD1	Matrisome-associated	ECM Regulators
31.96041	31.95989	31.88143	30	30	323.31	34482000000	Plod2	Matrisome-associated	ECM Regulators
30.06805	29.86781	30.08119	13	13	96.305	6500600000	PLOD3	Matrisome-associated	ECM Regulators
27.34934	27.44624	27.48116	7	7	48.654	1086400000	SERPINC1	Matrisome-associated	ECM Regulators
29.02327	29.17724	29.05391	14	14	132.22	4556300000	SERPINF1	Matrisome-associated	ECM Regulators
35.60673	35.64528	35.25188	18	18	323.31	3.3455E+11	SERPINH1	Matrisome-associated	ECM Regulators
27.5534	27.79947	28.05719	9	9	89.398	1780800000	TGM2	Matrisome-associated	ECM Regulators
30.17081	30.22699	30.06394	13	13	158.01	8819200000	LEPRE1	Matrisome-associated	ECM Regulators
26.7252	NaN	26.37607	3	3	19.936	495150000	LEPREL2	Matrisome-associated	ECM Regulators
29.68924	29.62697	29.56518	15	15	122.04	7705600000	SERPINB9	Matrisome-associated	ECM Regulators
30.26338	29.81638	30.25169	13	13	173.79	7681200000	ANXA1	Matrisome-associated	ECM-affiliated Proteins
27.87467	27.85317	27.91359	9	9	70.727	1791400000	ANXA11	Matrisome-associated	ECM-affiliated Proteins
32.21393	32.22866	32.23914	29	29	323.31	35792000000	ANXA2	Matrisome-associated	ECM-affiliated Proteins
30.03957	30.40507	30.29702	9	8	103.12	10727000000	ANXA4	Matrisome-associated	ECM-affiliated Proteins
32.66708	32.66643	32.40561	21	20	293.02	46716000000	ANXA5	Matrisome-associated	ECM-affiliated Proteins
30.7024	30.50398	30.48164	31	31	242.73	12276000000	ANXA6	Matrisome-associated	ECM-affiliated Proteins
31.3205	30.4074	30.02115	16	16	129.91	10928000000	ANXA8	Matrisome-associated	ECM-affiliated Proteins
28.34024	28.1053	28.5023	6	6	48.191	2113500000	C1QTNF3	Matrisome-associated	ECM-affiliated Proteins
29.93649	30.0177	30.14601	9	9	112	6667900000	CLEC11A	Matrisome-associated	ECM-affiliated Proteins
30.97965	31.01319	31.14224	11	11	142.19	29212000000	CLEC3A	Matrisome-associated	ECM-affiliated Proteins
27.43118	27.30583	27.42806	2	2	87.663	1712600000	CLEC3B	Matrisome-associated	ECM-affiliated Proteins
29.56518	29.41272	29.47785	21	21	194.85	4834300000	CSPG4	Matrisome-associated	ECM-affiliated Proteins
25.20717	25.26567	NaN	2	2	11.626	207290000	HPX	Matrisome-associated	ECM-affiliated Proteins
27.25629	27.44443	NaN	2	2	14.171	802540000	LGALS1	Matrisome-associated	ECM-affiliated Proteins
27.41941	27.73389	27.81464	4	4	26.907	1295200000	LMAN1	Matrisome-associated	ECM-affiliated Proteins
29.91997	29.79854	29.8561	17	16	285.18	5931200000	ANGPTL2	Matrisome-associated	Secreted Factors
28.34807	28.48416	28.43865	7	7	48.848	2235900000	ANGPTL5	Matrisome-associated	Secreted Factors
28.20969	28.06322	28.11615	3	3	19.077	2403500000	CCL16	Matrisome-associated	Secreted Factors
28.50832	28.83723	28.79272	5	5	43.366	2943100000	IL17B	Matrisome-associated	Secreted Factors
27.60717	27.43333	27.28374	2	2	15.483	1119300000	S100A12	Matrisome-associated	Secreted Factors
28.85332	28.34236	27.83117	4	4	28.869	2188500000	S100A8	Matrisome-associated	Secreted Factors
27.90438	27.82917	27.3864	4	4	29.775	1405700000	S100A9	Matrisome-associated	Secreted Factors
29.14664	28.26222	28.29255	3	3	38.991	2825200000	S100A10	Matrisome-associated	Secreted Factors

31.50323	31.3741	32.4775	32	16	323.31	23890000000	ACL	#N/A	#N/A
28.40718	28.47073	28.71954	10	10	120.58	2439900000	ACO2	#N/A	#N/A
24.50567	24.38476	24.31299	2	2	12.458	132160000	ACOT9	#N/A	#N/A
31.17003	31.28234	31.66941	10	10	116	18428000000	ACP5	#N/A	#N/A
31.2302	31.40806	31.27075	22	1	62.619	18211000000	ACTA1	#N/A	#N/A
34.96073	35.22834	35.03014	28	9	323.31	2.5729E+11	ACTB	#N/A	#N/A
30.62235	30.56837	30.66391	31	23	323.31	11522000000	ACTN1	#N/A	#N/A
27.39591	27.38862	27.31207	4	4	36.755	1020900000	ACTR2	#N/A	#N/A
28.14676	28.19075	28.45525	6	6	44.15	2250900000	ACTR3	#N/A	#N/A
25.76152	26.10079	NaN	4	4	23.815	326700000	AHNAK	#N/A	#N/A
32.43261	32.47528	32.3395	11	11	133.55	34306000000	AHSG	#N/A	#N/A
26.14235	NaN	26.11265	3	3	19.016	399960000	AK1	#N/A	#N/A
25.85201	25.71552	25.88143	4	4	28.648	491890000	AKR1A1	#N/A	#N/A
26.09394	NaN	26.67425	4	4	28.795	431010000	AKT1	#N/A	#N/A
30.407	30.28571	30.18092	6	2	13.301	7975300000	ALB	#N/A	#N/A
33.91421	33.70718	33.67167	40	36	323.31	92479000000	ALB	#N/A	#N/A
27.29973	27.08091	27.53208	8	8	59.935	1137800000	ALDH18A1	#N/A	#N/A
27.97224	28.1247	28.3333	8	8	54.406	1939800000	ALDH1A1	#N/A	#N/A
27.74817	28.05424	28.11664	5	4	41.231	2872100000	ALDOC	#N/A	#N/A
29.22741	29.27881	29.81293	4	2	31.685	4330600000	ALPL	#N/A	#N/A
27.51345	27.549	27.78594	6	6	52.133	1546600000	ANG	#N/A	#N/A
25.66568	NaN	25.75277	2	2	14.09	314070000	AP1B1	#N/A	#N/A
28.76572	28.83397	28.86142	9	9	65.026	2843300000	APOA1	#N/A	#N/A
28.38496	28.48999	28.67539	5	5	43.398	2724500000	APOD	#N/A	#N/A
27.89053	27.86396	28.13305	7	7	46.807	1532200000	APOE	#N/A	#N/A
27.59939	27.91199	27.65226	6	6	54.459	1312500000	APOH	#N/A	#N/A
28.12544	28.03852	28.27586	9	9	81.385	2176200000	ARCN1	#N/A	#N/A
29.03514	29.21313	29.30767	3	2	28.757	3675200000	ARF4	#N/A	#N/A
NaN	25.48533	25.7572	6	6	52.163	346350000	ARHGDIA	#N/A	#N/A
28.05284	27.63464	27.92093	7	7	54.992	1463400000	ARPC1B	#N/A	#N/A
27.67553	27.9921	27.48078	3	3	44.396	1560300000	ARPC3	#N/A	#N/A
27.32096	26.96576	26.70741	3	3	24.318	809150000	ARPC4	#N/A	#N/A
26.25915	NaN	26.72546	7	7	53.157	459640000	ATP12A	#N/A	#N/A
31.97354	32.04908	31.99112	23	23	208.38	30242000000	ATP5A1	#N/A	#N/A
31.24949	31.35574	31.66936	15	15	209.77	19781000000	ATP5B	#N/A	#N/A
27.27985	28.9911	28.83204	3	3	21.885	2039300000	ATP5H	#N/A	#N/A
25.96825	25.91798	NaN	2	2	14.475	355080000	ATP5J2	#N/A	#N/A
28.86573	28.9223	28.95407	5	5	49.189	3055600000	ATP5O	#N/A	#N/A
27.64293	27.84631	28.24095	8	8	112.34	1492800000	ATP6V1A	#N/A	#N/A
26.00288	25.93944	NaN	5	5	32.906	363630000	ATP6V1B1	#N/A	#N/A
28.55248	28.50714	28.84903	6	6	60.611	2449800000	AZU1	#N/A	#N/A
26.69869	26.603	26.71135	5	5	33.538	675660000	BAT1	#N/A	#N/A
26.73828	26.84733	26.86124	6	6	42.834	735130000	BF	#N/A	#N/A
28.42878	28.50211	28.43269	3	3	20.136	2337200000	BSG	#N/A	#N/A
25.16909	25.09225	25.44881	3	3	18.108	241470000	BUB3	#N/A	#N/A
25.5576	NaN	25.60659	3	3	18.631	251890000	BZW1	#N/A	#N/A
26.94257	26.84326	27.0403	2	2	21.04	773410000	C19ORF10	#N/A	#N/A
24.60371	24.83205	NaN	2	2	13.026	182530000	C2ORF40	#N/A	#N/A

196

28.88963	28.97378	29.09966	19	5	120.82	3205600000	C3	#N/A	#N/A
NaN	24.20142	23.55274	2	2	12.895	64246000	C4	#N/A	#N/A
26.16638	NaN	26.51904	3	3	19.639	481590000	C4BPA	#N/A	#N/A
27.19141	NaN	27.07439	6	6	44.987	760990000	C9	#N/A	#N/A
25.49201	25.43705	26.25838	3	3	20.858	331510000	CA2	#N/A	#N/A
28.25354	27.89678	27.7916	4	4	56.292	2271600000	CALM1	#N/A	#N/A
30.42882	30.17021	30.26081	12	12	98.089	11352000000	CALR	#N/A	#N/A
29.77508	29.60851	29.64979	9	9	115.77	6296800000	CALU	#N/A	#N/A
28.87367	29.01654	28.70091	10	10	86.254	3408300000	CANX	#N/A	#N/A
26.76471	26.8853	NaN	3	3	24.638	599280000	CAPZA	#N/A	#N/A
26.53769	26.73867	26.79724	6	6	42.979	656780000	CAT	#N/A	#N/A
27.71529	27.86189	27.81207	5	5	42.405	1382500000	CBF-A	#N/A	#N/A
29.01361	29.70393	29.73656	17	17	133.16	4991400000	CCDC80	#N/A	#N/A
28.57672	28.15943	28.44825	12	12	98.273	2274400000	CCT3	#N/A	#N/A
28.28542	27.92892	28.23713	8	8	51.005	2101400000	CCT4	#N/A	#N/A
27.56776	27.13516	27.42246	9	9	60.341	1203000000	CCT5	#N/A	#N/A
28.54252	28.14122	28.53263	10	10	64.906	2755600000	CCT6	#N/A	#N/A
27.84781	28.03354	28.06564	7	7	49.133	1575800000	CCT7	#N/A	#N/A
29.21803	29.19369	29.15704	19	19	141.11	3790100000	CCT8	#N/A	#N/A
25.43679	25.44714	25.82138	2	2	24.466	397030000	CD59	#N/A	#N/A
27.42454	27.33194	27.67714	4	4	31.318	2672500000	CDH1	#N/A	#N/A
29.3522	29.16907	29.42392	16	16	158.89	4268700000	CERCAM	#N/A	#N/A
27.89342	28.30587	28.46533	2	2	16.093	1980600000	CFL1	#N/A	#N/A
NaN	26.35232	26.53478	6	6	41.07	934250000	PHGDH	#N/A	#N/A
25.89053	NaN	25.86067	3	3	20.406	330700000	CHID1	#N/A	#N/A
31.92476	31.91784	32.03148	20	20	323.31	27773000000	CKAP4	#N/A	#N/A
30.09258	29.68407	29.70905	27	27	197.12	7037500000	CLTC	#N/A	#N/A
29.8269	29.65634	29.70901	17	17	323.31	6512300000	CLU	#N/A	#N/A
27.05258	27.04874	27.2516	5	5	34.394	948810000	CMPK1	#N/A	#N/A
26.12692	26.0975	26.44338	4	4	27.778	476530000	COLGALT2	#N/A	#N/A
29.35628	29.38809	29.65294	24	24	174.45	5735700000	COPA	#N/A	#N/A
27.37227	27.39468	27.34443	8	8	57.849	1121500000	COPB1	#N/A	#N/A
29.37507	28.91701	29.0961	19	19	166.35	4734800000	COPB2	#N/A	#N/A
27.09999	27.21206	27.26356	5	5	37.494	1068900000	COPE	#N/A	#N/A
27.88011	27.79092	27.84452	5	5	40.511	2004400000	COPG1	#N/A	#N/A
25.79124	26.12504	NaN	4	4	28.803	369620000	COX4I1	#N/A	#N/A
NaN	26.14094	26.3582	4	4	26.234	451130000	COX5A	#N/A	#N/A
27.17646	26.98087	27.00785	8	8	56.518	919730000	CPNE1	#N/A	#N/A
28.66034	28.49732	28.59099	4	4	30.451	2540000000	CRP	#N/A	#N/A
NaN	27.56993	27.82742	3	3	22.305	1197100000	CRTAP	#N/A	#N/A
30.4716	29.79551	29.45374	10	10	94.573	6978300000	CRYAB	#N/A	#N/A
27.89741	28.23695	28.06512	8	8	65.16	1973600000	CYB5R3	#N/A	#N/A
25.98235	26.00717	26.42905	5	5	36.617	463380000	CYP20A1	#N/A	#N/A
27.03265	NaN	26.90495	6	6	37.508	745600000	DARS	#N/A	#N/A
28.80104	29	29.03042	7	7	49.739	4142300000	DDOST	#N/A	#N/A
28.18002	28.1821	28.42858	11	9	88.717	2432700000	DDX17	#N/A	#N/A
27.4807	27.51028	27.66614	11	10	65.712	1240400000	DDX3X	#N/A	#N/A
25.78699	NaN	25.78816	5	3	17.743	462450000	DDX5	#N/A	#N/A

197

32.15777	32.00825	31.77702	32	29	323.31	30683000000	DES	#N/A	#N/A
25.25122	25.15395	25.61248	2	2	14.279	247520000	DHRS4	#N/A	#N/A
29.64349	28.64258	29.31471	19	19	154.79	4473500000	DHX9	#N/A	#N/A
25.32694	NaN	25.61813	3	3	20.489	251240000	DLAT	#N/A	#N/A
26.58864	26.58778	26.7078	5	5	33.428	666670000	DLD	#N/A	#N/A
26.04987	26.28003	26.50927	6	6	40.833	469030000	DLST	#N/A	#N/A
27.2154	26.91957	27.29518	5	5	35.43	1499100000	DPYSL2	#N/A	#N/A
33.27156	33.31352	32.94864	19	19	179.55	75663000000	EEF1A	#N/A	#N/A
27.09909	26.91991	27.05206	5	2	58.286	784700000	EEF1D	#N/A	#N/A
29.96444	29.83348	29.87129	11	11	84.006	7925800000	EEF1G	#N/A	#N/A
31.58679	31.50711	31.56129	32	31	285.65	23747000000	EEF2	#N/A	#N/A
25.10282	NaN	25.23411	4	4	25.045	180380000	EHD2	#N/A	#N/A
27.18234	27.38121	27.17255	6	6	42.795	974910000	EIF2S3	#N/A	#N/A
26.86938	26.66452	27.04656	7	7	40.93	748690000	EIF3A	#N/A	#N/A
26.73324	26.65935	26.59335	5	5	28.817	633480000	EIF3B	#N/A	#N/A
NaN	25.4587	25.59181	3	3	16.279	181300000	EIF3E	#N/A	#N/A
NaN	25.9662	26.22742	3	3	20.737	403240000	EIF3I	#N/A	#N/A
30.4179	30.03708	29.87505	18	8	182.43	7777200000	EIF4A1	#N/A	#N/A
26.05753	NaN	26.42252	3	3	23.483	395500000	ELAVL1	#N/A	#N/A
30.70668	30.60267	30.41397	17	15	312.31	12254000000	ENO1	#N/A	#N/A
28.39354	28.61646	28.66492	4	2	31.89	3502000000	ENO3	#N/A	#N/A
28.55753	28.14967	28.26074	11	11	82.059	2072600000	ENPP1	#N/A	#N/A
26.92128	27.12307	27.53059	9	6	59.219	1078900000	EPRS	#N/A	#N/A
28.62694	28.6326	28.84751	10	8	64.574	2613500000	EPX	#N/A	#N/A
26.87982	26.98348	26.39289	3	3	24.022	746750000	ERP29	#N/A	#N/A
27.54642	27.53118	27.46762	7	7	42.353	1215700000	ERP44	#N/A	#N/A
27.03915	26.59306	NaN	3	3	23.236	605340000	ETFA	#N/A	#N/A
26.46151	26.34885	26.58878	5	5	30.732	547760000	ETFB	#N/A	#N/A
25.03616	25.07333	25.06973	2	2	11.661	214800000	FAM162A	#N/A	#N/A
25.87949	25.44285	25.89537	2	2	19.333	395530000	FAM3C	#N/A	#N/A
30.40466	30.53046	30.7647	29	1	256.14	9664200000	FASN	#N/A	#N/A
28.95374	29.15593	29.4145	3	3	20.557	3696600000	FAU	#N/A	#N/A
26.78768	26.8846	26.96719	3	3	22.672	731400000	FBL	#N/A	#N/A
30.96451	30.98203	31.26746	11	10	99.671	16645000000	FKBP10	#N/A	#N/A
28.10104	28.18485	28.17479	5	5	33.461	1965800000	FKBP11	#N/A	#N/A
27.48401	27.08396	NaN	3	3	27.122	710340000	FKBP7	#N/A	#N/A
30.37555	29.83974	29.72524	12	11	87.956	7753900000	FKBP9	#N/A	#N/A
26.32354	26.31579	26.3304	6	6	46.178	585880000	FLNB	#N/A	#N/A
27.58226	27.33782	27.35951	4	4	23.905	1576500000	FLNC	#N/A	#N/A
26.54218	26.29165	26.57845	4	4	25.919	561030000	FSCN1	#N/A	#N/A
26.23237	26.18208	26.0536	5	5	29.698	501800000	FUBP1	#N/A	#N/A
26.49413	NaN	26.48313	3	3	24.368	507700000	FUS	#N/A	#N/A
28.03228	27.93568	27.93517	7	7	49.994	1953200000	GALE	#N/A	#N/A
30.06766	29.57398	29.60871	23	23	204.23	6940300000	GANAB	#N/A	#N/A
32.92352	33.29885	33.28389	21	19	323.31	78498000000	GAPDH	#N/A	#N/A
26.19378	26.44899	26.21625	6	6	38.774	543470000	GARS	#N/A	#N/A
30.2911	30.19543	30.19554	25	14	205.17	8535100000	GBF1	#N/A	#N/A
28.30348	28.28096	28.37799	6	1	43.349	2192400000	GBI1	#N/A	#N/A

25.71427	25.8148	NaN	9	4	29.635	473930000	GDI1	#N/A	#N/A
28.00089	27.93517	27.89169	10	5	73.41	2562800000	GDI2	#N/A	#N/A
30.38206	29.99981	29.99994	23	1	200.56	8690000000	GFPT1	#N/A	#N/A
28.9955	29.05577	29.36728	15	10	106.54	3606400000	GFPT2	#N/A	#N/A
26.3084	NaN	26.15742	8	8	52.492	834410000	GLG1	#N/A	#N/A
28.44241	28.2208	28.72621	11	11	90.99	2373200000	GLUD1	#N/A	#N/A
NaN	26.02878	26.08829	4	3	20.785	360240000	GNAS	#N/A	#N/A
29.87703	30.03013	30.2732	13	13	129.3	8457300000	GNB2L1	#N/A	#N/A
28.00956	28.29097	28.15325	4	4	29.515	1972100000	GNB3	#N/A	#N/A
28.52294	28.47139	28.77703	10	10	85.308	3169300000	GOT2	#N/A	#N/A
27.28047	27.17864	27.32517	9	9	65.849	1277500000	GPI	#N/A	#N/A
26.05976	NaN	26.42248	5	5	32.683	470220000	GPX7	#N/A	#N/A
25.87138	NaN	26.24603	4	4	26.358	326400000	GPX8	#N/A	#N/A
26.30252	NaN	26.194	4	4	29.995	393290000	GRB2	#N/A	#N/A
31.79153	31.68704	31.7878	29	29	276.11	28153000000	GRP-58	#N/A	#N/A
30.29975	30.28383	30.15316	19	19	202.4	10286000000	GSN	#N/A	#N/A
27.30982	27.57895	27.71188	6	6	45.982	1628700000	H1FX	#N/A	#N/A
32.58791	32.23532	32.04221	5	1	104.75	38764000000	H2AFX	#N/A	#N/A
27.4635	27.49732	27.74458	3	3	17.462	1328300000	H2AFY	#N/A	#N/A
33.72913	33.79042	33.6852	10	10	71.035	1.165E+11	H3F3A	#N/A	#N/A
26.94447	26.84158	27.25997	8	8	50.567	980200000	HADHA	#N/A	#N/A
27.86938	27.78862	28.02237	9	9	76.794	1507800000	HADHB	#N/A	#N/A
33.74595	34.0833	33.84642	10	10	155.19	1.0671E+11	HBA	#N/A	#N/A
35.61998	35.59965	35.27649	16	8	323.31	3.1071E+11	HBB	#N/A	#N/A
27.72754	27.78936	29.00525	15	15	115.23	2626600000	HDLBP	#N/A	#N/A
31.86589	31.90142	32.08423	26	17	323.31	30435000000	HSP90	#N/A	#N/A
31.75127	31.76224	31.9546	17	10	92.793	32376000000	HIST1H1B	#N/A	#N/A
33.43166	33.74845	33.49905	20	7	182.26	1.1772E+11	HIST1H1T	#N/A	#N/A
35.01692	34.96297	34.50912	13	3	214.7	2.1713E+11	HIST1H2BA	#N/A	#N/A
35.33993	35.15285	34.64124	15	15	167.79	2.4993E+11	HIST1H4A	#N/A	#N/A
29.63263	30.99665	30.23375	13	3	21.645	9990000000	HIST3H2BB	#N/A	#N/A
27.49526	27.02612	28.08091	8	8	56.101	1279900000	HK1	#N/A	#N/A
27.67607	27.73518	27.41828	5	5	38.775	1249200000	HMGB1	#N/A	#N/A
25.87893	25.98681	NaN	4	4	35.048	257420000	HNRNPA1	#N/A	#N/A
28.41546	27.88629	28.12045	8	4	68.695	2245500000	HNRNPA2/B1	#N/A	#N/A
27.58054	27.60964	27.11486	5	5	45.785	1187800000	HNRNPA3	#N/A	#N/A
26.34374	26.80292	26.62993	2	2	16.847	605220000	HNRNPC	#N/A	#N/A
27.54525	28.10229	27.78581	4	3	28.333	1489200000	HNRNPH1	#N/A	#N/A
28.33765	28.38451	28.61593	12	12	93.274	2265900000	HNRNPK	#N/A	#N/A
26.52105	26.9015	26.96906	3	3	30.643	723810000	HNRNPL	#N/A	#N/A
29.29883	28.87979	29.39667	15	15	118.35	4537100000	HNRNPM	#N/A	#N/A
29.76574	29.96582	30.08525	17	17	147.87	8575600000	HNRNPU	#N/A	#N/A
26.20193	25.96327	26.22514	3	3	18.278	515490000	HNRNPUL2	#N/A	#N/A
28.45246	28.37811	28.59648	5	5	60.157	2226200000	HP	#N/A	#N/A
26.77102	26.71934	26.83894	5	5	31.218	714550000	HP1BP3	#N/A	#N/A
25.51485	25.12542	25.8235	4	4	42.193	336270000	HSD17B10	#N/A	#N/A
NaN	25.65706	25.92859	5	5	31.041	242730000	HSD17B4	#N/A	#N/A
27.68211	27.5154	27.49732	16	7	115.7	1844000000	HSP70	#N/A	#N/A

32.68685	32.716	32.59877	33	31	323.31	48917000000	HSP90B1	#N/A	#N/A
NaN	28.82086	29.15567	14	4	38.779	3723000000	HSPA2	#N/A	#N/A
32.66732	32.6338	32.41008	34	32	323.31	46947000000	HSPA5	#N/A	#N/A
29.47787	29.88622	29.50156	7	1	11.789	5391700000	HSPA6	#N/A	#N/A
27.96615	28.01839	28.00051	11	11	88.448	1608600000	HSPA9	#N/A	#N/A
30.7198	30.19331	30.6193	16	16	162.89	10002000000	HSPD1	#N/A	#N/A
28.02073	28.01036	28.52526	7	7	46.519	1862300000	HSPE1	#N/A	#N/A
26.22179	25.67853	24.56593	6	5	31.484	366080000	IDH1	#N/A	#N/A
28.78852	28.80603	28.89862	12	11	82.798	2796100000	IDH2	#N/A	#N/A
26.80033	26.52419	26.78144	5	5	34.858	644830000	IDH3A	#N/A	#N/A
25.9376	25.75934	NaN	2	2	12.694	383370000	IGHA	#N/A	#N/A
28.72377	28.80511	28.76765	8	8	84.857	2702000000	IGHD	#N/A	#N/A
30.50815	30.41155	30.68445	9	0	68.35	9845100000	IGHG	#N/A	#N/A
30.91257	31.07508	31.13277	11	1	175.36	13813000000	IGHG	#N/A	#N/A
29.61472	29.48646	29.2656	31	31	323.31	20828000000	IL1RAP	#N/A	#N/A
27.49595	27.21919	27.53934	3	3	25.406	1106400000	ILF2	#N/A	#N/A
26.9968	27.23708	27.0559	5	5	37.931	1214400000	ILF3	#N/A	#N/A
NaN	24.83195	25.58832	3	2	18.756	198340000	IMPDH2	#N/A	#N/A
25.47537	NaN	25.82828	3	3	18.579	238440000	IPO5	#N/A	#N/A
26.90104	26.9327	27.1671	13	13	93.836	1090300000	IQGAP1	#N/A	#N/A
27.31614	27.09235	27.41836	5	5	31.627	983850000	KPNB1	#N/A	#N/A
27.20284	27.85079	27.9571	12	6	120.81	2112900000	KRT1	#N/A	#N/A
NaN	26.00239	26.39568	4	4	28.506	484480000	LAMP1	#N/A	#N/A
24.99404	NaN	24.73862	4	4	25.698	162370000	LCP1	#N/A	#N/A
30.8915	30.94391	31.01611	15	13	126.1	17606000000	LDHA	#N/A	#N/A
28.23512	28.20992	28.33947	8	3	44.76	2986600000	LDHB	#N/A	#N/A
30.94224	30.72477	30.88881	5	5	50.349	24717000000	LECT2	#N/A	#N/A
25.54834	25.59092	25.5501	2	2	16.133	296420000	LMAN2	#N/A	#N/A
30.41246	30.3911	30.37171	30	1	288.53	13692000000	LMNA	#N/A	#N/A
27.48884	27.47011	27.24291	8	7	48.213	1104500000	LMNB1	#N/A	#N/A
24.72718	NaN	24.87056	4	3	18.431	150120000	LMNB2	#N/A	#N/A
31.88718	31.83579	31.72106	15	0	301.26	28470000000	LOC100127131	#N/A	#N/A
32.27673	32.16414	31.80505	15	6	45.068	26403000000	LOC100154783	#N/A	#N/A
25.8877	NaN	25.80003	2	2	11.562	342840000	LOC100155889	#N/A	#N/A
26.77568	NaN	26.41901	7	2	34.832	606460000	LOC100156325	#N/A	#N/A
33.511	33.56898	33.36202	27	27	323.31	86014000000	LOC100156689	#N/A	#N/A
NaN	26.14009	26.26293	5	5	36.854	435880000	LOC100157249	#N/A	#N/A
37.52262	36.05809	35.82691	4	4	207.32	7.9947E+11	LOC100302368	#N/A	#N/A
29.51232	29.23396	29.77057	9	9	74.431	9184200000	LOC100510904	#N/A	#N/A
25.06443	25.56863	NaN	2	2	16.152	200270000	LOC100511690	#N/A	#N/A
25.66139	25.54416	25.64678	4	4	25.749	340520000	LOC100512253	#N/A	#N/A
26.7986	NaN	26.79067	3	3	17.52	579800000	LOC100512637	#N/A	#N/A
28.46673	28.48097	28.66729	9	9	91.985	2577600000	LOC100513892	#N/A	#N/A
32.43378	32.38105	32.43966	15	10	177.45	36297000000	LOC100514666	#N/A	#N/A
30.18553	30.13931	30.25586	9	9	55.756	9409000000	LOC100516261	#N/A	#N/A
30.24728	29.86729	29.87935	23	1	252.87	7078000000	LOC100516776	#N/A	#N/A
30.63027	30.48894	30.61404	7	7	68.388	11384000000	LOC100517228	#N/A	#N/A
26.53662	NaN	26.36885	4	4	27.646	629210000	LOC100517744	#N/A	#N/A

200

28.62006	28.31713	28.66166	10	10	90.457	3364900000	LOC100518254	#N/A	#N/A
26.31771	26.31237	26.67949	4	4	28.063	544100000	LOC100518399	#N/A	#N/A
28.99213	28.8966	28.8328	11	11	93.326	3713100000	LOC100519984	#N/A	#N/A
30.15473	29.79314	29.8419	8	8	123.1	6266500000	LOC100521468	#N/A	#N/A
28.37559	28.12465	28.37455	4	4	64.337	2019600000	LOC100523213	#N/A	#N/A
29.02398	28.85807	28.41921	4	4	28.881	3077000000	LOC100523526	#N/A	#N/A
27.70074	28.04338	28.16868	3	3	29.28	1561700000	LOC100523801	#N/A	#N/A
29.74562	29.74674	29.9806	5	5	33.773	9254800000	LOC100523846	#N/A	#N/A
27.46684	27.702	27.72936	4	4	36.417	1240500000	LOC100524170	#N/A	#N/A
26.50127	27.4419	27.37435	2	2	13.207	851300000	LOC100524880	#N/A	#N/A
26.23478	26.05641	26.33028	8	2	70.549	597780000	LOC100525988	#N/A	#N/A
27.03612	26.51281	26.63492	8	2	13.903	859850000	LOC100526167	#N/A	#N/A
30.41094	30.49534	30.41488	8	8	70.409	9378000000	LOC100620439	#N/A	#N/A
27.1029	27.22784	27.48424	5	3	41.062	956810000	LOC100620941	#N/A	#N/A
26.49945	26.34272	26.78918	14	3	42.832	617770000	LOC100621981	#N/A	#N/A
29.85441	30.12817	30.10487	12	12	164.47	6514100000	LOC100622330	#N/A	#N/A
NaN	26.93078	27.67674	17	3	36.604	911570000	LOC100623583	#N/A	#N/A
29.13506	29.18307	29.06252	5	5	51.604	3589000000	LOC100623679	#N/A	#N/A
NaN	24.5373	25.47649	3	3	20.356	155740000	LOC100623684	#N/A	#N/A
30.21071	30.37472	30.45865	9	9	63.036	10171000000	LOC100623913	#N/A	#N/A
28.81821	28.82259	29.19934	6	6	37.585	3071800000	LOC100624417	#N/A	#N/A
29.20886	29.4109	29.17229	6	6	39.68	4363500000	LOC100624537	#N/A	#N/A
31.02723	30.95913	31.17075	2	2	19.775	13163000000	LOC100625180	#N/A	#N/A
24.77761	24.99606	24.80307	2	2	27.683	186160000	LOC100626266	#N/A	#N/A
30.87826	30.78994	30.87547	12	12	126.82	18367000000	LOC100626701	#N/A	#N/A
28.39938	27.83593	26.3784	10	10	69.362	8739200000	LOC100737120	#N/A	#N/A
24.4431	NaN	25.28718	3	3	19.594	151940000	LOC100737246	#N/A	#N/A
27.47205	27.8951	28.17617	11	11	74.667	1495600000	LOC100737407	#N/A	#N/A
31.19143	31.13492	30.93157	9	8	89.431	16435000000	LOC100737553	#N/A	#N/A
32.8752	32.9347	32.82758	15	6	264.78	57354000000	LOC100737887	#N/A	#N/A
26.63437	26.07938	26.4654	5	5	41.55	592510000	LOC100737962	#N/A	#N/A
30.57073	30.55536	30.70074	13	13	107.33	11447000000	LOC100738304	#N/A	#N/A
27.75066	27.81592	28.04129	8	8	50.388	1464900000	LOC100738388	#N/A	#N/A
26.42707	26.09603	25.65704	2	2	15.113	853750000	LOC100738863	#N/A	#N/A
26.49063	26.21098	NaN	2	2	15.116	553810000	LOC100739851	#N/A	#N/A
27.37592	27.62303	27.5755	3	3	18.726	1239600000	LOC102163847	#N/A	#N/A
29.39387	29.33089	29.39204	6	6	70.58	5517200000	LOC102164134	#N/A	#N/A
28.23594	28.3006	27.89481	1	1	6.9641	2455200000	LOC102165647	#N/A	#N/A
31.19372	30.80878	30.48731	14	14	220.35	22820000000	LOC102165939	#N/A	#N/A
26.86231	26.72273	26.21095	4	4	28.54	643750000	LOC494560	#N/A	#N/A
29.94182	29.69495	29.86366	18	5	43.179	9224400000	LOC595122	#N/A	#N/A
27.41296	27.31959	27.06312	4	4	56.415	1036300000	LOC733637	#N/A	#N/A
NaN	25.44168	25.30159	4	4	36.356	452930000	LPL	#N/A	#N/A
28.62808	28.52548	28.70777	27	27	193.17	3279400000	LRP1	#N/A	#N/A
28.07005	27.83599	27.77605	7	6	83.746	1553700000	LTF	#N/A	#N/A
29.09126	29.74549	29.96279	16	3	82.218	13295000000	LYZ	#N/A	#N/A
27.53356	27.41321	27.7649	14	2	46.004	1199000000	LYZ	#N/A	#N/A
31.90638	31.61824	31.91528	16	4	323.31	64996000000	LYZ3	#N/A	#N/A

NaN	25.053	25.29674	2	2	14.209	231610000	MAGT1	#N/A	#N/A
27.47383	27.03507	26.55476	4	4	35.543	943520000	MATR3	#N/A	#N/A
27.06897	26.76053	26.94715	4	4	29.228	784420000	MDH1	#N/A	#N/A
27.79476	27.74663	27.79092	9	8	61.683	1486700000	ME1	#N/A	#N/A
26.7433	26.78506	26.93809	9	9	70.856	1455300000	MFI2	#N/A	#N/A
25.86186	NaN	25.50425	2	2	15.921	262650000	MIF	#N/A	#N/A
26.83316	26.63312	26.98131	7	5	32.403	680460000	MPO	#N/A	#N/A
30.23968	30.08297	30.12866	20	11	141.37	8078400000	MSN	#N/A	#N/A
25.42621	NaN	25.34133	3	3	17.271	198150000	MYH1	#N/A	#N/A
30.19742	29.54222	29.96513	31	21	234.22	6612200000	MYH9	#N/A	#N/A
29.46059	29.50465	29.71204	5	5	70.046	5327000000	MYL6	#N/A	#N/A
25.87242	25.55271	25.78848	2	2	11.561	334350000	MYO1B	#N/A	#N/A
25.97496	25.32656	25.70406	4	4	27.518	475620000	MYO1C	#N/A	#N/A
26.59377	26.69763	NaN	2	1	14.791	516980000	NAP1L4	#N/A	#N/A
25.82355	25.68985	25.8541	4	4	42.651	329920000	NAPA	#N/A	#N/A
25.65499	NaN	25.60065	2	2	12.55	257540000	NDUFS1	#N/A	#N/A
30.13638	30.08639	30.00517	8	4	61.131	8499500000	NME2	#N/A	#N/A
28.73434	28.64667	28.81693	1	1	7.4825	3134600000	NME3	#N/A	#N/A
28.27742	28.26096	28.60368	9	9	63.917	2305600000	NONO	#N/A	#N/A
28.60791	28.31268	28.02041	6	6	39.847	2721500000	NPM1	#N/A	#N/A
24.75807	NaN	24.78517	3	3	17.499	159610000	NT5E	#N/A	#N/A
26.9257	26.92366	27.02422	8	7	60.867	862880000	NUCB1	#N/A	#N/A
29.59267	29.57124	29.64709	16	16	152.03	5872600000	OAT	#N/A	#N/A
24.72281	24.96243	NaN	2	2	12.865	175390000	OLA1	#N/A	#N/A
25.95782	26.29063	26.12445	3	3	21.147	430970000	ORM1	#N/A	#N/A
33.93649	33.9948	33.79401	35	35	323.31	1.1865E+11	P4HB	#N/A	#N/A
29.09053	28.48719	29.16572	14	9	142.81	3284900000	PABPC1	#N/A	#N/A
25.87881	25.70564	25.95067	8	3	21.736	380010000	PABPC4	#N/A	#N/A
27.42414	26.59918	26.51399	8	7	50.692	1043500000	PAPSS1	#N/A	#N/A
31.82608	31.65284	31.76268	25	24	214.19	27433000000	PAPSS2	#N/A	#N/A
24.48726	NaN	24.25875	3	3	19.748	107110000	PARP1	#N/A	#N/A
25.8305	25.7263	NaN	4	2	14.702	321930000	PCBP2	#N/A	#N/A
31.27991	31.23957	31.3408	31	31	282.8	19455000000	PDIA4	#N/A	#N/A
29.63663	29.78269	29.93438	13	13	184.03	8820900000	pdi-p5	#N/A	#N/A
26.79947	26.83135	27.06815	3	3	22.134	813580000	PEBP1	#N/A	#N/A
27.39411	27.34942	27.48378	11	8	76.408	1665000000	PFKL	#N/A	#N/A
27.33219	27.19235	27.54495	13	11	107.3	1649000000	PFKP	#N/A	#N/A
28.50158	28.77737	28.50506	7	7	71.709	2502200000	PFN1	#N/A	#N/A
29.64234	29.40532	29.39356	12	12	138.61	7244700000	PGAM1	#N/A	#N/A
30.4981	30.03354	30.44431	22	0	237.22	12687000000	PGK1	#N/A	#N/A
25.18492	NaN	25.43463	3	3	21.452	233350000	PGRMC2	#N/A	#N/A
27.76129	27.90805	28.19653	7	7	59.593	1558600000	PHB2	#N/A	#N/A
29.2151	29.13545	29.22867	8	8	57.028	3655000000	PHOSPHO1	#N/A	#N/A
31.50744	31.05388	31.38515	18	18	188.41	29736000000	PKLR	#N/A	#N/A
26.63824	26.49323	26.8334	5	4	35.279	803740000	PLCD1	#N/A	#N/A
27.91553	27.80839	27.91741	23	22	146.84	1556200000	PLEC	#N/A	#N/A
29.77582	29.62643	29.54793	6	1	132.72	5029100000	PMAP23	#N/A	#N/A
26.64883	26.83244	26.75659	6	6	38.168	691680000	PPP2R1A	#N/A	#N/A

202

30.01691	29.86614	29.88434	8	5	49.279	6868200000	PRDX1	#N/A	#N/A
28.49179	28.35825	28.34452	6	6	42.555	2883900000	PRDX2	#N/A	#N/A
27.17769	27.11763	27.07327	5	5	35.659	891250000	PRDX3	#N/A	#N/A
30.13504	30.56438	30.05634	10	7	86.057	10038000000	PRDX4	#N/A	#N/A
25.97895	NaN	26.26327	6	6	40.881	1882500000	PRDX6	#N/A	#N/A
28.76563	28.89954	28.68852	11	11	130.81	3223100000	PRKCSH	#N/A	#N/A
29.63223	29.83186	29.70603	8	8	80.811	5148600000	PROC	#N/A	#N/A
NaN	26.43567	26.78967	3	3	24.862	518380000	PRTN3	#N/A	#N/A
26.44643	25.57594	25.65261	3	3	22.07	438510000	PSMA6	#N/A	#N/A
25.86093	25.84352	NaN	2	2	13.873	357400000	PSMB4	#N/A	#N/A
25.79054	NaN	25.76142	3	3	20.306	280430000	PSMD11	#N/A	#N/A
25.44364	25.27092	NaN	3	3	20.181	273120000	PSMD14	#N/A	#N/A
NaN	24.72583	25.56465	4	4	27.577	241680000	PSMD2	#N/A	#N/A
26.84577	27.1208	27.49587	5	5	29.593	941920000	PTBP1	#N/A	#N/A
26.47994	26.26696	26.38181	6	6	36.445	536240000	PTK7	#N/A	#N/A
25.97042	25.96506	26.13457	4	4	24.293	435180000	PURA	#N/A	#N/A
27.22343	27.22186	27.43516	13	13	79.427	1036600000	PYGB	#N/A	#N/A
26.81885	26.91843	26.99658	5	5	29.603	776980000	RAB11A	#N/A	#N/A
NaN	26.06632	26.19043	5	5	31.979	335520000	RAB18	#N/A	#N/A
NaN	27.03999	27.44806	3	3	28.864	846540000	RAB39A	#N/A	#N/A
25.58124	25.71301	25.79702	2	2	18.08	331690000	RALY	#N/A	#N/A
29.10247	29.21155	29.07948	10	10	74.396	4235300000	RAN	#N/A	#N/A
27.70682	27.87156	27.96719	2	2	14.053	1496500000	RAP1A	#N/A	#N/A
27.94648	27.8282	27.50499	5	5	45.408	2722700000	RARRES2	#N/A	#N/A
26.44664	26.54181	26.62185	4	4	37.454	607560000	RBMX	#N/A	#N/A
28.7303	28.80372	28.40272	10	10	86.596	3080800000	RCN1	#N/A	#N/A
30.14783	30.23478	30.06201	8	8	142.03	8716200000	RCN3	#N/A	#N/A
27.51503	27.70589	27.86508	4	4	33.413	1397900000	RHOA	#N/A	#N/A
30.18778	29.25311	29.30843	8	8	163.62	10890000000	RNASE4	#N/A	#N/A
30.64272	30.30149	30.18542	11	11	145.69	11088000000	RPL10	#N/A	#N/A
29.49072	29.27026	29.31023	7	2	64.965	5413100000	RPL10A	#N/A	#N/A
29.3538	29.48955	29.48871	10	10	108.75	5713200000	RPL11	#N/A	#N/A
30.13638	30.2589	30.509	8	8	80.759	10270000000	RPL13	#N/A	#N/A
29.86796	30.08411	30.28339	13	13	80.826	8108200000	RPL13A	#N/A	#N/A
28.16677	28.41961	28.267	4	4	33.359	2117000000	RPL17	#N/A	#N/A
30.83334	30.91257	30.86267	7	7	108.74	15583000000	RPL18	#N/A	#N/A
30.6501	30.49219	30.27197	11	11	78.765	10878000000	RPL18A	#N/A	#N/A
29.7891	29.38332	29.4245	5	5	68.931	5758500000	RPL19	#N/A	#N/A
30.09597	30.14224	30.20466	7	7	66.002	7672100000	RPL21	#N/A	#N/A
29.97774	30.10837	30.22481	7	6	63.332	8971600000	RPL22	#N/A	#N/A
28.28109	27.83352	28.48623	3	3	21.804	2315600000	RPL23	#N/A	#N/A
30.26282	30.12016	30.03078	9	9	64.07	7681600000	RPL23A	#N/A	#N/A
29.92804	29.76538	29.91171	5	5	36.69	6580800000	RPL24	#N/A	#N/A
28.92198	28.68281	28.45509	11	11	70.039	3001200000	RPL26	#N/A	#N/A
29.82611	29.78761	29.74774	8	8	63.301	6320600000	RPL27	#N/A	#N/A
28.4739	28.61894	28.54893	4	4	34.297	2393100000	RPL29	#N/A	#N/A
30.58289	30.3909	30.29909	17	17	135.71	12049000000	RPL3	#N/A	#N/A
29.03554	28.78516	28.9884	7	7	60.51	3751600000	RPL30	#N/A	#N/A

28.24776	28.19009	28.3362	4	4	24.16	1914200000	RPL34	#N/A	#N/A
31.4515	31.21616	31.11923	22	10	186.3	17135000000	RPL4	#N/A	#N/A
30.17379	30.23945	29.92649	10	10	88.252	8693100000	RPL5	#N/A	#N/A
32.62061	32.32254	32.56844	18	18	225.46	40983000000	RPL6	#N/A	#N/A
30.83349	30.65284	31.00979	14	7	108.18	13182000000	RPL7	#N/A	#N/A
30.32732	30.48769	30.54176	6	6	48.737	11490000000	RPL7A	#N/A	#N/A
31.34884	31.33431	31.59081	13	13	98.211	19941000000	RPL8	#N/A	#N/A
29.7756	29.86024	29.67813	6	6	44.379	6601000000	RPL9	#N/A	#N/A
29.70999	29.11078	29.38245	8	8	79.191	5270300000	RPLP0	#N/A	#N/A
29.87976	29.83882	29.74934	17	17	134.04	7482500000	RPN1	#N/A	#N/A
30.52999	30.53278	30.60231	14	14	99.938	11454000000	RPS11	#N/A	#N/A
28.81268	28.76452	29.07844	3	3	19.956	3285300000	RPS12	#N/A	#N/A
28.77165	28.55076	28.65612	6	6	45.377	3466200000	RPS13	#N/A	#N/A
30.78784	30.88925	30.57822	12	12	91.65	14745000000	RPS16	#N/A	#N/A
29.65971	29.68351	29.85131	3	3	21.802	5780300000	RPS17	#N/A	#N/A
30.48961	30.55655	30.75613	12	12	83.13	12547000000	RPS2	#N/A	#N/A
28.65683	28.78066	28.99949	4	4	32.479	4437700000	RPS20	#N/A	#N/A
27.00389	27.42486	27.64595	2	2	16.053	1034500000	RPS21	#N/A	#N/A
30.8097	30.60311	30.70594	6	6	53.499	11253000000	RPS25	#N/A	#N/A
29.40621	29.45488	29.58606	4	4	40.246	5027600000	RPS27	#N/A	#N/A
28.2539	27.64423	27.28833	3	3	27.718	1331500000	RPS27A	#N/A	#N/A
30.97972	31.14096	30.97965	21	21	172.52	15605000000	RPS3	#N/A	#N/A
31.07954	31.1098	31.24921	18	18	141.28	17611000000	RPS3A	#N/A	#N/A
31.62139	31.39397	31.23928	16	16	157.93	21434000000	RPS4	#N/A	#N/A
29.47605	29.43078	29.5349	8	8	86.23	5280900000	RPS5	#N/A	#N/A
30.91648	30.86142	30.77172	15	7	124.15	13145000000	RPS6	#N/A	#N/A
29.47667	29.44969	29.63843	6	6	39.632	5340800000	RPS7	#N/A	#N/A
30.36234	30.37192	30.18601	13	13	179.15	11049000000	RPS8	#N/A	#N/A
NaN	28.24504	28.05455	13	2	13.079	1160700000	RPS9	#N/A	#N/A
30.30932	30.36286	30.28273	13	2	85.755	9704400000	RPS9	#N/A	#N/A
29.16591	29.69428	29.71362	11	11	149.77	4991100000	RPSA	#N/A	#N/A
30.26539	30.39826	30.42902	26	26	234.95	9770500000	RRBP1	#N/A	#N/A
27.23178	27.2498	27.47723	11	11	73.16	1141100000	RTCB	#N/A	#N/A
27.70589	27.7916	NaN	5	5	35.971	967330000	SAR1A	#N/A	#N/A
28.88629	28.9305	29.05719	13	13	123.39	4748600000	SCIN	#N/A	#N/A
27.31354	27.3652	27.34113	7	7	51.334	1028800000	SDHA	#N/A	#N/A
25.6216	25.74291	NaN	2	2	13.122	309750000	SEC11A	#N/A	#N/A
25.30239	NaN	25.46588	2	2	21.327	264940000	SEC13	#N/A	#N/A
27.16749	26.879	27.12751	9	8	75.475	1091000000	SEC23A	#N/A	#N/A
27.31691	27.30269	27.45537	7	7	56.494	1174900000	SEC24D	#N/A	#N/A
27.12485	26.89908	27.57838	7	7	44.03	1091900000	SEC31A	#N/A	#N/A
NaN	28.42198	28.75411	2	2	17.039	1897500000	SEC61B	#N/A	#N/A
26.64609	26.91798	26.49974	5	5	32.853	819690000	SEPT9	#N/A	#N/A
29.56491	29.29263	29.36967	12	9	89.982	4296600000	SERPINA3-2	#N/A	#N/A
27.08679	26.92479	27.18272	5	5	37.343	820270000	SLC25A1	#N/A	#N/A
28.02844	28.18154	28.37206	7	7	48.959	1734700000	SLC25A3	#N/A	#N/A
30.68913	30.77635	30.9685	9	3	60.283	11981000000	SLC25A6	#N/A	#N/A
26.78918	26.73104	27.26973	6	6	48.27	733530000	SMPD3	#N/A	#N/A

28.91957	28.91789	29.01398	14	14	102.05	3767200000	SND1	#N/A	#N/A
27.10239	26.91696	26.88902	5	5	30.484	800790000	SNRNP70	#N/A	#N/A
24.94244	NaN	25.14503	2	2	13.12	183880000	SNRPA	#N/A	#N/A
28.82177	28.69122	28.89709	7	7	80.896	2874000000	SPP2	#N/A	#N/A
25.02606	24.81436	NaN	2	2	12.498	183870000	SRM	#N/A	#N/A
26.67546	26.53623	26.59648	5	5	29.108	603010000	SRPR	#N/A	#N/A
NaN	25.87526	26.26093	3	3	17.241	310390000	SRPRB	#N/A	#N/A
27.13604	27.0878	27.19366	3	3	22.717	854350000	SSB	#N/A	#N/A
28.29413	28.29079	28.43535	2	2	13.358	2175700000	SSR1	#N/A	#N/A
28.97678	28.75538	28.41973	4	4	34.982	3151900000	SSR4	#N/A	#N/A
25.59537	26.16984	26.14587	4	4	38.031	416210000	ST13	#N/A	#N/A
28.39444	28.4251	28.72481	8	7	54.654	2382800000	STT3A	#N/A	#N/A
24.42675	NaN	24.21416	2	2	12.402	94824000	SUB1	#N/A	#N/A
27.37368	27.21771	27.59106	2	2	13.998	1251200000	SURF4	#N/A	#N/A
27.06157	27.15422	27.27684	5	3	44.551	1009800000	SYNCRIP	#N/A	#N/A
26.74727	26.54346	26.80907	4	4	30.961	651880000	TBL2	#N/A	#N/A
28.3782	28.38784	29.0004	11	11	75.793	2723700000	TCP1	#N/A	#N/A
25.48253	26.05922	25.9018	2	2	19.269	346700000	TECR	#N/A	#N/A
29.32862	29.44743	29.44269	16	15	124.99	4147600000	TF	#N/A	#N/A
28.54292	28.43289	28.40864	13	13	98.54	3383500000	TKT	#N/A	#N/A
28.37534	28.32569	28.18674	18	18	118.69	2071600000	TLN1	#N/A	#N/A
NaN	25.97158	25.99155	2	2	12.075	306880000	TM9SF3	#N/A	#N/A
28.71702	28.59833	28.51164	5	5	39.731	3811200000	TMED10	#N/A	#N/A
27.06219	26.84577	26.99863	3	3	24.051	794360000	TMED2	#N/A	#N/A
26.45249	27.12623	27.07449	3	3	37.348	789980000	TMED9	#N/A	#N/A
26.07995	NaN	25.91962	2	2	15.065	432410000	TMEM43	#N/A	#N/A
28.98027	28.6514	28.67956	9	9	116.04	3631600000	TPI1	#N/A	#N/A
26.56977	26.07971	25.94726	5	5	36.861	487290000	TPM1	#N/A	#N/A
27.81146	27.1489	27.93511	4	4	39.803	1502100000	TPT1	#N/A	#N/A
26.49747	26.39682	25.73368	4	4	32.818	461470000	TRPV4	#N/A	#N/A
32.10465	32.01292	32.16447	17	2	263.11	33599000000	TUBB	#N/A	#N/A
27.36135	27.58606	27.68372	7	7	46.529	1177400000	TUFM	#N/A	#N/A
31.10961	31.04179	31.37124	20	20	268.3	17166000000	UGDH	#N/A	#N/A
27.60031	27.8381	28.08816	16	16	121.36	2597000000	UGP2	#N/A	#N/A
26.99873	NaN	27.40519	4	4	25.169	807460000	UQCRC1	#N/A	#N/A
27.6231	27.30025	27.95964	7	7	47.691	1300800000	VDAC1	#N/A	#N/A
29.21491	29.29483	29.59587	7	7	73.542	4733800000	VDAC2	#N/A	#N/A
27.37542	27.29929	27.31614	9	9	68.96	1022000000	WDR1	#N/A	#N/A
26.68445	26.46641	26.8839	9	9	68.728	681990000	XYLT1	#N/A	#N/A
27.52783	27.15846	26.94592	7	2	42.662	1175400000	YWHAB	#N/A	#N/A
28.03585	27.95394	28.16787	6	6	42.696	1669000000	YWHAE	#N/A	#N/A
NaN	25.65597	25.76552	7	4	29.143	556970000	YWHAG	#N/A	#N/A
27.82366	27.68612	27.87033	7	5	128.12	1643100000	YWHAZ	#N/A	#N/A
32.27436	32.2434	32.12325	4	4	38.913	33554000000	Uncharacterized	#N/A	#N/A
31.95102	31.89291	31.43301	24	15	247.17	26045000000	Uncharacterized	#N/A	#N/A
NaN	26.56763	25.95356	3	3	32.428	573920000	Uncharacterized	#N/A	#N/A
25.93997	26.16411	25.69163	2	2	26.854	392540000	Uncharacterized	#N/A	#N/A
32.5177	32.23732	32.31503	12	12	162.18	40411000000	Uncharacterized	#N/A	#N/A

205

| 26.78656 | 26.38722 | NaN | 6 | 3 | 23.694 | 526620000 | Uncharacterized | #N/A | #N/A |
| 32.27689 | 32.31141 | 32.21289 | 14 | 14 | 159.62 | 40425000000 | Uncharacterized | #N/A | #N/A |

9.2. String curated matrisome protein list

9.2.1. List of proteins that were found predominantly in the AC Matrisome and the preview information provided by STRING that was used to find the targets of interest

Protein name	String associated information
DCN	Decorin; May affect the rate of fibrils formation; Small leucine rich repeat proteoglycans (359 aa)
CHADL	Chondroadherin-like protein; Potential negative modulator of chondrocyte differentiation. Inhibits collagen fibrillogenesis in vitro. May influence chondrocyte's differentiation by acting on its cellular collagenous microenvironment; Belongs to the small leucine-rich proteoglycan (SLRP) family. SLRP class IV subfamily (762 aa)
COMP	Cartilage oligomeric matrix protein; May play a role in the structural integrity of cartilage via its interaction with other extracellular matrix proteins such as the collagens and fibronectin. Can mediate the interaction of chondrocytes with the cartilage extracellular matrix through interaction with cell surface integrin receptors. Could play a role in the pathogenesis of osteoarthritis. Potent suppressor of apoptosis in both primary chondrocytes and transformed cells. Suppresses apoptosis by blocking the activation of caspase-3 and by inducing the IAP family of survival proteins (BI [...] (757 aa)
PCOLCE	Procollagen C-endopeptidase enhancer 1; Binds to the C-terminal propeptide of type I procollagen and enhances procollagen C-proteinase activity (449 aa)
CPXM2	Inactive carboxypeptidase-like protein X2; May be involved in cell-cell interactions; M14 carboxypeptidases (756 aa)
THBS1	Thrombospondin-1; Adhesive glycoprotein that mediates cell-to-cell and cell-to-matrix interactions. Binds heparin. May play a role in dentinogenesis and/or maintenance of dentin and dental pulp (By similarity). Ligand for CD36 mediating antiangiogenic properties. Plays a role in ER stress response, via its interaction with the activating transcription factor 6 alpha (ATF6) which produces adaptive ER stress response factors (By similarity) (1170 aa)
EPYC	Epiphycan; May have a role in bone formation and also in establishing the ordered structure of cartilage through matrix organization; Belongs to the small leucine-rich proteoglycan (SLRP) family. SLRP class III subfamily (322 aa)
OGN	Mimecan; Induces bone formation in conjunction with TGF-beta-1 or TGF-beta-2; Small leucine rich repeat proteoglycans (298 aa)
LOXL3	Lysyl oxidase homolog 3; Protein-lysine 6-oxidase that mediates the oxidation of peptidyl lysine residues to allysine in target proteins. Catalyzes the post- translational oxidative deamination of peptidyl lysine residues in precursors of elastin and different types of collagens, a prerequisite in the formation of cross-links between collagens and elastin. Required for somite boundary formation by catalyzing oxidation of fibronectin (FN1), enhancing integrin signaling in myofibers and their adhesion to the myotendinous junction (MTJ) (By similarity). Acts as a regulator of inflammatory [...] (753 aa)
VCAN	Versican core protein; May play a role in intercellular signaling and in connecting cells with the extracellular matrix. May take part in the regulation of cell motility, growth and differentiation. Binds hyaluronic acid; C-type lectin domain containing (3396 aa)
TNC	Tenascin; Extracellular matrix protein implicated in guidance of migrating neurons as well as axons during development, synaptic plasticity as well as neuronal regeneration. Promotes neurite outgrowth from cortical neurons grown on a monolayer of astrocytes. Ligand for integrins alpha-8/beta-1, alpha-9/beta-1, alpha-V/beta-3 and alpha-V/beta-6. In tumors, stimulates angiogenesis by elongation, migration and sprouting of endothelial cells; Belongs to the tenascin family (2201 aa)
HAPLN1	Hyaluronan and proteoglycan link protein 1; Stabilizes the aggregates of proteoglycan monomers with hyaluronic acid in the extracellular cartilage matrix; V-set domain containing (354 aa)
CILP2	Cartilage intermediate layer protein 2; May play a role in cartilage scaffolding; Immunoglobulin like domain containing (1156 aa)

FRZB   Secreted frizzled-related protein 3; Soluble frizzled-related proteins (sFRPS) function as modulators of Wnt signaling through direct interaction with Wnts. They have a role in regulating cell growth and differentiation in specific cell types. SFRP3/FRZB appears to be involved in limb skeletogenesis. Antagonist of Wnt8 signaling. Regulates chondrocyte maturation and long bone development (325 aa)

COL6A3   Collagen alpha-3(VI) chain; Collagen VI acts as a cell-binding protein; Collagens (3177 aa)

COL14A1   Collagen alpha-1(XIV) chain; Plays an adhesive role by integrating collagen bundles. It is probably associated with the surface of interstitial collagen fibrils via COL1. The COL2 domain may then serve as a rigid arm which sticks out from the fibril and protrudes the large N-terminal globular domain into the extracellular space, where it might interact with other matrix molecules or cell surface receptors (By similarity); Collagens (1796 aa)

CLEC3A   C-type lectin domain family 3 member A; Promotes cell adhesion to laminin-332 and fibronectin; C-type lectin domain containing (206 aa)

COL6A2   Collagen alpha-2(VI) chain; Collagen VI acts as a cell-binding protein; Collagens (1019 aa)

C1QB   Complement C1q subcomponent subunit B; C1q associates with the proenzymes C1r and C1s to yield C1, the first component of the serum complement system. The collagen-like regions of C1q interact with the Ca(2+)-dependent C1r(2)C1s(2) proenzyme complex, and efficient activation of C1 takes place on interaction of the globular heads of C1q with the Fc regions of IgG or IgM antibody present in immune complexes (253 aa)

FBN1   Fibrillin-1; Fibrillin-1- Structural component of the 10-12 nm diameter microfibrils of the extracellular matrix, which conveys both structural and regulatory properties to load-bearing connective tissues. Fibrillin-1- containing microfibrils provide long-term force bearing structural support. In tissues such as the lung, blood vessels and skin, microfibrils form the periphery of the elastic fiber, acting as a scaffold for the deposition of elastin. In addition, microfibrils can occur as elastin-independent networks in tissues such as the ciliary zonule, tendon, cornea and glomerulus w [...] (2871 aa)

BGN   Biglycan; May be involved in collagen fiber assembly; Small leucine rich repeat proteoglycans (368 aa)

CTHRC1   Collagen triple helix repeat-containing protein 1; May act as a negative regulator of collagen matrix deposition (243 aa)

FBLN7   Fibulin-7; An adhesion molecule that interacts with extracellular matrix molecules in developing teeth and may play important roles in differentiation and maintenance of odontoblasts as well as in dentin formation; Fibulins (439 aa)

THBS4   Thrombospondin-4; Adhesive glycoprotein that mediates cell-to-cell and cell-to-matrix interactions and is involved in various processes including cellular proliferation, migration, adhesion and attachment, inflammatory response to CNS injury, regulation of vascular inflammation and adaptive responses of the heart to pressure overload and in myocardial function and remodeling. Binds to structural extracellular matrix (ECM) proteins and modulates the ECM in response to tissue damage, contributing to cardioprotective and adaptive ECM remodeling. Plays a role in ER stress response, via its [...] (961 aa)

SMOC2   SPARC-related modular calcium-binding protein 2; Promotes matrix assembly and cell adhesiveness (By similarity). Can stimulate endothelial cell proliferation, migration, as well as angiogenesis; SPARC family (457 aa)

FMOD   Fibromodulin; Affects the rate of fibrils formation. May have a primary role in collagen fibrillogenesis (By similarity); Belongs to the small leucine-rich proteoglycan (SLRP) family. SLRP class II subfamily (376 aa)

COL9A1   Collagen alpha-1(IX) chain; Structural component of hyaline cartilage and vitreous of the eye; Collagen proteoglycans (921 aa)

HAPLN3   Hyaluronan and proteoglycan link protein 3; May function in hyaluronic acid binding; V-set domain containing (360 aa)

COL6A1   Collagen alpha-1(VI) chain; Collagen VI acts as a cell-binding protein; Belongs to the type VI collagen family (1028 aa)

HTRA1   Serine protease HTRA1; Serine protease with a variety of targets, including extracellular matrix proteins such as fibronectin. HTRA1-generated fibronectin fragments further induce synovial cells to up-regulate MMP1 and MMP3 production. May also degrade proteoglycans, such as aggrecan, decorin and fibromodulin. Through cleavage of proteoglycans, may release soluble FGF-glycosaminoglycan complexes that promote the range and intensity of FGF signals in the extracellular space. Regulates the availability of insulin-like growth factors (IGFs) by cleaving IGF-binding proteins. Inhibits signa [...] (480 aa)

MATN4   Matrilin-4; Major component of the extracellular matrix of cartilage; Matrilins (581 aa)

SRPX2   Sushi repeat-containing protein SRPX2; Acts as a ligand for the urokinase plasminogen activator surface receptor. Plays a role in angiogenesis by inducing endothelial cell migration and the formation of vascular network (cords). Involved in cellular migration and adhesion. Increases the phosphorylation levels of FAK. Interacts with and increases the mitogenic activity of HGF. Promotes synapse formation. May have a role in the perisylvian region, critical for language and cognitive development; Sushi domain containing (465 aa)

COL16A1	Collagen alpha-1(XVI) chain; Involved in mediating cell attachment and inducing integrin-mediated cellular reactions, such as cell spreading and alterations in cell morphology; Collagens (1604 aa)
MATN1	Cartilage matrix protein; Cartilage matrix protein is a major component of the extracellular matrix of non-articular cartilage. It binds to collagen; Matrilins (496 aa)
C1QC	Complement C1q subcomponent subunit C; C1q associates with the proenzymes C1r and C1s to yield C1, the first component of the serum complement system. The collagen-like regions of C1q interact with the Ca(2+)-dependent C1r(2)C1s(2) proenzyme complex, and efficient activation of C1 takes place on interaction of the globular heads of C1q with the Fc regions of IgG or IgM antibody present in immune complexes (245 aa)
C1QA	Complement C1q subcomponent subunit A; C1q associates with the proenzymes C1r and C1s to yield C1, the first component of the serum complement system. The collagen-like regions of C1q interact with the Ca(2+)-dependent C1r(2)C1s(2) proenzyme complex, and efficient activation of C1 takes place on interaction of the globular heads of C1q with the Fc regions of IgG or IgM antibody present in immune complexes (245 aa)
HSPG2	Basement membrane-specific heparan sulfate proteoglycan core protein; Integral component of basement membranes. Component of the glomerular basement membrane (GBM), responsible for the fixed negative electrostatic membrane charge, and which provides a barrier which is both size- and charge-selective. It serves as an attachment substrate for cells. Plays essential roles in vascularization. Critical for normal heart development and for regulating the vascular response to injury. Also required for avascular cartilage development; I-set domain containing (4391 aa)
COL11A2	Collagen alpha-2(XI) chain; May play an important role in fibrillogenesis by controlling lateral growth of collagen II fibrils; Collagens (1650 aa)
MFAP2	Microfibrillar-associated protein 2; Component of the elastin-associated microfibrils; Belongs to the MFAP family (183 aa)
SRPX	Sushi repeat-containing protein SRPX; May be involved in phagocytosis during disk shedding, cell adhesion to cells other than the pigment epithelium or signal transduction; Sushi domain containing (464 aa)
VIT	Vitrin; Promotes matrix assembly and cell adhesiveness (693 aa)
SERPINB9	Serpin B9; Granzyme B inhibitor; Serpin peptidase inhibitors (376 aa)
MATN3	Matrilin-3; Major component of the extracellular matrix of cartilage and may play a role in the formation of extracellular filamentous networks; Matrilins (486 aa)
ACAN	Aggrecan core protein; This proteoglycan is a major component of extracellular matrix of cartilagenous tissues. A major function of this protein is to resist compression in cartilage. It binds avidly to hyaluronic acid via an N-terminal globular region; C-type lectin domain containing (2530 aa)
TGFBI	Transforming growth factor-beta-induced protein ig-h3; Plays a role in cell adhesion. May play a role in cell-collagen interactions (By similarity) (683 aa)
CHAD	Chondroadherin; Promotes attachment of chondrocytes, fibroblasts, and osteoblasts. This binding is mediated (at least for chondrocytes and fibroblasts) by the integrin alpha(2)beta(1). May play an important role in the regulation of chondrocyte growth and proliferation (By similarity); Belongs to the small leucine-rich proteoglycan (SLRP) family. SLRP class IV subfamily (359 aa)
CCL16	C-C motif chemokine 16; Shows chemotactic activity for lymphocytes and monocytes but not neutrophils. Also shows potent myelosuppressive activity, suppresses proliferation of myeloid progenitor cells. Recombinant SCYA16 shows chemotactic activity for monocytes and THP-1 monocytes, but not for resting lymphocytes and neutrophils. Induces a calcium flux in THP-1 cells that were desensitized by prior expression to RANTES; Belongs to the intercrine beta (chemokine CC) family (120 aa)
GREM1	Gremlin-1; Cytokine that may play an important role during carcinogenesis and metanephric kidney organogenesis, as a BMP antagonist required for early limb outgrowth and patterning in maintaining the FGF4-SHH feedback loop. Down-regulates the BMP4 signaling in a dose-dependent manner (By similarity). Antagonist of BMP2; inhibits BMP2-mediated differentiation of osteoblasts (in vitro). Acts as inhibitor of monocyte chemotaxis. Can inhibit the growth or viability of normal cells but not transformed cells when is overexpressed (By similarity); Belongs to the DAN family (184 aa)

9.2.2. List of proteins that were found predominantly in GP Matrisome and the preview information provided by STRING that was used to find the targets of interest

Protein name	String associated information
PLOD1	Procollagen-lysine,2-oxoglutarate 5-dioxygenase 1; Part of a complex composed of PLOD1, P3H3 and P3H4 that catalyzes hydroxylation of lysine residues in collagen alpha chains and is required for normal assembly and cross-linkling of collagen fibrils (By similarity). Forms hydroxylysine residues in -Xaa-Lys-Gly- sequences in collagens. These hydroxylysines serve as sites of attachment for carbohydrate units and are essential for the stability of the intermolecular collagen cross-links (Probable) (727 aa)
CTSG	Cathepsin G; Serine protease with trypsin- and chymotrypsin-like specificity. Cleaves complement C3. Has antibacterial activity against the Gram-negative bacterium P.aeruginosa, antibacterial activity is inhibited by LPS from P.aeruginosa, Z-Gly-Leu-Phe- CH2Cl and phenylmethylsulfonyl fluoride; Belongs to the peptidase S1 family (255 aa)
PLOD3	Procollagen-lysine,2-oxoglutarate 5-dioxygenase 3; Forms hydroxylysine residues in -Xaa-Lys-Gly- sequences in collagens. These hydroxylysines serve as sites of attachment for carbohydrate units and are essential for the stability of the intermolecular collagen cross-links (738 aa)
VTN	Vitronectin; Vitronectin is a cell adhesion and spreading factor found in serum and tissues. Vitronectin interact with glycosaminoglycans and proteoglycans. Is recognized by certain members of the integrin family and serves as a cell-to-substrate adhesion molecule. Inhibitor of the membrane-damaging effect of the terminal cytolytic complement pathway; Endogenous ligands (478 aa)
IBSP	Bone sialoprotein 2; Binds tightly to hydroxyapatite. Appears to form an integral part of the mineralized matrix. Probably important to cell-matrix interaction. Promotes Arg-Gly-Asp-dependent cell attachment; SIBLING family (317 aa)
LAMA4	Laminin subunit alpha-4; Binding to cells via a high affinity receptor, laminin is thought to mediate the attachment, migration and organization of cells into tissues during embryonic development by interacting with other extracellular matrix components (1823 aa)
SPARC	SPARC; Appears to regulate cell growth through interactions with the extracellular matrix and cytokines. Binds calcium and copper, several types of collagen, albumin, thrombospondin, PDGF and cell membranes. There are two calcium binding sites; an acidic domain that binds 5 to 8 Ca(2+) with a low affinity and an EF-hand loop that binds a Ca(2+) ion with a high affinity; SPARC family (303 aa)
HRG	Histidine-rich glycoprotein; Plasma glycoprotein that binds a number of ligands such as heme, heparin, heparan sulfate, thrombospondin, plasminogen, and divalent metal ions. Binds heparin and heparin/glycosaminoglycans in a zinc-dependent manner. Binds heparan sulfate on the surface of liver, lung, kidney and heart endothelial cells. Binds to N-sulfated polysaccharide chains on the surface of liver endothelial cells. Inhibits rosette formation. Acts as an adapter protein and is implicated in regulating many processes such as immune complex and pathogen clearance, cell chemotaxis, cell [...] (525 aa)
LEPRE1	Prolyl 3-hydroxylase 1; Basement membrane-associated chondroitin sulfate proteoglycan (CSPG). Has prolyl 3-hydroxylase activity catalyzing the post-translational formation of 3-hydroxyproline in -Xaa-Pro- Gly- sequences in collagens, especially types IV and V. May be involved in the secretory pathway of cells. Has growth suppressive activity in fibroblasts (804 aa)
CTSD	Cathepsin D; Acid protease active in intracellular protein breakdown. Plays a role in APP processing following cleavage and activation by ADAM30 which leads to APP degradation. Involved in the pathogenesis of several diseases such as breast cancer and possibly Alzheimer disease; Cathepsins (412 aa)
CLEC11A	C-type lectin domain family 11 member A; Promotes osteogenesis by stimulating the differentiation of mesenchymal progenitors into mature osteoblasts. Important for repair and maintenance of adult bone (By similarity); C-type lectin domain containing (323 aa)
LMAN1	Protein ERGIC-53; Mannose-specific lectin. May recognize sugar residues of glycoproteins, glycolipids, or glycosylphosphatidyl inositol anchors and may be involved in the sorting or recycling of proteins, lipids, or both. The LMAN1-MCFD2 complex forms a specific cargo receptor for the ER-to-Golgi transport of selected proteins (510 aa)
MMP13	Collagenase 3; Plays a role in the degradation of extracellular matrix proteins including fibrillar collagen, fibronectin, TNC and ACAN. Cleaves triple helical collagens, including type I, type II and type III collagen, but has the highest activity with soluble type II collagen. Can also degrade collagen type IV, type XIV and type X. May also function by activating or degrading key regulatory proteins, such as TGFB1 and CTGF. Plays a role in wound healing, tissue remodeling, cartilage degradation, bone development, bone mineralization and ossification. Required for normal embryonic bon [...] (471 aa)
LOXL4	Lysyl oxidase homolog 4; May modulate the formation of a collagenous extracellular matrix; Scavenger receptor cysteine rich domain containing (756 aa)
IL17B	Interleukin-17B; Stimulates the release of tumor necrosis factor alpha and IL-1-beta from the monocytic cell line THP-1; Interleukins (180 aa)
P4HA1	Prolyl 4-hydroxylase subunit alpha-1; Catalyzes the post-translational formation of 4-hydroxyproline in -Xaa-Pro-Gly- sequences in collagens and other proteins; Belongs to the P4HA family (534 aa)

F13A1   Coagulation factor XIII A chain; Factor XIII is activated by thrombin and calcium ion to a transglutaminase that catalyzes the formation of gamma-glutamyl- epsilon-lysine cross-links between fibrin chains, thus stabilizing the fibrin clot. Also cross-link alpha-2-plasmin inhibitor, or fibronectin, to the alpha chains of fibrin (732 aa)

ITIH4   Inter-alpha-trypsin inhibitor heavy chain H4; Type II acute-phase protein (APP) involved in inflammatory responses to trauma. May also play a role in liver development or regeneration (930 aa)

CTSK   Cathepsin K; Closely involved in osteoclastic bone resorption and may participate partially in the disorder of bone remodeling. Displays potent endoprotease activity against fibrinogen at acid pH. May play an important role in extracellular matrix degradation; Cathepsins (329 aa)

ITIH1   Inter-alpha-trypsin inhibitor heavy chain H1; May act as a carrier of hyaluronan in serum or as a binding protein between hyaluronan and other matrix protein, including those on cell surfaces in tissues to regulate the localization, synthesis and degradation of hyaluronan which are essential to cells undergoing biological processes (911 aa)

CD109   CD109 antigen; Modulates negatively TGFB1 signaling in keratinocytes; Belongs to the protease inhibitor I39 (alpha-2- macroglobulin) family (1445 aa)

ANXA5   Annexin A5; This protein is an anticoagulant protein that acts as an indirect inhibitor of the thromboplastin-specific complex, which is involved in the blood coagulation cascade; Annexins (320 aa)

EDIL3   EGF-like repeat and discoidin I-like domain-containing protein 3; Promotes adhesion of endothelial cells through interaction with the alpha-v/beta-3 integrin receptor. Inhibits formation of vascular-like structures. May be involved in regulation of vascular morphogenesis of remodeling in embryonic development (480 aa)

COL1A2   Collagen alpha-2(I) chain; Type I collagen is a member of group I collagen (fibrillar forming collagen); Belongs to the fibrillar collagen family (1366 aa)

HTRA3   Serine protease HTRA3; Serine protease that cleaves beta-casein/CSN2 as well as several extracellular matrix (ECM) proteoglycans such as decorin/DCN, biglycan/BGN and fibronectin/FN1. Inhibits signaling mediated by TGF-beta family proteins possibly indirectly by degradation of these ECM proteoglycans (By similarity). May act as a tumor suppressor. Negatively regulates, in vitro, trophoblast invasion during placental development and may be involved in the development of the placenta in vivo. May also have a role in ovarian development, granulosa cell differentiation and luteinization; B [...] (453 aa)

COL3A1   Collagen alpha-1(III) chain; Collagen type III occurs in most soft connective tissues along with type I collagen. Involved in regulation of cortical development. Is the major ligand of ADGRG1 in the developing brain and binding to ADGRG1 inhibits neuronal migration and activates the RhoA pathway by coupling ADGRG1 to GNA13 and possibly GNA12 (1466 aa)

FGB   Fibrinogen beta chain; Cleaved by the protease thrombin to yield monomers which, together with fibrinogen alpha (FGA) and fibrinogen gamma (FGG), polymerize to form an insoluble fibrin matrix. Fibrin has a major function in hemostasis as one of the primary components of blood clots. In addition, functions during the early stages of wound repair to stabilize the lesion and guide cell migration during re-epithelialization. Was originally thought to be essential for platelet aggregation, based on in vitro studies using anticoagulated blood. However subsequent studies have shown that it is [...] (491 aa)

F2   Prothrombin; Thrombin, which cleaves bonds after Arg and Lys, converts fibrinogen to fibrin and activates factors V, VII, VIII, XIII, and, in complex with thrombomodulin, protein C. Functions in blood homeostasis, inflammation and wound healing; Belongs to the peptidase S1 family (622 aa)

EFEMP2   EGF containing fibulin extracellular matrix protein 2; Belongs to the fibulin family (443 aa)

CSPG4   Chondroitin sulfate proteoglycan 4; Proteoglycan playing a role in cell proliferation and migration which stimulates endothelial cells motility during microvascular morphogenesis. May also inhibit neurite outgrowth and growth cone collapse during axon regeneration. Cell surface receptor for collagen alpha 2(VI) which may confer cells ability to migrate on that substrate. Binds through its extracellular N- terminus growth factors, extracellular matrix proteases modulating their activity. May regulate MPP16-dependent degradation and invasion of type I collagen participating in melanoma c [...] (2322 aa)

A2M   Alpha-2-macroglobulin; Is able to inhibit all four classes of proteinases by a unique 'trapping' mechanism. This protein has a peptide stretch, called the 'bait region' which contains specific cleavage sites for different proteinases. When a proteinase cleaves the bait region, a conformational change is induced in the protein which traps the proteinase. The entrapped enzyme remains active against low molecular weight substrates (activity against high molecular weight substrates is greatly reduced). Following cleavage in the bait region, a thioester bond is hydrolyzed and mediates the c [...] (1474 aa)

COL10A1   Collagen alpha-1(X) chain; Type X collagen is a product of hypertrophic chondrocytes and has been localized to presumptive mineralization zones of hyaline cartilage; Collagens (680 aa)

ANGPTL5   Angiopoietin-related protein 5; Fibrinogen C domain containing; Angiopoietin like (388 aa)

ANXA2	Annexin A2; Calcium-regulated membrane-binding protein whose affinity for calcium is greatly enhanced by anionic phospholipids. It binds two calcium ions with high affinity. May be involved in heat-stress response. Inhibits PCSK9-enhanced LDLR degradation, probably reduces PCSK9 protein levels via a translational mechanism but also competes with LDLR for binding with PCSK9; Belongs to the annexin family (357 aa)
FN1	Fibronectin type III domain containing; Endogenous ligands (2477 aa)
ITIH2	Inter-alpha-trypsin inhibitor heavy chain H2; May act as a carrier of hyaluronan in serum or as a binding protein between hyaluronan and other matrix protein, including those on cell surfaces in tissues to regulate the localization, synthesis and degradation of hyaluronan which are essential to cells undergoing biological processes; Belongs to the ITIH family (946 aa)
SERPINC1	Antithrombin-III; Most important serine protease inhibitor in plasma that regulates the blood coagulation cascade. AT-III inhibits thrombin, matriptase-3/TMPRSS7, as well as factors IXa, Xa and XIa. Its inhibitory activity is greatly enhanced in the presence of heparin; Serpin peptidase inhibitors (464 aa)
THBS3	Thrombospondin-3; Adhesive glycoprotein that mediates cell-to-cell and cell-to-matrix interactions. Can bind to fibrinogen, fibronectin, laminin and type V collagen (956 aa)
S100A8	Protein S100-A8; S100A8 is a calcium- and zinc-binding protein which plays a prominent role in the regulation of inflammatory processes and immune response. It can induce neutrophil chemotaxis and adhesion. Predominantly found as calprotectin (S100A8/A9) which has a wide plethora of intra- and extracellular functions. The intracellular functions include- facilitating leukocyte arachidonic acid trafficking and metabolism, modulation of the tubulin-dependent cytoskeleton during migration of phagocytes and activation of the neutrophilic NADPH-oxidase. Activates NADPH- oxidase by facilit [...] (93 aa)
S100A12	Protein S100-A12; S100A12 is a calcium-, zinc- and copper-binding protein which plays a prominent role in the regulation of inflammatory processes and immune response. Its proinflammatory activity involves recruitment of leukocytes, promotion of cytokine and chemokine production, and regulation of leukocyte adhesion and migration. Acts as an alarmin or a danger associated molecular pattern (DAMP) molecule and stimulates innate immune cells via binding to receptor for advanced glycation endproducts (AGER). Binding to AGER activates the MAP-kinase and NF-kappa-B signaling pathways leadin [...] (92 aa)
S100A9	Protein S100-A9; S100A9 is a calcium- and zinc-binding protein which plays a prominent role in the regulation of inflammatory processes and immune response. It can induce neutrophil chemotaxis, adhesion, can increase the bactericidal activity of neutrophils by promoting phagocytosis via activation of SYK, PI3K/AKT, and ERK1/2 and can induce degranulation of neutrophils by a MAPK-dependent mechanism. Predominantly found as calprotectin (S100A8/A9) which has a wide plethora of intra- and extracellular functions. The intracellular functions include- facilitating leukocyte arachidonic acid [...] (114 aa)
S100A10	Protein S100-A10; Because S100A10 induces the dimerization of ANXA2/p36, it may function as a regulator of protein phosphorylation in that the ANXA2 monomer is the preferred target (in vitro) of tyrosine- specific kinase; Belongs to the S-100 family (97 aa)
COL11A1	Collagen alpha-1(XI) chain; May play an important role in fibrillogenesis by controlling lateral growth of collagen II fibrils; Collagens (1806 aa)
MMP9	Matrix metalloproteinase-9; May play an essential role in local proteolysis of the extracellular matrix and in leukocyte migration. Could play a role in bone osteoclastic resorption. Cleaves KiSS1 at a Gly-|-Leu bond. Cleaves type IV and type V collagen into large C-terminal three quarter fragments and shorter N-terminal one quarter fragments. Degrades fibronectin but not laminin or Pz-peptide; M10 matrix metallopeptidases (707 aa)
COL9A2	Collagen alpha-2(IX) chain; Structural component of hyaline cartilage and vitreous of the eye; Collagen proteoglycans (689 aa)
ANGPTL2	Angiopoietin-related protein 2; Induces sprouting in endothelial cells through an autocrine and paracrine action; Angiopoietin like (493 aa)
F10	Coagulation factor X; Factor Xa is a vitamin K-dependent glycoprotein that converts prothrombin to thrombin in the presence of factor Va, calcium and phospholipid during blood clotting; Gla domain containing (488 aa)
ANXA1	Annexin A1; Plays important roles in the innate immune response as effector of glucocorticoid-mediated responses and regulator of the inflammatory process. Has anti-inflammatory activity. Plays a role in glucocorticoid-mediated down- regulation of the early phase of the inflammatory response (By similarity). Promotes resolution of inflammation and wound healing. Functions at least in part by activating the formyl peptide receptors and downstream signaling cascades. Promotes chemotaxis of granulocytes and monocytes via activation of the formyl peptide receptors. Contributes to the adapt [...] (346 aa)
C1QTNF3	Complement C1q tumor necrosis factor-related protein 3; C1q and TNF related 3 (319 aa)
LAMB2	Laminin subunit beta-2; Binding to cells via a high affinity receptor, laminin is thought to mediate the attachment, migration and organization of cells into tissues during embryonic development by interacting with other extracellular matrix components (1798 aa)

SERPINH1   Serpin H1; Binds specifically to collagen. Could be involved as a chaperone in the biosynthetic pathway of collagen; Serpin peptidase inhibitors (418 aa)

ELANE   Neutrophil elastase; Modifies the functions of natural killer cells, monocytes and granulocytes. Inhibits C5a-dependent neutrophil enzyme release and chemotaxis (267 aa)

ANXA8   Annexin A8; Annexins (365 aa)

HIST1H4A   Histone cluster 1 H4 family member a; Core component of nucleosome. Nucleosomes wrap and compact DNA into chromatin, limiting DNA accessibility to the cellular machineries which require DNA as a template. Histones thereby play a central role in transcription regulation, DNA repair, DNA replication and chromosomal stability. DNA accessibility is regulated via a complex set of post-translational modifications of histones, also called histone code, and nucleosome remodeling (103 aa)

PAMR1   Inactive serine protease PAMR1; May play a role in regeneration of skeletal muscle; Belongs to the peptidase S1 family (737 aa)

10. CHAPTER - APENDIX

10.1. Principles of freeze-drying

10.1.1.   Introduction

This appendix was developed to introduce the principles of freeze-drying to novice users in Trinity Centre for Biomedical Engineering. Part of the content was adapted from Biopharma Technology Ltd (BTL)'s course.

Freeze-drying, or lyophilization as it is referred to in the pharmaceutical and diagnostic industries, is a dehydration technique, which enables frozen solutions or frozen slurry products to be dried under a vacuum. The theoretical principle of freeze-drying process is defined in the red square of the figure below (**Figure 10-1**), illustrating a typical phase diagram.
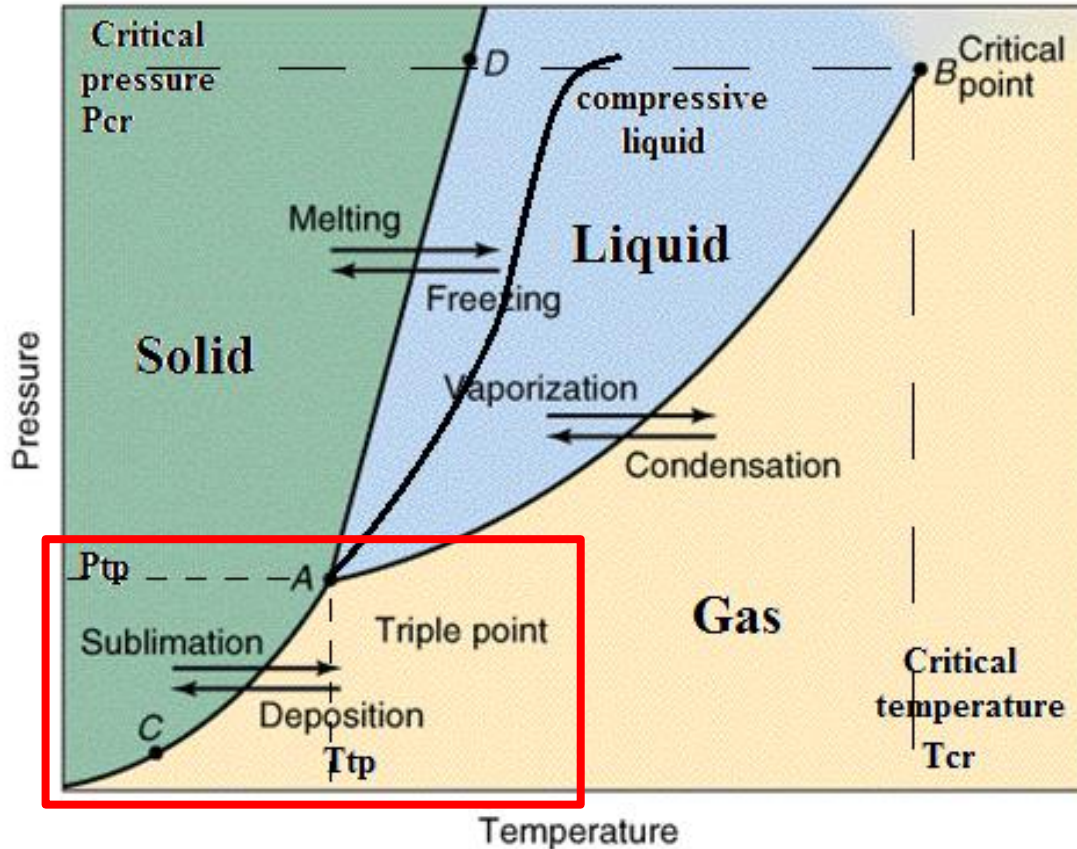
Figure 10-1. Phase diagram (pressure Vs temperature).

The main aim is to enhance product preservation, storage life and marketing of a product by removal of water content. It is a method of drying while maintaining the original structure and activity. It is a reversible process and easily reconstitutes.

Disadvantages of freeze-drying can be summarized into (i) high capital cost of equipment and cost of running equipment (energy costs), (ii) it is a batch process and (iii) it takes a lot of time (2-5 days).

Generally, the freeze-drying cycle is divided in 3 phases:

- Freezing phase: freezes both solvent and solute. This means, it immobilizes the material and defines the structure ready for drying.
- Primary drying: it consists on the removal of the frozen moisture by a process of sublimation, i.e., the evaporation of ice to vapour without passing through the liquid phase.

- Secondary drying: the product is further dried by a process of desorption. This step is used to control the level of final moisture (some products require more moisture than others to maintain stability).

10.1.2.   *The essential apparatus*

The essential apparatus of a freeze-drying system, illustrated in **Figure 10-2**, contains:

1) Chamber shelves upon which the product is supported.

2) Process "condenser" (depositor) that acts as a "cold trap" to deposit the vapour leaving the drying product.

3) Thermal fluid, typically silicone oil based, is pumped through the shelves, heat exchangers to control their temperature in order to transfer energy into and out of the product.

4) Refrigeration system used to cool the thermal fluid. It is important to freeze the product to a required temperature. It is also used to lower the temperature of the condenser, which is important for sublimation phase.

5) Heating system, normally electrical, used to add heat to the thermal fluid. It is important for drying at a required temperature. It is also used to heat the condenser, which is important to remove deposited solvent in the cleaning step.

6) Vacuum pump used to evacuate the chamber and condenser down to working pressure. The suction is normally taken from the condenser to help protect the pump from any ingress of moisture.

7) Machine control used to regulate shelf temperature and chamber vacuum. This control can be integrated within the freeze-drier with EPROM (erasable programmable read only memory) or remotely supervised by SCADA (supervisory, control and data acquisition) and implemented through PLC (programmable logic controller). Probes to measure condenser, shelf and product temperatures and pressure levels are included in the system.
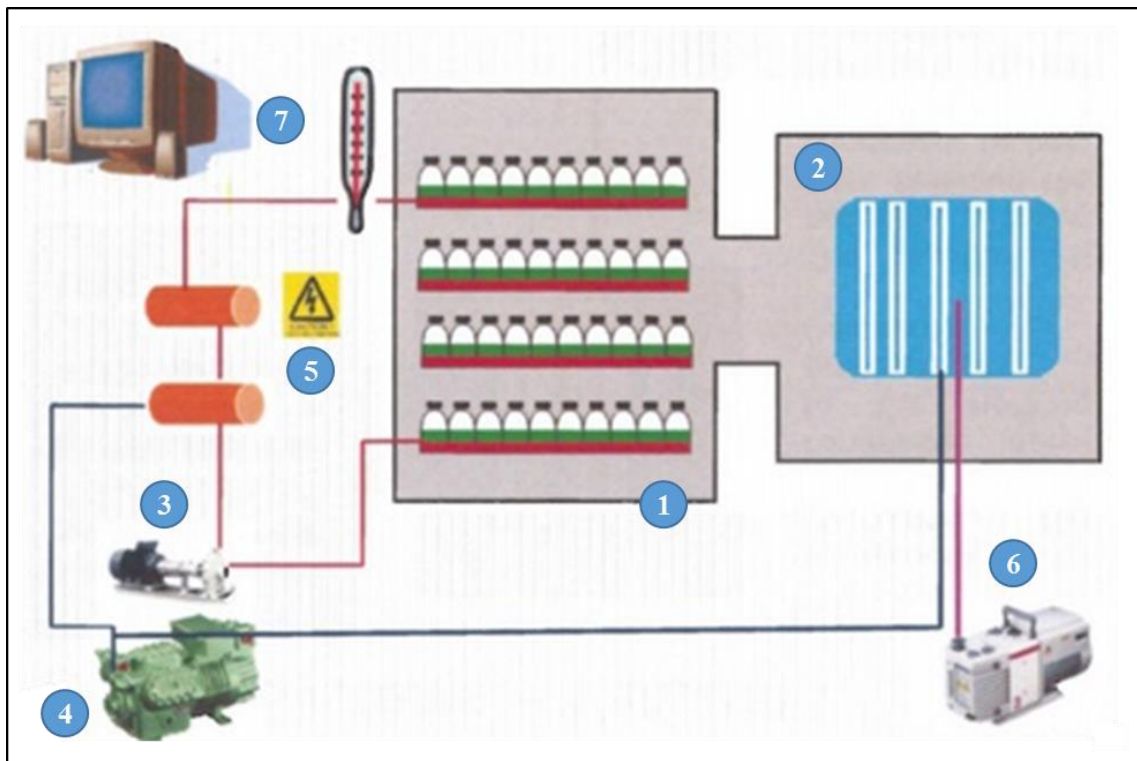
Figure 10-2. *The essential apparatus of a freeze-drying system.*

10.1.3.   Applications and uses

Main applications in bioengineering lab

- Enhance product preservation, storage life and marketing of a product by removal of water content.
- Water removal for dry weight measurement used as normalization factor in biochemical assays.
- Water removal for further concentration implementation upon rehydration within a known volume.
- Drying technique for further surface topography characterization by scanning electron microscopy (SEM).
- Scaffold fabrication with tailored pore size or shape depending on initial freezing characteristics (freezing rate, annealing, heat transfer direction…).

Other common applications

- Achievement of a chemical balance, such as for biological reagents.

- Preservation of temperature sensitive products, particularly those of biological origin, such as growth factors, enzymes, blood plasma, vaccines...

- A practical solution for certain delivery problems, for example, the packaging of constituents that cannot be mixed in the liquid state, but which are solidified in successive stages and then freeze dried.

- A solution for certain filling problems. It may be difficult, for instance, to divide several milligrams of powder into precise vial dosages, due to the difficulty of measuring tiny amounts, homogeneity, granulation, static electricity... The distribution of the product from the liquid state eliminates such production problems.

10.1.4.   The process of freeze-drying

1) Freezing phase

- In this phase the product temperature is lowered until the solution and the solute are frozen. This temperature is held for a time to equilibrate temperatures.

- This temperature has to be below the glass transition temperature (sometimes confused with collapse, melting or eutectic temperature). Fundamentally, it is important to ensure that the product is thoroughly frozen before the drying stage starts as the vacuum applied in primary drying will cause any unfrozen product to "boil". (e.g. 23.3% NaCl solution has an collapse temperature of -21 ºC, thus we may freeze our solution at the critical temperature of -25 ºC, to be safe).

- Ice formation can happen by:
  o Nucleation: solvent molecules arranging from random positions or gathering around "impurities"
  o Crystal growth: either dendritic or spherulitic formation

- The rate and the heat transfer direction at which this temperature is achieved are important as can influence ice crystal structure, defining how the product dries, and final pore size and shape of the dried structure.
  o Slower cooling rate leads to larger ice crystals and better ice "networking" (useful for making scaffolds with big and interconnected pores)
  o Rapid cooling can give a more even distribution of solutes (useful for SEM characterization)

- Annealing is a technique that comprises warming a product following initial freezing step. It can help achieve the advantages of both slow and rapid cooling. On the other hand, it can be detrimental for proteins that are sensitive to changes in the frozen state.
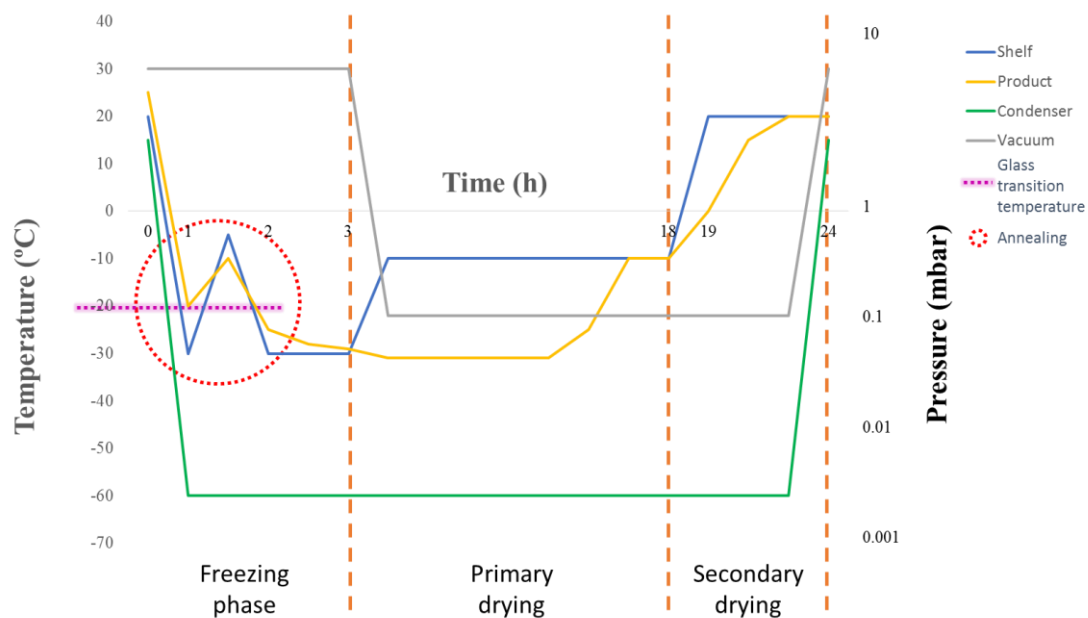
2) Primary drying (sublimation) phase

- Primary drying consists on the removal of frozen *free* water by the process of sublimation. Primary drying is complete when the last crystal of ice has sublimed into vapour (most of the solvent is removed in this phase, leaving 5-7% residual moisture). The sublimation characteristics of the product are greatly dependent of the frozen structure.
- The temperature provides the heat energy available to be absorbed by the product in drying. There are three ways to provide heat:
  - Radiation: transferred from the apparatus elements.
  - Convection: transferred through the solvent vapour.
  - Conduction: transferred from the temperature-regulated shelf (shelf temperature set at -10 ℃).
- The energy supplied in the form of heat is used to sublime the ice without increasing the product temperature. This is the reason, that even if we rise the shelf temperature (-10 ℃), product temperature remains below the glass transition temperature (collapse temperature).
- The pressure provides the vehicle for the amount of heat energy transferred into the product. Thus, there has to be a vacuum level sufficient for this transfer (200 mtorr or 0.2 mbar).
- Freeze-drying above a product's collapse temperature can lead to:
  - Loss of physical structure
  - Incomplete drying (high moisture content)
  - Decreased solubility, activity and/or stability
- The driving force in this phase is the vapour pressure differential, not simply the vacuum level itself. To enhance this differential, the condenser is kept colder than the frozen product to increase the pressure gradient (in this case, based upon the temperature difference).

3) Secondary drying

- At the end of primary drying, whilst there is no ice remaining, the product may not be sufficiently dry for storage. Secondary drying consists on the removal of additional water which remains physically adsorbed to the product. This is achieved by desorption.
- This process can be promoted by having a higher shelf temperature (> +20 ℃) and a lower chamber pressure than in primary drying (although the latest is more used at industrial scale).
- The duration of this phase will depend on the level of moisture desired (usually around 1%-4%; as general rule, a lower water content is better, however certain products require some moisture for storage stability).

At the completion of the process, the treated product should have retained its original mould form and original volume. The product can then be stored off-the-shelf (provided packaging is effective for the reduction of moisture migration; *e.g.* parafilm wrapped tube) for an almost indefinite period.

Figure 10-3. *Typical process of freeze-drying divided in its three phases: initial freezing step, primary drying (sublimation) and secondary drying. For simplification purposes, time scale intervals are not constant.*

10.1.5.   Common misconceptions

Colder condenser temperatures mean faster freeze-drying. Lowering the temperature of the condenser is less efficient than raising the temperature of the product. (Of course, the product temperature cannot be forced above its collapse point during primary drying). Remember the driving force is the difference in vapour pressure between product and condenser, not the condenser temperature alone.

"One size fits all" cycle development. The reality is, a freeze-drying cycle needs to be optimized for a specific product, batch parameters and freeze-dryer. An unsuitable cycle will be inefficient at best and can even risk process failure.

Vials can be filled to any depth. Product freeze-dries from the top (surface) down and as it does, a layer of dried product gradually builds up on top of the remaining frozen product. This dried layer creates an increasing impediment to the sublimated water vapour trying to escape from below. The thicker the layer of dried product, the more difficult it is for the vapour to escape. Where conditions allow, maximum product depth should be in the region of 12-15 mm.

It does not matter how a product is frozen – it is the drying that is important. Slow freezing rate will create large ice crystals. Large crystals create an open structure with large paths through which vapour can escape, facilitating easier drying. However, large ice crystals may cause high solute concentration and surface induced denaturation of proteins as well as changes in the original microstructure. Fast freezing (*e.g.* with liquid nitrogen) will create small crystals that will maintain original structure, essential to preserve for surface characterization purposes (*e.g.* by SEM).

Drier (lower final moisture content) is always better. Biological products such as cells, proteins and vaccines will typically require higher moisture content than simple chemicals, but the target final moisture content will depend on the specifics of each product and formulation.

Lower chamber pressure means faster freeze-drying. The vacuum within a freeze-drying chamber is intended only to create the necessary conditions for the moisture to sublime directly from ice to vapour. The moisture is not "sucked out" of the product and,

in fact, chamber pressures that are unnecessarily low will slow freeze-drying. Heat enters the product by conduction and by radiation but also convection from the remaining air molecules. As the pressure in the chamber drops, the effect of convection decreases. Control of the pressure/vacuum in the chamber is therefore one way of influencing the overall speed of the process. The driving force of freeze-drying is the vapour pressure differential between condenser and the product, not simply the pressure or the flow of gas created by a vacuum pump.

Space between sample containers is not necessary. Shelf spacing calculations are made to ensure that not only can we easily load product onto shelves, but that there is also sufficient space above the drying containers to allow unhindered vapour escape. Vapour can leave the drying vials at a high rate and with insufficient space for that vapour to escape above the vials it is possible to set up local drying conditions in the centre of a shelf, for example, with different drying conditions than those vials nearer the edge of a shelf.

Any vacuum pump will do. Most commonly, a two stage, oil sealed, rotary vane vacuum pump is sufficient for most freeze-drying applications. With the pump's ultimate achievable vacuum typically of the order of < 1 mtorr (measured directly at the pump according to pump manufacturer data), this provides near 100% of the pumping speed performance across the typical working range of freeze-drying vacuum requirements. If the freeze-drying system is specified correctly then the condenser will trap all condensable vapours and the pump will provide initial pull down and maintain set vacuum in the case of minor vacuum fluctuations and control by gas bleed. In all vacuum applications, it is useful to site the pump as close as possible to where performance is required as long length, small bore tubes have a significant effect on reducing vacuum pump performance.

10.2. SOP: Unidirectional freeze-casting of ECM

10.2.1.   *Custom-made moulds*

Two different moulds were used for the generation of random or aligned pores in the freeze-dried scaffolds. The design of the moulds was based on previous work in my laboratory[351] and others[182,348,363,390,391]. Briefly, the mould used for obtaining random pores was made of a single material (tufset polyurethane). A single material favours multidirectional heat transfer, thus generating random ice nucleation points when freezing the product. This would leave random pores after freeze-drying of the product. On the other hand, the second mould was a combination of a metal base and silicon wells made to favour unidirectional heat transfer. This would create water crystals growing unidirectional and perpendicularly to metal base surface, thus generating aligned pores in the freeze-dried scaffolds (Figure 10-4).

The single material mould was based on a solid works design by Dr. Henrique Almeida and fabricated in workshop in Trinity College. The silicon wells of the second mould were made by casting the silicon onto a 3D printed (using Ultimaker) PLA negative mould. Once set, the silicon was screwed to a metal plate for completing the two-material mould.
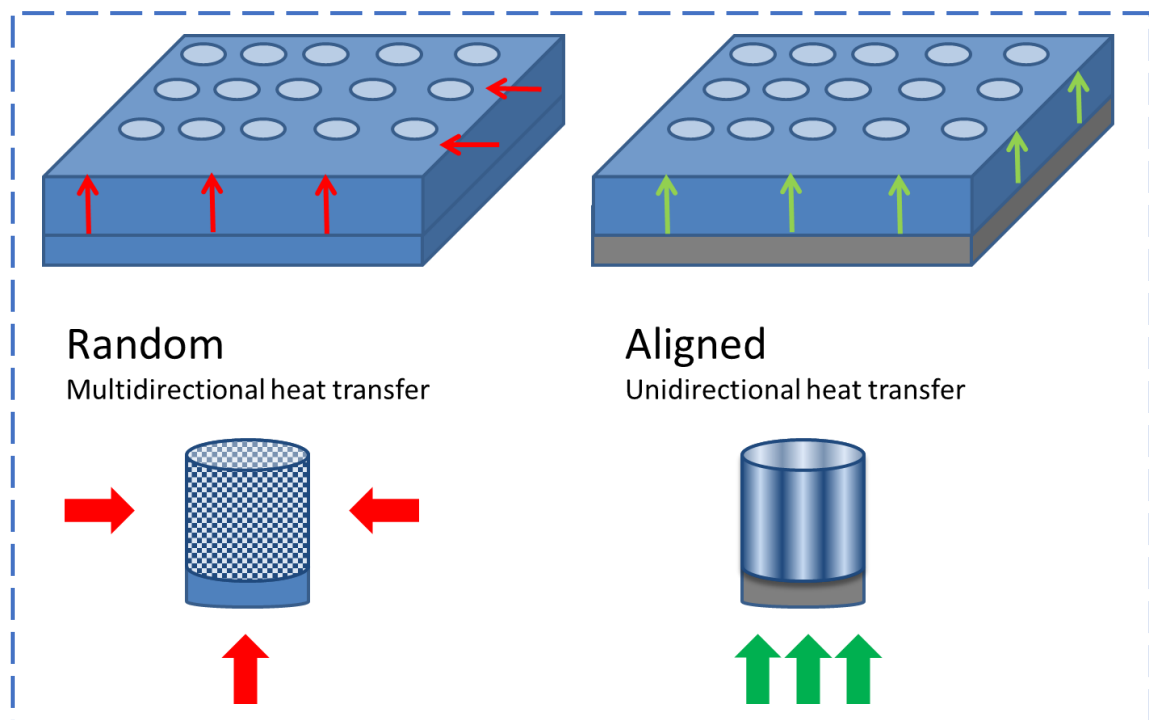
Figure 10-4. Schematic design of custom-made moulds use to fabricate ECM derived scaffolds by freeze drying. On the left, single material mould made to favour

10.2.2. *Freeze-drying protocol optimization: achieving pore alignment*

The formation of random or aligned pores it is not a simple process. Not only depends on the direction of heat transfer but also on the freezing rate, the nucleation temperature and the material composition. Thus, several protocols were tried to find the 'sweet spot' that would arise with controlled pore architecture.

(i)   Random pore protocol: standard protocol based on previous work in the laboratory[30,32] was used to generate random pores. Briefly, the slurry ECM was pour onto the tufset mould. Then, the moulds were placed in the freeze-drier (FreeZone Triad, Labconco®, KC, USA) and lyophilized to produce 5mm in diameter by 3 mm high porous scaffolds from either cryomilled/solubilised AC or GP derived ECM. Herein named as AC ECM/sECM and GP ECM/sECM, respectively. Briefly, the protocol was:

    a. Freezing phase: the slurry was frozen to -30 °C (1 °C/min) and kept at that temperature for 1 h at atmospheric pressure.

    b. Primary drying: pressure was lowered to 0.200 mbar. The temperature was then increased to -10 °C (1 °C/min), followed by a hold of 18 h.

    c. Secondary drying: the temperature was increased to room temperature (1 °C/min), follow by a hold of 4 h under vacuum.

(ii)   Aligned pore protocol: in this case the bi-material mould (metal base and silicon wells) was used to generate the scaffolds. The only phase that was changed was the first phase of the freeze-drying, the freezing phase. Parameters for the primary and secondary drying were kept the same as above.

a. Option 1: same protocol as above but with the bi-material mould.

b. Option 3: Freeze to -30 °C (uncontrolled rate; UR) and hold for 1 hour.

c. Option 2: freeze to -30 °C (1 °C/min). Increase to +25 °C (UR) and hold for 10 min. Freeze to -30 °C (UR) and hold for 1 hour.

d. Option 4: freeze to -190 °C (liquid nitrogen, UR) for 2 min. Increase to -30 °C (UR) and hold for 1 h.

e. Option 5: freeze to -190 °C (liquid nitrogen, UR) for 2 min. Increase to +25 °C (UR) for 10 min. Freeze to -30 °C (UR) and hold for 1 h.

After freeze-drying, the scaffolds then underwent dehydrothermal (DHT) crosslinking. The DHT process was performed in a vacuum oven (VD23, Binder, Germany), at 115 °C, in 2 mbar for 24 hr, as previously described in the literature[358]. After DHT, some scaffolds were further crosslinked by EDAC.

10.2.3. *ECM preparation*

Two different methods were used to fabricate scaffolds from two different ECM materials. The first method consisted on the solubilisation of collagenous ECM described above. Briefly, the ECM was digested in pepsin, precipitated with NaCl and re-solubilised with acetic acid before lyophilisation for concentration implementation. The second method was based on a previously used method for making scaffolds in our lab, which consisted on the cryomilling of the native ECM under liquid nitrogen.

To fabricate the scaffolds, the ECM derived materials were freeze-dried following protocols described above. 20 mg/ml and 50 mg/ml (dry weight) of solubilised and native ECM were used, respectively.

10.2.4. *Characterization method: macroscopic visualisation and scanning electron microscopy (SEM)*

Before running scaffolds through SEM, aligned microarchitecture was assessed by macroscopic visualisation. Only the scaffolds from successful protocols to obtain macroscopic aligned structures were chosen for further SEM characterisation (n FD samples per protocol = 8, n SEM samples of successful protocol = 2).

Freeze-dried and DHT crosslinked scaffolds were placed in PBS (or EDAC treated) to rehydrate them and allow for pores to fill in a culture-like condition. Then, the scaffolds were placed in liquid nitrogen for a brief period to snap freeze the structure for further characterization. The constructs were re-freeze-dried. Finally, the scaffolds were loaded onto aluminium studs where they were coated with gold nanoparticles and examined under a field emission scanning electron microscope (Tescan MIra Variable Pressure Field Emission SEM).

10.2.5. *Scanning electron microscopy images*

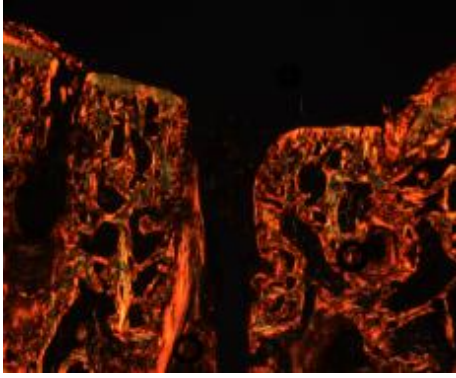|	DHT only	DHT + EDAC
Random		
Aligned		
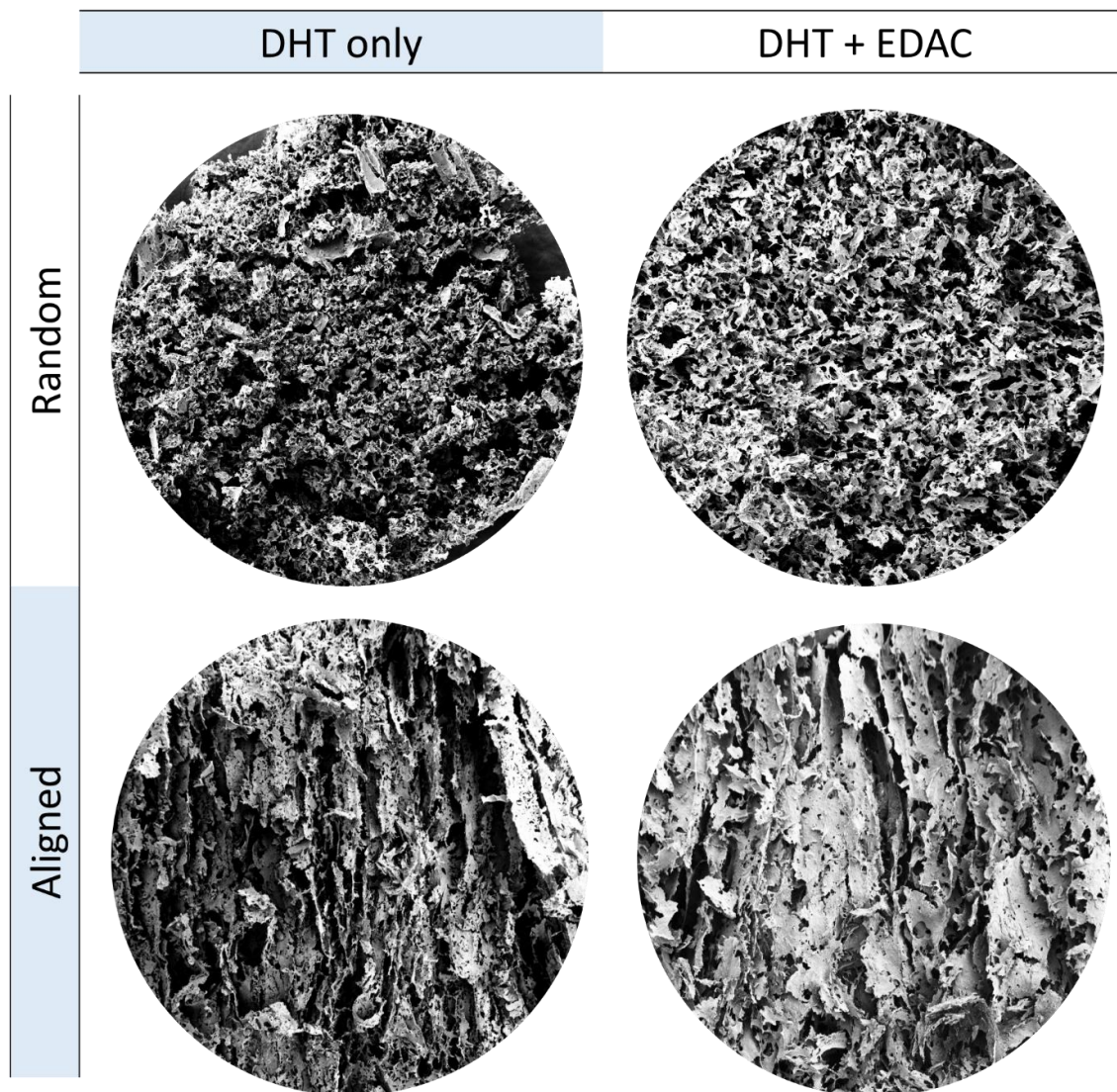
10.3. SOP: Fiji Orientation analysis protocol

1. Fiji > Image > Type > 8-bit
2. Orientation analysis
   a. Visual analysis: OrientationJ plugin > OrientationJ Analysis:
      i. Gaussian window: 10 (you may have to change the number based on the resulting overlapped image but keep constant for all images)
      ii. Cubic Spline Gradient (default).
      iii. Hue: Orientation.
      iv. Saturtion: Coherency.
      v. Brightness: Original image.
      vi. Make sure the 8 bit image is selected and press Run.
      vii. Save as new image (CTRL+S).
   b. Numerical analysis: Analyze > Directionality:

        i. Select ROI
            1. If ROI is all image just select the image
            2. Automatic: Edit > Selection > Specify
            3. Manual: draw ROI with tools
        ii. Set parameters for Directionality and press ok
            1. Method: Fourier components.
            2. Nbins: default.
            3. Histogram start: -90
            4. Tick: Display table
        iii. Copy results values for Direction and Dispersion (orientation data)
        iv. Copy table data to Excel and save (histogram data)
    3. Open Graph pad
        a. Plot table data to obtain histogram.
        b. Plot Direction (X) Vs Dispersion (Y) to obtain correlation graph and be able to compare not only average alignment but how good is this alignment.
    4. Reference the following paper: DOI: 10.1016/j.biomaterials.2018.09.044

10.4. SOP: Polarised Light Microscopy Analysis

Merge PLM pictures

1. Picrosirius red stained samples are used for polarised light microscopy (PLM) at the desired magnification (2x image width length is about 4-5mm).
2. Orient the superficial tangential zone of the sample parallel with the horizontal axis,
3. Capture a brightfield image.
4. Insert PLM filter.
5. Capture at least two PLM images (less than two angles is not acceptable for publication):
    a. bottom 0° / top 5°. Save picture as *Name_1.*
    b. bottom 45° / top 50°. Save picture as *Name_2.*
    c. (If the filter is decalibrated, for the bottom choose two angles that differ in 45 degrees. On the top look for the angle that creates the darkest picture).
6. Open FIJI.
7. File > Open image or images of interest.
8. Process > Image calculator > Operation "Max" > Tick "Create a new window". These images are then merged in ImageJ by adding them to a stack and then creating a maximum intensity projection of the two channels. This merged image can be used for analysis as required.
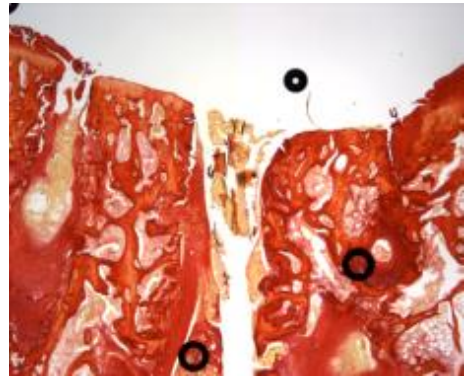
PLM 0-5
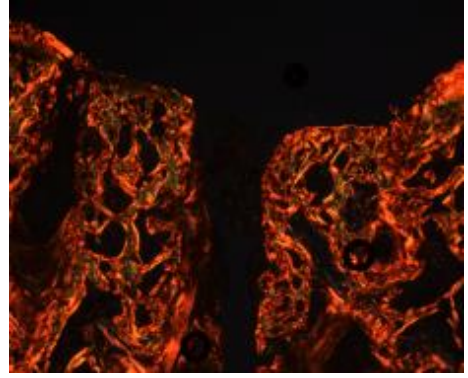
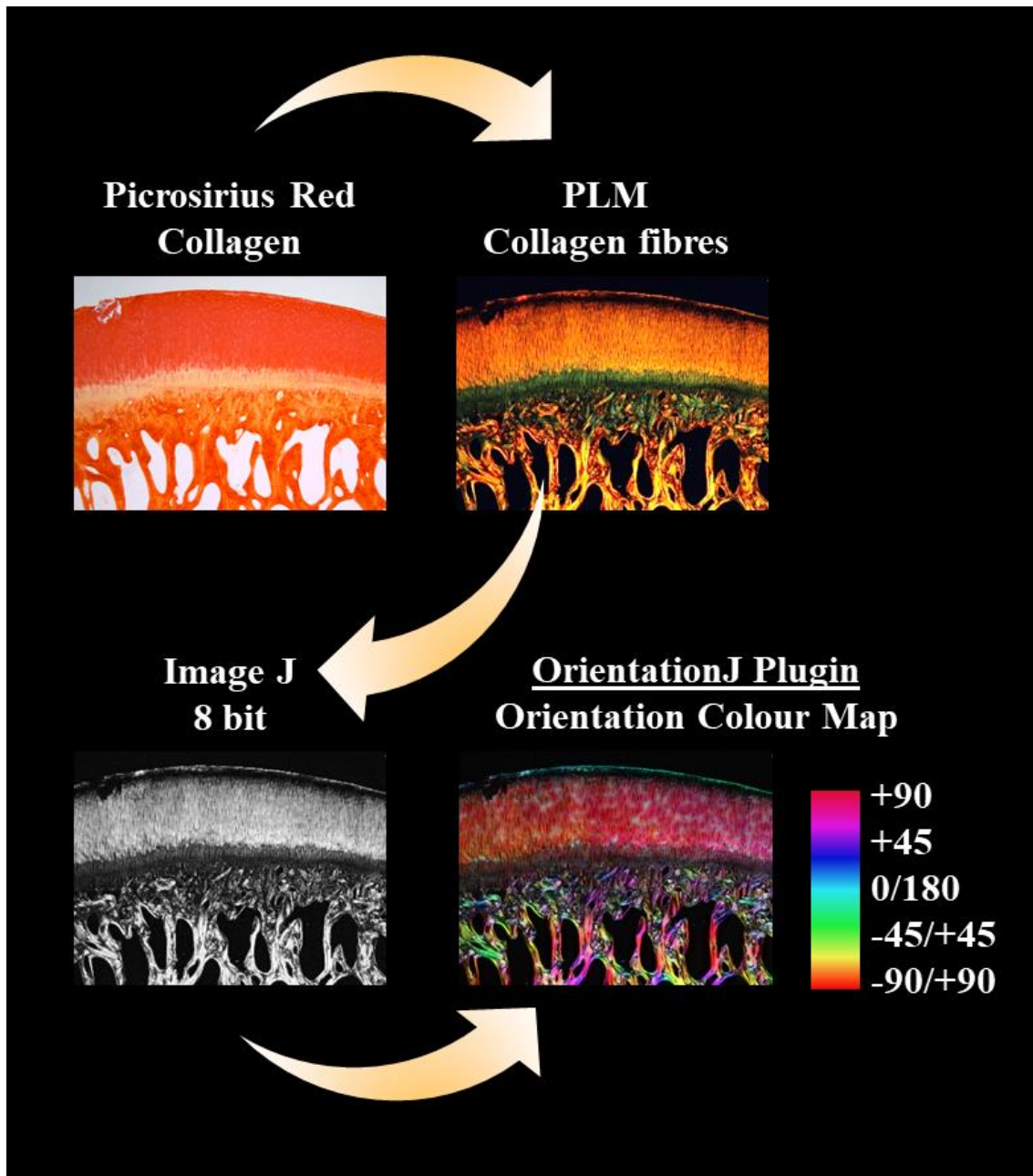**PLM 45-50**
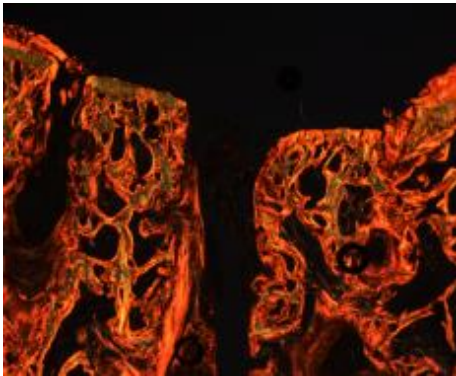
PLM merged

BF

Orientation analysis

9. Fiji > Image > Type > 8-bit
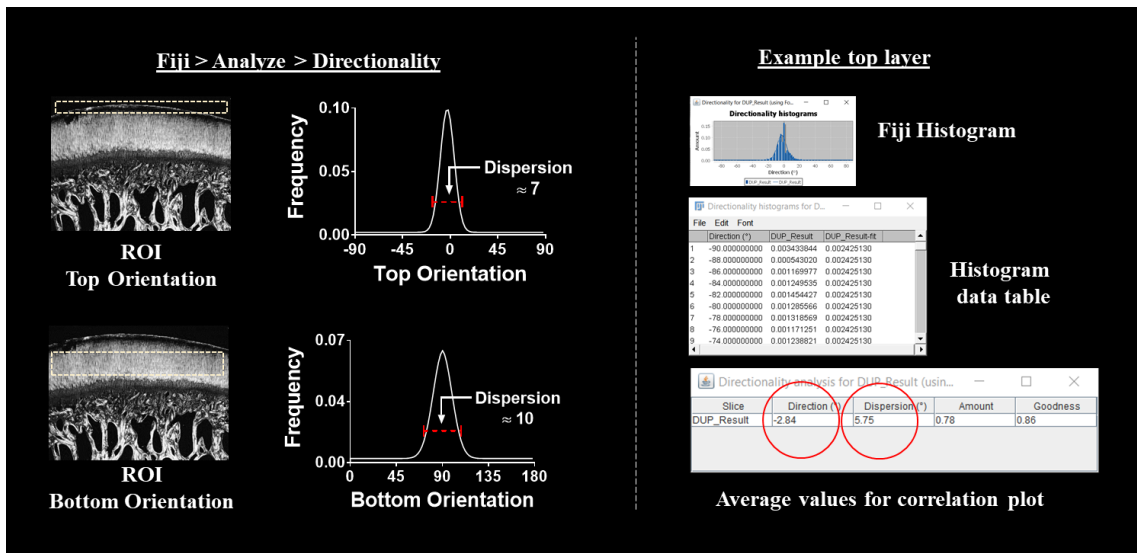10. Orientation analysis
    a. Visual analysis: OrientationJ plugin > OrientationJ Analysis:
        i. Gaussian window: 10 (you may have to change the number based on the resulting overlapped image but keep constant for all images)
        ii. Cubic Spline Gradient (default).
        iii. Hue: Orientation.
        iv. Saturtion: Coherency.
        v. Brightness: Original image.
        vi. Make sure the 8 bit image is selected and press Run.
        vii. Save as new image (CTRL+S).

b. Numerical analysis: Analyze > Directionality:
- **i.** Select ROI
    - **1.** If ROI is all image just select the image
    - **2.** Automatic: Edit > Selection > Specify
    - **3.** Manual: draw ROI with tools
- **ii.** Set parameters for Directionality and press ok
    - **1.** Method: Fourier components.
    - **2.** Nbins: default.
    - **3.** Histogram start: -90
    - **4.** Tick: Display table
- **iii.** Copy results values for Direction and Dispersion (orientation data)
- **iv.** Copy table data to Excel and save (histogram data)

Fiji > Analyze > Directionality / Example top layer

ROI Top Orientation / Top Orientation / Fiji Histogram / Histogram data table / Average values for correlation plot

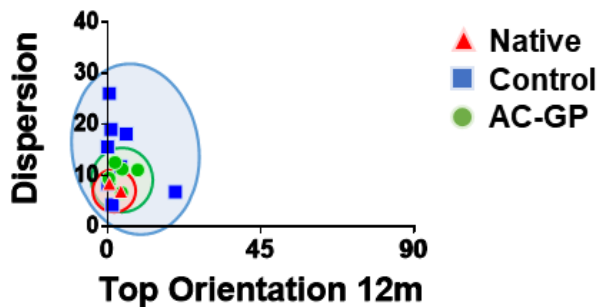ROI Bottom Orientation / Bottom Orientation

11. Open Graph pad
     a. Plot table data to obtain histogram.
     b. Plot Direction (X) Vs Dispersion (Y) to obtain correlation graph and be able to compare not only average alignment but how good is this alignment.
12. Reference the following paper: DOI: 10.1016/j.biomaterials.2018.09.044

Example

10.5. SOP: Color quantification with PS6

1. Open Photoshop 6th edition (it mays still work with newer editions).
2. File > Open image or images of interest (CTRL + select).
3. Select region of interest:
     a. If ROI is all image:
          i. Select > All (CTRL+A).
          ii. Window > Histogram > Refresh histogram.

   iii. Copy pixels value to Excel (this will be TOTAL PIXEL value).

   iv. Continue to step 5.

  b. If ROI can be selected with a predefined shape (eg, square) use the appropriate marquee tool. Use Style for:

   i. Normal: draw the shape with the tool manually.

   ii. Fixed: knowing the ratio distance:pixel you can define a square o exact proportions to keep consistency throughout the samples.

   iii. Pixel width multiplied by height = TOTAL PIXEL value. Copy value to Excel.

  c. If ROI is a random shape:

   i. Use quick selection tool (with +).

   ii. Window > Histogram > Refresh histogram.

   iii. Copy pixels value to Excel (this will be TOTAL PIXEL value).

4. Create a layer via copy (right click on the mouse). From now on, this layer will be the object of analysis. Make sure the layer is selected before further continuing. You can make invisible the original image if it helps you.

5. Use Magic wand tool to select a pixel from the image that represents the color you want to measure. Use sample size and tolerance to optimise selection. Use same parameters for all images of the same analysis.

6. Window > histogram > Refresh histogram. Copy pixels value to Excel (this will be your SAMPLE PIXEL value).

7. File > Save as > into a new file (if you save into the original you will be carrying extra data from layers).

8. File > Close image.

9. Calculate ratio SAMPLE PIXEL/TOTAL PIXEL to compare with other images

10. Plot ratio values in % in GraphPad.

11. Reference the following paper: DOI: 10.1016/j.biomaterials.2018.09.044

10.6. SOP: Quantification of Safranin-O in OC samples with PS6

1. Open Photoshop 6th edition (it mays still work with newer editions).

2. Copy Action file: "SafO – 2 layers.atn" into a known folder (link below).

3. Window > Actions.

4. Press the symbol on the top right corner of the *action* window (▼≡).

5. Load actions > Load "SafO – 2 layers.atn" or similar.

6. File > Open image or images of interest (CTRL + select).

7. Make sure to orient the superficial tangential zone of the sample parallel with the horizontal axis. See limitations section below.

8. Window > Actions.

9. You should be able to see the *action* name. Expand the *action.*

10. Select the line "Select and press play".

11. Press play (at the bottom of the action window).

12. Follow the instructions.

13. You may have to edit the "Set selection" line depending on the pixels of the image you are analyzing. This can be done by recording a new

selection into the action and deleting the current "Set selection" line. See SOP "Color quantification with PS6 – general" for details on selecting a ROI. Once this is sorted, continue to next step.
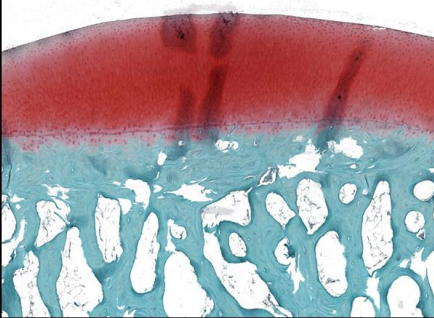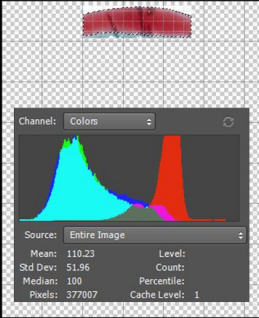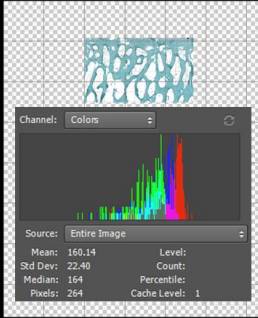
14. Reference the following paper: DOI: 10.1016/j.biomaterials.2018.09.044

Pathway

Tcbe(\\mme182208)\#GENERAL\SOPs\New SOPs (to be added to SOP book)\SOFTWARE SOPs.

Limitations

1. Images need to be properly oriented before analysis.
   a. Edit > Transform > Rotate (CTRL+T).
   b. File > Save as > New file to avoid modifying the original.
2. This is a semi-automatic *action* due to lack of PS6 programming skills.

Safranin-O
(sGAG/cartilage: red)

Pictures needs to be properly
oriented for analysis.
See limitations section.

Selection of top layer
(1.5 mm)

Chondral Region
Total pixel = 1.5 mm x 5 mm
% = Red pixels/Total pixel
e.g. 377007/480700*100
~ 80% Cartilage in ROI

Selection of bottom layer
(3.5 mm)

Subchondral bone Region
Total pixel = 3.5 mm x 5 mm
% = Red pixel/Total pixel
e.g. 264/960135*100
~ 0% Cartilage in ROI

11. CHAPTER: Bibliography

1. Mow, V. & Setton, L. Mechanical properties of normal and osteoarthritic articular cartilage. *Osteoarthritis* **61,** 108–122 (1998).

2. Hoemann, C. D. in *Cartil. Osteoarthr.* (eds. De Ceuninck, F., Sabatini, M. & Pastoureau, P.) **101,** 127–156 (2004).

3. MSD Impact - Arthritis Ireland. at <http://www.arthritisireland.ie/go/fit_for_work/msds/msd_facts#1>

4. EUMUSC. Musculoskeletal Health in Europe. 12 (2013).

5. Oliveria, S. A., Felson, D. T., Reed, J. I., Cirillo, P. A. & Walker, A. M. Incidence of symptomatic hand, hip, and knee osteoarthritis among patients in a health maintenance organization. *Arthritis Rheum.* **38,** 1134–41 (1995).

6. Death and DALY estimates for 2004 by cause for World Health Organization (WHO) Member States - Department of Measurement and Health Information. (2009). at <http://www.who.int/healthinfo/global_burden_disease/estimates_country/en/>

7. Hunter, W. Of the structure and diseases of articulating cartilages. *Philos. Trans.* **42,** 514–521 (1742).

8. Rowland, C. R., Little, D. & Guilak, F. Factors influencing the long-term behavior of extracellular matrix-derived scaffolds for musculoskeletal soft tissue repair. *J. Long. Term. Eff. Med. Implants* **22,** 181–193 (2013).

9. Caplan, A. I. The extracellular matrix is instructive. *Bioessays* **5,** 129–32 (1986).

10. Sawkins, M. J., Bowen, W., Dhadda, P., Markides, H., Sidney, L. E., Taylor, a J., Rose, F. R. a J., Badylak, S. F., Shakesheff, K. M. & White, L. J. Hydrogels derived from demineralized and decellularized bone extracellular matrix. *Acta Biomater.* **9,** 7865–73 (2013).

11. Badylak, S. F. The extracellular matrix as a biologic scaffold material. *Biomaterials* **28,** 3587–93 (2007).

12. Macchiarini, P., Jungebluth, P., Go, T., Asnaghi, M. A., Rees, L. E., Cogan, T. A., Dodson, A., Martorell, J., Bellini, S., Parnigotto, P. P., Dickinson, S. C., Hollander, A. P., Mantero, S., Conconi, M. T. & Birchall, M. A. Clinical transplantation of a tissue-engineered airway. *Lancet* **372,** 2023–30 (2008).

13. Martinello, T., Bronzini, I., Volpin, A., Vindigni, V., Maccatrozzo, L., Caporale, G., Bassetto, F. & Patruno, M. Successful recellularization of human tendon scaffolds using adipose-derived mesenchymal stem cells and collagen gel. *J. Tissue Eng. Regen. Med.* **8,** 612–9 (2014).

14. Ricchetti, E. T., Aurora, A., Iannotti, J. P. & Derwin, K. A. Scaffold devices for rotator cuff repair. *J. shoulder Elb. Surg.* **21,** 251–65 (2012).

15. D'Onofrio, A., Cresce, G. D., Bolgan, I., Magagna, P., Piccin, C., Auriemma, S. & Fabbri, A. Clinical and hemodynamic outcomes after aortic valve replacement with stented and stentless pericardial xenografts: a propensity-matched analysis. *J. Heart Valve Dis.* **20,** 319–326 (2011).

16. Meyer, T., Schwarz, K., Ulrichs, K. & Höcht, B. A new biocompatible material (Lyoplant) for the therapy of congenital abdominal wall defects: first experimental results in rats. *Pediatr. Surg. Int.* **22,** 369–74 (2006).

17. Yang, Z., Shi, Y., Wei, X., He, J., Yang, S., Dickson, G., Tang, J., Xiang, J., Song, C. & Li, G. Fabrication and repair of cartilage defects with a novel acellular cartilage matrix scaffold. *Tissue Eng. Part C. Methods* **16,** 865–76 (2010).

18. Kheir, E., Stapleton, T., Shaw, D., Jin, Z., Fisher, J. & Ingham, E. Development and characterization of an acellular porcine cartilage bone matrix for use in tissue engineering. *J. Biomed. Mater. Res. A* **99,** 283–94 (2011).

19. Gilbert, T. W., Sellaro, T. L. & Badylak, S. F. Decellularization of tissues and organs. *Biomaterials* **27,** 3675–83 (2006).

20. Benders, K. E. M., van Weeren, P. R., Badylak, S. F., Saris, D. B. F., Dhert, W. J. A., Malda, J., Weeren, P. R. van, Badylak, S. F., Saris, D. B. F., Dhert, W. J. A., Malda, J., van Weeren, P. R., Badylak, S. F., Saris, D. B. F., Dhert, W. J. A. & Malda, J. Extracellular matrix scaffolds for cartilage and bone regeneration. *Trends Biotechnol.* **31,** 169–76 (2013).

21.	Peretti, G. M., Campo-Ruiz, V., Gonzalez, S., Randolph, M. a, Wei Xu, J., Morse, K. R., Roses, R. E. & Yaremchuk, M. J. Tissue engineered cartilage integration to live and devitalized cartilage: a study by reflectance mode confocal microscopy and standard histology. *Connect. Tissue Res.* **47,** 190–9 (2006).

22.	Pieske, O., Wittmann, A., Zaspel, J., Löffler, T., Rubenbauer, B., Trentzsch, H. & Piltz, S. Autologous bone graft versus demineralized bone matrix in internal fixation of ununited long bones. *J. Trauma Manag. Outcomes* **3,** 1–8 (2009).

23.	Berven, S., Tay, B. K., Kleinstueck, F. S. & Bradford, D. S. Clinical applications of bone graft substitutes in spine surgery: Consideration of mineralized and demineralized preparations and growth factor supplementation. *Eur. Spine J.* **10,** 169–177 (2001).

24.	Van Der Stok, J., Hartholt, K. A., Schoenmakers, D. A. L. & Arts, J. J. C. The available evidence on demineralised bone matrix in trauma and orthopaedic surgery. *Bone Jt. Res.* **6,** 423–432 (2017).

25.	Kim, B. J., Kim, S. H., Lee, H., Lee, S. H., Kim, W. H. & Jin, S. W. Demineralized bone matrix (DBM) as a bone void filler in lumbar interbody fusion: A prospective pilot study of simultaneous DBM and autologous bone grafts. *J. Korean Neurosurg. Soc.* **60,** 225–231 (2017).

26.	Gilbert, T. W. Strategies for tissue and organ decellularization. *J. Cell. Biochem.* **113,** 2217–22 (2012).

27.	Crapo, P. M., Gilbert, T. W. & Badylak, S. F. An overview of tissue and whole organ decellularization processes. *Biomaterials* **32,** 3233–43 (2011).

28.	Luo, L., Eswaramoorthy, R., Mulhall, K. J. & Kelly, D. J. Decellularization of porcine articular cartilage explants and their subsequent repopulation with human chondroprogenitor cells. *J. Mech. Behav. Biomed. Mater.* **55,** 21–31 (2015).

29.	Cunniffe, G. M. M., Díaz-Payno, P. J. J., Ramey, J. S. S., Mahon, O. R. R., Dunne, A., Thompson, E. M. M., O'Brien, F. J. J. & Kelly, D. J. J. Growth plate extracellular matrix-derived scaffolds for large bone defect healing. *Eur. Cell. Mater.* **33,** 130–142 (2017).

30.	Almeida, H. V., Liu, Y., Cunniffe, G. M., Mulhall, K. J., Matsiko, A., Buckley, C.

T., O'Brien, F. J. & Kelly, D. J. Controlled release of transforming growth factor-β3 from cartilage-extra-cellular-matrix-derived scaffolds to promote chondrogenesis of human-joint-tissue-derived stem cells. *Acta Biomater.* **10,** 4400–9 (2014).

31. Almeida, H. V, Cunniffe, G. M., Vinardell, T., Buckley, C. T., O'Brien, F. J. & Kelly, D. J. Coupling freshly isolated CD44(+) infrapatellar fat pad-derived stromal cells with a TGF-β3 eluting cartilage ECM-derived scaffold as a single-stage strategy for promoting chondrogenesis. *Adv. Healthc. Mater.* **4,** 1043–53 (2015).

32. Cunniffe, G. M., Díaz-Payno, P. J., Sheehy, E. J., Critchley, S. E., Almeida, H. V., Pitacco, P., Carroll, S. F., Mahon, O. R., Dunne, A., Levingstone, T. J., Moran, C. J., Brady, R. T., O'Brien, F. J., Brama, P. A. J. & Kelly, D. J. Tissue-specific extracellular matrix scaffolds for the regeneration of spatially complex musculoskeletal tissues. *Biomaterials* **188,** 63–73 (2019).

33. Beachley, V. Z., Wolf, M. T., Sadtler, K., Manda, S. S., Jacobs, H., Blatchley, M. R., Bader, J. S., Pandey, A., Pardoll, D. & Elisseeff, J. H. Tissue matrix arrays for high-throughput screening and systems analysis of cell function. **12,** 7–9 (2015).

34. Díaz-payno, P. J., Cunniffe, G. M., Sheehy, E. J., Critchley, S. E. & Almeida, H. V. A bilayered scaffold derived from growth plate and articular cartilage extracellular matrix for osteochondral tissue regeneration in a caprine model. **31,** 2262 (2016).

35. Smith, B. D. & Grande, D. A. The current state of scaffolds for musculoskeletal regenerative applications. *Nat Rev Rheumatol* **11,** 213–222 (2015).

36. Makris, E. A., Gomoll, A. H., Malizos, K. N., Hu, J. C. & Athanasiou, K. A. Repair and tissue engineering techniques for articular cartilage. *Nat. Rev. Rheumatol.* **11,** 21–34 (2015).

37. Eichholz, K. F. & Hoey, D. A. Mediating human stem cell behaviour via defined fibrous architectures by melt electrospinning writing. *Acta Biomater.* **75,** 140–151 (2018).

38. Mendler, M., Eich-Bender, S. G., Vaughan, L., Winterhalter, K. H. & Bruckner,

P. Cartilage contains mixed fibrils of collagen types II, IX, and XI. *J. Cell Biol.* **108,** 191–197 (1989).

39. Hsueh, M. F., Khabut, A., Kjellström, S., Önnerfjord, P. & Kraus, V. B. Elucidating the Molecular Composition of Cartilage by Proteomics. *J. Proteome Res.* **15,** 374–388 (2016).

40. Wu, J. J., Woods, P. E. & Eyre, D. R. Identification of cross-linking sites in bovine cartilage type IX collagen reveals an antiparallel type II-type IX molecular relationship and type IX to type IX bonding. *J. Biol. Chem.* **267,** 23007–23014 (1992).

41. Hinek, A., Reiner, A. & Poole, A. R. The calcification of cartilage matrix in chondrocyte culture: studies of the C-propeptide of type II collagen (chondrocalcin). *J. Cell Biol.* **104,** 1435–1441 (1987).

42. Van der Rest, M., Rosenberg, L. C., Olsen, B. R. & Poole, A. R. Chondrocalcin is identical with the C-propeptide of type II procollagen. *Biochem. J.* **237,** 923–5 (1986).

43. Alini, M., Matsui, Y., Dodge, G. R. & Poole, A. R. The extracellular matrix of cartilage in the growth plate before and during calcification: changes in composition and degradation of type II collagen. *Calcif. Tissue Int.* **50,** 327–35 (1992).

44. Bantsimba-Malanda, C., Cottet, J., Netter, P., Dumas, D., Mainard, D., Magdalou, J. & Vincourt, J.-B. Chondrocalcin is internalized by chondrocytes and triggers cartilage destruction via an interleukin-1β-dependent pathway. *Matrix Biol.* **32,** 443–51 (2013).

45. Shen, G. The role of type X collagen in facilitating and regulating endochondral ossification of articular cartilage. *Orthod. Craniofac. Res.* **8,** 11–7 (2005).

46. Madry, H., van Dijk, C. N. & Mueller-Gerbl, M. The basic science of the subchondral bone. *Knee Surg. Sports Traumatol. Arthrosc.* **18,** 419–33 (2010).

47. Lyons, T. J., Stoddart, R. W., McClure, S. F. & McClure, J. The tidemark of the chondro-osseous junction of the normal human knee joint. *J. Mol. Histol.* **36,** 207–215 (2005).

48. Imhof, H., Breitenseher, M., Kainberger, F., Rand, T. & Trattnig, S. Importance of subchondral bone to articular cartilage in health and disease. *Top. Magn. Reson. Imaging* **10,** 180–192 (1999).

49. Sophia Fox, A. J., Bedi, A. & Rodeo, S. A. The basic science of articular cartilage: structure, composition, and function. *Sports Health* **1,** 461–8 (2009).

50. Gottardi, R., Hansen, U., Raiteri, R., Loparic, M., D??ggelin, M., Mathys, D., Friederich, N. F., Bruckner, P. & Stolz, M. Supramolecular organization of collagen fibrils in healthy and osteoarthritic human knee and hip joint cartilage. *PLoS One* **11,** 1–13 (2016).

51. Singh, I. The architecture of cancellous bone. *J. Anat.* **127,** 305–310 (1978).

52. Dhandayuthapani, B., Yoshida, Y., Maekawa, T. & Kumar, D. S. Polymeric scaffolds in tissue engineering application: a review. *Int. J. Polym. Sci.* **2011,** 1–19 (2011).

53. Hunziker, E. B. & Rosenberg, L. C. Repair of partial-thickness defects in articular cartilage: cell recruitment from the synovial membrane. *J. Bone Joint Surg. Am.* **78,** 721–33 (1996).

54. Hunziker, E. B., Driesang, I. M. & Saager, C. Structural barrier principle for growth factor-based articular cartilage repair. *Clin. Orthop. Relat. Res.* **391,** 182–9 (2001).

55. Hunziker, E. Functional barrier principle for growth-factor-based articular cartilage repair. *Osteoarthr. Cartil.* **11,** 320–327 (2003).

56. Johnstone, B., Alini, M., Cucchiarini, M., Dodge, G. R., Eglin, D., Guilak, F., Madry, H., Mata, A., Mauck, R. L., Semino, C. E. & Stoddart, M. J. Tissue engineering for articular cartilage repair - the state of the art. *Eur. Cell. Mater.* **25,** 248–67 (2013).

57. Kim, S. *Techniques in Cartilage Repair Surgery.* (2014). doi:10.1007/978-3-642-41921-8

58. Vanlauwe, J., Saris, D. B. F., Victor, J., Almqvist, K. F., Bellemans, J., Luyten, F. P., Bohnsack, M., Claes, T., Fortems, Y., Handelberg, F., Haspl, M., Jelic, M., Lagae, K., Vandekerckhove, B., Vandenneucker, H., van der Bauwhede, J. &

Verdonk, R. Five-Year Outcome of Characterized Chondrocyte Implantation Versus Microfracture for Symptomatic Cartilage Defects of the Knee. *Am. J. Sports Med.* **39,** 2566–2574 (2011).

59. Kreuz, P. C., Steinwachs, M. R., Erggelet, C., Krause, S. J., Konrad, G., Uhl, M. & Südkamp, N. Results after microfracture of full-thickness chondral defects in different compartments in the knee. *Osteoarthritis Cartilage* **14,** 1119–25 (2006).

60. Mithoefer, K., Williams, R. J., Warren, R. F., Potter, H. G., Spock, C. R., Jones, E. C., Wickiewicz, T. L. & Marx, R. G. The microfracture technique for the treatment of articular cartilage lesions in the knee. A prospective cohort study. *J. Bone Joint Surg. Am.* **87,** 1911–20 (2005).

61. Clar, C., Cummins, E., McIntyre, L., Thomas, S., Lamb, J., Bain, L., Jobanputra, P. & Waugh, N. Clinical and cost-effectiveness of autologous chondrocyte implantation for cartilage defects in knee joints: systematic review and economic evaluation. *Health Technol. Assess.* **9,** iii–iv, ix–x, 1–82 (2005).

62. Basad, E., Wissing, F. R., Fehrenbach, P., Rickert, M., Steinmeyer, J. & Ishaque, B. Matrix-induced autologous chondrocyte implantation (MACI) in the knee: clinical outcomes and challenges. *Knee Surgery, Sport. Traumatol. Arthrosc.* **23,** 3729–3735 (2015).

63. Basad, E., Ishaque, B., Bachmann, G., Stürz, H. & Steinmeyer, J. Matrix-induced autologous chondrocyte implantation versus microfracture in the treatment of cartilage defects of the knee: A 2-year randomised study. *Knee Surgery, Sport. Traumatol. Arthrosc.* **18,** 519–527 (2010).

64. Bartlett, W., Skinner, J., Gooding, C., Carrington, R., Flanagan, A., Briggs, T. & Bentley, G. Autologous chondrocyte implantation versus matrix-induced autologous chondrocyte implantation for osteochondral defects of the knee: a prospective, randomised study. *J. bone Jt. Surg. Br. Vol.* **87,** 640–645 (2005).

65. Brittberg, M., Lindahl, A., Nilsson, A., Ohlsson, C., Isaksson, O. & Peterson, L. Treatment of deep cartilage defects in the knee with autologous chondrocyte transplantation. *N. Engl. J. Med.* **331,** 889–895 (1994).

66. Bannuru, R. R., Natov, N. S., Obadan, I. E., Price, L. L., Schmid, C. H. &

McAlindon, T. E. Therapeutic trajectory of hyaluronic acid versus corticosteroids in the treatment of knee osteoarthritis: A systematic review and meta-analysis. *Arthritis Rheum.* **61,** 1704–1711 (2009).

67. Panseri, S., Russo, A., Cunha, C., Bondi, A., Di Martino, A., Patella, S. & Kon, E. Osteochondral tissue engineering approaches for articular cartilage and subchondral bone regeneration. *Knee Surg. Sports Traumatol. Arthrosc.* **20,** 1182–91 (2012).

68. Huey, D. J., Hu, J. C. & Athanasiou, K. Unlike bone, cartilage regeneration remains elusive. *Science* **338,** 917–21 (2012).

69. Bornes, T. D., Adesida, A. B. & Jomha, N. M. Articular Cartilage Repair with Mesenchymal Stem Cells After Chondrogenic Priming: A Pilot Study. *Tissue Eng. Part A* ten.tea.2017.0235 (2017). doi:10.1089/ten.tea.2017.0235

70. Liu, K., Zhou, G. D., Liu, W., Zhang, W. J., Cui, L., Liu, X., Liu, T. Y. & Cao, Y. The dependence of in vivo stable ectopic chondrogenesis by human mesenchymal stem cells on chondrogenic differentiation in vitro. *Biomaterials* **29,** 2183–2192 (2008).

71. Benya, P. D. & Shaffer, J. D. Dedifferentiated chondrocytes reexpress the differentiated collagen phenotype when cultured in agarose gels. *Cell* **30,** 215–224 (1982).

72. Stack, J. D., Levingstone, T. J., Lalor, W., Sanders, R., Kearney, C., O'Brien, F. J. & David, F. Repair of large osteochondritis dissecans lesions using a novel multilayered tissue engineered construct in an equine athlete. *J. Tissue Eng. Regen. Med.* (2016). doi:10.1002/term.2173

73. Berruto, M., Delcogliano, M., de Caro, F., Carimati, G., Uboldi, F., Ferrua, P., Ziveri, G. & De Biase, C. F. Treatment of Large Knee Osteochondral Lesions With a Biomimetic Scaffold: Results of a Multicenter Study of 49 Patients at 2-Year Follow-up. *Am. J. Sports Med.* **42,** 1607–17 (2014).

74. Bellamy, N., Campbell, J., Welch, V., Gee, T. L., Bourne, R. & Wells, G. A. Viscosupplementation for the treatment of osteoarthritis of the knee. *Cochrane Database Syst. Rev.* (2006). doi:10.1002/14651858.CD005321.pub2

75. McAlindon, T. E. & Bannuru, R. R. Osteoarthritis: Is viscosupplementation really so unsafe for knee OA? *Nat. Rev. Rheumatol.* **8,** 635–636 (2012).

76. DuRaine, G. D., Brown, W. E., Hu, J. C. & Athanasiou, K. A. Emergence of Scaffold-free Approaches for Tissue Engineering Musculoskeletal Cartilages. *Ann Biomed Eng* **43,** 543–554 (2015).

77. Dikina, A. D., Alt, D. S., Herberg, S., McMillan, A., Strobel, H. A., Zheng, Z., Cao, M., Lai, B. P., Jeon, O., Petsinger, V. I., Cotton, C. U., Rolle, M. W. & Alsberg, E. A Modular Strategy to Engineer Complex Tissues and Organs. *Adv. Sci.* **5,** (2018).

78. Mesallati, T., Buckley, C. T. & Kelly, D. J. Engineering articular cartilage-like grafts by self-assembly of infrapatellar fat pad-derived stem cells. *Biotechnol. Bioeng.* **111,** 1686–1698 (2014).

79. Yu, Y., Moncal, K. K., Li, J., Peng, W., Rivero, I., Martin, J. A. & Ozbolat, I. T. Three-dimensional bioprinting using self-Assembling scalable scaffold-free 'tissue strands' as a new bioink. *Sci. Rep.* **6,** 1–11 (2016).

80. Itokazu, M., Wakitani, S., Mera, H., Tamamura, Y., Sato, Y., Takagi, M. & Nakamura, H. Transplantation of Scaffold-Free Cartilage-Like Cell-Sheets Made from Human Bone Marrow Mesenchymal Stem Cells for Cartilage Repair: A Preclinical Study. *Cartilage* **7,** 361–372 (2016).

81. Khademhosseini, A. & Langer, R. A decade of progress in tissue engineering. *Nat. Protoc.* **11,** 1775–1781 (2016).

82. Armstrong, J. P. K., Shakur, R., Horne, J. P., Dickinson, S. C., Armstrong, C. T., Lau, K., Kadiwala, J., Lowe, R., Seddon, A., Mann, S., Anderson, J. L. R., Perriman, A. W. & Hollander, A. P. Artificial membrane-binding proteins stimulate oxygenation of stem cells during engineering of large cartilage tissue. *Nat. Commun.* **6,** 7405 (2015).

83. Park, J. S., Chu, J. S., Tsou, A. D., Diop, R., Wang, A. & Li, S. The Effect of Matrix Stiffness on the Differentiation of Mesenchymal Stem Cells in Response to TGF-β. *Biomaterials* **32,** 3921–3930 (2012).

84. Yang, C., Tibbitt, M. W., Basta, L. & Anseth, K. S. Mechanical memory and

dosing influence stem cell fate. *Nat. Mater.* **13,** 645–652 (2014).

85. Veiseh, O., Doloff, J. C., Ma, M., Vegas, A. J., Tam, H. H., Bader, A. R., Li, J., Langan, E., Wyckoff, J., Loo, W. S., Jhunjhunwala, S., Chiu, A., Siebert, S., Tang, K., Hollister-Lock, J., Aresta-Dasilva, S., Bochenek, M., Mendoza-Elias, J., Wang, Y., Qi, M., Lavin, D. M., Chen, M., Dholakia, N., Thakrar, R., Lacík, I., Weir, G. C., Oberholzer, J., Greiner, D. L., Langer, R. & Anderson, D. G. Size- and shape-dependent foreign body immune response to materials implanted in rodents and non-human primates. *Nat. Mater.* **14,** 643–651 (2015).

86. Hollister, S. J. Porous scaffold design for tissue engineering. *Nat. Mater.* **4,** 518–524 (2005).

87. Eisenstein, M. IPSCs: One cell to rule them all? *Nat. Methods* **7,** 81–85 (2010).

88. Ledford, H. Riding the CRISPR wave. *Nature* **531,** 156–159 (2016).

89. Sander, J. D. & Joung, J. K. CRISPR-Cas systems for editing, regulating and targeting genomes. *Nat. Biotechnol.* **32,** 347–55 (2014).

90. Phull, A.-R., Eo, S.-H., Abbas, Q., Ahmed, M. & Kim, S. J. Applications of Chondrocyte-Based Cartilage Engineering: An Overview. *Biomed Res. Int.* **2016,** 1879837 (2016).

91. Steinert, A. F., Rackwitz, L., Gilbert, F., Nöth, U. & Tuan, R. S. Concise review: the clinical application of mesenchymal stem cells for musculoskeletal regeneration: current status and perspectives. *Stem Cells Transl. Med.* **1,** 237–47 (2012).

92. Caplan, A. Why are MSCs therapeutic? New data: new insight. *J. Pathol.* **217,** 318–324 (2009).

93. Gao, F., Chiu, S. M., Motan, D. A. L., Zhang, Z., Chen, L., Ji, H.-L., Tse, H.-F., Fu, Q.-L. & Lian, Q. Mesenchymal stem cells and immunomodulation: current status and future prospects. *Cell Death Dis.* **7,** e2062 (2016).

94. Billing, A. M., Ben Hamidane, H., Dib, S. S., Cotton, R. J., Bhagwat, A. M., Kumar, P., Hayat, S., Yousri, N. A., Goswami, N., Suhre, K., Rafii, A. & Graumann, J. Comprehensive transcriptomic and proteomic characterization of human mesenchymal stem cells reveals source specific cellular markers. *Sci. Rep.*

6, 21507 (2016).

95. Caplan, A. I. Mesenchymal stem cells : cell-based reconstructive therapy. *Tissue Eng.* **11,** 1198–1211 (2005).

96. Martin, I., Miot, S., Barbero, A., Jakob, M. & Wendt, D. Osteochondral tissue engineering. *J. Biomech.* **40,** 750–65 (2007).

97. Nooeaid, P., Salih, V., Beier, J. P. & Boccaccini, A. R. Osteochondral tissue engineering: scaffolds, stem cells and applications. *J. Cell. Mol. Med.* **16,** 2247–70 (2012).

98. Alvarez, K. & Nakajima, H. Metallic scaffolds for bone regeneration. *Materials (Basel).* **2,** 790–832 (2009).

99. Yusop, A. H., Bakir, A. A., Shaharom, N. A., Abdul Kadir, M. R. & Hermawan, H. Porous biodegradable metals for hard tissue scaffolds: A review. *Int. J. Biomater.* **2012,** (2012).

100. Hänzi, A. C., Sologubenko, A. S. & Uggowitzer, P. J. Design Strategy for Microalloyed Ultra-Ductile Magnesium Alloys for Medical Applications. *Mater. Sci. Forum* **618–619,** 75–82 (2009).

101. Li, Z., Gu, X., Lou, S. & Zheng, Y. The development of binary Mg-Ca alloys for use as biodegradable materials within bone. *Biomaterials* **29,** 1329–1344 (2008).

102. Zhang, E., Yin, D., Xu, L., Yang, L. & Yang, K. Microstructure, mechanical and corrosion properties and biocompatibility of Mg-Zn-Mn alloys for biomedical application. *Mater. Sci. Eng. C* **29,** 987–993 (2009).

103. Witte, F., Kaese, V., Haferkamp, H., Switzer, E., Meyer-Lindenberg, A., Wirth, C. J. & Windhagen, H. In vivo corrosion of four magnesium alloys and the associated bone response. *Biomaterials* **26,** 3557–3563 (2005).

104. Peuster, M., Hesse, C., Schloo, T., Fink, C., Beerbaum, P. & von Schnakenburg, C. Long-term biocompatibility of a corrodible peripheral iron stent in the porcine descending aorta. *Biomaterials* **27,** 4955–4962 (2006).

105. Peuster, M., Wohlsein, P., Brügmann, M., Ehlerding, M., Seidler, K., Fink, C., Brauer, H., Fischer, a & Hausdorf, G. A novel approach to temporary stenting:

242

degradable cardiovascular stents produced from corrodible metal-results 6-18 months after implantation into New Zealand white rabbits. *Heart* **86,** 563–569 (2001).

106. Schinhammer, M., Hänzi, A. C., Löffler, J. F. & Uggowitzer, P. J. Design strategy for biodegradable Fe-based alloys for medical applications. *Acta Biomater.* **6,** 1705–1713 (2010).

107. Oh, S., Oh, N., Appleford, M. & Ong, J. L. Bioceramics for Tissue Engineering Applications â€" A Review. *Am. J. Biochem. Biotechnol.* **2,** 49–56 (2006).

108. Hench, L. L. Bioceramics – from concept to clinic. *Am. Ceram. Soc. Bull.* **72,** 93–98 (1993).

109. Jones, J. R., Lin, S., Yue, S., Lee, P. D., Hanna, J. V, Smith, M. E. & Newport, R. J. Bioactive glass scaffolds for bone regeneration and their hierarchical characterisation. *Proc. Inst. Mech. Eng. H.* **224,** 1373–1387 (2010).

110. Mesquita, P., Branco, R., Afonso, a, Vasconcelos, M. & Cavalheiro, J. Mineralised membranes for bone regeneration. *Bioceram. 16* **254–2,** 1091–1094 (2004).

111. Liu, X., Rahaman, M. N. & Fu, Q. Bone regeneration in strong porous bioactive glass (13-93) scaffolds with an oriented microstructure implanted in rat calvarial defects. *Acta Biomater.* **9,** 4889–4898 (2013).

112. Bohner, M. in *Degrad. Rate Bioresorbable Mater. Predict. Eval.* 95–114 (Elsevier, 2008). doi:10.1533/9781845695033.2.95

113. Balasubramanian, P., Grünewald, A., Detsch, R., Hupa, L., Jokic, B., Tallia, F., Solanki, A. K., Jones, J. R. & Boccaccini, A. R. Ion Release, Hydroxyapatite Conversion, and Cytotoxicity of Boron-Containing Bioactive Glass Scaffolds. *Int. J. Appl. Glas. Sci.* **7,** 206–215 (2016).

114. Lin, F., Yan, C., Zheng, W. & Fan, W. Preparation of mesoporous bioglass coated zirconia scaffold for bone tissue engineering. *Adv. Mater. Res.* **365,** 209–215 (2012).

115. Von Euw, S., Wang, Y., Laurent, G., Drouet, C., Babonneau, F., Nassif, N. & Azaïs, T. Bone mineral: new insights into its chemical composition. *Sci. Rep.* **9,**

1–11 (2019).

116. Oshima, Y., Harwood, F. L., Coutts, R. D., Kubo, T. & Amiel, D. Variation of mesenchymal cells in polylactic acid scaffold in an osteochondral repair model. *Tissue Eng. - Part C Methods* **15,** 595–604 (2009).

117. Schaefer, D., Martin, I., Jundt, G., Seidel, J., Heberer, M., Grodzinsky, A., Bergin, I., Vunjak-Novakovic, G. & Freed, L. E. Tissue-engineered composites for the repair of large osteochondral defects. *Arthritis Rheum.* **46,** 2524–34 (2002).

118. Rodrigues, M. T., Lee, S. J., Gomes, M. E., Reis, R. L., Atala, A. & Yoo, J. J. Bilayered constructs aimed at osteochondral strategies: the influence of medium supplements in the osteogenic and chondrogenic differentiation of amniotic fluid-derived stem cells. *Acta Biomater.* **8,** 2795–806 (2012).

119. Lam, J., Lu, S., Meretoja, V. V, Tabata, Y., Mikos, A. G. & Kasper, F. K. Generation of osteochondral tissue constructs with chondrogenically and osteogenically predifferentiated mesenchymal stem cells encapsulated in bilayered hydrogels. *Acta Biomater.* **10,** 1112–23 (2014).

120. Masek, A. & Zaborski, M. ENR/PCL Polymer biocomposites from renewable resources. *Comptes Rendus Chim.* **17,** 944–951 (2014).

121. Drumright, R. E., Gruber, P. R. & Henton, D. E. Polylactic acid technology. *Adv. Mater.* **12,** 1841–1846 (2000).

122. Gilding, D. K. & Reed, A. M. Biodegradable polymers for use in surgery— polyglycolic/poly(actic acid) homo- and copolymers: 1. *Polymer (Guildf).* **20,** 1459–1464 (1979).

123. Woodruff, M. A. & Hutmacher, D. W. The return of a forgotten polymer— Polycaprolactone in the 21st century. *Prog. Polym. Sci.* **35,** 1217–1256 (2010).

124. Kinard, L. A., Kasper, F. K. & Mikos, A. G. Synthesis of oligo(poly(ethylene glycol) fumarate). *Nat. Protoc.* **7,** 1219–27 (2012).

125. Waldman, S. D., Couto, D. C., Omelon, S. J. & Kandel, R. A. Effect of sodium bicarbonate on extracellular pH, matrix accumulation, and morphology of cultured articular chondrocytes. *Tissue Eng.* **10,** 1633–40 (2004).

126. Wu, M.-H., Urban, J. P. G., Cui, Z. F., Cui, Z. & Xu, X. Effect of extracellular ph on matrix synthesis by chondrocytes in 3D agarose gel. *Biotechnol. Prog.* **23,** 430–4 (2007).

127. Sung, H.-J., Meredith, C., Johnson, C. & Galis, Z. S. The effect of scaffold degradation rate on three-dimensional cell growth and angiogenesis. *Biomaterials* **25,** 5735–42 (2004).

128. Camacho, P., Busari, H., Seims, K. B., Schwarzenberg, P., Dailey, H. L. & Chow, L. W. 3D printing with peptide–polymer conjugates for single-step fabrication of spatially functionalized scaffolds. *Biomater. Sci.* **7,** 4237–4247 (2019).

129. Daly, A. C., Cunniffe, G. M., Sathy, B. N., Jeon, O., Alsberg, E. & Kelly, D. J. 3D Bioprinting of Developmentally Inspired Templates for Whole Bone Organ Engineering. *Adv. Healthc. Mater.* **5,** 2353–2362 (2016).

130. Kang, H.-W., Lee, S. J., Ko, I. K., Kengla, C., Yoo, J. J. & Atala, A. A 3D bioprinting system to produce human-scale tissue constructs with structural integrity. *Nat. Biotechnol.* **34,** 312–319 (2016).

131. Li, J., Mareddy, S., Tan, D. M., Crawford, R., Long, X., Miao, X. & Xiao, Y. A minimal common osteochondrocytic differentiation medium for the osteogenic and chondrogenic differentiation of bone marrow stromal cells in the construction of osteochondral graft. *Tissue Eng. Part A* **15,** 2481–90 (2009).

132. Gao, J., Dennis, J. E., Solchaga, L. A., Goldberg, V. M. & Caplan, A. I. Repair of osteochondral defect with tissue engineered two - phase composite material of injectable calcium phosphate and hyaluronan sponge. *Tissue Eng.* **8,** 827–37 (2002).

133. Cao, Z., Hou, S., Sun, D., Wang, X. & Tang, J. Osteochondral regeneration by a bilayered construct in a cell-free or cell-based approach. *Biotechnol. Lett.* **34,** 1151–7 (2012).

134. Guo, X., Park, H., Liu, G., Liu, W., Cao, Y., Tabata, Y., Kasper, F. K. & Mikos, A. G. In vitro generation of an osteochondral construct using injectable hydrogel composites encapsulating rabbit marrow mesenchymal stem cells. *Biomaterials* **30,** 2741–52 (2009).

135. Frenkel, S. R., Bradica, G., Brekke, J. H., Goldman, S. M., Ieska, K., Issack, P., Bong, M. R., Tian, H., Gokhale, J., Coutts, R. D. & Kronengold, R. T. Regeneration of articular cartilage - Evaluation of osteochondral defect repair in the rabbit using multiphasic implants. *Osteoarthritis Cartilage* **13,** 798–807 (2005).

136. Mohan, N., Gupta, V., Sridharan, B., Sutherland, A. & Detamore, M. S. The potential of encapsulating 'raw materials' in 3D osteochondral gradient scaffolds. *Biotechnol. Bioeng.* **111,** 829–841 (2014).

137. Diduch, D. R., Jordan, L. C., Mierisch, C. M. & Balian, G. Marrow stromal cells embedded in alginate for repair of osteochondral defects. *Arthroscopy* **16,** 571–7 (2000).

138. Kolambkar, Y. M., Dupont, K. M., Boerckel, J. D., Huebsch, N., Mooney, D. J., Hutmacher, D. W. & Guldberg, R. E. An alginate-based hybrid system for growth factor delivery in the functional repair of large bone defects. *Biomaterials* **32,** 65–74 (2011).

139. Elbert, D. L. & Hubbell, J. A. Surface treatments of polymers for biocompatibility. *Annu. Rev. Mater. Res.* **26,** 365–394 (1996).

140. Wang, Z. Z., Wang, Z. Z., Lu, W. W., Zhen, W., Yang, D. & Peng, S. Novel biomaterial strategies for controlled growth factor delivery for biomedical applications. *NPG Asia Mater.* **9,** e435-17 (2017).

141. Place, E. S., Evans, N. D. & Stevens, M. M. Complexity in biomaterials for tissue engineering. *Nat. Mater.* **8,** 457–470 (2009).

142. Zisch, A. H., Schenk, U., Schense, J. C., Sakiyama-Elbert, S. E. & Hubbell, J. A. Covalently conjugated VEGF–fibrin matrices for endothelialization. *J. Control. Release* **72,** 101–113 (2001).

143. Backer, M. V., Patel, V., Jehning, B. T., Claffey, K. P. & Backer, J. M. Surface immobilization of active vascular endothelial growth factor via a cysteine-containing tag. *Biomaterials* **27,** 5452–5458 (2006).

144. Rothrauff, B. B., Yang, G. & Tuan, R. S. Tissue-specific bioactivity of soluble tendon-derived and cartilage-derived extracellular matrices on adult mesenchymal

stem cells. *Stem Cell Res. Ther.* **8,** 1–17 (2017).

145. Dziki, J. L., Wang, D. S., Pineda, C., Sicari, B. M., Rausch, T. & Badylak, S. F. Solubilized extracellular matrix bioscaffolds derived from diverse source tissues differentially influence macrophage phenotype. *J. Biomed. Mater. Res. - Part A* **105,** 138–147 (2017).

146. Rothrauff, B. B., Shimomura, K., Gottardi, R., Alexander, P. G. & Tuan, R. S. Anatomical region-dependent enhancement of 3-dimensional chondrogenic differentiation of human mesenchymal stem cells by soluble meniscus extracellular matrix. *Acta Biomater.* **49,** 140–151 (2016).

147. Sun, Y., Yan, L., Chen, S. & Pei, M. Functionality of decellularized matrix in cartilage regeneration: A comparison of tissue versus cell sources. *Acta Biomater.* **74,** 56–73 (2018).

148. Sheehy, E. J., Kelly, D. J. & O'Brien, F. J. Biomaterial-based endochondral bone regeneration: a shift from traditional tissue engineering paradigms to developmentally inspired strategies. *Mater. Today Bio* **3,** 100009 (2019).

149. Zhang, D., He, D., Wei, G., Zhang, Y., Zhang, Y., Yi, H., Wang, Z., Wu, R., Hu, Y., Deng, J., Criswell, T., Yoo, J., Zhou, Y., Atala, A. & Wei, S. Tissue-Specific Extracellular Matrix Enhances Skeletal Muscle Precursor Cell Expansion and Differentiation for Potential Application in Cell Therapy. *Tissue Eng. - Part A* **23,** 784–794 (2017).

150. Li, L., Liu, G., Timashev, P., Sun, X. S., Criswell, T., Atala, A. & Zhang, Y. Biofabrication of tissue-specific extracellular matrix proteins to enhance the expansion and differentiation of skeletal muscle progenitor cells. *Appl. Phys. Rev.* **6,** 021309 (2019).

151. Lam, D., Enright, H. A., Cadena, J., Peters, S. K. G., Sales, A. P., Osburn, J. J., Soscia, D. A., Kulp, K. S., Wheeler, E. K. & Fischer, N. O. Tissue-specific extracellular matrix accelerates the formation of neural networks and communities in a neuron-glia co-culture on a multi-electrode array. *Sci. Rep.* **9,** 1–15 (2019).

152. Tchetina, E., Mwale, F. & Poole, a R. Distinct phases of coordinated early and late gene expression in growth plate chondrocytes in relationship to cell

proliferation, matrix assembly, remodeling, and cell differentiation. *J. Bone Miner. Res.* **18,** 844–51 (2003).

153. Leijten, J. C. H., Emons, J., Sticht, C., Van Gool, S., Decker, E., Uitterlinden, A., Rappold, G., Hofman, A., Rivadeneira, F., Scherjon, S., Wit, J. M., Van Meurs, J., Van Blitterswijk, C. A. & Karperien, M. Gremlin 1, frizzled-related protein, and dkk-1 are key regulators of human articular cartilage homeostasis. *Arthritis Rheum.* **64,** 3302–3312 (2012).

154. Wu, M., Chen, G. & Li, Y.-P. TGF-β and BMP signaling in osteoblast, skeletal development, and bone formation, homeostasis and disease. *Bone Res.* **4,** 16009 (2016).

155. Alford, A. I., Kozloff, K. M. & Hankenson, K. D. Extracellular matrix networks in bone remodeling. *Int. J. Biochem. Cell Biol.* **65,** 20–31 (2015).

156. Tolar, J., Teitelbaum, S. L. & Orchard, P. J. Osteopetrosis. *N. Engl. J. Med.* **351,** 2839–2849 (2004).

157. Leali, P. T., Muresu, F., Melis, A., Ruggiu, A., Zachos, A. & Doria, C. Skeletal fragility definition. *Clin. Cases Miner. Bone Metab.* **8,** 11–13 (2011).

158. Badylak, S. F., Lantz, G. C., Coffey, A. & Geddes, L. a. Small intestinal submucosa as a large diameter vascular graft in the dog. *J. Surg. Res.* **47,** 74–80 (1989).

159. Aiken, S. W., Badylak, S. F., Toombs, J. P., Shelbourne, K. D., Hiles, M. C., Lantz, G. C. & Van Sickle, D. Small Intestinal Submucosa as an Intra-Articular Ligamentous Graft Material: A Pilot Study in Dogs. *Vet. Comp. Orthop. Traumatol.* **07,** 124–128 (1994).

160. Badylak, S. F. in *Tissue Eng.* 179–189 (Birkhäuser Boston, 1993).

161. Hangody, L., Kish, G., Kárpáti, Z. & Eberhart, R. Osteochondral plugs: Autogenous osteochondral mosaicplasty for the treatment of focal chondral and osteochondral articular defects. *Oper. Tech. Orthop.* **7,** 312–322 (1997).

162. Almeida, H. V., Eswaramoorthy, R., Cunniffe, G. M., Buckley, C. T., O'Brien, F. J. & Kelly, D. J. Fibrin Hydrogels Functionalized with Particulated Cartilage Extracellular Matrix and Incorporating Freshly Isolated Stromal Cells as an

Injectable for Cartilage Regeneration. *Acta Biomater.* **36,** 55–62 (2016).

163. Chen, C.-C., Liao, C.-H., Wang, Y.-H., Hsu, Y.-M., Huang, S.-H., Chang, C.-H. & Fang, H.-W. Cartilage fragments from osteoarthritic knee promote chondrogenesis of mesenchymal stem cells without exogenous growth factor induction. *J. Orthop. Res.* **30,** 393–400 (2012).

164. Ghanavi, P., Kabiri, M. & Doran, M. R. The rationale for using microscopic units of a donor matrix in cartilage defect repair. *Cell Tissue Res.* **347,** 643–648 (2012).

165. Tavassoli, A., Mahdavi-shahri, N. & Matin, M. M. Bovine articular cartilage decellularized matrix as a scaffold for use in cartilage tissue engineering. *Iran. J. Vet. Sci. Technol.* **4,** 1–8 (2012).

166. Aghdasi, B., Montgomery, S. R., Daubs, M. D. & Wang, J. C. A review of demineralized bone matrices for spinal fusion: The evidence for efficacy. *Surgeon* **11,** 39–48 (2013).

167. Gerhardt, L. C., Widdows, K. L., Erol, M. M., Nandakumar, A., Roqan, I. S., Ansari, T. & Boccaccini, A. R. Neocellularization and neovascularization of nanosized bioactive glass-coated decellularized trabecular bone scaffolds. *J. Biomed. Mater. Res. - Part A* **101 A,** 827–841 (2013).

168. Dehghani, S. N., Bigham, A. S., Torabi Nezhad, S. & Shafiei, Z. Effect of bovine fetal growth plate as a new xenograft in experimental bone defect healing: radiological, histopathological and biomechanical evaluation. *Cell Tissue Bank* **9,** 91–99 (2008).

169. Pei, M., Li, J. T., Shoukry, M. & Zhang, Y. A review of decellularized stem cell matrix: a novel cell expansion system for cartilage tissue engineering. *Eur Cell Mater* **22,** 333–43; discussion 343 (2011).

170. Dikina, A. D., Almeida, H. V., Cao, M., Kelly, D. J. & Alsberg, E. Scaffolds Derived from ECM Produced by Chondrogenically Induced Human MSC Condensates Support Human MSC Chondrogenesis. *ACS Biomater. Sci. Eng.* **3,** 1426–1436 (2017).

171. Lu, H., Hoshiba, T., Kawazoe, N., Koda, I., Song, M. & Chen, G. Cultured cell-derived extracellular matrix scaffolds for tissue engineering. *Biomaterials* **32,**

9658–9666 (2011).

172. Cunniffe, G. M., Vinardell, T., Murphy, J. M., Thompson, E. M., Matsiko, A., Brien, F. J. O., Kelly, D. J., O'Brien, F. J. & Kelly, D. J. Porous decellularized tissue engineered hypertrophic cartilage as a scaffold for large bone defect healing. *Acta Biomater.* **23,** 82–90 (2015).

173. Hutmacher, D. W., Woodfield, T. B. F. & Dalton, P. D. in *Tissue Eng. Second Ed.* 311- (Elsevier Inc., 2014). doi:10.1016/B978-0-12-420145-3.00009-2

174. Liao, C. J., Chen, C. F., Chen, J. H., Chiang, S. F., Lin, Y. J. & Chang, K. Y. Fabrication of porous biodegradable polymer scaffolds using a solvent merging/particulate leaching method. *J. Biomed. Mater. Res.* **59,** 676–681 (2002).

175. Zein, I., Hutmacher, D. W., Tan, K. C. & Teoh, S. H. Fused deposition modeling of novel scaffold architectures for tissue engineering applications. *Biomaterials* **23,** 1169–1185 (2002).

176. Liu, X. & Ma, P. X. Phase separation, pore structure, and properties of nanofibrous gelatin scaffolds. *Biomaterials* **30,** 4094–4103 (2009).

177. Holzwarth, J. M. & Ma, P. X. 3D nanofibrous scaffolds for tissue engineering. *J. Mater. Chem.* **21,** 10243–10251 (2011).

178. Ma, B., Xie, J., Jiang, J., Shuler, F. D. & Bartlett, D. E. Rational design of nanofiber scaffolds for orthopedic tissue repair and regeneration. *Nanomedicine (Lond).* **8,** 1459–81 (2013).

179. Toyokawa, N., Fujioka, H., Kokubu, T., Nagura, I., Inui, A., Sakata, R., Satake, M., Kaneko, H. & Kurosaka, M. Electrospun synthetic polymer scaffold for cartilage repair without cultured cells in an animal model. *Arthroscopy* **26,** 375–83 (2010).

180. Oliveira, J. T., Crawford, A., Mundy, J. M., Moreira, A. R., Gomes, M. E., Hatton, P. V. & Reis, R. L. A cartilage tissue engineering approach combining starch-polycaprolactone fibre mesh scaffolds with bovine articular chondrocytes. *J. Mater. Sci. Mater. Med.* **18,** 295–302 (2007).

181. Mikos, A. G., Bao, Y., Cima, L. G., Ingber, D. E., Vacanti, J. P. & Langer, R. *Preparation of poly(glycolic acid) bonded fiber structures for cell attachment and*

transplantation. J. Biomed. Mater. Res. **27,** 183–189 (John Wiley & Sons, Inc., 1993).

182. Lowe, C. J., Reucroft, I. M., Grota, M. C. & Shreiber, D. I. Production of Highly Aligned Collagen Scaffolds by Freeze-drying of Self-assembled, Fibrillar Collagen Gels. *ACS Biomater. Sci. Eng.* **2,** 643–651 (2016).

183. Yao, X., Yao, H. & Li, Y. Hierarchically aligned porous scaffold by ice-segregation-induced self-assembly and thermally triggered electrostatic self-assembly of oppositely charged thermosensitive microgels. *J. Mater. Chem.* **19,** 6516 (2009).

184. Nowicki, M. A., Castro, N. J., Plesniak, M. W. & Zhang, L. G. 3D printing of novel osteochondral scaffolds with graded microstructure. *Nanotechnology* **27,** 1–10 (2016).

185. Daly, A. C., Critchley, S. E., Rencsok, E. M. & Kelly, D. J. A comparison of different bioinks for 3D bioprinting of fibrocartilage and hyaline cartilage. *Biofabrication* **8,** 045002 (2016).

186. Lee, A., Hudson, A. R., Shiwarski, D. J., Tashman, J. W., Hinton, T. J., Yerneni, S., Bliley, J. M., Campbell, P. G. & Feinberg, A. W. 3D bioprinting of collagen to rebuild components of the human heart. *Science (80-.).* **365,** 482–487 (2019).

187. Daly, A. C. & Kelly, D. J. Biofabrication of spatially organised tissues by directing the growth of cellular spheroids within 3D printed polymeric microchambers. *Biomaterials* **197,** 194–206 (2019).

188. Murphy, S. V & Atala, A. 3D bioprinting of tissues and organs. *Nat. Biotechnol.* **32,** 773–785 (2014).

189. Shim, J., Lee, J., Kim, J. & Cho, D. Bioprinting of a mechanically enhanced three-dimensional dual cell-laden construct for osteochondral tissue engineering using a multi-head tissue/organ building. *J. Micromechanics Microengineering* **22,** 085014 (2012).

190. Caliari, S. R. & Harley, B. A. C. The effect of anisotropic collagen-GAG scaffolds and growth factor supplementation on tendon cell recruitment, alignment, and metabolic activity. *Biomaterials* **32,** 5330–5340 (2011).

191. Kroehne, V., Heschel, I., Schügner, F., Lasrich, D., Bartsch, J. W. & Jockusch, H. Use of a novel collagen matrix with oriented pore structure for muscle cell differentiation in cell culture and in grafts. *J. Cell. Mol. Med.* **12,** 1640–1648 (2008).

192. Harley, B. A., Hastings, A. Z., Yannas, I. V. & Sannino, A. Fabricating tubular scaffolds with a radial pore size gradient by a spinning technique. *Biomaterials* **27,** 866–874 (2006).

193. Jia, S., Liu, L., Pan, W., Meng, G., Duan, C., Zhang, L., Xiong, Z. & Liu, J. Oriented cartilage extracellular matrix-derived scaffold for cartilage tissue engineering. *J. Biosci. Bioeng.* **113,** 647–653 (2012).

194. Lynch, H. A. Effect of Fiber Orientation and Strain Rate on the Nonlinear Uniaxial Tensile Material Properties of Tendon. *J. Biomech. Eng.* **125,** 726 (2003).

195. Mulder, E. L. W. De, Hannink, G., Kuppevelt, T. H. Van, Daamen, W. F. & Buma, P. Similar Hyaline-Like Cartilage Repair of Osteochondral and Anisotropic Collagen Scaffolds. *Tissue Eng. Part A* **20,** 635–645 (2014).

196. Jia, S., Zhang, T., Xiong, Z., Pan, W., Liu, J. & Sun, W. In vivo evaluation of a novel oriented scaffold-BMSC construct for enhancing full-thickness articular cartilage repair in a rabbit model. *PLoS One* **10,** 1–16 (2015).

197. Sun, M., Chi, G., Li, P., Lv, S., Xu, J., Xu, Z., Xia, Y., Tan, Y., Xu, J., Li, L. & Li, Y. Effects of matrix stiffness on the morphology, adhesion, proliferation and osteogenic differentiation of mesenchymal stem cells. *Int. J. Med. Sci.* **15,** 257–268 (2018).

198. Mullen, C. A., Vaughan, T. J., Billiar, K. L. & McNamara, L. M. The effect of substrate stiffness, thickness, and cross-linking density on osteogenic cell behavior. *Biophys. J.* **108,** 1604–1612 (2015).

199. Ehrbar, M., Sala, A., Lienemann, P., Ranga, A., Mosiewicz, K., Bittermann, A., Rizzi, S. C., Weber, F. E. & Lutolf, M. P. Elucidating the role of matrix stiffness in 3D cell migration and remodeling. *Biophys. J.* **100,** 284–293 (2011).

200. Charrier, E. E., Pogoda, K., Wells, R. G. & Janmey, P. A. Control of cell morphology and differentiation by substrates with independently tunable elasticity

and viscous dissipation. *Nat. Commun.* **9,** 1–13 (2018).

201. Olivares-navarrete, R., Lee, E. M., Smith, K., Hyzy, S. L., Doroudi, M., Williams, J. K., Gall, K., Boyan, B. D. & Schwartz, Z. Substrate Stiffness Controls Osteoblastic and Chondrocytic Differentiation of Mesenchymal Stem Cells without Exogenous Stimuli. **1,** 1–18 (2017).

202. Bischofs, I. B. & Schwarz, U. S. Cell organization in soft media due to active mechanosensing. *Proc. Natl. Acad. Sci. U. S. A.* **100,** 9274–9279 (2003).

203. Bell, E., Merrill, C. & Solomon, D. Production of a tissue-like structure by contraction of collagen lattices by human fibroblasts of different proliferative potential in vitro. *J. Cell Biol* **76,** 1274–1278 (1979).

204. Ploetz, C., Zycband, E. I. & Birk, D. E. Collagen fibril assembly and deposition in the developing dermis: Segmental deposition in extracellular compartments. *J. Struct. Biol.* **106,** 73–81 (1991).

205. Yannas, I. V. Similarities and differences between induced organ regeneration in adults and early foetal regeneration. *J. R. Soc. Interface* **2,** 403–417 (2005).

206. Luo, L., Chu, J. Y. J., Eswaramoorthy, R., Mulhall, K. J. & Kelly, D. J. Engineering Tissues That Mimic the Zonal Nature of Articular Cartilage Using Decellularized Cartilage Explants Seeded with Adult Stem Cells. *ACS Biomater. Sci. Eng.* **3,** 1933–1943 (2017).

207. Petersen, A., Princ, A., Korus, G., Ellinghaus, A., Leemhuis, H., Herrera, A., Klaumünzer, A., Schreivogel, S., Woloszyk, A., Schmidt-Bleek, K., Geissler, S., Heschel, I. & Duda, G. N. A biomaterial with a channel-like pore architecture induces endochondral healing of bone defects. *Nat. Commun.* **9,** (2018).

208. Olvera, D., Sathy, B. N., Carroll, S. F. & Kelly, D. J. Modulating microfibrillar alignment and growth factor stimulation to regulate mesenchymal stem cell differentiation. *Acta Biomater.* **64,** 148–160 (2017).

209. Pauly, H. M., Sathy, B. N., Olvera, D., McCarthy, H. O., Kelly, D. J., Popat, K. C., Dunne, N. J. & Haut Donahue, T. L. Hierarchically structured electrospun scaffolds with chemically conjugated growth factor for ligament tissue engineering. *Tissue Eng. Part A* **23,** 823–836 (2017).

210. Rowland, C. R., Colucci, L. A. & Guilak, F. Fabrication of anatomically-shaped cartilage constructs using decellularized cartilage-derived matrix scaffolds. *Biomaterials* **91,** 57–72 (2016).

211. Zhang, T., Zhang, H., Zhang, L., Jia, S., Liu, J., Xiong, Z. & Sun, W. Biomimetic design and fabrication of multilayered osteochondral scaffolds by low-temperature deposition manufacturing and thermal-induced phase-separation techniques. *Biofabrication* **9,** (2017).

212. Domingues, R. M. A., Chiera, S., Gershovich, P., Motta, A., Reis, R. L. & Gomes, M. E. Enhancing the Biomechanical Performance of Anisotropic Nanofibrous Scaffolds in Tendon Tissue Engineering: Reinforcement with Cellulose Nanocrystals. *Adv. Healthc. Mater.* **5,** 1364–1375 (2016).

213. O'Brien, F. J., Harley, B. A., Yannas, I. V. & Gibson, L. J. The effect of pore size on cell adhesion in collagen-GAG scaffolds. *Biomaterials* **26,** 433–441 (2005).

214. Karageorgiou, V. & Kaplan, D. Porosity of 3D biomaterial scaffolds and osteogenesis. *Biomaterials* **26,** 5474–91 (2005).

215. Murphy, C. M., Haugh, M. G. & O'Brien, F. J. The effect of mean pore size on cell attachment , proliferation and migration in collagen glycosaminoglycan scaffolds for tissue engineering. **31,** (2010).

216. Matsiko, A., Levingstone, T. J., O'Brien, F. J. & Gleeson, J. P. Addition of hyaluronic acid improves cellular infiltration and promotes early-stage chondrogenesis in a collagen-based scaffold for cartilage tissue engineering. *J. Mech. Behav. Biomed. Mater.* **11,** 41–52 (2012).

217. Tsuruga, E., Takita, H., Itoh, H., Wakisaka, Y. & Kuboki, Y. Pore size of porous hydroxyapatite as the cell-substratum controls BMP-induced osteogenesis. *J. Biochem.* **121,** 317–24 (1997).

218. Murphy, C. M. & O'Brien, F. J. Understanding the effect of mean pore size on cell activity in collagen-glycosaminoglycan scaffolds. *Cell Adh. Migr.* **4,** 377–381 (2010).

219. Occhetta, P., Stüdle, C., Barbero, A. & Martin, I. Learn, simplify and implement: developmental re-engineering strategies for cartilage repair. *Swiss Med. Wkly.* **146,**

w14346 (2016).

220. Applications of chondrocyte-based cartilage engineering: An overview Abdul-Rehman Phull.

221. Williams, R., Khan, I. M., Richardson, K., Nelson, L., McCarthy, H. E., Analbelsi, T., Singhrao, S. K., Dowthwaite, G. P., Jones, R. E., Baird, D. M., Lewis, H., Roberts, S., Shaw, H. M., Dudhia, J., Fairclough, J., Briggs, T. & Archer, C. W. Identification and clonal characterisation of a progenitor cell sub-population in normal human articular cartilage. *PLoS One* **5,** (2010).

222. Dowthwaite, G. P., Bishop, J. C., Redman, S. N., Khan, I. M., Rooney, P., Evans, D. J. R., Haughton, L., Bayram, Z., Boyer, S., Thomson, B., Wolfe, M. S. & Archer, C. W. The surface of articular cartilage contains a progenitor cell populations. *J. Cell Sci.* **117,** 889–897 (2004).

223. Anderson, D. E., Markway, B. D., Weekes, K. J., McCarthy, H. E. & Johnstone, B. Physioxia Promotes the Articular Chondrocyte-Like Phenotype in Human Chondroprogenitor-Derived Self-Organized Tissue. *Tissue Eng. - Part A* **24,** 264–274 (2018).

224. Seol, D., McCabe, D. J., Choe, H., Zheng, H., Yu, Y., Jang, K., Walter, M. W., Lehman, A. D., Ding, L., Buckwalter, J. A. & Martin, J. A. Chondrogenic progenitor cells respond to cartilage injury. *Arthritis Rheum.* **64,** 3626–37 (2012).

225. Nakayama, N., Lee, J. Y., Matthias, N., Umeda, K., Yan, Q. & Huard, J. Cartilage Regeneration Using Pluripotent Stem Cell-Derived Chondroprogenitors: Promise and Challenges. *Pluripotent Stem Cells - From Bench to Clin.* (2016). doi:10.5772/63052

226. Bardsley, K., Kwarciak, A., Freeman, C., Brook, I., Hatton, P. & Crawford, A. Repair of bone defects in??vivo using tissue engineered hypertrophic cartilage grafts produced from nasal chondrocytes. *Biomaterials* **112,** 313–323 (2017).

227. Mumme, M., Barbero, A., Miot, S., Wixmerten, A., Feliciano, S., Wolf, F., Asnaghi, A. M., Baumhoer, D., Bieri, O., Kretzschmar, M., Pagenstert, G., Haug, M., Schaefer, D. J., Martin, I. & Jakob, M. Nasal chondrocyte-based engineered autologous cartilage tissue for repair of articular cartilage defects: an observational

first-in-human trial. *Lancet* **388,** 1985–1994 (2016).

228.   Lai, J. H., Kajiyama, G., Smith, R. L., Maloney, W. & Yang, F. Stem cells catalyze cartilage formation by neonatal articular chondrocytes in 3D biomimetic hydrogels. *Sci. Rep.* **3,** 1–9 (2013).

229.   Somoza, R. A., Correa, D., Labat, I., Sternberg, H., Forrest, M. E., Khalil, A. M., West, M. D., Tesar, P. & Caplan, A. I. Transcriptome-Wide Analyses of Human Neonatal Articular Cartilage and Human Mesenchymal Stem Cell-Derived Cartilage Provide a New Molecular Target for Evaluating Engineered Cartilage. *Tissue Eng. - Part A* **24,** 335–350 (2018).

230.   Lo, B. & Parham, L. Ethical issues in stem cell research. *Endocr. Rev.* **30,** 204–13 (2009).

231.   Yamanaka, S. A fresh look at iPS cells. *Cell* **137,** 13–7 (2009).

232.   Caplan, A. I. Mesenchymal stem cells. *J. Orthop. Res.* **9,** 641–50 (1991).

233.   Pittenger, M. F., Mackay, A. M., Beck, S. C., Jaiswal, R. K., Douglas, R., Mosca, J. D., Moorman, M. A., Simonetti, D. W., Craig, S. & Marshak, D. R. Multilineage Potential of Adult Human Mesenchymal Stem Cells. *Science (80-.).* **284,** 143–147 (1999).

234.   Barry, F. P. & Murphy, J. M. Mesenchymal stem cells: clinical applications and biological characterization. *Int. J. Biochem. Cell Biol.* **36,** 568–84 (2004).

235.   Sadler, T. W. Chapter 12: Limb growth and development. *Langman's Med. Embryol.* **12,** (2011).

236.   Kronenberg, H. M. & Kronenberg, H. M. Developmental regulation of the growth plate. *Nature* **423,** 332–6 (2003).

237.   Nerem, R. M. Regenerative medicine: The emergence of an industry. *J. R. Soc. Interface* **7,** S771–S775 (2010).

238.   Narbona-Carceles, J., Vaquero, J., B.S, S. S.-S., Forriol, F. & Fernández-Santos, M. E. Bone marrow mesenchymal stem cell aspirates from alternative sources Is the knee as good as the iliac crest? *Injury* **45,** S42–S47 (2014).

239.   Kim, M., Pinto, S. M., Getnet, D., Nirujogi, R. S., Manda, S. S., Chaerkady, R.,

Madugundu, A. K., Kelkar, D. S., Isserlin, R., Jain, S., Thomas, J. K., Muthusamy, B., Leal-rojas, P., Kumar, P., Sahasrabuddhe, N. A., Balakrishnan, L., Advani, J., George, B., Renuse, S., Selvan, L. D. N., Patil, A. H., Nanjappa, V., Radhakrishnan, A., Prasad, S., Jayaram, S., Rajagopalan, P., Sharma, J., Murthy, K. R., Syed, N., Goel, R., Khan, A. A., Freed, D., Zahari, M. S., Mukherjee, K. K., Shankar, S., Mahadevan, A. & Lam, H. A draft map of the human proteome. *Nature* **509,** 575–581 (2014).

240. Aebersold, R. & Mann, M. Mass-spectrometric exploration of proteome structure and function. *Nature* **537,** 347–355 (2016).

241. Hynes, R. O. & Naba, A. Overview of the matrisome-An inventory of extracellular matrix constituents and functions. *Cold Spring Harb. Perspect. Biol.* **4,** (2012).

242. Naba, A., Clauser, K. R., Hoersch, S., Liu, H., Carr, S. A. & Hynes, R. O. The Matrisome : In Silico Definition and In Vivo Characterization by Proteomics of Normal and Tumor Extracellular Matrices * □. 1–18 (2012). doi:10.1074/mcp.M111.014647

243. Szklarczyk, D., Franceschini, A., Wyder, S., Forslund, K., Heller, D., Huerta-Cepas, J., Simonovic, M., Roth, A., Santos, A., Tsafou, K. P., Kuhn, M., Bork, P., Jensen, L. J. & Von Mering, C. STRING v10: Protein-protein interaction networks, integrated over the tree of life. *Nucleic Acids Res.* **43,** D447–D452 (2015).

244. Szklarczyk, D., Morris, J. H., Cook, H., Kuhn, M., Wyder, S., Simonovic, M., Santos, A., Doncheva, N. T., Roth, A., Bork, P., Jensen, L. J. & Von Mering, C. The STRING database in 2017: Quality-controlled protein-protein association networks, made broadly accessible. *Nucleic Acids Res.* **45,** D362–D368 (2017).

245. Wellbrock, J., Sheikhzadeh, S., Oliveira-Ferrer, L., Stamm, H., Hillebrand, M., Keyser, B., Klokow, M., Vohwinkel, G., Bonk, V., Otto, B., Streichert, T., Balabanov, S., Hagel, C., Rybczynski, M., Bentzien, F., Bokemeyer, C., Von Kodolitsch, Y. & Fiedler, W. Overexpression of gremlin-1 in patients with Loeys-Dietz syndrome: Implications on pathophysiology and early disease detection. *PLoS One* **9,** (2014).

246. Khokha, M. K., Hsu, D., Brunet, L. J., Dionne, M. S. & Harland, R. M. Gremlin

is the BMP antagonist required for maintenance of Shh and Fgf signals during limb patterning. *Nat. Genet.* **34,** 303–307 (2003).

247. Duboule, D., Dono, R. & Zeller, R. Mouse limb deformity mutations disrupt a global control region within the large regulatory landscape required for Gremlin expression. *Genes Dev.* **18,** 1553–1564 (2004).

248. Chiodelli, P., Mitola, S., Ravelli, C., Oreste, P., Rusnati, M. & Presta, M. Heparan sulfate proteoglycans mediate the angiogenic activity of the vascular endothelial growth factor receptor-2 agonist gremlin. *Arterioscler. Thromb. Vasc. Biol.* **31,** 116–127 (2011).

249. Cox, J., Neuhauser, N., Michalski, A., Scheltema, R. A., Olsen, J. V. & Mann, M. Andromeda: A peptide search engine integrated into the MaxQuant environment. *J. Proteome Res.* **10,** 1794–1805 (2011).

250. Sampath, K. T. *Bone Morphogenetic Proteins: Systems Biology Regulators.* (2017). doi:10.1007/978-3-319-47507-3

251. Occhetta, P., Pigeot, S., Rasponi, M., Dasen, B., Mehrkens, A., Ullrich, T., Kramer, I., Guth-Gundel, S., Barbero, A. & Martin, I. Developmentally inspired programming of adult human mesenchymal stromal cells toward stable chondrogenesis. *Proc. Natl. Acad. Sci.* **115,** 4625–4630 (2018).

252. Muzio, G., Martinasso, G., Baino, F., Frairia, R., Vitale-Brovarone, C. & Canuto, R. A. Key role of the expression of bone morphogenetic proteins in increasing the osteogenic activity of osteoblast-like cells exposed to shock waves and seeded on bioactive glass-ceramic scaffolds for bone tissue engineering. *J. Biomater. Appl.* **29,** 728–736 (2014).

253. Brazil, D. P., Church, R. H., Surae, S., Godson, C. & Martin, F. BMP signalling: Agony and antagony in the family. *Trends Cell Biol.* **25,** 249–264 (2015).

254. Ki onaite, M., Wang, X. & Hyvonen, M. Structure of Gremlin-1 and analysis of its interaction with BMP-2. *Biochem. J.* **473,** 1593–1604 (2016).

255. Leijten, J. C. H., Landman, E. B. M., Georgi, N., Post, J. N., Karperien, M., Bos, S. D., Meulenbelt, I., Jahr, H. & van Blitterswijk, C. A. GREM1, FRZB and DKK1 mRNA levels correlate with osteoarthritis and are regulated by osteoarthritis-

associated factors. *Arthritis Res. Ther.* **15,** 1–11 (2013).

256. Di Luca, A., Van Blitterswijk, C. & Moroni, L. The osteochondral interface as a gradient tissue: From development to the fabrication of gradient scaffolds for regenerative medicine. *Birth Defects Res. Part C Embryo Today Rev.* **105,** 34–52 (2015).

257. Rawadi, G., Vayssiere, B., Dunn, F., Baron, R. & Roman-Roman, S. BMP-2 Controls Alkaline Phosphatase Expression and Osteoblast Mineralization by a Wnt Autocrine Loop. *J. Bone Miner. Res.* **18,** 1842–1853 (2003).

258. Leijten, J., Georgi, N., Moreira Teixeira, L., van Blitterswijk, C. A., Post, J. N. & Karperien, M. Metabolic programming of mesenchymal stromal cells by oxygen tension directs chondrogenic cell fate. *Proc. Natl. Acad. Sci.* **111,** 13954–13959 (2014).

259. Kerkhofs, J., Leijten, J., Bolander, J., Luyten, F. P., Post, J. N. & Geris, L. A qualitative model of the differentiation network in chondrocyte maturation: A holistic view of chondrocyte hypertrophy. *PLoS One* **11,** 1–27 (2016).

260. SKONIER, J., NEUBAUER, M., MADISEN, L., BENNETT, K., PLOWMAN, G. D. & PURCHIO, A. F. cDNA Cloning and Sequence Analysis of βig-h3, a Novel Gene Induced in a Human Adenocarcinoma Cell Line after Treatment with Transforming Growth Factor-β. *DNA Cell Biol.* **11,** 511–522 (1992).

261. Ferguson, J. W., Mikesh, M. F., Wheeler, E. F. & LeBaron, R. G. Developmental expression patterns of Beta-ig (βIG-H3) and its function as a cell adhesion protein. *Mech. Dev.* **120,** 851–864 (2003).

262. Hashimoto, K., Noshiro, M., Ohno, S., Kawamoto, T., Satakeda, H., Akagawa, Y., Nakashima, K., Okimura, A., Ishida, H., Okamoto, T., Pan, H., Shen, M., Yan, W. & Kato, Y. Characterization of a cartilage-derived 66-kDa protein (RCD-CAP/βig-h3) that binds to collagen. *Biochim. Biophys. Acta - Mol. Cell Res.* **1355,** 303–314 (1997).

263. Thapa, N., Lee, B. H. & Kim, I. S. TGFBIp/βig-h3 protein: A versatile matrix molecule induced by TGF-β. *Int. J. Biochem. Cell Biol.* **39,** 2183–2194 (2007).

264. LeBaron, R. G., Bezverkov, K. I., Zimber, M. P., Pavelec, R., Skonier, J. &

Purchio, A. F. βIG-H3, a novel secretory protein inducible by transforming growth factor-β, is present in normal skin and promotes the adhesion and spreading of dermal fibroblasts in vitro. *J. Invest. Dermatol.* **104,** 844–849 (1995).

265. Ohno, S., Noshiro, M., Makihira, S., Kawamoto, T., Shen, M., Yan, W., Kawashima-Ohya, Y., Fujimoto, K., Tanne, K. & Kato, Y. RGD-CAP (βig-h3) enhances the spreading of chondrocytes and fibroblasts via integrin α1β1. *Biochim. Biophys. Acta - Mol. Cell Res.* **1451,** 196–205 (1999).

266. Skonier, J., Bennett, K., Rothwell, V., Kosowski, S., Plowman, G., Wallace, P., Edelhoff, S., Disteche, C., Neubauer, M., Marquardt, H., Rodgers, J. & Purchio, A. F. βig-h3: A Transforming Growth Factor-β-Responsive Gene Encoding a Secreted Protein That Inhibits Cell Attachment In Vitro and Suppresses the Growth of CHO Cells in Nude Mice. *DNA Cell Biol.* **13,** 571–584 (1994).

267. Stewart, H. S., Ridgway, A. E., Dixon, M. J., Bonshek, R., Parveen, R. & Black, G. Heterogeneity in granular corneal dystrophy: Identification of three causative mutations in the TGFBI (BIGH3) genes - Lessons for corneal amyloidogenesis. *Hum. Mutat.* **14,** 126–132 (1999).

268. Munier, F. L., Korvatska, E., Djemaï, A., Paslier, D. Le, Zografos, L., Pescia, G. & Schorderet, D. F. Kerato-epithelin mutations in four 5q31-linked corneal dystrophies. *Nat. Genet.* **15,** 247–251 (1997).

269. Ohno, S., Doi, T., Fujimoto, K., Ijuin, C., Tanaka, N., Tanimoto, K., Honda, K., Nakahara, M., Kato, Y. & Tanne, K. RGD-CAP (βig-h3) exerts a negative regulatory function on mineralization in the human periodontal ligament. *J. Dent. Res.* **81,** 822–825 (2002).

270. Ohno, S., Doi, T., Tsutsumi, S., Okada, Y., Yoneno, K., Kato, Y. & Tanne, K. RGD-CAP (βig-h3) is expressed in precartilage condensation and in prehypertrophic chondrocytes during cartilage development. *Biochim. Biophys. Acta - Gen. Subj.* **1572,** 114–122 (2002).

271. Page, L., Polok, B., Bustamante, M. & Schorderet, D. F. Bigh3 Is Upregulated in Regenerating Zebrafish Fin. *Zebrafish* **10,** 36–42 (2013).

272. Keller, C. C., Ouma, C., Ouma, Y., Awandare, G. A., Davenport, G. C., Were, T.,

Hittner, J. B., Vulule, J. M., Ong'echa, J. M. & Perkins, D. J. Suppression of a novel hematopoietic mediator in children with severe malarial anemia. *Infect. Immun.* **77,** 3864–3871 (2009).

273. Hiraoka, A., Yano, K., Kagami, N., Takeshige, K., Mio, H., Anazawa, H. & Sugimoto, S. Stem cell growth factor: in situ hybridization analysis on the gene expression, molecular characterization and in vitro proliferative activity of a recombinant preparation on primitive hematopoietic progenitor cells. *Hematol. J.* **2,** 307–315 (2001).

274. Yue, R., Shen, B. & Morrison, S. J. Clec11a/osteolectin is an osteogenic growth factor that promotes the maintenance of the adult skeleton. *Elife* **5,** 27 (2016).

275. Yang, L., Yeung, K., Ching, H., Chan, D. & Cheah, K. S. E. Hypertrophic chondrocytes can become osteoblasts and osteocytes in endochondral bone formation. **111,** (2014).

276. Ono, N., Ono, W., Nagasawa, T. & Kronenberg, H. M. A subset of chondrogenic cells provides early mesenchymal progenitors in growing bones. *Nat. Cell Biol.* **16,** 1157–1167 (2014).

277. Donato, R., R. Cannon, B., Sorci, G., Riuzzi, F., Hsu, K., J. Weber, D. & L. Geczy, C. Functions of S100 Proteins. *Curr. Mol. Med.* **13,** 24–57 (2013).

278. Gillette, J. M. The role of annexin 2 in osteoblastic mineralization. *J. Cell Sci.* **117,** 441–449 (2003).

279. Svenningsson, P., Chergui, K., Rachleff, I., Flajolet, M. & Zhang, X. Alterations in 5-HT1B receptor function by p11 in depression-like states. *Science (80-.).* **311,** 77–80 (2006).

280. Warner-Schmidt, J. L., Flajolet, M., Maller, A., Chen, E. Y., Qi, H., Svenningsson, P. & Greengard, P. Role of p11 in Cellular and Behavioral Effects of 5-HT4 Receptor Stimulation. *J. Neurosci.* **29,** 1937–1946 (2009).

281. Egeland, M., Warner-Schmidt, J., Greengard, P. & Svenningsson, P. Co-expression of serotonin 5-HT1B and 5-HT4 receptors in p11 containing cells in cerebral cortex, hippocampus, caudate-putamen and cerebellum. *Neuropharmacology* **61,** 442–450 (2011).

282. Warner-Schmidt, J. L., Chen, E. Y., Zhang, X., Marshall, J. J., Morozov, A., Svenningsson, P. & Greengard, P. A role for p11 in the antidepressant action of brain-derived neurotrophic factor. *Biol. Psychiatry* **68,** 528–535 (2010).

283. Kwon, Mijung. S100A10, annexin A2, and annexin a2 heterotetramer as candidate plasminogen receptors. *Front. Biosci.* **10,** 300 (2005).

284. Yabluchanskiy, A., Ma, Y., Iyer, R. P., Hall, M. E. & Lindsey, M. L. Matrix Metalloproteinase-9: Many Shades of Function in Cardiovascular Disease. *Physiology* **28,** 391–403 (2013).

285. O'Connell, P. A., Surette, A. P., Liwski, R. S., Svenningsson, P. & Waisman, D. M. S100A10 regulates plasminogen-dependent macrophage invasion. *Blood* **116,** 1136–1146 (2010).

286. van de Graaf, S. F. J., Hoenderop, J. G. J., Gkika, D., Lamers, D., Prenen, J., Rescher, U., Gerke, V., Staub, O., Nilius, B. & Bindels, R. J. M. Functional expression of the epithelial Ca2+ channels (TRPV5 and TRPV6) requires association of the S100A10-annexin 2. **22,** 1478–1487 (2003).

287. Chen, F., Ni, B., Yang, Y. O., Ye, T. & Chen, A. Knockout of TRPV6 causes osteopenia in mice by increasing osteoclastic differentiation and activity. *Cell. Physiol. Biochem.* **33,** 796–809 (2014).

288. Cmoch, A., Strzelecka-Kiliszek, A., Palczewska, M., Groves, P. & Pikula, S. Matrix vesicles isolated from mineralization-competent Saos-2 cells are selectively enriched with annexins and S100 proteins. *Biochem. Biophys. Res. Commun.* **412,** 683–687 (2011).

289. Cmoch, A., Strzelecka-Kiliszek, A., Palczewska, M., Groves, P. & Pikula, S. S100A4 and S100A10 proteins as regulators of matrix vesicle mediated mineralization of osteoblast-like cells. *Bone* **50,** S69–S70 (2012).

290. Deutsch, E. W., Overall, C. M., Van Eyk, J. E., Baker, M. S., Paik, Y. K., Weintraub, S. T., Lane, L., Martens, L., Vandenbrouck, Y., Kusebauch, U., Hancock, W. S., Hermjakob, H., Aebersold, R., Moritz, R. L. & Omenn, G. S. Human Proteome Project Mass Spectrometry Data Interpretation Guidelines 2.1. *J. Proteome Res.* **15,** 3961–3970 (2016).

291. Tyanova, S., Temu, T. & Cox, J. The MaxQuant computational platform for mass spectrometry-based shotgun proteomics. *Nat. Protoc.* **11,** 2301–2319 (2016).

292. Tyanova, S., Temu, T., Sinitcyn, P., Carlson, A., Hein, M. Y., Geiger, T., Mann, M. & Cox, J. The Perseus computational platform for comprehensive analysis of (prote)omics data. *Nat. Methods* **13,** 731–40 (2016).

293. Naba, A., Clauser, K. R., Ding, H., Whittaker, C. A., Carr, S. A. & Hynes, R. O. The extracellular matrix: Tools and insights for the 'omics' era. *Matrix Biol.* **49,** 10–24 (2016).

294. Thorpe, S. D., Buckley, C. T., Vinardell, T., O'Brien, F. J., Campbell, V. A. & Kelly, D. J. The Response of Bone Marrow-Derived Mesenchymal Stem Cells to Dynamic Compression Following TGF-β3 Induced Chondrogenic Differentiation. *Ann. Biomed. Eng.* **38,** 2896–2909 (2010).

295. Fukushi, J., Makagiansar, I. T. & Stallcup, W. B. NG2 proteoglycan promotes endothelial cell motility and angiogenesis via engagement of galectin-3 and alpha3beta1 integrin. *Mol. Biol. Cell* **15,** 3580–90 (2004).

296. Ozerdem, U. & Stallcup, W. B. Pathological angiogenesis is reduced by targeting pericytes via the NG2 proteoglycan. *Angiogenesis* **7,** 269–276 (2004).

297. Kadomatsu, T., Endo, M., Miyata, K. & Oike, Y. Diverse roles of ANGPTL2 in physiology and pathophysiology. *Trends Endocrinol. Metab.* **25,** 245–254 (2014).

298. Kubota, Y. Unveiling Angptl2, a rising HSC expander. *Blood* **124,** 833–834 (2014).

299. Inada, M., Wang, Y., Byrne, M. H., Rahman, M. U., Miyaura, C., Lopez-Otin, C. & Krane, S. M. Critical roles for collagenase-3 (Mmp13) in development of growth plate cartilage and in endochondral ossification. *Proc. Natl. Acad. Sci.* **101,** 17192–17197 (2004).

300. Stickens, D. Altered endochondral bone development in matrix metalloproteinase 13-deficient mice. *Development* **131,** 5883–5895 (2004).

301. Sadatsuki, R., Kaneko, H., Kinoshita, M., Futami, I., Nonaka, R., Culley, K. L., Otero, M., Hada, S., Goldring, M. B., Yamada, Y., Kaneko, K., Arikawa-Hirasawa, E. & Ishijima, M. Perlecan is required for the chondrogenic

differentiation of synovial mesenchymal cells through regulation of Sox9 gene expression. *J. Orthop. Res.* **35,** 837–846 (2017).

302.   Arikawa-Hirasawa, E., Watanabe, H., Takami, H., Hassell, J. R. & Yamada, Y. Perlecan is essential for cartilage and cephalic development. *Nat. Genet.* **23,** 354–358 (1999).

303.   von der Mark, K. & Mollenhauer, J. Annexin V interactions with collagen. *Cell. Mol. Life Sci.* **53,** 539–545 (1997).

304.   Cleland, T. P., Voegele, K. & Schweitzer, M. H. Empirical evaluation of bone extraction protocols. *PLoS One* **7,** 1–9 (2012).

305.   Zimmerman, L. J., Li, M., Yarbrough, W. G., Slebos, R. J. C. & Liebler, D. C. Global Stability of Plasma Proteomes for Mass Spectrometry-Based Analyses. *Mol. Cell. Proteomics* **11,** M111.014340-M111.014340 (2012).

306.   Fukushi, J. I., Inatani, M., Yamaguchi, Y. & Stallcup, W. B. Expression of NG2 proteoglycan during endochondral and intramembranous ossification. *Dev. Dyn.* **228,** 143–148 (2003).

307.   De Spiegelaere, W., Cornillie, P., Casteleyn, C., Burvenich, C. & Van den Broeck, W. Detection of Hypoxia Inducible Factors and Angiogenic Growth Factors during Foetal Endochondral and Intramembranous Ossification. *J. Vet. Med. Ser. C Anat. Histol. Embryol.* **39,** 376–384 (2010).

308.   Vu, T. H., Shipley, J. M., Bergers, G., Berger, J. E., Helms, J. A., Hanahan, D., Shapiro, S. D., Senior, R. M. & Werb, Z. MMP-9/gelatinase B is a key regulator of growth plate angiogenesis and apoptosis of hypetrophic chondrocytes. *Cell* **93,** 411–422 (1998).

309.   Nagai, H. & Aoki, M. Inhibition of growth plate angiogenesis and endochondral ossification with diminished expression of MMP-13 in hypertrophic chondrocytes in FGF-2-treated rats. *J. Bone Miner. Metab.* **20,** 142–147 (2002).

310.   Lourido, L. L., Calamia, V., Mateos, J. J., Fernandez-Puente, P., Fernandez-Tajes, J., Blanco, F. J., Ruiz-Romero, C., Fernández-Puente, P., Fernández-Tajes, J., Blanco, F. J. & Ruiz-Romero, C. Quantitative proteomic profiling of human articular cartilage degradation in osteoarthritis. *J. Proteome Res.* **13,** 6096–106

(2014).

311. Anderson, H. C., Hodges, P. T., Aguilera, X. M., Missana, L. & Moylan, P. E. Bone Morphogenetic Protein (BMP) Localization in Developing Human and Rat Growth Plate, Metaphysis, Epiphysis, and Articular Cartilage. *J. Histochem. Cytochem.* **48,** 1493–1502 (2000).

312. Tamaddon, M., Burrows, M., Ferreira, S. A., Dazzi, F., Apperley, J. F., Bradshaw, A., Brand, D. D., Czernuszka, J. & Gentleman, E. Monomeric, porous type II collagen scaffolds promote chondrogenic differentiation of human bone marrow mesenchymal stem cells in vitro. *Sci. Rep.* **7,** 1–10 (2017).

313. Önnerfjord, P., Khabut, A., Reinholt, F. P., Svensson, O. & Heinegård, D. Quantitative proteomic analysis of eight cartilaginous tissues reveals characteristic differences as well as similarities between subgroups. *J. Biol. Chem.* **287,** 18913–24 (2012).

314. Gazzerro, E., Pereira, R. C., Jorgetti, V., Olson, S., Economides, A. N. & Canalis, E. Skeletal overexpression of gremlin impairs bone formation and causes osteopenia. *Endocrinology* **146,** 655–665 (2005).

315. Hu, K., Sun, H., Gui, B. & Sui, C. Gremlin-1 suppression increases BMP-2-induced osteogenesis of human mesenchymal stem cells. *Mol. Med. Rep.* **15,** 2186–2194 (2017).

316. Redman, S. N., Oldfield, S. F., Archer, C. W., Roughley, P. J. & Lee, C. Current strategies for articular cartilage repair. *Eur. Cells Mater.* **9,** 23–32 (2005).

317. Hussey, G. S., Dziki, J. L. & Badylak, S. F. Extracellular matrix-based materials for regenerative medicine. *Nat. Rev. Mater.* **3,** 159–173 (2018).

318. Fiona Freeman et al. Biofabrication of multiscale bone extracellular matrix scaffolds for bone tissue engineering. *Eur. Cell. Mater.* (2019).

319. Browe, D. C., Mahon, O. R., Díaz-Payno, P. J., Cassidy, N., Dudurych, I., Dunne, A., Buckley, C. T. & Kelly, D. J. Glyoxal cross-linking of solubilized extracellular matrix to produce highly porous, elastic, and chondro-permissive scaffolds for orthopedic tissue engineering. *J. Biomed. Mater. Res. Part A* **107,** 2222–2234 (2019).

320. For, M., Study, T. H. E., Collagen, O. F. & Disorders, O. F. C. Separation treatment methods for the study of collagen and of collagen disorders. **488,** 161–197 (1989).

321. Schiller, J., Fuchs, B., Arnhold, J. & Arnold, K. Contribution of Reactive Oxygen Species to Cartilage Degradation in Rheumatic Diseases: Molecular Pathways, Diagnosis and Potential Therapeutic Strategies. *Curr. Med. Chem.* **10,** 2123–2145 (2005).

322. Cao, H., Xu, S., Ge, H. & Xu, F. Molecular characterisation of type II collagen from chick sternal cartilage and its anti-rheumatoid arthritis activity. *Food Agric. Immunol.* **25,** 119–136 (2014).

323. Vaz, Â. U. M., Graaf, L. a D. E. & Reis, R. U. I. L. Effect of crosslinking , thermal treatment and UV irradiation on the mechanical properties and in vitro degradation behavior of several natural proteins aimed to be used in the biomedical ® eld. *In Vitro* **4,** 789–796 (2003).

324. Bowes, J. H. & Cater, C. W. The interaction of aldehydes with collagen. *BBA - Protein Struct.* **168,** 341–352 (1968).

325. Davis, P. & Tabor, B. E. Kinetic study of the crosslinking of gelatin by formaldehyde and glyoxal. *J. Polym. Sci. Part A Gen. Pap.* **1,** 799–815 (1963).

326. Glomb, M. A. & Monnier, V. M. Mechanism of protein modification by glyoxal and glycolaldehyde, reactive intermediates of the Maillard reaction. *J. Biol. Chem.* **270,** 10017–10026 (1995).

327. Mattson, G., Conklin, E., Desai, S., Nielander, G., Savage, M. D. & Morgensen, S. A practical approach to crosslinking. *Mol. Biol. Rep.* **17,** 167–183 (1993).

328. Wang, L. & Stegemann, J. P. Glyoxal Crosslinking of Cell-Seeded Chitosan/Collagen Hydrogels for Bone Regeneration. *Acta Biomater.* **7,** 2410–2417 (2011).

329. Hoemann, C. D., Chenite, A., Sun, J., Hurtig, M., Serreqi, A., Lu, Z., Rossomacha, E. & Buschmann, M. D. Cytocompatible gel formation of chitosan-glycerol phosphate solutions supplemented with hydroxyl ethyl cellulose is due to the presence of glyoxal. *J. Biomed. Mater. Res. Part A* **83A,** 521–529 (2007).

330. Ignat'eva, N. Y., Danilov, N. A., Averkiev, S. V., Obrezkova, M. V., Lunin, V. V. & Sobol', E. N. Determination of hydroxyproline in tissues and the evaluation of the collagen content of the tissues. *J. Anal. Chem.* **62,** 51–57 (2007).

331. Kaplan, A. L. & Pesce, A. *Clinical Chemistry*. (Mosby Ed., 1996).

332. Corrigan, M. A., Johnson, G. P., Stavenschi, E., Riffault, M., Labour, M. N. & Hoey, D. A. TRPV4-mediates oscillatory fluid shear mechanotransduction in mesenchymal stem cells in part via the primary cilium. *Sci. Rep.* **8,** 1–13 (2018).

333. Ummarino, D. Osteoarthritis: Hypoxia protects against cartilage loss by regulating Wnt signalling. *Nat. Rev. Rheumatol.* **12,** 2016 (2016).

334. Bouaziz, W., Sigaux, J., Modrowski, D., Devignes, C.-S., Funck-Brentano, T., Richette, P., Ea, H.-K., Provot, S., Cohen-Solal, M. & Haÿ, E. Interaction of HIF1α and β-catenin inhibits matrix metalloproteinase 13 expression and prevents cartilage damage in mice. *Proc. Natl. Acad. Sci.* **113,** 5453–5458 (2016).

335. Lu, Z., Doulabi, B. Z., Huang, C., Bank, R. A. & Helder, M. N. Collagen type II enhances chondrogenesis in adipose tissue-derived stem cells by affecting cell shape. *Tissue Eng. Part A* **16,** 81–90 (2010).

336. Stabile, H., Mitola, S., Moroni, E., Belleri, M., Nicoli, S., Coltrini, D., Peri, F., Pessi, A., Orsatti, L., Talamo, F., Castronovo, V., Waltregny, D., Cotelli, F., Ribatti, D. & Presta, M. Bone morphogenic protein antagonist Drm/gremlin is a novel proangiogenic factor. *Blood* **109,** 1834–1840 (2007).

337. Chang, S. H., Mori, D., Kobayashi, H., Mori, Y., Nakamoto, H., Okada, K., Taniguchi, Y., Sugita, S., Yano, F., Chung, U. il, Kim-Kaneyama, J. ri, Yanagita, M., Economides, A., Canalis, E., Chen, D., Tanaka, S. & Saito, T. Excessive mechanical loading promotes osteoarthritis through the gremlin-1–NF-κB pathway. *Nat. Commun.* **10,** 1–5 (2019).

338. Ortega, N., Behonick, D. J. & Werb, Z. Matrix remodeling during endochondral ossification. *Trends Cell Biol.* **14,** 86–93 (2004).

339. Gawlitta, D., van Rijen, M. H. P., Schrijver, E. J. M., Alblas, J. & Dhert, W. J. A. Hypoxia Impedes Hypertrophic Chondrogenesis of Human Multipotent Stromal Cells. *Tissue Eng. Part A* **18,** 1957–1966 (2012).

340. Gómez-Leduc, T., Desancé, M., Hervieu, M., Legendre, F., Ollitrault, D., de Vienne, C., Herlicoviez, M., Galéra, P. & Demoor, M. Hypoxia is a critical parameter for chondrogenic differentiation of human umbilical cord blood mesenchymal stem cells in type I/III collagen sponges. *Int. J. Mol. Sci.* **18,** 1–23 (2017).

341. Pattappa, G., Johnstone, B., Zellner, J., Docheva, D. & Angele, P. The importance of physioxia in mesenchymal stem cell chondrogenesis and the mechanisms controlling its response. *Int. J. Mol. Sci.* **20,** (2019).

342. Zhu, M., Feng, Q. & Bian, L. Differential effect of hypoxia on human mesenchymal stem cell chondrogenesis and hypertrophy in hyaluronic acid hydrogels. *Acta Biomater.* **10,** 1333–1340 (2014).

343. Leijten, J. C. H., Moreira Teixeira, L. S., Landman, E. B. M., van Blitterswijk, C. A. & Karperien, M. Hypoxia Inhibits Hypertrophic Differentiation and Endochondral Ossification in Explanted Tibiae. *PLoS One* **7,** 1–7 (2012).

344. Abramovitch, R., Frenkiel, D. & Neeman, M. Analysis of subcutaneous angiogenesis by gradient echo magnetic resonance imaging. *Magn. Reson. Med.* **39,** 813–824 (1998).

345. Rathan, S., Dejob, L., Schipani, R., Haffner, B., Möbius, M. E. & Kelly, D. J. Fiber Reinforced Cartilage ECM Functionalized Bioinks for Functional Cartilage Tissue Engineering. *Adv. Healthc. Mater.* **8,** 1–11 (2019).

346. Haugh, M. G., Murphy, C. M. & O'Brien, F. J. Novel freeze-drying methods to produce a range of collagen-glycosaminoglycan scaffolds with tailored mean pore sizes. *Tissue Eng. Part C. Methods* **16,** 887–94 (2010).

347. Divakar, P., Yin, K. & Wegst, U. G. K. Values and property charts for anisotropic freeze-cast collagen scaffolds for tissue regeneration. *Data Br.* **22,** 502–507 (2019).

348. Wu, X., Liu, Y., Li, X., Wen, P., Zhang, Y., Long, Y., Wang, X., Guo, Y., Xing, F. & Gao, J. Preparation of aligned porous gelatin scaffolds by unidirectional freeze-drying method. *Acta Biomater.* **6,** 1167–1177 (2010).

349. Davidenko, N., Gibb, T., Schuster, C., Best, S. M., Campbell, J. J., Watson, C. J.

& Cameron, R. E. Biomimetic collagen scaffolds with anisotropic pore architecture. *Acta Biomater.* **8,** 667–676 (2012).

350. Divakar, P., Yin, K. & Wegst, U. G. K. Anisotropic freeze-cast collagen scaffolds for tissue regeneration: How processing conditions affect structure and properties in the dry and fully hydrated states. *J. Mech. Behav. Biomed. Mater.* **90,** 350–364 (2019).

351. Almeida, H. V., Sathy, B. N., Dudurych, I., Buckley, C. T., O'Brien, F. J. & Kelly, D. J. Anisotropic Shape-Memory Alginate Scaffolds Functionalized with Either Type I or Type II Collagen for Cartilage Tissue Engineering. *Tissue Eng. Part A* **23,** 55–68 (2017).

352. Oliveira, A. L., Sun, L., Kim, H. J., Hu, X., Rice, W., Kluge, J., Reis, R. L. & Kaplan, D. L. Aligned silk-based 3-D architectures for contact guidance in tissue engineering. *Acta Biomater.* **8,** 1530–1542 (2012).

353. Zhou, Y., Fu, S., Pu, Y., Pan, S. & Ragauskas, A. J. Preparation of aligned porous chitin nanowhisker foams by directional freeze-casting technique. *Carbohydr. Polym.* **112,** 277–283 (2014).

354. Yin, K., Divakar, P., Hong, J., Moodie, K. L., Rosen, J. M., Sundback, C. A., Matthew, M. K. & Wegst, U. G. K. Freeze-cast Porous Chitosan Conduit for Peripheral Nerve Repair. *MRS Adv.* **3,** 1677–1683 (2018).

355. Chen, C. W., Tsai, Y. H., Deng, W. P., Shih, S. N., Fang, C. L., Burch, J. G., Chen, W. H. & Lai, W. F. Type I and II collagen regulation of chondrogenic differentiation by mesenchymal progenitor cells. *J. Orthop. Res.* **23,** 446–453 (2005).

356. Rutgers, M., Saris, D. B., Vonk, L. A., van Rijen, M. H., Akrum, V., Langeveld, D., Van Boxtel, A., Dhert, W. J. & Creemers, L. B. Effect of collagen type I or type II on chondrogenesis by cultured human articular chondrocytes. *Tissue Eng. Part A* **19,** 59–65 (2013).

357. Venkatesan, J., Vinodhini, P. A., Sudha, P. N. & Kim, S. K. *Chitin and chitosan composites for bone tissue regeneration*. *Adv. Food Nutr. Res.* **73,** (Elsevier Inc., 2014).

358. Haugh, M. G., Jaasma, M. J. & O'Brien, F. J. The effect of dehydrothermal treatment on the mechanical and structural properties of collagen- GAG scaffolds. *J. Biomed. Mater. Res. A* **89,** 363–369 (2009).

359. Kiec-Swierczynska, M., Krecisz, B., Krysiak, B., Kuchowicz, E. & Rydzynski, K. Occupational allergy to aldehydes in health care workers. Clinical observations. Experiments. *Int. J. Occup. Med. Environ. Health* (1998).

360. Bencherif, S. A., Sands, R. W., Bhatta, D., Arany, P., Verbeke, C. S., Edwards, D. A. & Mooney, D. J. Injectable preformed scaffolds with shape-memory properties. *Proc. Natl. Acad. Sci.* **109,** 19590–19595 (2012).

361. Shen, Z. L., Dodge, M. R., Kahn, H., Ballarini, R. & Eppell, S. J. Stress-Strain Experiments on Individual Collagen Fibrils. *Biophys. J.* **95,** 3956–3963 (2008).

362. Peacock, C. J. & Kreplak, L. Nanomechanical mapping of single collagen fibrils under tension. *Nanoscale* (2019). doi:10.1039/c9nr02644d

363. Arora, A., Kothari, A. & Katti, D. S. Pore orientation mediated control of mechanical behavior of scaffolds and its application in cartilage-mimetic scaffold design. *J. Mech. Behav. Biomed. Mater.* **51,** 169–183 (2015).

364. Tijore, A., Irvine, S. A., Sarig, U., Mhaisalkar, P., Baisane, V. & Venkatraman, S. Contact guidance for cardiac tissue engineering using 3D bioprinted gelatin patterned hydrogel. *Biofabrication* **10,** (2018).

365. Nguyen, L. H., Gao, M., Lin, J., Wu, W., Wang, J. & Chew, S. Y. Three-dimensional aligned nanofibers-hydrogel scaffold for controlled non-viral drug/gene delivery to direct axon regeneration in spinal cord injury treatment. *Sci. Rep.* **7,** 1–12 (2017).

366. Li, W., Xu, R., Huang, J., Bao, X. & Zhao, B. Treatment of rabbit growth plate injuries with oriented ECM scaffold and autologous BMSCs. *Sci. Rep.* **7,** 1–11 (2017).

367. Mansour, J. M. in *Kinesiol. Mech. pathomechanics Hum. Mov.* (ed. A. Oatis, C.) 69–83 (Wolters Kluwer Health, 2013). doi:10.1002/art.23548

368. Storm, T., Wulf, K., Teske, M., Löbler, M., Kundt, G., Luderer, F., Schmitz, K. P., Sternberg, K. & Hovakimyan, M. Chemical activation and changes in surface

morphology of poly(ε-caprolactone) modulate VEGF responsiveness of human endothelial cells. *J. Mater. Sci. Mater. Med.* **25,** 2003–2015 (2014).

369. Wang, W., Caetano, G., Ambler, W. S., Blaker, J. J., Frade, M. A., Mandal, P., Diver, C. & Bï¿½rtolo, P. Enhancing the hydrophilicity and cell attachment of 3D printed PCL/graphene scaffolds for bone tissue engineering. *Materials (Basel).* **9,** (2016).

370. Camarero-Espinosa, S., Rothen-Rutishauser, B., Weder, C. & Foster, E. J. Directed cell growth in multi-zonal scaffolds for cartilage tissue engineering. *Biomaterials* **74,** 42–52 (2016).

371. Kang, H., Zeng, Y. & Varghese, S. Functionally graded multilayer scaffolds for in vivo osteochondral tissue engineering. *Acta Biomater.* **78,** 365–377 (2018).

372. Seibel, M. J. Biochemical markers of bone turnover: part I: biochemistry and variability. *Clin. Biochem. Rev.* **26,** 97–122 (2005).

373. Levingstone, T. J., Ramesh, A., Brady, R. T., Brama, P. A. J., Kearney, C., Gleeson, J. P., O'Brien, F. J., Levingstone, T. J., Ramesh, A., Gleeson, J. P., Brady, R. T., Brama, P. A. J. & Kearney, C. Cell-free multi-layered collagen-based scaffolds demonstrate layer specific regeneration of functional osteochondral tissue in caprine joints. *Biomaterials* **87,** 69–81 (2016).

374. Kurpinski, K., Stephenson, J., Janairo, R. R. R., Lee, H. & Li, S. The Effect of Fiber Alignment and Heparin Coating on Cell Infiltration into Nanofibrous PLLA Scaffolds. *Biomaterials* **31,** 3536–3542 (2010).

375. O'Brien, F. J., Harley, B. A., Waller, M. A., Yannas, I. V, Gibson, L. J. & Prendergast, P. J. The effect of pore size on permeability and cell attachment in collagen scaffolds for tissue engineering. *Technol. Health Care* **15,** 3–17 (2007).

376. Elder, B. D. & Athanasiou, K. A. Hydrostatic pressure in articular cartilage tissue engineering: from chondrocytes to tissue regeneration. *Tissue Eng. Part B. Rev.* **15,** 43–53 (2009).

377. Lee, H.-H., Chang, C.-C., Shieh, M.-J., Wang, J.-P., Chen, Y.-T., Young, T.-H. & Hung, S.-C. Hypoxia enhances chondrogenesis and prevents terminal differentiation through PI3K/Akt/FoxO dependent anti-apoptotic effect. *Sci. Rep.*

3, 2683 (2013).

378. Thorpe, S. D., Nagel, T., Carroll, S. F. & Kelly, D. J. Modulating Gradients in Regulatory Signals within Mesenchymal Stem Cell Seeded Hydrogels: A Novel Strategy to Engineer Zonal Articular Cartilage. *PLoS One* **8,** e60764; 1–13 (2013).

379. Gannon, A. R., Nagel, T., Bell, A. P., Avery, N. C. & Kelly, D. J. Postnatal changes to the mechanical properties of articular cartilage are driven by the evolution of its Collagen network. *Eur. Cells Mater.* **29,** 105–123 (2015).

380. Brown, B. N. & Badylak, S. F. in *Transl. Regen. Med. to Clin.* **163,** 11–29 (Mosby, Inc, 2015).

381. Qiang, Y., Yanhong, Z., Jiang, P., Shibi, L., Quanyi, G., Xinlong, M., Qun, X., Baoshan, X., Bin, Z., Aiyuan, W., Li, Z., Wengjing, X. & Chao, Z. Xenoimplantation of an extracellular-matrix-derived, biphasic, cell-scaffold construct for repairing a large femoral-head high-load-bearing osteochondral defect in a canine model. *Sci. World J.* **2014,** (2014).

382. Papadimitropoulos, A., Scotti, C., Bourgine, P., Scherberich, A. & Martin, I. Engineered decellularized matrices to instruct bone regeneration processes. *Bone* **70,** 66–72 (2015).

383. Smith, C. A., Board, T. N., Rooney, P., Eagle, M. J., Richardson, S. M. & Hoyland, J. A. Human decellularized bone scaffolds from aged donors show improved osteoinductive capacity compared to young donor bone. *PLoS One* **12,** 1–15 (2017).

384. Qin, C., Baba, O. & Butler, W. T. Post-translational modifications of SIBLING proteins and their roles in osteogenesis and dentinogenesis. *Crit. Rev. Oral Biol. Med.* **15,** 126–136 (2004).

385. Weis, M. A., Hudson, D. M., Kim, L., Scott, M., Wu, J. J. & Eyre, D. R. Location of 3-Hydroxyproline residues in collagen types I, II, III, and V/XI implies a role in fibril supramolecular assembly. *J. Biol. Chem.* **285,** 2580–2590 (2010).

386. Szpak, P. Fish bone chemistry and ultrastructure: Implications for taphonomy and stable isotope analysis. *J. Archaeol. Sci.* **38,** 3358–3372 (2011).

387. Chen, Y., Huang, Y. C., Yan, C. H., Chiu, K. Y., Wei, Q., Zhao, J., Guo, X. E.,

Leung, F. & Lu, W. W. Abnormal subchondral bone remodeling and its association with articular cartilage degradation in knees of type 2 diabetes patients. *Bone Res.* **5,** (2017).

388. Morales, T. I., Joyce, M. E., Sobel, M. E., Daniepour, D. & Roberts, A. B. Transforming growth factor-beta in calf articular cartilage organ cultures: synthesis and distribution. *Arch. Biochem. Biophys.* **288,** 397–405 (1991).

389. Carroll, S. F., Buckley, C. T. & Kelly, D. J. Cyclic Tensile Strain Can Play a Role in Directing both Intramembranous and Endochondral Ossification of Mesenchymal Stem Cells. *Front. Bioeng. Biotechnol.* **5,** 1–12 (2017).

390. Bai, H., Chen, Y., Delattre, B., Tomsia, A. P. & Ritchie, R. O. Bioinspired large-scale aligned porous materials assembled with dual temperature gradients. *Sci. Adv.* **1,** e1500849 (2015).

391. Zhang, H., Hussain, I., Brust, M., Butler, M. F., Rannard, S. P. & Cooper, A. I. Aligned two- and three-dimensional structures by directional freezing of polymers and nanoparticles. *Nat. Mater.* **4,** 787–793 (2005).